CRANFIELD UNIVERSITY

XIANGFANG XU

WIRE + ARC ADDITIVE MANUFACTURE OF NEW AND MULTIPLE MATERIALS

SCHOOL OF AEROSPACE, TRANSPORT AND MANUFACTURING
Welding Engineering and Laser Processing Centre

PhD
Academic Year: 2018-2019

Supervisor: Dr. Supriyo Ganguly
Associate Supervisor: Dr. Jialuo Ding
August 2018

CRANFIELD UNIVERSITY

SCHOOL OF AEROSPACE, TRANSPORT AND MANUFACTURING
Welding Engineering and Laser Processing Centre

PhD

Academic Year 2018-2019

XIANGFANG XU

Wire + arc additive manufacture of new and multiple materials

Supervisor: Dr. Supriyo Ganguly
Associate Supervisor: Dr. Jialuo Ding
August 2018

This thesis is submitted in partial fulfilment of the requirements for the degree of Doctor of Philosophy

ABSTRACT

Wire + Arc Additive Manufacture (WAAM) features high deposition rates, short lead times and low equipment investment. WAAM is especially suitable for producing large-scale parts made from highly demanding and expensive materials and provides design freedom for multi-material structures. Although WAAM has been successfully applied to titanium alloys, its feasibility to deposit various other single material and multiple materials are yet to be studied, and the resulting WAAM material properties are largely unknown.

Maraging steel and Inconel 718 are highly advanced alloys widely used for critical components in aerospace, and Inconel 625 cladded steel pipes are extensively applied in Oil & Gas industry, all of which require an alternative manufacturing process to forging and casting. The present work aims at utilizing WAAM to deposit maraging steel, Inconel 718, and Inconel 625/low alloy steel multi-material structures complying with the industrial standard. The objective for the single material is to develop the strength comparable to wrought alloy, while dilution control is the concern for the multi-material deposition. Material characterization was carried out to understand the WAAM microstructure resulting from the inherent thermal history and explain the strength inferiority to the wrought material from a crystallographic scale. Industry standard heat treatment and interpass cold rolling were applied to improve the strength of WAAM material to the wrought level based on the understanding of the strengthening mechanisms of a particular material. Besides, environmental factors affecting the deposition feasibility was studied, and strategies controlling the dilution level for multi-material deposition was developed.

The research contributes to the WAAM material database of maraging steel and Inconel 718 and proves the capability of building multi-material structures using WAAM. A research pattern for applying WAAM to various new materials and applications is established, and a scientific understanding of the relationship between the WAAM process and material properties was gained.

Keywords: maraging steel, Inconel 718, aging, oxides, mechanical properties, microstructure, dilution, rolling, recrystallization.

ACKNOWLEDGEMENTS

I would like to firstly acknowledge the financial support from China Scholarship Council (CSC, NO.201506680057) and the WAAMMat program industrial partners who make this three-year PhD research possible.

I wish to express my sincere gratitude to my supervisors as well as good friends, Dr. Supriyo Ganguly and Dr. Jialuo Ding, for their scientific and technical guidance and support throughout the research. It could have never been a more enjoyable three-year journey with you both.

Special regards to Prof. Stewart Williams who offered me the PhD position 3 years ago; many thanks to Mr. Andrew Mills who chaired all my review meetings.

I would also like to thank Flemming Nielsen, Nisar Shah, and Jonathan Pratt for their assistance during the experimental work, Dr Xianwei Liu, Steve Pope, Dr Christine Kimpton, and Dr Tracey Roberts for their assistance during the metallographic and SEM/XRD/EBSD analysis, Ben Hopper for the assistance in the mechanical testing lab, and Cui Er Seow (from TWI) for the help in EBSD.

To my amazing colleagues as well as good friends, who are or were at WELPC, I want to say a big thank you for making me feel like being part of this big family. Armando, Gianrocco, Eloise, Kwasi, Jan, Sergio, Yashwanth, Zsolt, Florent, Leonor, Junny, Kuladeep, Julio, Pawel, Sonia, Goncalo, Uzoma, Philip, Philippe, Qiong Gao, Chenglei Diao, Shun Guo, Xingwang Bai, Chong Wang, Xiaoyong Zhang, Chao Liu, Dr Filomeno Martina, Dr Paul Colegrove, Dr Wojciech Suder and so on, thank you all. Special thanks to my good friends Ye Xie, Yicheng Sun, Kanming Wang and Yuzhi Chen for your friendship during the PhD period.

Finally, I would like to thank my family, as well as my girlfriend's family, for being so supportive of me doing a PhD abroad at the age when I was supposed to work and support the family; gratefulness is beyond words and I know your pain behind so as to make me focus on research. I would like to owe this PhD to my beloved girlfriend, my wife soon, Boya Wang, the source of my passion, inspiration and motivation; she is the one who makes me believe I can be a better myself.

LIST OF PUBLICATIONS

Journals

- ***X. Xu***, J. Ding, S. Ganguly, C. Diao, S. Williams, Oxide accumulation effects on wire + arc layer-by-layer additive manufacture process, J. Mater. Process. Tech. 252 (2018) 739–750. (Q1, IF=3.647)
- ***X. Xu***, S. Ganguly, J. Ding, S. Guo, S. Williams, F. Martina, Microstructural evolution and mechanical properties of maraging steel produced by wire + arc additive manufacture process, Mater. Charact. 143 (2018) 152–162. (Q1, IF=2.892)
- ***X. Xu***, J. Ding, S. Ganguly, C. Diao, S. Williams, Preliminary Investigation of Building Strategies of Maraging Steel Bulk Material Using Wire + Arc Additive Manufacture, J. Mater. Eng. Perform. (2018) 1–7. (Q3, IF=1.340)
- S. Guo, Q. Zhou, Y. Peng, ***X. Xu***, C. Diao, J. Kong, T. Luo, K. Wang, J. Zhu, Study on strengthening mechanism of Ti/Cu electron beam welding, Mater. Des. 121 (2017) 51–60. (Q1, IF=4.525)
- ***X. Xu***, S. Ganguly, J. Ding, D. Philip, F. Martina, X. Liu, S. Williams, Improving mechanical properties of wire + arc additively manufactured maraging steel through plastic deformation enhanced aging response. Mater. Sci. Eng. A. (Revise)
- ***X. Xu***, J. Ding, S. Ganguly, S. Williams, Investigation of process factors affecting mechanical properties of INCONEL 718 superalloy in wire + arc additive manufacture process, J. Mater. Process. Tech. (under review)
- ***X. Xu***, S. Ganguly, J. Ding, C. Seow, S. Williams, Enhancing mechanical properties of wire + arc additively manufactured INCONEL 718 superalloy through in-process thermomechanical processing, Mater. Des. (Revise)

Conferences

- ***X. Xu***, J. Ding, S. Ganguly, S. Williams. Wire + arc additive manufacture of inconel 625/low alloy steel multi-material functional structure for Oil & Gas applications. Proceedings of MSSM2018, 07-10 Aug 2018, UWS, Paisley, Glasgow, UK, P49-54.

- ***X. Xu***, J. Ding, S. Ganguly, C. Diao, S. Williams. Wire + arc additive manufacture for maraging steels. MS&T17, 08-12 Oct 2017, Pittsburgh, USA.
- F. Martina, ***X. Xu***, A. Caballero, Z. Pinter, J. Ding, P. Colegrove, S. Ganguly, S. Williams, 2018. Applications of wire + arc additive manufacture to critical components in the Oil & Gas industry, 2nd Conference & Expo, Genoa, Italy.
- E. Eimer, J. Honnige, ***X. Xu***, S. Ganguly, Residual stress measurement wire + arc additive manufactured IN718. ILL & ESS European User Meeting, Oct. 10-12, 2018, Grenoble, France. (Accepted as poster)
- P. Dirisu, S. Ganguly, F. Martina, ***X. Xu***. The effect of surface waviness on the fatigue properties of wire + arc additively manufactured mild steel combined with high pressure rolling. International Conference on Fatigue Damage of Structural Materials XII, 16-21 Sep 2018, Hyannis, MA, USA.

Course notes

The work of Inconel 718, Chapter 7 and 8, are used as the source by Senior Lecturer Paul Colegrove at Cranfield University when he created the course notes on Nickel deposition.

- Topic 5 Nickel and nickel alloys.
  - 3. Deposition of IN718 (courtesy of Xiangfang Xu)

TABLE OF CONTENTS

LIST OF FIGURES

LIST OF TABLES

LIST OF EQUATIONS

LIST OF ABBREVIATIONS

A	aging (without prior solution)
AD	as deposited
A_f	austenite finishing temperature
AM	Additive Manufacture, Additive Manufacturing
AMS	Aerospace Material Specifications
bcc	body-centred cubic
bct	body-centred tetragonal
CC	constant current
CMT	cold metal transfer
CNC	computer numerical control
CTE	coefficient of thermal expansion
CTWD	contact tip-to-work distance
DC	direct current
DE	deposition efficiency
DMD	direct metal deposition
EBSD	electron backscatter diffraction
EDS	energy-dispersive spectrometry
EWA	effective wall area
EWW	effective wall width
fcc	face-centred cubic
FIB	focused ion beam
GA	gas atomized
H	horizontal
hcp	hexagonal close packed
HIP	hot isostatic pressing
HSA	homogenization + solution + aging
IN625	Inconel 625
IN718	Inconel 718
MIG	metal inert gas
M_s	martensite start temperature
OM	optical microscopy
PBF	powder bed fusion

PREP	plasma rotation electrode preparation
S	solution treatment, solutionizing
SA	solution plus aging
SEM	Scanning Electron Microscope
SLM	selective laser melting
SMD	shaped metal deposition
SW	surface waviness
TEM	transmission electron microscopy
TIG	tungsten inert gas
TRL	technology readiness level
TS	travel speed
TTT	time temperature transformation
TWA	total wall area
TWW	total wall width
UTS	ultimate tensile strength
V	vertical
VAR	vacuum arc remelting
VIM	vacuum induction melting
WAAM	Wire + Arc Additive Manufacture
WELPC	Welding Engineering and Laser Processing Centre
WFS	wire feed speed
XRD	X-ray diffraction
YS	yield strength

1 Introduction

1.1 Research background

Metal additive manufacturing (AM), as opposed to the conventional subtractive manufacturing, has gained extensive attention from various industrial sectors over the past decades due to its immanent benefits in providing greater design freedom, reducing material wastage and shortening lead times. Among various AM processes, Wire + Arc Additive Manufacture (WAAM) can directly fabricate large-scale (meter scale), fully-dense, and near net-shaped metallic components. In this process, a wire is fed at a controlled rate into an electric arc, and the deposition paths are controlled by a robot or a computer numerical controlled (CNC) motion system to form the desired shape in a layer by layer manner. Due to the high deposition rate and low equipment investment, WAAM has been gaining more and more interest from the industry.

However, before its implementation in mass production, extensive efforts are required to improve the technology readiness level (TRL) of WAAM. The Welding Engineering and Laser Processing Centre (WELPC) at Cranfield University is internationally leading the WAAM research by initiating and managing the WAAMMat program which aims at increasing the maturity level of WAAM process to enable rapid industrial exploitation. WAAMMat is a rolling technology development programme comprising a series of individual projects and activities which are brought together under one umbrella programme.

While efforts are being made to make WAAM a reliable and robust production system, the core prerequisite of the WAAM application is to produce metallic components with adequate mechanical and metallurgical features for particular applications. From the materials aspect, WAAM should prove its feasibility to deposit various metals and alloys, and a detailed knowledge of the microstructure and mechanical properties is the prerequisite to achieve reliability and consistency of the WAAM process, which is necessary for a successful transition from the experimental state to mass production. However, as an early-stage technology, WAAM has so far been successfully experimented with limited

materials including titanium, aluminium, carbon steel, and stainless steel. The feasibility to deposit other advanced materials and the resulting microstructure and mechanical properties in response to the inherent thermal cycles are largely unknown. Besides, the previous researches are focused on a single material, and the capability of WAAM to deposit multi-material structures is also unclear.

One benefit of WAAM is the considerable reduction in material wastage and lead-time, which is attractive to manufacturing parts made of expensive and advanced alloys. Two kinds of such alloys, maraging steel (ferrous) and IN718 superalloy (non-ferrous), are studied in this PhD research. Maraging steel is widely used for its ultrahigh strength (yield strength from 1030 to 3450 MPa). The ease of fabrication in the annealed condition, good dimension stability during aging and excellent weldability make maraging steel widely used in the aerospace, weapon and tooling sectors. IN718 superalloy possesses excellent tensile, fatigue, creep, and rupture strength. IN718 is the most widely used superalloy in today's turbine engine applications. Apart from being expensive, IN718 is also known as a hard-to-machine alloy due to the significant work hardening. Demands of rapid fabrication, cost saving and design freedom of large-scale functional maraging steel and IN718 parts while still maintaining the same strength level come from these sectors and WAAM could be a promising alternative process. Besides, in order to deposit a WAAM part with a satisfactory geometric accuracy, factors affecting the surface tension and the wetting and spreading of the weld pool need to be understood; oxygen is known to change the surface tension of the liquid metal, and oxides are known to deteriorate the surface condition of the metal, which will further affect the wetting and spreading behaviour of the weld pool. A proper shielding during the deposition is crucial to expel the oxygen from the liquid metal and minimize the oxide formation. Hence, the research focus for the respective single material covers how to produce the WAAM alloy with comparable strength to the wrought alloy and how oxidation and shielding affect the WAAM process.

Another benefit of WAAM is the possibility to control the composition and phase fraction within a layer; thus, it would be possible to build multi-material

components with controlled composition through different layers, or from one end to the other. In Oil & Gas industry, steel pipelines with IN625 internal cladding is widely used to transport corrosive medium. The corrosion resistance of the clad layer comes from the control of dilution between steel and IN625 such that the Fe content in the clad layer is below a certain level. However, the production of such multi-material components is a multi-step process which involves forging, bending, welding and cladding. Demands come from the Oil & Gas sector of reducing the lead-time while still maintaining the same corrosion resistance, and WAAM is a promising one-stop manufacturing candidate. The research focus of the multi-material study is how to control the dilution when depositing two different materials.

The present PhD study serves as part of the WAAMMat programme, aiming at broadening the material database of WAAM. The feasibility of depositing maraging steel, IN718 superalloy and IN625/low alloy steel multi-material structures, and structural integrity and material properties of the WAAM alloy need to be understood; the correlation between WAAM process and material properties is yet to be elucidated.

1.2 Research gap

From the literature review, no research was found to apply WAAM to produce maraging steel and multi-material structures; though limited studies prove the feasibility of depositing IN718 using shaped metal deposition (SMD, the same principle as WAAM), a detailed microstructure and heat treatment study is absent. Hence, the following research gaps are figured out.

1. Feasibility of depositing maraging steel, IN718, and multiple materials (IN625/low alloy steel) using WAAM needs to be verified.
2. Microstructure evolution and mechanical properties of WAAM alloys are yet to be elucidated and correlated with the inherent thermal history of WAAM process.
3. Solutions enhancing the WAAM alloy properties to match the wrought counterparts need to be proposed and the underlying strengthening mechanisms need to be addressed.

4. Effect of uncertainties introduced by oxides formation on the surface finish and mechanical properties need to be understood.
5. Strategies for controlling the dilution at the interface need to be investigated when depositing multiple materials using WAAM.

1.3 Aim and objectives

The aim of the PhD research is utilizing WAAM to produce maraging steel and IN718 with comparable strength to the wrought alloy, and produce IN625/low alloy steel multi-material structures complying with the dilution standard.

The objectives are listed as below.

1. To understand the effect of environmental oxygen on the surface finish and mechanical properties of WAAM maraging steel.
2. To understand the microstructural evolution and mechanical properties of maraging steel subject to inherent thermal history and standard heat treatment.
3. To verify the effectiveness of cold rolling in improving mechanical properties of WAAM maraging steel and understand the underlying strengthening mechanisms.
4. To understand the effect of process factors on the microstructural and mechanical properties of IN718 subject to inherent thermal history and standard heat treatment.
5. To verify the effectiveness of cold rolling in improving mechanical properties of WAAM IN718 and understand the underlying strengthening mechanisms.
6. To develop process parameters and deposition strategies for IN625/low alloy steel multi-material structure and control the Fe content below 5 wt.% in the clad layer.

1.4 Thesis structure

The entire thesis is structured in a paper format, an alternative to the monograph format, according to Cranfield University (*Guidance Document: Format options for PhD Thesis, V1.3 Jan 2017*). The thesis consists of ten chapters altogether. Chapter 1 and Chapter 2 concern the introduction and methodology respectively,

and Chapter 10 concerns the overall summary. Chapter 4 to 9 are the main technical chapters presenting the major outcomes of the PhD research, of which Chapter 4 to 6 present the maraging steel research, Chapter 7 to 8 present the IN718 work, and Chapter 9 presents the multiple materials work. A separate literature review chapter is not required for the paper format thesis since each technical chapter has its own literature review as part of the paper. However, to make the thesis more readable, a short literature review, Chapter 3, is also included. To avoid repetition, only those missing in Chapter 4 to 9 and are important to understand the research are presented. A brief introduction to the content in each chapter is shown as follows.

Chapter 1. This chapter presents the research background, research gap, aim and objectives, and the thesis structure.

Chapter 2. This chapter presents the principal research methodology adopted to carry out the entire PhD research.

Chapter 3. This chapter presents a supplementary literature review covering the physical metallurgy of the alloys of concern.

Chapter 4. This chapter presents the study of oxides effect on the surface finish and mechanical properties of the WAAM maraging steel.

Chapter 5. This chapter presents the microstructure and mechanical properties of the WAAM maraging steel in response to the inherent thermal cycles and standard heat treatment.

Chapter 6. This chapter presents the work of applying interpass cold rolling to WAAM of maraging steel.

Chapter 7. This chapter presents a systematically study evaluating the effect of oxides, wire source and heat treatment on the mechanical properties of WAAM IN718.

Chapter 8. This chapter presents the work of applying interpass cold rolling to WAAM of IN718.

Chapter 9. This chapter presents the study of applying WAAM to produce IN625/low alloy steel multi-material structures.

Chapter 10. This chapter presents the overall discussion, conclusion and future work.

2 Methodology

2.1 Literature review

The literature review covers the research of WAAM process, physical and metallurgical properties of maraging steel, IN718 and IN625 superalloy, heat treating and strengthening mechanism of those alloys and dilution control theory. The following procedures are followed to carry out the literature review.

1. Keywords identification. The following keywords are used for preliminary paper search: additive manufacture, maraging steel, Inconel, multiple materials, heat treatment, aging, rolling.
2. Paper search. The database provided by Cranfield University, such as Scopus, is utilized to search the keywords. Further papers are obtained from the references listed in the downloaded paper. Google scholar is also frequently used. Mendeley is used to manage the references.
3. Paper analysis. Papers are filtered according to the relevance after reading the title and abstract. The most relevant papers are read through and summarised to figure out the research gap.

2.2 Research focus identification

The identified research gap and the variety of the alloys of interest narrow the research focus into the following topics.

1. Maraging steel. Since only a few preliminary parametric studies have been reported using SLM and no research has been carried out on WAAM of maraging steel, a comprehensive study concerning WAAM parameters, microstructure, mechanical properties, heat treatment and interpass rolling was carried out.
2. IN718. There are various research on AM of IN718, mostly using laser and electron beam as the heat source; some preliminary studies using arc based AM process claimed that the material properties were comparable to the castings, however, the heat treatment was not studied and it was unknown if heat treatment would result in the mechanical properties comparable to the

wrought alloy. The gaps need to be filled are the heat treatment and rolling of the WAAM alloy.

3. Multiple materials. Cladding itself is a widely applied process but using WAAM for the whole pipeline production with cladding integrated is an innovation. The main concern lies in ensuring the structural integrity as well as controlling the dilution level at the interface.

2.3 Experimental work and characterization methods

The experimental work is carried out in the world-class WAAM lab at Cranfield University which is equipped with various welding power sources (CMT, TIG, TOPTIG, and Plasma), robots, CNC motion systems, and shielding devices to allow the assembly of various WAAM deposition setups to suit different applications. The high-pressure rolling system is used for the interpass cold rolling study, the furnace is used to do heat treatment of the WAAM alloys, and the welding camera and AMV are used for process monitoring.

The room temperature tensile test is carried out to evaluate the mechanical properties of the WAAM material. Optical microscope (OM) and scanning electron microscope (SEM) are used for microstructure observation, energy-dispersive spectrometry is used for elemental analysis, X-ray diffraction (XRD) is used for phase identification, electron backscatter diffraction (EBSD) is used to characterized the grain structure, and TEM is used to observe the dislocations.

2.4 Research route

The research starts with understanding the physical and metallurgical properties of the alloy given, then moves on to the design of building strategies under the guideline of classic theory of welding, metallurgy, heat and mass transfer, solidification and thermal-mechanical processing, followed by the material characterization and mechanical property testing methods (tensile test in this research) to correlate the macroscopic properties of the WAAM alloys with the microstructure, and ends up with heat treating or thermomechanical processing to enhance the material performance.

3 Literature review

An exclusive literature review with its own focus serving each individual technical chapter (Chapter 4 to 9) is included in the Introduction section of each chapter. The present chapter serves as a supplementary literature review aiming at providing the fundamental pre-knowledge (mostly concerning the physical metallurgy) necessary to understand the research focus of the thesis.

3.1 Maraging steel

3.1.1 Introduction

Maraging steel (a portmanteau of “martensitic” and “aging”) refers to a special class of highly-alloyed low-carbon steel that is known for its superior strength (yield strength varies from 1030MPa to 3450MPa) and fracture toughness to most of the carbon-hardened steels [1], as shown in Fig. 3-1. The name maraging steel derives from the strengthening mechanism of this steel, i.e., age hardening the low-carbon, Fe-Ni lath martensitic matrix.

The most widely used maraging steels are 18Ni 200, 18Ni 250 and 18Ni 300, and the nominal compositions are given in Table 3-1, featuring 18%Ni and very low carbon. Carbon is actually an impurity in maraging steel and is kept as low as possible to avoid the formation of TiC which is detrimental to the strength and toughness. The combination of simple heat treatment, good machinability and weldability, excellent dimension stability during aging, and high strength-to-weight ratio makes maraging steel widely used in the aerospace and tolling industry [2].

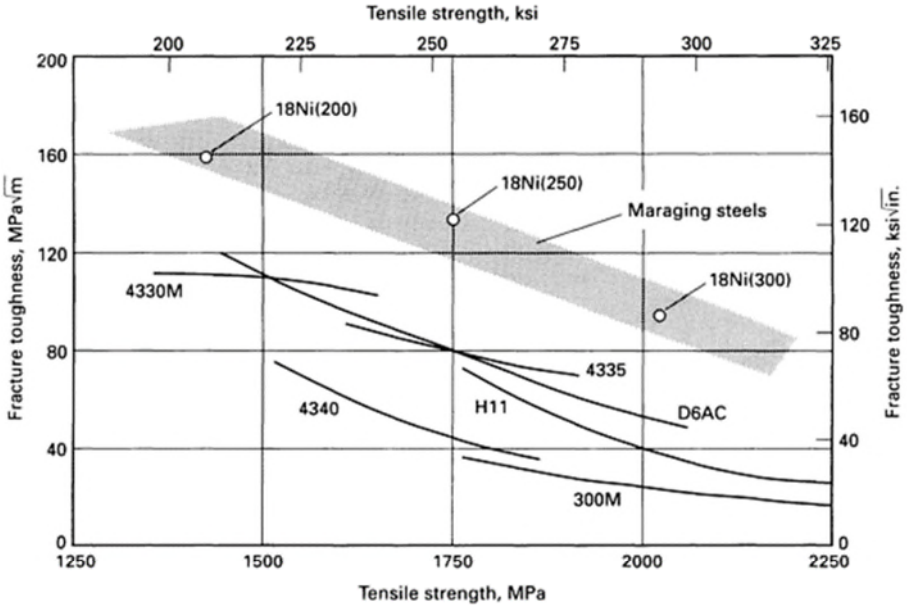

Figure 3-1 Strength/toughness combination of maraging steels compared to conventional high-strength carbon steels [3].

Table 3-1 Nominal compositions of commercial maraging steels (wt. %).

	C	Ni	Mo	Co	Ti	Al	Fe
18Ni 200	≤0.03%	18	3.3	8.5	0.2	0.1	Balance
18Ni 250	≤0.03%	18	5.0	8.5	0.4	0.1	Balance
18Ni 300	≤0.03%	18	5.0	9.0	0.7	0.1	Balance

3.1.2 Development history

In 1927, the thermal hysteresis of phase transformations in Fe-Ni alloys was reported (see Section 3.1.5.1). Based on this, the International Nickel Company (currently Inco Ltd.) firstly conducted extensive research to develop the commercial Fe-Ni maraging steel in the late 1950s. The first two representative products contained 20% or 25% Ni (other composition: 0.4% Nb, 0.3% Al, and 1.4% Ti) which were reported to combine good strength and ductility but were abandoned later on due to the brittleness at very high strength levels. Subsequent research on Fe-Ni alloy system showed that the addition of Co and Mo could harden the martensite significantly, and 18% Ni was chosen as Ni content higher than 18% would result in the retention of austenite in the as-quenched state [3]. Further, by the early 1960s, the 18 Ni maraging steel 200, 250 and 300 (numbers

representing the yield strength in the unit of ksi) are developed and are still used till now.

3.1.3 Production of maraging steel

Maraging steel is processed in the mill following the same general procedures and using the same equipment as are used for the mill production of other alloy steels.

3.1.3.1 Melting and ingot break down

Maraging steel is mainly manufactured in two routes (see Fig. 3-2). The first is the traditional route: melting in an electric arc furnace followed by ladle metallurgy, and the electrodes are remelted in a vacuum arc furnace; the second is the double vacuum melting route, i.e., vacuum melting followed by vacuum remelting [4]. Ingot breakdown can be completed by hot rolling, press or hammer forging, or a combination of forging and rolling. Common products include slabs, blooms and billets; plates are produced by rolling directly from the ingot stage.

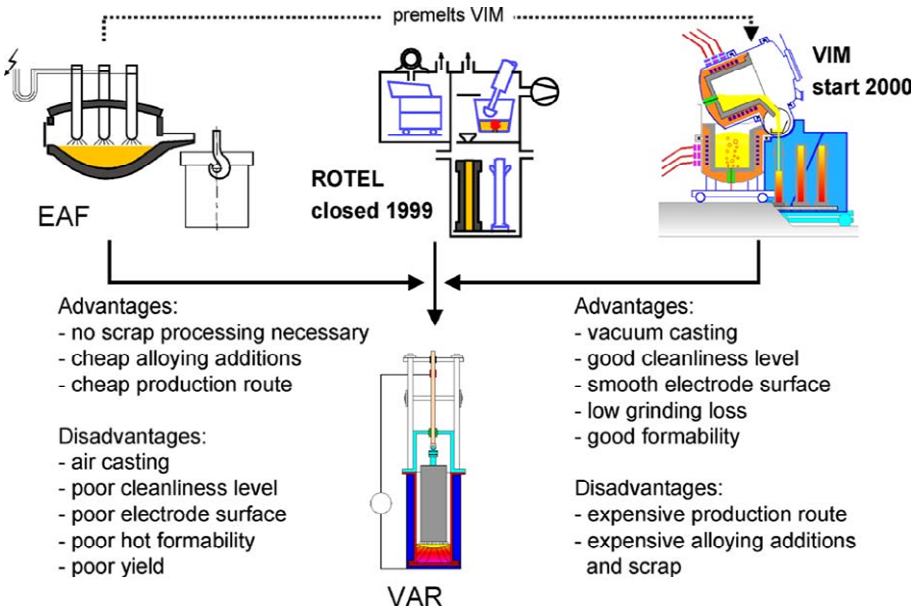

Figure 3-2 Production routes for maraging steels [4].

3.1.3.2 Control of inclusions

By air melting in the electric-arc furnace, the content of major alloying elements, as well as C, S, P, Mn and Si, can be controlled satisfactorily; however, the

gaseous elements such as H, O and N cannot be reduced to low levels. Large and non-uniformly distributed non-metallic inclusions formed in this stage. For instance, Ti has been added for precipitation hardening, but its combination with C, N and O as non-metallic inclusions depletes the Ti necessary for precipitation hardening; these Ti-containing inclusions are also known to form stringers in the finished product which is detrimental to the ductility and toughness.

Vacuum degassing reduces the gaseous elements notably. The spraying action of the arc generated in the consumable-electrode vacuum-arc process offers the opportunity to break the large masses and clusters of non-metallic inclusions into small and uniformly distributed particles which will do minimum harm to the mechanical properties.

3.1.3.3 Elemental segregation

Like other highly-alloyed materials, maraging steel is subject to significant dendritic segregation upon freezing. Ni, Mo and Ti segregate the mostly to the extent that the austenite remains stable to room temperature; these alloy-rich zones still persist but elongate even after forging and rolling, which, after etching, shows as bands. The bands are usually associated with reduced ductility and strength and delamination issue in the final product. Such elemental segregation is not affected by the melting practice, but the solidification rate; homogenization at a temperature well above which most of the secondary phases and precipitates dissolve but safely below solidus can also help mitigate segregation by diffusion of the segregated elements.

3.1.4 Physical metallurgy

Maraging steel can be described as high-alloy, low-carbon, body-centred cubic (bcc) Fe-Ni lath martensites. The most representative phase transformations in maraging steel can be understood with Fig. 3-3 which is taken from the Fe-rich end of Fe-Ni binary system. Fig. 3-3a shows the austenite-to-martensite transformation upon cooling and the martensite-to-austenite reversion upon reheating. Upon cooling after solution-annealing (austenizing), the high-temperature face-centred cubic (fcc) austenite transforms to the bcc martensite

through a diffusionless shear reaction without decomposing into the equilibrium structures [1]. Fig. 3-3b shows that at 18%Ni the equilibrium phases are austenite and ferrite at low temperatures (below 600°C).

The Ms temperature at which martensite starts to transform from austenite for most grades of maraging steel is around 200-300°C, which is high enough to allow a complete transformation to martensite before the steel cools down to room temperature [3]. The transformation is largely independent of cooling rate. Maraging steels are generally fully martensitic at room temperature; even very slow cooling of the heavy sections results in a fully martensitic structure.

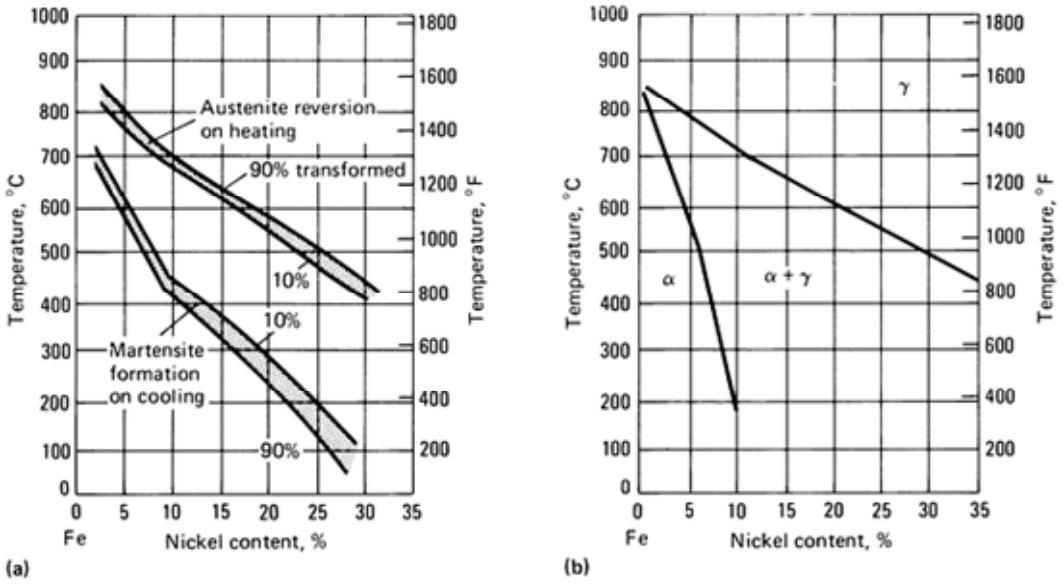

Figure 3-3 Phase transformation in Fe-Ni system (a) metastable (b) equilibrium [1].

3.1.5 Heat treatment

The low-carbon, bcc Fe-Ni lath martensite formed after annealing is relatively soft (30-35HRC) and extremely ductile with good strength, as shown in Table 3-2. During age hardening, the main target is to produce a uniform distribution of fine precipitates and minimize the reversion of martensite to austenite and ferrite. Typical mechanical properties achieved in maraging steels after aged hardening are also listed in Table 3-2.

Table 3-2 Typical mechanical properties of maraging steels in solution annealed (815°C, 1 h, air cooled) and age hardened (815°C, 1h + 480°C, 3h) condition [3].

		Yield strength /MPa	Tensile strength /MPa	Elongation /%	Hardness /HRC
18Ni 200	unaged	760-807	965-1000	17-18	28-30
	aged	1400	1500	10	-
18Ni 250	unaged	725-895	1000-1140	8-16	28-35
	aged	1700	1800	8	-
18Ni 300	unaged	760-895	1000-1170	6-15	30-37
	aged	2000	2050	7	-

3.1.5.1 Thermal hysteresis and precipitation kinetics

From Fig. 3-3a, the reversion of martensite to austenite during reheating take place at a higher temperature range than that for austenite-to-martensite transformation upon cooling, which is known as thermal hysteresis and is the basis of heat treatment of maraging steel. Although from Fig. 3-3b the martensite tends to revert to the equilibrium phases (austenite and ferrite) during prolonged aging, the kinetics of the precipitation reactions in maraging steels are such that significant hardening occurs before the onset of the austenite and ferrite reversion [5].

3.1.5.2 Heat treating procedure

The heat treatment is usually comprised of two stages: solution annealing and aging. During solution annealing, the alloy is heated well above the austenite finishing temperature (A_f), holding for a sufficient period to dissolve all the solute atoms and create a supersaturated matrix. The common solution treatment procedure for maraging steel is heating to 815°C for 1h for each 25mm (1inch) of section size; the cooling rate is not important but the steel must be cooled completely to room temperature before aging to avoid retained austenite. Aging is usually conducted for 3-6hrs at the temperature range of 480°C at which the matrix remains martensitic while metallurgical reactions result in the formation of a large amount of precipitates to strengthen the matrix. The aging temperature and duration must be selected carefully; with longer aging time and higher

temperature, the hardness will reach a peak value and then drop down due to overaging (coarsening of precipitates) and austenite reversion, as shown in Fig. 3-4. The continuous cooling transformation (CCT) diagrams are shown in Fig. 3-5. The Vickers hardness appears in the circles at the end of each cooling curve (the horizontal lines at the bottom of each graph represent the percentage of material transformed to martensite at a given time and temperature) [1].

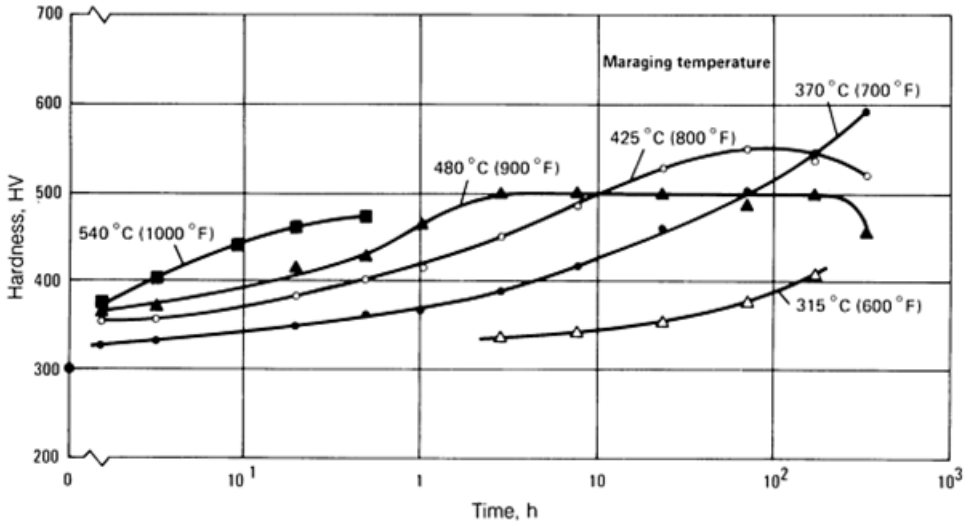

Figure 3-4 Hardness of 18Ni 250 maraging steel versus aging time for various aging temperatures [1].

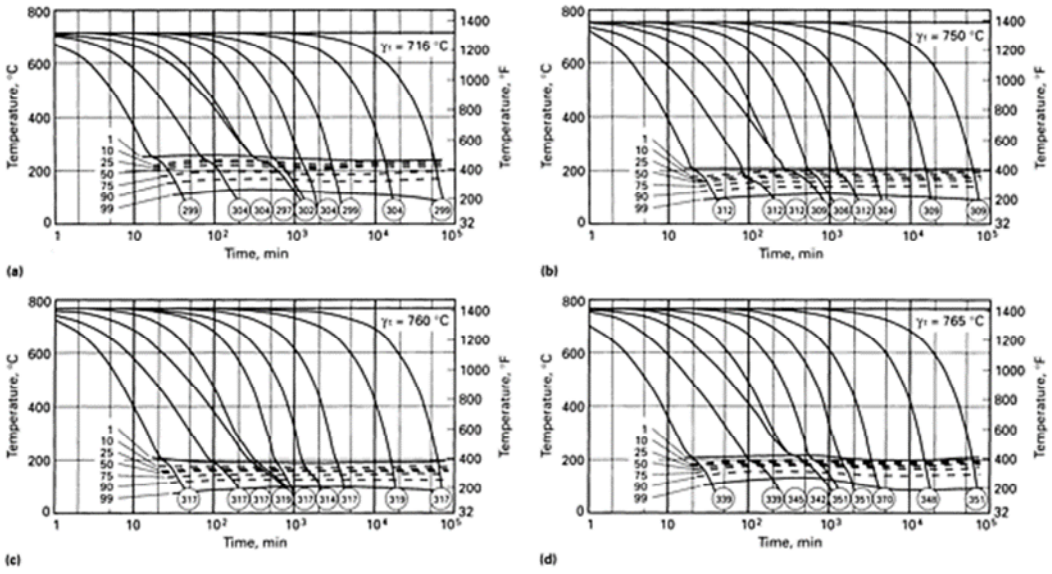

Figure 3-5 CCT diagrams for maraging steels solution treated at 845 °C for 20 min (a) 18Ni 200 (b) 18Ni 250 (c) 18Ni 300 (d) 18Ni 350 [3].

3.1.5.3 Precipitation reactions

The precipitation reactions during the martensitic aging process are rather complex and are still disputable [6]. The prevailing opinions are summarized here.

Among various alloying elements in maraging steel, Ti is a strong hardener and Mo is a moderate hardener, both of which form precipitates to strengthen maraging steel. Co does not form precipitates but contributes to the strengthening indirectly through the Co/Mo interaction, i.e., Co reduces the solubility of Mo in the martensitic matrix and thereby promoting the formation of Ni_3Mo. The Ti and Mo-bearing precipitates usually nucleate at dislocations or at lath boundaries, and they are coherent with the matrix. There is no incubation period during the precipitation reaction in maraging steel and pronounced hardening takes place after a very short time (<1min), indicating a lack of free-energy barrier in maraging steel due to the heterogeneous nucleation on dislocations, high degree of solute supersaturation, and good structural fit between the A_3B precipitates and the bcc martensitic matrix. Typical precipitates are summarized in Fig. 3-6.

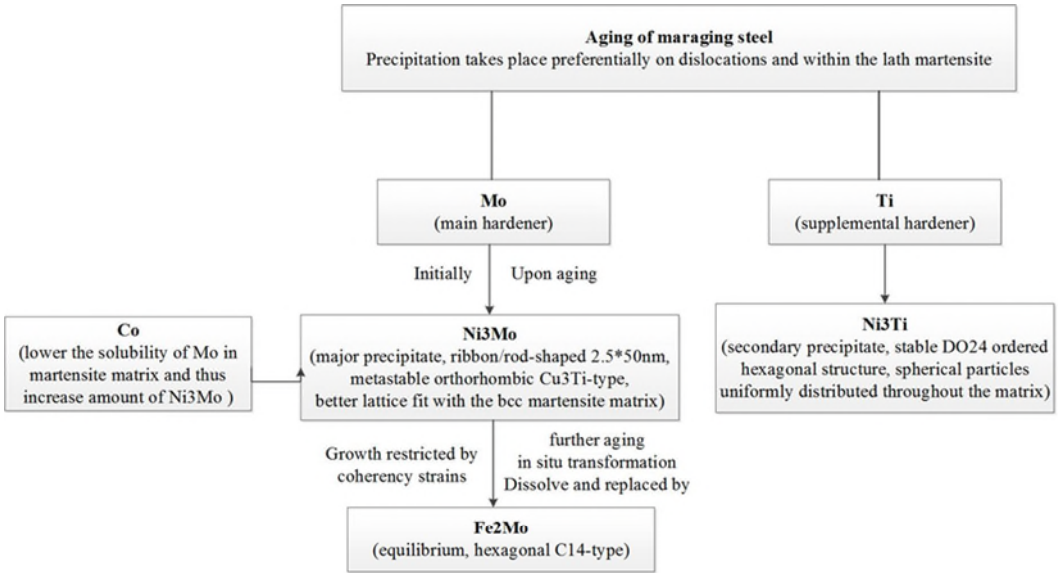

Figure 3-6 Precipitation reactions in maraging steel during aging.

3.1.6 Welding considerations

Maraging steel has an excellent weldability mostly due to the low carbon content which produces the soft and ductile martensite upon cooling [7]. All the

conventional welding techniques have been used to weld maraging steel; the weld metal strength is independent of the welding techniques and joint efficiency higher than 90% can mostly be achieved.

The heat affected zone can be divided into three regions: the region closest to the fusion line is coarse martensite formed after solution annealing; next is a narrow region containing reverted austenite formed by heating up to 595-805°C; the final region has been heated up to 595°C and contains aged hardened martensite. The hardness across the three regions are shown in Fig. 3-7. Since the material immediately surrounding the weld is soft and ductile, the residual stress is low and weld cracking is not an issue.

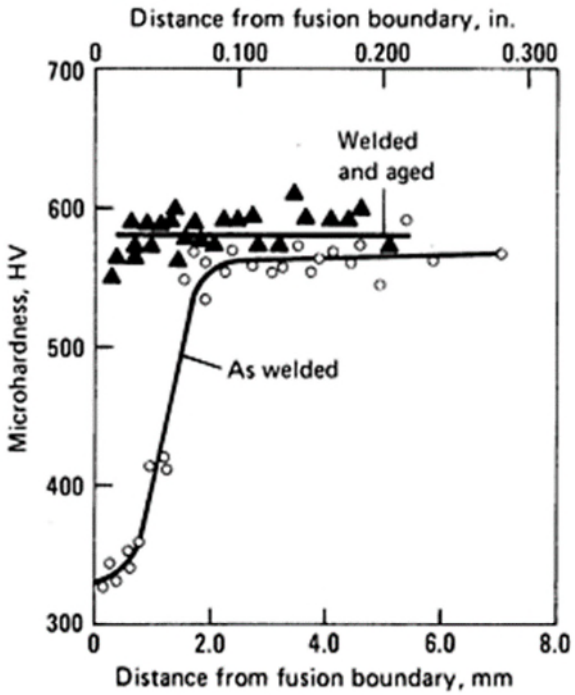

Figure 3-7 Microhardness of a weld heat-affected zone in 18Ni 250 maraging steel [1].

Generally, the following tips are given for welding maraging steel [8].

1. Avoid prolonged dwell times at high temperatures.
2. Avoid preheat and keep interpass temperatures below 120°C.
3. Minimize weld energy input.
4. Avoid slow cooling rates.

5. Keep welds as clean as possible.

3.1.7 Other issues

3.1.7.1 Austenite reversion

Austenite reversion results from the Ni enrichment in the martensitic matrix. Usually in a homogeneous composition, stable austenite is formed most readily at about 648°C; however, the elemental segregation (Mo and Ti) can lower the austenite reversion temperature. The product is a soft and stable austenite which does not harden during aging thereby decreasing the strength of maraging steel. At the same strength level, the toughness of welds with little austenite is much better than that with some austenite. As such, austenite formation should be avoided to guarantee the strength and toughness of maraging steel.

3.1.7.2 Cold working

Maraging steels can be cold worked by all the common techniques in the solution-annealed condition. Due to the very low work-hardening rates, maraging steel can be cold worked with great thickness reduction (>50%) but only slight accompanying hardness increase. Cold reductions of more than 50% should be avoided as the delamination may occur.

3.2 Inconel 718

3.2.1 Introduction

Inconel refers to a family of austenite Ni-Cr based superalloys and it is known as an oxidation and corrosion resistant material [9] suitable for service in extreme environments subject to pressure and heat. IN718 is a solution-annealed and precipitation-hardened Ni-Cr alloy with high-strength, good fatigue, creep, and rupture strength, and corrosion-resistant properties [10] working in the temperature range of -252° to 704°C. IN718 is widely used in liquid-fuelled rockets, gas turbines, spacecraft, nuclear reactors, rocket motors, pumps and tooling. Noteworthy is that Inconel superalloys can be used in load-bearing applications at temperatures in excess of 80% of their incipient melting

temperatures, a fraction higher than any other engineering alloys [11]. The chemical composition of IN718 is listed in Table 3-3.

Table 3-3 Chemical composition of IN718 (wt. %).

Ni	Cr	Fe	Mo	Nb	Al	Ti	Mn	C
50-55	17-21	12.82-24.17	2.8-3.3	4.75-5.5	0.2-0.8	0.65-1.15	<0.35	<0.08

3.2.2 Development history

The Inconel alloys were first developed in the 1940s by research teams at Wiggin Alloys (Hereford, England) which has since been acquired by Special Metals Corporation in support of the development of the Whittle jet engine. Ironically, the initial development effort was made to produce a solid solution strengthened and non-aged hardenable alloy; however, during the subsequent research unexpectedly pronounced aging response was observed when Nb was added to the based composition, which led to the development for a new age-hardenable alloy [12]. Nowadays, Inconel is the trademark of a family of more than twenty alloys produced by Special Metals Corporation.

3.2.3 Production of IN718

Production of Inconel starts with the production of large ingots (around 2500kg to 27500kg) which are produced using vacuum induction melting (VIM) in a refractory crucible to consolidate elemental and/or revert materials to form a base alloy [11]. These ingots are then remelted and used for the following three routes: casting, wrought, and powder metallurgy. Wrought Inconel alloys are usually produced by remelting the ingots using vacuum arc remelting (VAR) to remove the compositional inhomogeneity and inclusions. The conventional routes to manufacture Inconel superalloy are shown in Fig. 3-8.

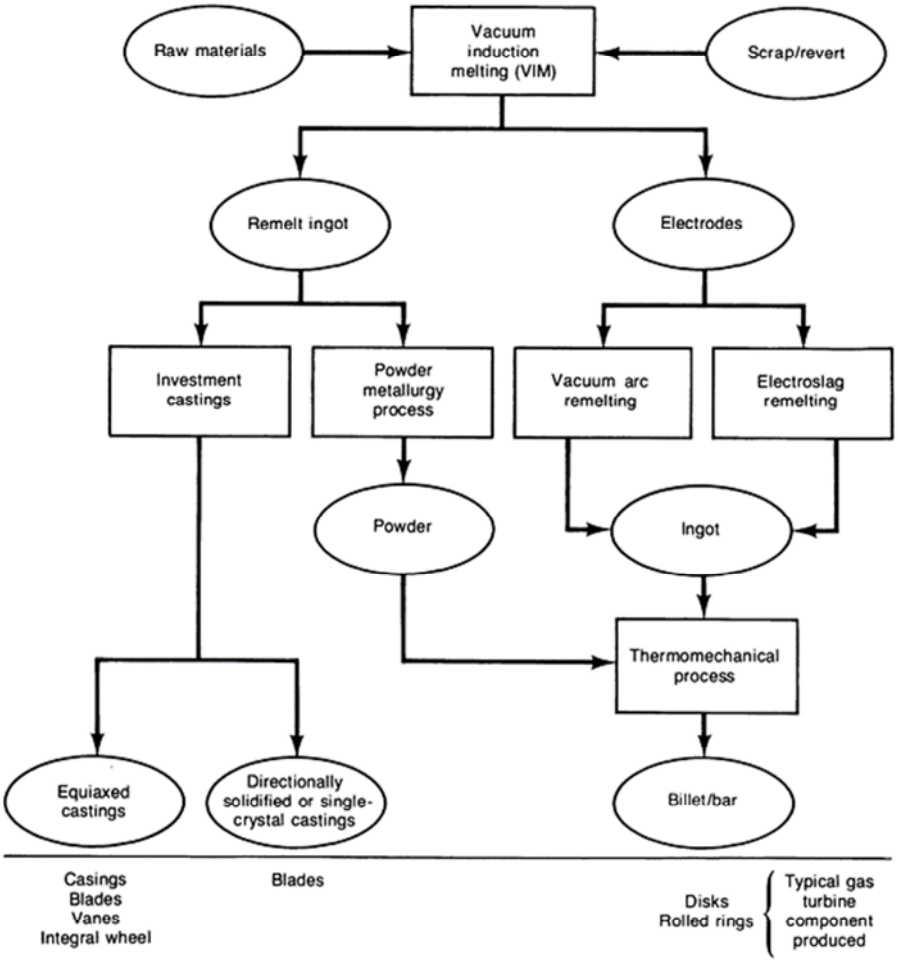

Figure 3-8 Typical production procedure of superalloys [11].

3.2.4 Physical metallurgy

The physical metallurgy of Inconel alloying system is extremely complex, perhaps being the most challenging alloying system. IN718 has an austenitic matrix (γ phase) and contains a wide variety of secondary phases including carbides, gamma prime (γ′ phase) and gamma double prime (γ" phase). Other phases formed due to the variations in composition and processing are generally undesirable; the most typical such phases include δ phase and Laves phase. γ′ and γ" are the principal strengthening precipitates, while other precipitates such as δ phase and Laves phase can provide grain size control [3]. The time temperature transformation (TTT) diagrams of IN718 is shown in Fig. 3-9. A brief introduction to the most important phases in IN718 is given as follows.

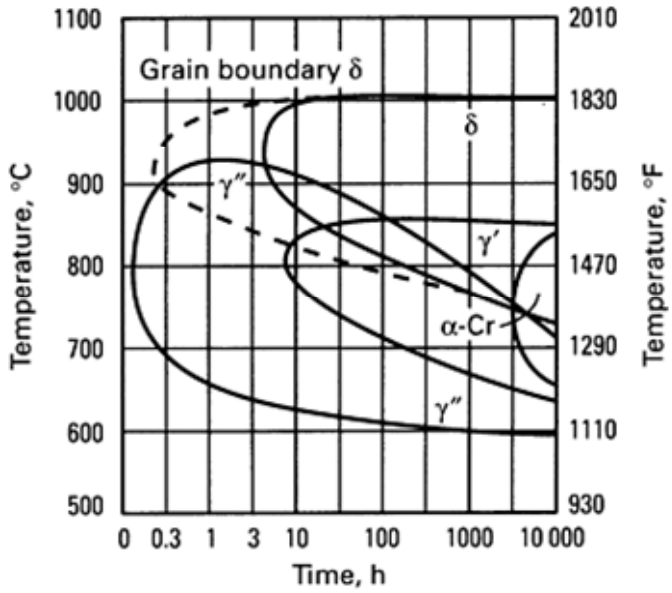

Figure 3-9 TTT diagram for vacuum-melted and hot-forged IN718 bar [1].

3.2.4.1 Gamma double prime

In superalloys containing Nb or Nb+Ta, like IN718, the primary strengthening phase is gamma double prime (γ", Ni_3Nb,). γ" has a bct ordered D022 crystal structure and shows as coherent disk-shaped particles (diameter 60nm, thickness 5-9nm) that form on the {100} planes. After a full heat treatment γ" normally has a volume fraction of around 16% [13].

3.2.4.2 Gamma prime

Gamma prime (γ′, $Ni_3(Al,Ti)$) is usually the principal strengthening phase for most Ni-based alloys. γ′ has an fcc ordered L12 structure which is similar to the γ matrix, with only less than 0.5% mismatch in the lattice constant. The close matching allows low surface energy and long-time stability. The normal volume fraction of γ′ after a full heat treatment is approximately 4% [13]. The shape varies from spherical to cubic and the size varies with exposure time and temperature [14]. Strengthening from γ′ is a function of its particle size: the hardness of the alloy increases with the particle size growth [15]; however, the effective strengthening from γ′ decreases above about $0.6T_m$ (T_m-melting temperature) due to the particles coarsening.

3.2.4.3 Delta phase

γ′ phase can transform to metastable η phase (Ni_3Ti, hcp D024 structure); excess Nb would result in metastable η transforming to γ" and ultimately to the equilibrium delta phase (δ, Ni_3Nb, orthorhombic ordered Cu_3Ti type). Transformation to coarse and elongated δ phase results in a decrease in hardness thus is undesirable in IN718. δ phase usually shows an acicular shape, and it forms by cellular reaction at a low aging temperature and by intragranular precipitation at high aging temperatures [14].

3.2.4.4 Laves phase

The solidification process of cast or welded IN178 is often associated with segregation of high concentration refractory elements, such as Nb and Mo [13]; Nb segregation to the interdendritic regions results in the formation of brittle Laves phase (hexagonal structure) represented as $(Ni,Cr,Fe)_2(Nb,Mo,Ti)$ [16]. Laves phase is detrimental to the material fatigue, tensile ductility, and creep rupture properties, as it depletes the principle elements needed for precipitation hardening and aids in easy crack initiation and propagation [13,17]. Laves phase usually appears as irregularly shaped globules, often elongated [14]; however, the morphology and composition of the Laves phase depend strongly on the heat input and the cooling rate of the manufacturing process [18].

3.2.5 Heat treatment

3.2.5.1 Principle

IN718 is hardened by the precipitation of secondary phases into the matrix. To ensure the precipitation to take place properly, all the hardening constituents must go into solution; if they are combined in other forms or precipitated as other phases, the full strength will not be achieved [19]. When more than one phase can be precipitated, the selection of aging temperature is important since it greatly affects the size distribution of the precipitates. A double aging treatment is usually applied to control the size distribution of γ′ and γ", as well as the grain boundary carbide morphology [3].

3.2.5.2 Procedures

Heat treatment of IN718 is extensively studied and different procedures are developed for different applications. Heat treatment provided by two suppliers, Haynes International and Special Metals, as well as the expected mechanical properties are summarized in Fig. 3-10. Among various procedures, HT1 and HT2 are applied to most of the applications. HT1 produces the highest room temperature tensile and fatigue strength due to the fine grains developed, while HT2 produces the best transverse ductility, impact strength and low-temperature notch tensile strength [19].

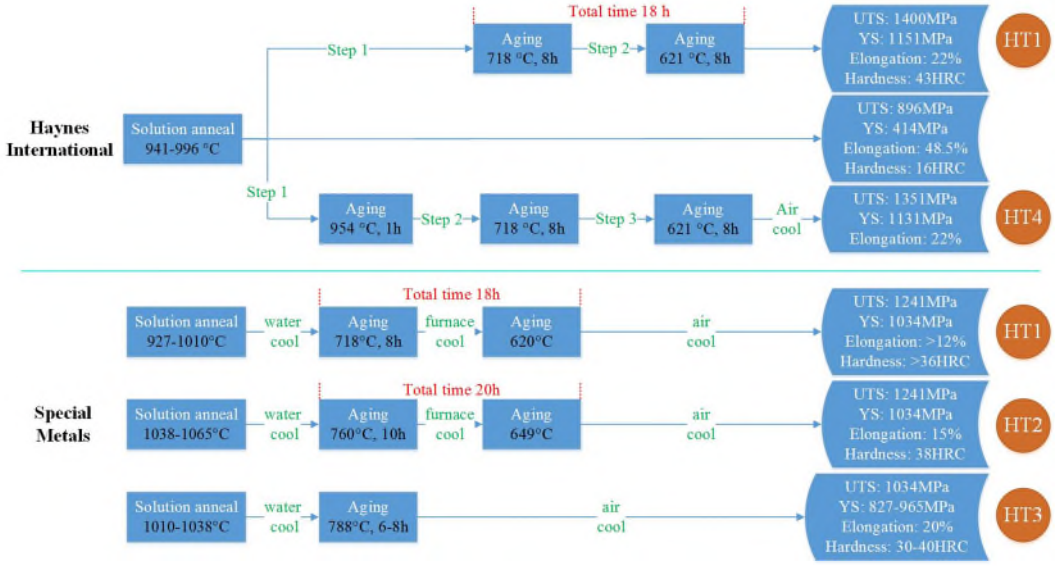

Figure 3-10 Different heat treatment procedures and the resulting mechanical properties.

3.2.5.3 Sluggish aging response

The age hardening Nb-Al-Ti alloying system of IN718 has a very slow aging response as compared to the Al-Ti system. As a result, IN718 can be heated up and cooled down through the aging temperature range at normal rates, whereas no appreciable age hardening would take place and the material retains ductility and softness. From Fig. 3-11, no hardening occurs during the first 2-3 minutes of aging; usually this time is long enough for air cooling of a weld [19].

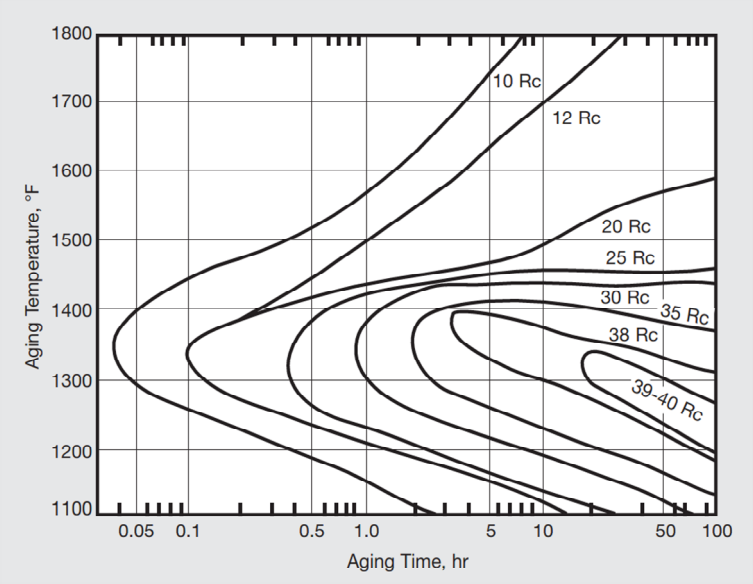

Figure 3-11 Effect of aging conditions on the hardness of annealed IN718 [19].

3.2.6 Welding considerations

IN718 possesses excellent weldability and outstanding resistance to postweld cracking. IN718 can be welded with all the conventional welding processes. Plates annealed, welded and aged could have the joint efficiency very close to 100%. The slow aging response of IN718 allows the parts to be welded and directly aged without the intermediate stress relief [19]. Segregation of Nb to the interdendritic area is a common problem associated with welding IN718 [20,21] due to the non-equilibrium thermal cycles; the brittle Laves phase, forming as a result of the segregation, is known to adversely affect the structural integrity and could lead to premature failure of critical components during service [22].

3.2.7 Other issues

3.2.7.1 Cold working

IN718 has a high work hardening coefficient [23] and can be cold worked following the same procedure as are used for steels. A comparison of the work hardening rate between IN718 and other materials are shown in Fig. 3-12. Cold working has an influence on the aging response of the age hardenable Fe-Ni based superalloys by affecting the recrystallization and grain growth behaviour

during the subsequent solution treatment and the reaction kinetics of aging treatment.

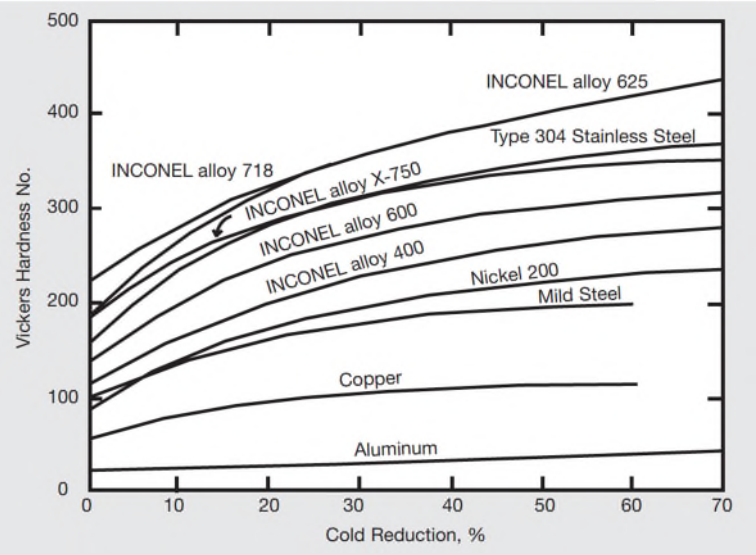

Figure 3-12 Effect of cold work on the hardness of IN718 [19].

3.2.7.2 Grain size

Grain size is an important microstructural parameter in IN718. Fine grains provide excellent room-temperature properties (strength, toughness and fatigue resistance), whereas coarse grains provide better creep resistance at elevated temperatures. Grain size also affects the carbides precipitation at grain boundaries; if the grains are coarse, there will be less grain boundary surface area and the carbides precipitation will be more continuous and thicker, which is detrimental to the mechanical properties. A uniform and intermediate grain size is preferred to a duplex grain structure.

3.3 Steel pipe cladding

3.3.1 Introduction

Steel pipes are widely used in Oil & Gas industry to transport high-temperature and corrosive fluids. In order to extend and prolong the service life of pipes in the hostile operating environment, the metal cladding of the internal surfaces of carbon steel pipes using a corrosion resistant material is widely implemented. In

this way, full use is made of the strength and touchiness of the steel and the corrosion resistance of the clad material and the overall cost is kept low.

3.3.2 Steel pipe production

Steel pipes are the most widely used products in steel industry, and they are generally manufactured in two distinct means which lead to either a seamless or a welded pipe. Raw steel is firstly produced and then made into pipes by either stretching the steel out into a seamless tube or forcing the edges together and welding them together [24]. There are generally three steps in pipe production: ingot production, bloom and slab production, and pipe making. Ingot production involves conventional iron and steel making and enormous pressure shaping; bloom and slab production involves multiple cycles of rolling, cutting, and further processing such as heat treatment and pickling; pipe making involves grooved rolling and welding, or high temperature, great pressure, a bullet-shaped piercer and subsequent series of rolling mills.

Elbow structure is a necessary pipe fitting used to connect two linear pipes with different orientations. There are generally three methods to manufacture elbows: hot forming (Mandrel method), cold extrusion, and UO method. The most widely used method is hot forming, as shown in Fig. 3-13; in this method, an induction heating coil heats the pipe which is pushed by a hydraulic ram over a die called “mandrel” allowing the pipe to expand and bend simultaneously [25].

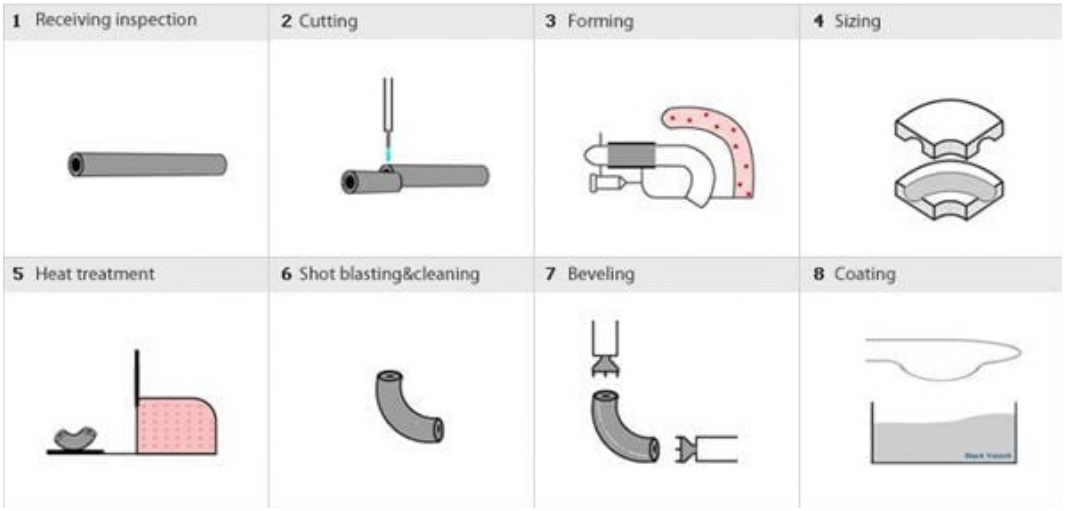

Figure 3-13 Procedures of manufacturing elbow structure using Mandrel method [25].

3.3.3 Metal Cladding

3.3.3.1 Introduction

Cladding is defined as “bonding of thin sheet metal cladding to the substrate surface by diffusion bonding, forging, rolling, extrusion, and other methods” [26]. The principal cladding techniques cover hot or cold roll bonding, centrifugal casting, explosive bonding, brazing and weld cladding. To achieve a good bonding, the clad material should have a similar coefficient of thermal expansion to the substrate.

3.3.3.2 Weld cladding

As one of the most widely used cladding techniques, weld overlay cladding is usually conducted using the arc welding technology in which one of the metals is molten when the metal-to-metal bond is established. The commonly used corrosion resistant material includes Cu-base alloys, stainless steels, and Ni-base alloys. When weld overlay the corrosion-resistant alloy to steel, the Fe content in the clad layer would increase due to the inter-diffusion of the base material in the overlay [27], which has a negative impact on corrosion-resistance [28,29]. To ensure the corrosion resistance, the Fe content in the clad layer is required to be below 5 wt.% [30] (hereinafter 5%). The following principles should be complied with so as to keep the dilution to a minimum [26].

1. Maximizing the amount of metal deposited per unit length. The beads being deposited should be overlapped as much as possible.
2. Minimizing the amount of heat input in order to reduce the amount of base metal melting. The use of straight-polarity direct current (DC) will help decrease the penetration.

3.3.3.3 IN625

IN625 is widely used for weld cladding due to its outstanding corrosion resistance and wide service temperature range (from cryogenic to 982°C) [31,32]. The chemical composition of IN625 is listed in Table 3-4; the addition of 9% Mo plus 3% Nb offers both high-temperature and wet corrosion resistance. IN625 possesses excellent weldability and can be easily welded with all the conventional processes without the need of postweld heat treatments to maintain the high strength and ductility.

Table 3-4 Chemical composition of IN625 (wt. %).

Ni	Cr	Fe	Mo	Nb	Al	Ti	Mn	C
>58	20-23	<5	8-10	3.15-4.15	<0.4	<0.4	<0.5	<0.1

3.4 Summary

The literature review has summarized the basic physical metallurgy of maraging steel and IN718 concerning mainly how the strength is developed in these alloys, which will be the guidance to understand how the microstructure and mechanical properties of the WAAM alloy will respond to the inherent thermal history and to propose solutions to improve the mechanical behaviours of the WAAM alloy. The factors determining the dilution level during cladding process has also been summarized, which will be the guideline of designing the deposition strategies during WAAM of multiple materials.

3.5 References

[1] ASM International, ASM Handbook: Volume 1 Properties and selection: irons steels and high performance alloys, 10th ed., ASM International, Materials Park, Ohio, 2001. doi:10.1016/S0026-0576(03)90166-8.

[2] A. Fortunato, A. Lulaj, S. Melkote, E. Liverani, A. Ascari, D. Umbrello, Milling of maraging steel components produced by selective laser melting, Int. J. Adv. Manuf. Technol. (2017). doi:10.1007/s00170-017-0922-9.

[3] A. International, ASM Handbook: Volume 4 Heat Treating, in: ASM Handb., ASM International, 1991: p. 2173. doi:10.1016/S0026-0576(03)90166-8.

[4] P. Würzinger, R. Rabitsch, W. Meyer, Production of maraging steel grades and the influence of specified and nonspecified elements for special applications, J. Mater. Sci. 39 (2004) 7295–7302. doi:10.1023/B:JMSC.0000048744.03279.ec.

[5] K. Kempen, E. Yasa, L. Thijs, J.P. Kruth, J. Van Humbeeck, Microstructure and mechanical properties of selective laser melted 18Ni-300 steel, Phys. Procedia. 12 (2011) 255–263. doi:10.1016/j.phpro.2011.03.033.

[6] O. Moshka, M. Pinkas, E. Brosh, V. Ezersky, L. Meshi, Addressing the issue of precipitates in maraging steels - Unambiguous answer, Mater. Sci. Eng. A. 638 (2015) 232–239. doi:10.1016/j.msea.2015.04.067.

[7] S.L. Campanelli, A. Angelastro, C.G. Signorile, G. Casalino, Investigation on direct laser powder deposition of 18 Ni (300) marage steel using mathematical model and experimental characterisation, Int. J. Adv. Manuf. Technol. 89 (2017) 885–895. doi:10.1007/s00170-016-9135-x.

[8] F.H. Lang, N. Kenyon, Welding of Maraging Steels, Weld. Res. Concil. (1971) 41.

[9] B.S. Yilbas, H. Ali, N. Al-Aqeeli, C. Karatas, [INVITED] Laser treatment of Inconel 718 alloy and surface characteristics, Opt. Laser Technol. 78, Part B (2016) 153–158. doi:http://dx.doi.org/10.1016/j.optlastec.2015.11.006.

[10] Y. Lu, S. Wu, Y. Gan, T. Huang, C. Yang, L. Junjie, J. Lin, Study on the microstructure, mechanical property and residual stress of SLM Inconel-718 alloy manufactured by differing island scanning strategy, Opt. Laser Technol. 75 (2015) 197–206. doi:10.1016/j.optlastec.2015.07.009.

[11] E. Akca, A. Gürsel, A Review on Superalloys and IN718 Nickel-Based INCONEL Superalloy, Period. Eng. Nat. Sci. 3 (2015). doi:10.21533/pen.v3i1.43.

[12] a Lingenfelter, Welding of Inconel Alloy 718: A Historical Overview, Superalloys 718 Metall. Appl. (1989) 673–683. doi:10.7449/1989/Superalloys_1989_673_683.

[13] H. Qi, M. Azer, a. Ritter, Studies of Standard Heat Treatment Effects on Microstructure and Mechanical Properties of Laser Net Shape Manufactured INCONEL 718, Metall. Mater. Trans. A. 40 (2009) 2410–2422. doi:10.1007/s11661-009-9949-3.

[14] J. Belan, GCP and TCP Phases Presented in Nickel-base Superalloys, Mater. Today Proc. 3 (2016) 936–941. doi:10.1016/j.matpr.2016.03.024.

[15] G. Çam, M. Koçak, Progress in joining of advanced materials, Int. Mater. Rev. 43 (1998) 1–44. doi:10.1179/imr.1998.43.1.1.

[16] S. Singh, S. Ramakrishna, R. Singh, Material issues in additive manufacturing: A review, J. Manuf. Process. 25 (2017) 185–200. doi:10.1016/j.jmapro.2016.11.006.

[17] A. Mitchell, Primary carbides in Alloy 718, 7th Int. Symp. Superalloy 718 Deriv. (2010) 161–167. doi:10.1002/9781118495223.ch11.

[18] F. Xu, Y. Lv, Y. Liu, B. Xu, P. He, Effect of heat treatment on microstructure and mechanical properties of inconel 625 alloy fabricated by pulsed plasma arc deposition, Phys. Procedia. 50 (2013) 48–54. doi:10.1016/j.phpro.2013.11.010.

[19] Special Metals, INCONEL alloy 718, in: 2007: pp. 1–28. doi:SMC-066.

[20] G.D.J. Ram, A.V. Reddy, K.P. Rao, G.M. Reddy, Microstructure and mechanical properties of Inconel 718 electron beam welds, Mater. Sci. Technol. 21 (2005) 1132–1138. doi:10.1179/174328405X62260.

[21] Benoit, Study of Inconel 718 weldability using MIG CMT process, Sci. Technol. Weld. Join. 16 (2011) 477–482. doi:10.1179/1362171811Y.0000000031.

[22] C.H. Radhakrishna, K. Prasad Rao, The formation and control of Laves phase in superalloy 718 welds, J. Mater. Sci. 32 (1997) 1977–1984. doi:10.1023/A:1018541915113.

[23] D.G. Thakur, B. Ramamoorthy, L. Vijayaraghavan, Effect of cutting parameters on the degree of work hardening and tool life during high-speed machining of Inconel 718, Int. J. Adv. Manuf. Technol. 59 (2012) 483–489. doi:10.1007/s00170-011-3529-6.

[24] H.P. are Made, Steel Pipe, (n.d.). http://www.madehow.com/Volume-5/Steel-Pipe.html.

[25] HardHat Engineer, Pipe Fittings Manufacturing Process, (n.d.). https://hardhatengineer.com/pipe-fittings/pipe-fittings-manufacturing-process/.

[26] ASM International, ASM Handbook: Volume 5 Surface Engineering, 1994. doi:10.1007/s11548-011-0634-9.

[27] J.K. M. Rozmus-Górnikowska*, M. Blicharski, Influence of weld overlaying methods on microstructure and chemical composition of Inconel 625 boiler pipe coatings, Kov. Mater. 52 (2014) 1–7.

[28] S.-H. Lee, N.J. Themelis, M.J. Castaldi, High-Temperature Corrosion in Waste-to-Energy Boilers, J. Therm. Spray Technol. 16 (2007) 104–110. doi:10.1007/s11666-006-9005-4.

[29] J. Adamiec, High temperature corrosion of power boiler components cladded with nickel alloys, Mater. Charact. 60 (2009) 1093–1099. doi:10.1016/j.matchar.2009.03.017.

[30] M. Rozmus-Górnikowska, Ł. Cieniek, M. Blicharski, J. Kusiński, Microstructure and Microsegregation of an Inconel 625 Weld Overlay Produced on Steel Pipes by the Cold Metal Transfer Technique, Arch. Metall. Mater. 59 (2014) 16–19. doi:10.2478/amm-2014-0185.

[31] Special Metals, INCONEL alloy 625, in: 2013: pp. 1–18. doi:SMC-066.

[32] P. Ganesh, R. Kaul, C.P. Paul, P. Tiwari, S.K. Rai, R.C. Prasad, L.M. Kukreja, Fatigue and fracture toughness characteristics of laser rapid manufactured Inconel 625 structures, Mater. Sci. Eng. A. 527 (2010) 7490–7497. doi:10.1016/j.msea.2010.08.034.

4 Oxide accumulation effects on wire + arc layer-by-layer additive manufacture process

This chapter is based on the following publication.

X. Xu*, J. Ding, S. Ganguly, C. Diao, S. Williams, Oxide accumulation effects on wire + arc layer-by-layer additive manufacture process, J. Mater. Process. Tech. 252 (2018) 739–750. doi:10.1016/j.jmatprotec.2017.10.030.*

The first step of maraging steel research is to study the feasibility of depositing maraging steel using WAAM. Initial studies showed that it was difficult to deposit even a simple linear wall feature using normal deposition procedure since the molten pool was unstable and collapsed easily when it came to a certain number of layers. Attention was drawn to the factors affecting the wetting and spreading behaviour of the molten pool, i.e., oxide formation and accumulation, which has not been studied before, hence the publication. This chapter studies the oxides formation and accumulation mechanism and how oxides affect the surface waviness and mechanical properties of the WAAM material. The outcome of this study is the intentionally applied extra shielding during WAAM.

Abstract: A maraging steel wall structure was built layer-by-layer to study oxide accumulation mechanisms and the influence of oxides on the subsequent deposition. An online arc welding camera was also applied to investigate the wetting and spreading behaviour of the deposition on different surface conditions. Two maraging steel walls were deposited under torch shielding only and torch plus tent shielding conditions respectively to study the effect of oxides on the mechanical properties. Upon deposition a mixture of Fe, Al and Ti oxides formed, floated to the weld pool surface and accumulated layer by layer, deteriorating the surface condition such that it was rough and porous, which adversely affected the stability of arc and the wetting and spreading process of the weld pool in subsequent layers. The accumulation of oxides added to the uncertainty of the layer dimension and worsened the surface finish to reduce the structural integrity. Despite that the majority of the oxides floated to the weld pool surface, oxides (up to a few hundred nanometers in diameter) were found to be dispersed in the

additively manufactured structure and might be one of the strengthening sources resulting in a 11% increase in UTS and a 19% decrease in elongation compared to the structure built in the torch plus tent shielding condition.

Keywords: wire + arc additive manufacture; oxides accumulation; wetting and spreading; maraging steel.

4.1 Introduction

Additive manufacturing (AM) was initially developed for rapid prototyping to allow greater design freedom, less material wastage, and shorter lead-time in a layer-by-layer manner [1]. Extensive research was devoted to plastic parts initially and as Atzeni and Salmi [2] summarised, AM technology makes the economic production of small quantities of final plastic parts more feasible. After decades of development, the research interest has now moved to metals, which is attractive to many industrial sectors such as aerospace, shipbuilding and oil and gas where massive large-scale metallic structures are fabricated.

Almeida and Williams [3] developed the wire + arc additive manufacture (WAAM) process, aimed at producing massive (meter scale) metallic structures with full density, high deposition rate, and low equipment cost. Ding et al. [4] described that in WAAM the commercial welding power source is utilised to generate the electric arc as the heat source and an external wire is fed as the feedstock; usually, a preprogrammed robot arm is applied to control the deposition path to build a functional part in a layer-by-layer manner. So far, WAAM has been proved feasible for a broad range of materials from steel, titanium, Inconel superalloy, high strength aluminium to refractory metals, as stated by Williams et al. [5].

Ever since WAAM has been proposed, various researches have been carried out to fully understand this process. Cong et al. [6] investigated the effects of power source mode on the porosity characteristic of additively manufactured high strength aluminium alloy with cold metal transfer (CMT) process and studied the relationship between deposition mode and WAAM materials properties [7]. The interpass rolling technology has been applied by Gu et al. [8] and Colegrove et al. [9] to WAAM for aluminium and steel to induce recrystallization and eliminate

porosities in aluminium and to reduce distortion and residual stress in steel, respectively. Various in-situ inspection of metal AM processes has been applied as well. For example, Berumen et al. [10] utilized an in-line camera based set-up to measure the dimensions of the melt pool and the mean radiation emitted; Furumoto et al. [11] assembled a high-speed camera to monitor the consolidation of the metal powder during irradiation. Similar technologies are also being investigated in WAAM now.

In WAAM, two aspects are of most concern: surface finish and mechanical properties, which represents the surface and interior qualities, respectively. A component built by WAAM is built up on a layer by layer basis. Each layer except the first is formed by solidifying the liquid weld pool on the surface of the previously solidified layers. Therefore, the surface condition and the wetting and spreading behaviour of the weld pool play a dominant role in controlling the surface finish of WAAM parts. The geometry feature of the weld pool results from the interaction between the arc power, travel speed, deposition rate, interpass temperature and material properties [12], and the surface waviness of the WAAM part is highly dependent on the effective wall width and layer height. The shape of the weld pool is determined by the forces acting on it [13,14], and in the simplest analysis of a static sessile drop there are two forces, hydrostatic pressure and capillary pressure, the values of which are functions of density, gravitational acceleration, height of the liquid column above the point of interest, the surface tension and the curvature of the surface [12]. Of these variants, the surface tension is reported to be affected by the amount of dissolved oxygen in various metals [15,16].

As reported by Cáceres and Selling [17], defects such as inclusions, entrapped dross and gas porosity could lead to a decrease in tensile ductility and strength which can be correlated with the area fraction of defects in the fracture surface. In another AM process, selective laser melting (SLM), experiments are carried out in an inert atmosphere in a sealed chamber. Despite this, Kempen et al. [18] and Yasa et al. [19] reported that in their research on 18Ni-300 maraging steel Ti and Al combined oxides (TiO_2: Al_2O_3) were present as large inclusions (in the

size of 10-20 µm) in the matrix. These inclusions reduced the toughness especially in the aged condition when the material was brittle. Thijs et al. [20] applied microscopy and spectroscopy to investigate the initiation of these oxides (size ranging from 10-120 µm). It was found that an oxide layer containing Al and Ti was created on top of each layer; upon depositing the next layer, the oxide layer was broken and dragged further. Such accumulation of oxides in the bulk resulted in the large and irregularly shaped inclusions inside the final component.

Similarly to SLM, WAAM is also a layer-by-layer process so oxide accumulation could be an issue, the only difference being that the main source of oxide in the SLM process is the powder (oxide surface, humidity, entrapped gas and so on) while in the WAAM process the atmosphere is the most significant source of oxygen. Thus, oxides formation mechanism and how oxides will affect the surface finish and mechanical properties of WAAM parts have been studied in this research. Furthermore, WAAM is characterised by a much larger weld pool and a much slower cooling rate compared to SLM. Therefore, for WAAM wetting and spreading of the liquid weld pool on the as-solidified surface will be a significant issue determining the surface finish. Furthermore, the slow cooling rate allows enough time for the low-density oxides to escape from the inner weld pool and float to the surface. Successive thermal cycles lead to the part being built being kept at a high temperature for long periods, increasing the likelihood of forming more undesirable oxides on the surface.

A common practice in AM is to melt the metallic powder or wire in an inert atmosphere; however, few researches have been carried out to investigate the benefits of this. Customising an inert atmosphere and reducing the oxygen level to a certain low level is not always practical and economic and could be time-consuming especially when manufacturing large-scale parts. The preceding inclusions issue found in SLM showed that it is hard to eliminate oxides using a low oxygen atmosphere so more understanding needs to be gained on how these oxides could affect the AM process.

AM research has been very focused on achieving mechanical properties comparable to the wrought materials, with relatively few studies specifically on

understanding the influence of surface conditions on subsequent layer deposition and the resultant surface finish and mechanical properties of the components. Therefore, this paper aims to investigate the formation and accumulation mechanisms of oxides and effect of oxides on the wetting and spreading of the deposition, arc stability and structure integrity and mechanical properties of the WAAM products.

4.2 Materials and methodology

The WAAM system comprises a welding power source, a wire feeding system, a tent (filled with pure Ar when required, as shown in Fig. 4-1b), a 6-axis ABB robot with a welding torch mounted, and a working platform. A 10 mm thick mild steel plate was used as the substrate, and the 1.2 mm maraging steel wire (MARVAL 18S, equivalent to maraging 250-grade steel) was used as the feedstock. The chemical composition of the wire is listed in Table 4-1.

Table 4-1 Chemical composition of the MARVAL 18S filler wire (wt. %).

Ni	Mo	Co	Ti	Al	C	Si	Mn	Fe
18.28	4.69	8.21	0.44	0.11	<0.01	<0.1	<0.1	Balance

The experimental procedure consists of two phases to represent two different WAAM processes. In phase 1, a plasma power source and a plasma torch were assembled to the robot arm to apply the plasma-WAAM process in an open atmosphere (Ar for plasma gas: 0.8 l/min, Ar for shielding gas: 10 l/min). A 9-layer wall structure was built in the form of stairs (see Fig. 4-1a) in which the length of each layer was reduced by a predetermined value (10 mm) to investigate oxides accumulation process. An online arc welding camera (Redman MC500) was attached to the torch to investigate the formation of oxides and monitor the wetting and spreading behaviour of the deposition on different layers (as shown in Fig. 4-1a). Meanwhile, an AMV 5000 arc monitor was deployed to monitor the arc voltage variation pattern in real time. In phase 2, a CMT power source and a CMT torch were fixed to the set-up to perform the CMT-WAAM process. Two 6-layer walls were built in comparison: one in the open atmosphere with standard torch shielding only and the other one in an argon-filled tent (where oxygen level

was controlled below 300 ppm by using Z230 Oxygen Analyser, Hitech Instruments and the measurement was taken at the bottom of the tent) to investigate the influence of the ambient condition on the surface finish and structure integrity of the WAAM structures, as shown in Fig. 4-1b. Two additional walls were built under identical conditions and tensile samples were sectioned across the layers to study the effect of oxides on the mechanical properties of the WAAM products. Three samples in each wall were tested for averaging.

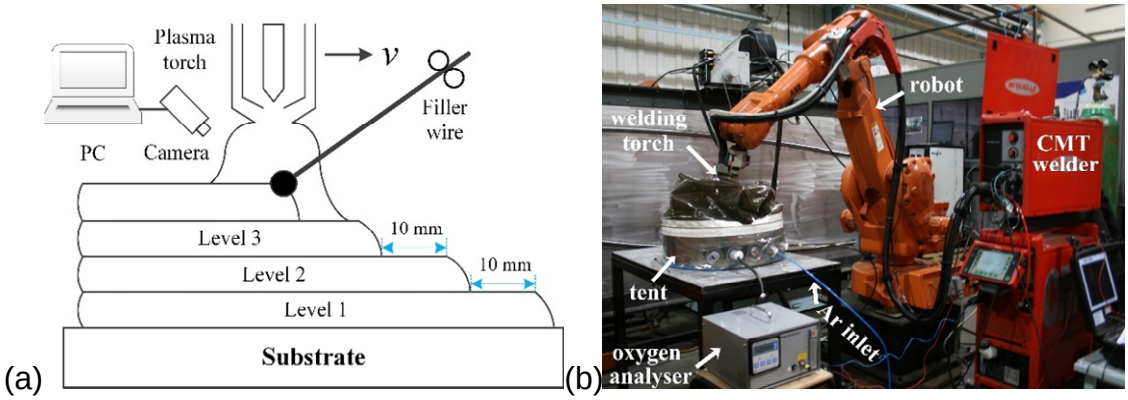

Figure 4-1 Experimental setups of the WAAM process (a) phase 1 (b) phase 2.

Samples were cross-sectioned in a plane perpendicular to the substrate and the wall length direction to examine different layers of deposit and a procedure consisting of mounting, grinding and polishing were followed to prepare the specimens for oxide analysis. Scanning Electron Microscope (SEM, FEI XL30-SFEG) equipped with the energy-dispersive spectrometry detector (EDS, Oxford Instrument, acquisition time 60s, acceleration voltage 10kV) was used to analyse the morphology, thickness and chemical composition of the oxide layers on top of the different layers of the wall structure. The Zwick/Roell hardness tester was utilised to measure the microhardness under a load of 1 kg and holding time of 15s. Tensile coupons were designed and machined as per ASTM-E8 standard, and the tensile test was carried out with Instron 5500R electromechanical testing machine (crosshead speed: 0.5 mm/min) at room temperature.

4.3 Results and discussion

4.3.1 Morphology of the oxide layer

Fig. 4-2 shows the macro-morphology of the oxide layers on the top of different levels in the open atmosphere. Each level of the stair-shaped wall consists of a different number of deposition layers ranging from 1 to 9. The surface of the first layer is very smooth although the dark colour of the bead reveals the surface oxidation. As the number of layer increases, the top surface progressively becomes rougher with different orientation of the oxide scales with different colours (9 layers).

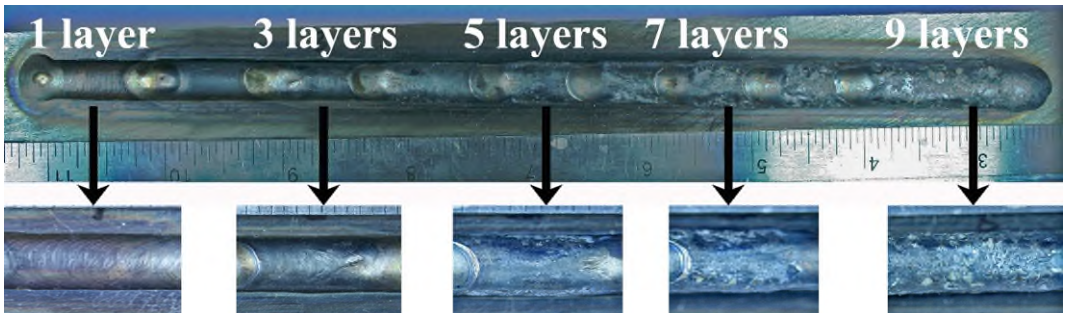

Figure 4-2 Macro-morphology of oxides (phase 1 using plasma arc, current=180A, WFS=1.8m/min, TS=0.2m/min).

Fig. 4-3 presents the micro-morphology of the oxide layer at different levels from the top view through SEM (in secondary electron mode, SE mode). As can be seen, the oxides morphology and constituents at the early stage (1 layer) are rather simple with only two kinds of distinct regions (Fig. 4-3a): the dark regions are the oxidised areas while the bright regions reveal the exposed metal. In comparison, the surface of the 9th layer deposit contains complex oxides which are revealed by the contours of different contrasting regions under SEM (Fig. 4-3b).

(a) 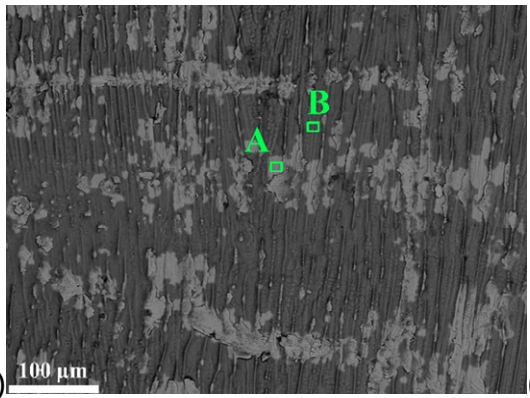

(b) 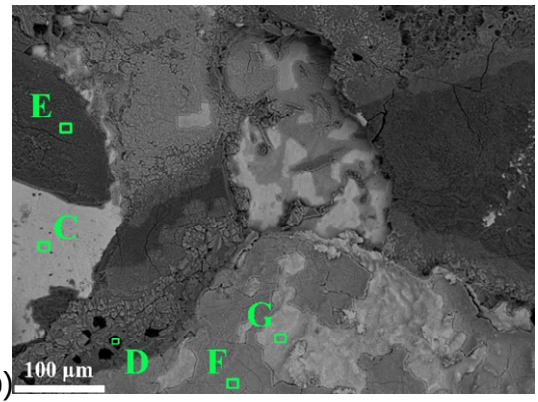

Figure 4-3 Micro-morphology of oxides when there is (a) 1 layer and (b) 9 layers deposition (Acc.V=10kV, Spot=3.0, Magn=200, Det=SE, WD=4.8).

Table 4-2 shows the EDS analysis results of different regions as labelled in Fig. 4-3. It was found that the whiter area is less oxidised compared to the darker area and as the number of layers increased, more areas containing different oxygen levels (ranging from 9.97% to 47.43%) and various combinations of oxides were found non-uniformly distributed throughout the oxide layer. Given the elemental content of the filler wire, the oxides were primarily comprised of Al oxides, Ti oxides, and Fe oxides. It should also be noted that among oxide islands there are also some areas where the oxide scale is dislodged, resulting in the exposure of fresh metallic surface e.g. Zone C in Fig. 4-3b. Such areas, on the one hand, separate oxides islands and leads to increased roughness and thickness variation; on the other hand, would have a lower melting point compared to oxides, which may result in non-uniform melting-floating phenomenon during the transition of the weld pool. This will be further explained later.

Table 4-2 EDS analysis of marked areas in Fig. 4-3 (wt. %).

	Spectrum Label	O	Al	Ti	Fe	Co	Ni	Mo
1 layer	A	2.12	-	0.28	70.7	6.07	14.64	3.23
	B	16.21	-	0.63	63.36	5.46	11.13	3.19
9 layers	C	-	-	0.94	66.11	8.96	18.85	5.14
	D	43.98	3.63	25.67	25.89	-	-	-
	E	47.43	10.38	36.28	4.96	-	-	-
	F	24.89	-	-	62.41	6.68	5.33	0.69
	G	9.97	0.21	0.27	40.66	9.71	32.08	7.09

4.3.2 Oxide accumulation mechanism

Fig. 4-4 shows the SEM images of the cross-section of each level, which clearly displays the oxides accumulation process. When there is only one layer, a few oxides form a thin oxide layer and do not cover the entire surface (Fig. 4-4a). As more layers have been deposited, the oxide layer gradually grows and covers the entire surface and thickness increases, varying from 1.3 μm to 13.04 μm when the number of layers varies from 1 to 9 (Fig. 4-4f).

The oxide layers are rough and porous and do not distribute uniformly on the top of each layer. They are unstable structures with limited adherence to the matrix and may break with expansion and contraction of the base metal and oxides due to the accumulation of thermal stress. Such stress develops from the mismatch of coefficient of thermal expansion (CTE) between the oxides and the matrix, as explained by Guleryuz and Cimenoglu [21]. Also, oxides change phase with temperature and elemental diffusion and may decompose into several sub-layers as shown in Fig. 4-4e.

Generally, oxides stay on the surface of the deposits as big scales and oxide ingress is not observed within the deposited material which is clean and free from oxides. However, on occasions, oxides are found to be trapped as an inclusion during the solidification process as shown by the red arrow in Fig. 4-4d.

Fig. 4-4g shows the SEM linear scanning results from the maraging steel wall matrix to the oxide layer (as shown in Fig. 4-4d). It is clear that there are

significant variations of the elemental contents of Fe, Al, Ti and O from the matrix to the oxide layer with the Al, Ti and O content increasing and Fe content decreasing. From the outer surface of the oxide layer to the matrix, the Al, Ti and Fe oxides enrichment are observed in sequence. This could be due to different densities and diffusion directions and diffusion rates of oxides, as indicated by Guleryuz and Cimenoglu [21] since they are of different thermodynamics and kinetics. In successive layers, the Al and Ti oxides decompose under the high arc temperature and, after recombining with the additional oxygen they float to the surface and accumulate as fresh scales. In contrast, the iron oxides form in the solid state when the diffusion of atoms is minimised and the availability of Fe atoms is much higher beneath the Al and Ti oxides.

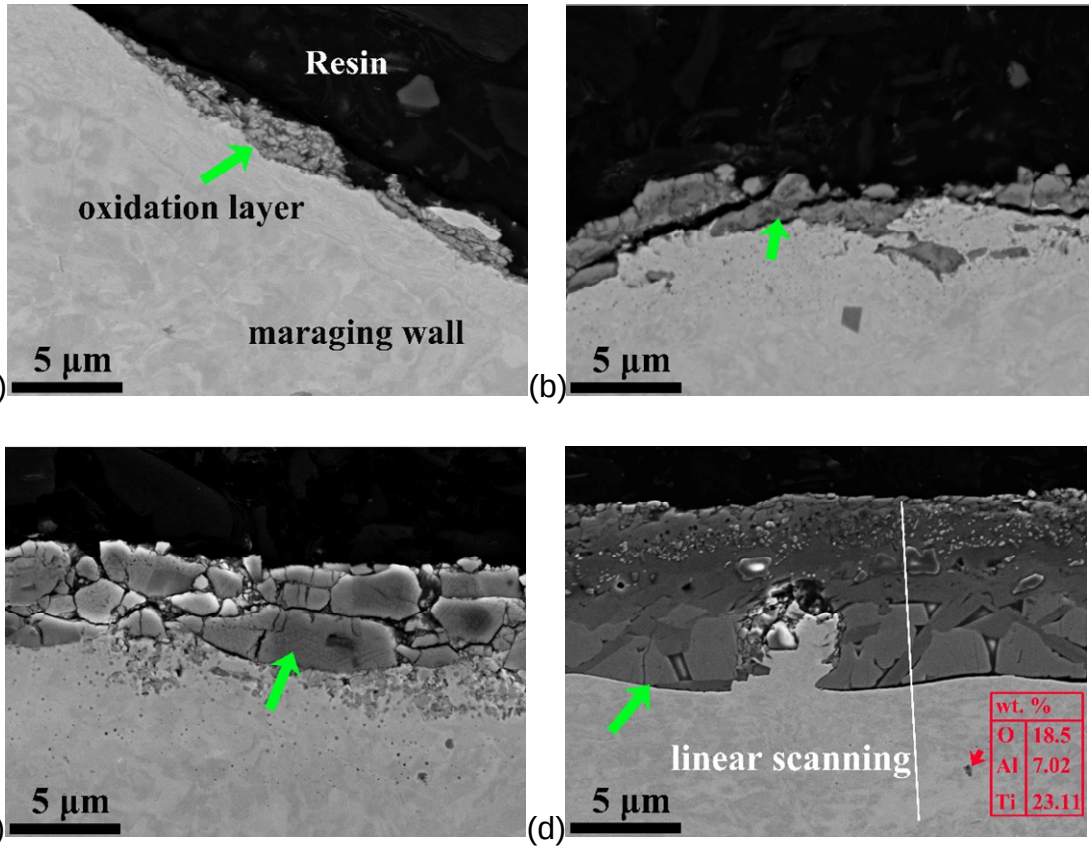

(a) (b) (c) (d)

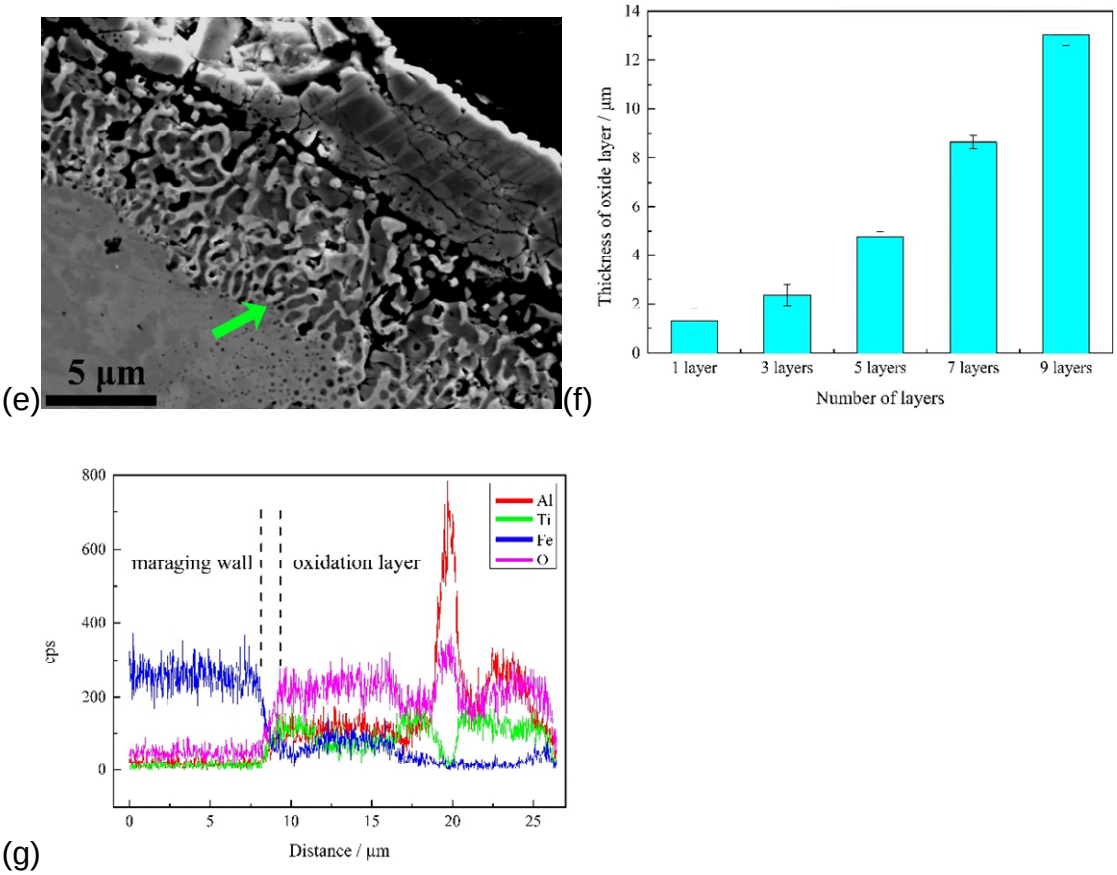

Figure 4-4 Cross-sections on each level when there is (a) 1 layer (b) 3 layers (c) 5 layers (d) 7 layers (e) 9 layers deposition (f) thickness of oxide layer (error bar: standard deviation) (g) linear scanning in Fig. 4-4d.

4.3.3 Oxides entrapped between layers

Oxides after formation would float to the weld pool surface due to their lower density compared with the density of the liquid metal pool. However, depending on the liquid flow of the melt pool, oxides could be found to be trapped within the liquid melt pool. This problem is likely to be exacerbated with increasing numbers of layers when the scale thickness increases which may lead to the entrapment of oxides between two successive passes, as shown in Fig. 4-5a. The oxide zone is embedded at the interface where the two layers join and extend from the surface into the as-deposited structure up to about 200 µm. Although the penetration could be neglected when compared to the surface waviness of the WAAM parts as such oxides will be removed during standard machining, the

presence of such unexpected oxides still leads to the structural and elemental discontinuity in the WAAM structure.

Figs. 4-5b-f show the SEM elemental mapping results of the trapped oxide zone. Similarly to the oxides on the top surface, these inner oxides also have a multi-layered structure, the composition of which is complex and not uniform. Different regions rich in Ti, Al and Fe are located in different layers.

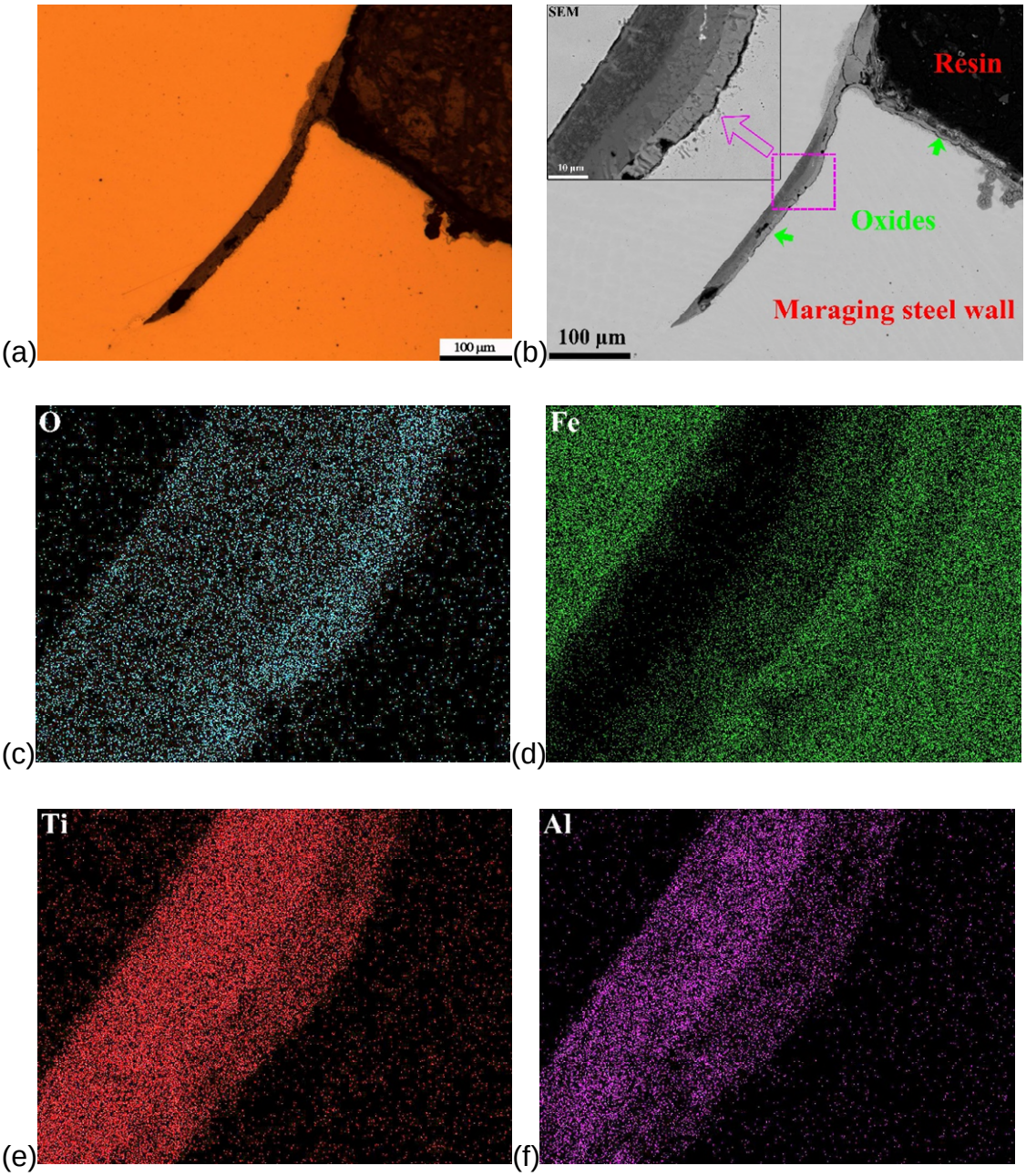

Figure 4-5 Entrapped oxide layer found between layer 6 and layer 7 (a,b) and its SEM elemental mapping results (c,d,e,f) (a) OM (b) SEM (c) O (d) Fe (e) Ti (f) Al.

4.3.4 Wetting and spreading on the oxide layer

Fig. 4-6 shows still images from footage of the deposition process on the top of 2nd and 8th layers to represent the wetting and spreading behaviour of the weld pool on a smooth and a rough surface condition, respectively. When depositing on a smoother surface, the curved line indicating wetting boundary maintains a temporally constant profile (indicated by the green dotted line in Fig. 4-6a), indicating a steady wetting and spreading process of the 3rd layer. Besides, the relatively smooth curve also implies the constant resistance from the surface against the weld pool along the depositing direction.

In comparison, when depositing on a rough surface, the wetting boundary shows temporal variation and shifting depending on the surface condition at the weld pool boundary: the rougher the surface, the greater variation of the curve (Fig. 4-6b). This is because the rough surface would alter the arc length which would change the total thermal energy applied which will impact the weld pool dimension and the wetting angle.

(a)

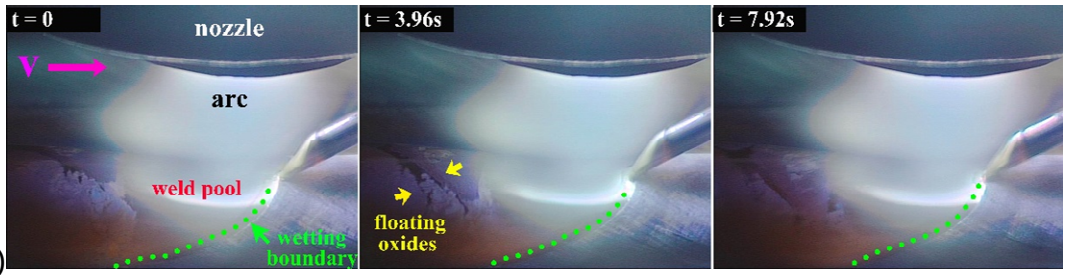

(b)

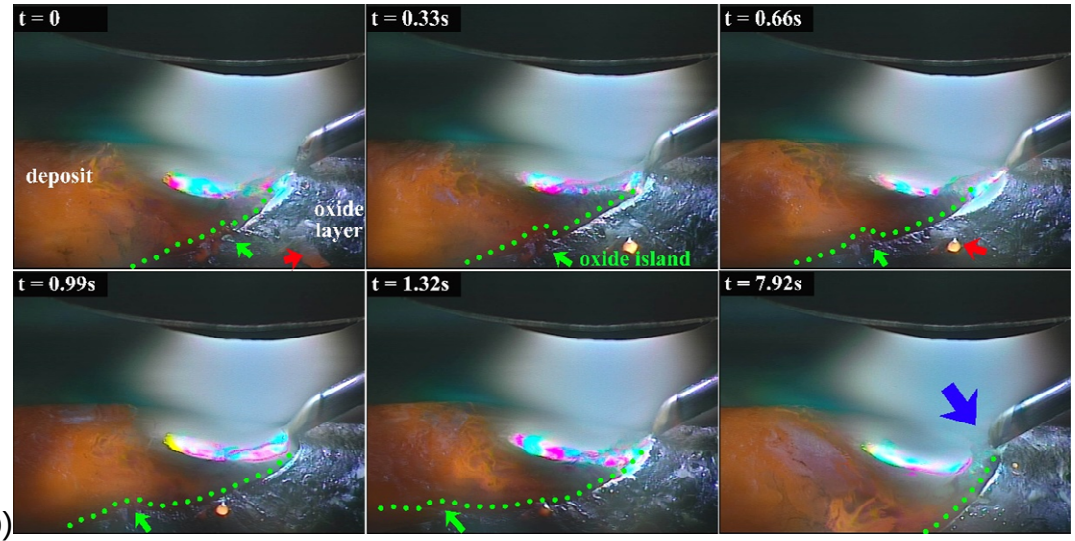

Figure 4-6 Footage of deposition process on different surface conditions on (a) the 2nd layer (a relatively smoother surface) (b) the 8th layer (a relatively rougher surface).

Bonn et al. [22] reported that for the wetting and spreading on a smooth surface (as shown schematically in Fig. 4-7a), the equilibrium system should conform to the following balance of forces to minimise the free energy of the system,

$$\gamma_{SG} = \gamma_{SL} + \gamma_{LG} \cos\theta \qquad \textbf{(4-1)}$$

Where γ_{SG} is the solid-gaseous surface tension, γ_{SL} is the solid-liquid surface tension, γ_{LG} is the liquid-gaseous surface tension and θ is the equilibrium contact angle.

For a particular solid-liquid-gaseous system the three surface tensions can be considered constant. Hence the equilibrium contact angle θ remains unchanged during the deposition on a smooth surface, which leads to a stable wetting and spreading process of the weld pool and the constant wetting boundary as indicated in Fig. 4-6a.

In contrast, when depositing on the rough surface, the variation of solid surface orientation (as shown in Fig. 4-7b) leads to the modified equilibrium equation as below,

$$\gamma_{SG} \cos\alpha = \gamma_{SL} + \gamma_{LG} \cos\theta' \qquad \textbf{(4-2)}$$

Where α is the angle of the rough surface with respect to the smooth surface.

On the rough surface, α is unpredictable, so the wetting angle θ' keeps changing to balance the forces and to establish a new equilibrium system, which is the driving force of the adaptive wetting boundary as shown in Fig. 4-6b. When α is positive (say, a convex oxide island blocking the way, Fig. 4-6b) more resistance is applied to the weld pool to prevent the spreading; when α is negative (say, a concave on the surface), the gravity-induced dragging force helps the wetting and spreading process. The wetting and spreading process in WAAM process on the rough surface is such an alternating manner between "dragging" and "blocking" in an adaptive mode over the deposition.

When depositing on such an oxide layer, oxides will float to the surface of the weld pool (as shown in Fig. 4-6a by yellow arrows) due to their higher melting point and lower density compared to the matrix. However, when facing a large oxide island (as indicated in Fig. 4-6b), instead of floating oxides, the weld pool bypasses oxide islands and changes the wetting boundary to an irregular curve until the weld pool entirely passes it. Besides, even before the weld pool arrives, the material beneath the thinner oxide layer (as indicated by the red arrow in t=0, Fig. 4-6b) and the less oxidized area among the oxide layer (as indicated by the red arrow in t=0.66s, Fig. 4-6b) will melt first, even before oxides float. As a consequence, the weld pool wets and spreads on a rough solid surface with dispersed liquid zones, which gives rise to a greater uncertainty of the position of the wetting boundary and bead shape; defects, such as lack of fusion may result from this.

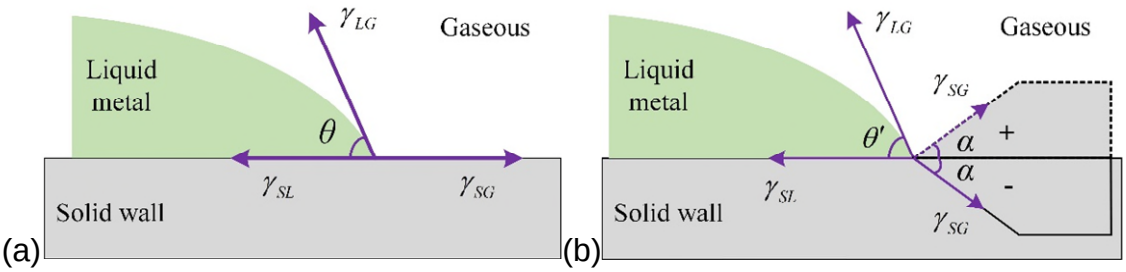

Figure 4-7 Wetting and spreading on different surface conditions. (a) on a smooth surface (b) on a rough surface.

4.3.5 Arc behaviour on an oxide layer

Miao et al. [23] reported that the arc behaviour greatly affects the weld pool stability due to the interaction of the different forces between the arc and the weld pool. Furthermore, a consistent metal transfer mode is also essential for the weld pool stability, as concluded by Miao et al.[24]. As with welding, the arc stability is dominant in controlling the deposition shape and quality in WAAM. The accumulated oxides have a significant effect on the arc behaviour. A smooth surface keeps the arc length and the weld pool dimension constant ensuring a constant wire feeding location with respect to the weld pool over the entire deposition length. It also provides a constant metal transfer mode (ideal liquid bridge mode as shown in Fig. 4-6a) minimising any disturbance to the weld pool. In contrast, when depositing on the rough surface, the arc length and change of wetting boundary dimension and profile lead to variations in wire feed position with reference to the as-deposited structure. In the plasma-WAAM process, the metal transfer mode depends heavily on the wire feeding position; thus, during the deposition process the liquid bridge can be unstable and could break (as indicated by the blue arrow in Fig. 4-6b, t=7.92s) at some point, or even transfer to globular transfer mode, which introduces more disturbance to the weld pool.

The stability of the arc behaviour is also indicated by the arc voltage. As shown in Fig. 4-8, the arc voltage of deposition on a smooth surface is much more stable than that of a rough surface with less fluctuation in the waveform. This is because oxides have different electron emission capabilities compared to the matrix and the waviness of the oxidised surface leads to arc length variation and therefore fluctuation of the arc voltage. Considering the constant current (CC) mode in the present WAAM-Plasma process, the heat input is also fluctuating at the same time as the voltage.

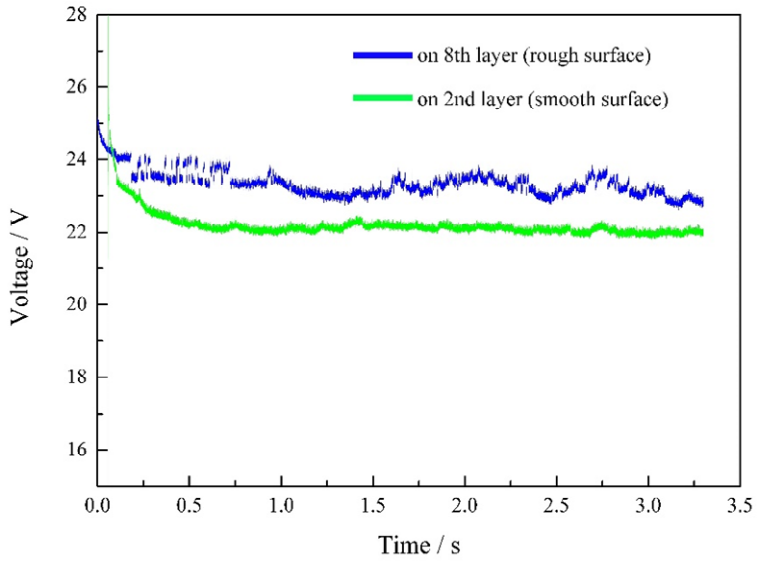

Figure 4-8 Arc voltage variation on different surface conditions.

4.3.6 Structural integrity

The effects of oxides are not only observed in the Plasma-WAAM process but also in CMT-WAAM process. Fig. 4-9 presents two 6-layer walls built by the CMT-WAAM process with torch shielding only (open atmosphere) and torch shielding plus inert environment (by depositing within a tent filled with Ar gas) conditions with the same parameters (WFS=8m/min, TS= 6mm/s). In the torch shielding only condition, oxides accumulate layer by layer, leading to a dark and rough surface of the wall structure; irregular bead shape, uneven layer surface, high waviness and voids in and between layers are observed (Fig. 4-9a). In contrast, when sufficient shielding is guaranteed, the wall structure is shiny with an almost equal width along the length direction; besides, the layer surface is flat with only a few oxides islands, and the waviness is reduced significantly (Fig. 4-9b). This is because the extra shielding prevents the as-solidified material from being exposed excessively to oxygen at high temperatures, thereby reducing the amount of oxides and providing a better surface condition for successive depositions.

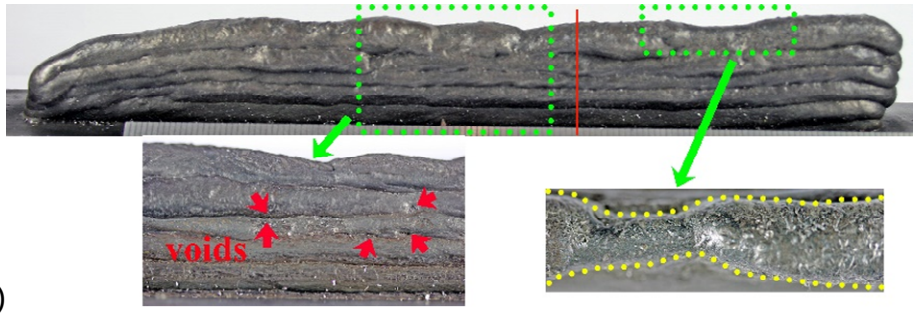

(a)

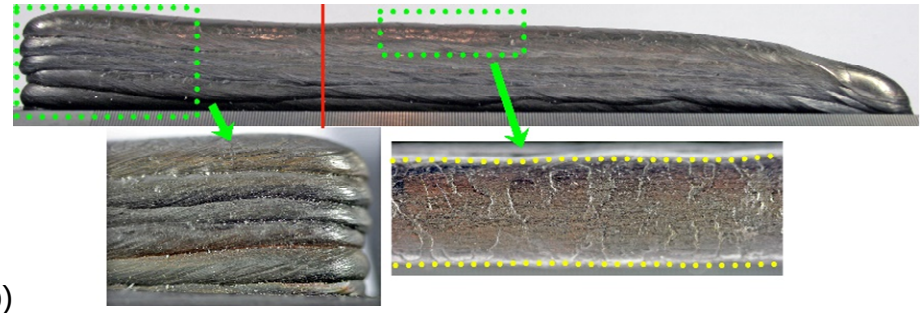

(b)

Figure 4-9 Bead shape of WAAM walls in different shielding conditions (phase 2 using CMT process, WFS=8m/min, TS=0.42m/min) (a) torch shielding only (b) torch + tent shielding.

The transverse cross-sections of the two preceding walls are displayed in Fig. 4-10 (section positions were indicated by the red line in Fig. 4-9). The wall with torch shielding only (Fig. 4-10a) is thinner and the edge is much more irregular compared to the torch plus tent shielding (Fig. 4-10b).

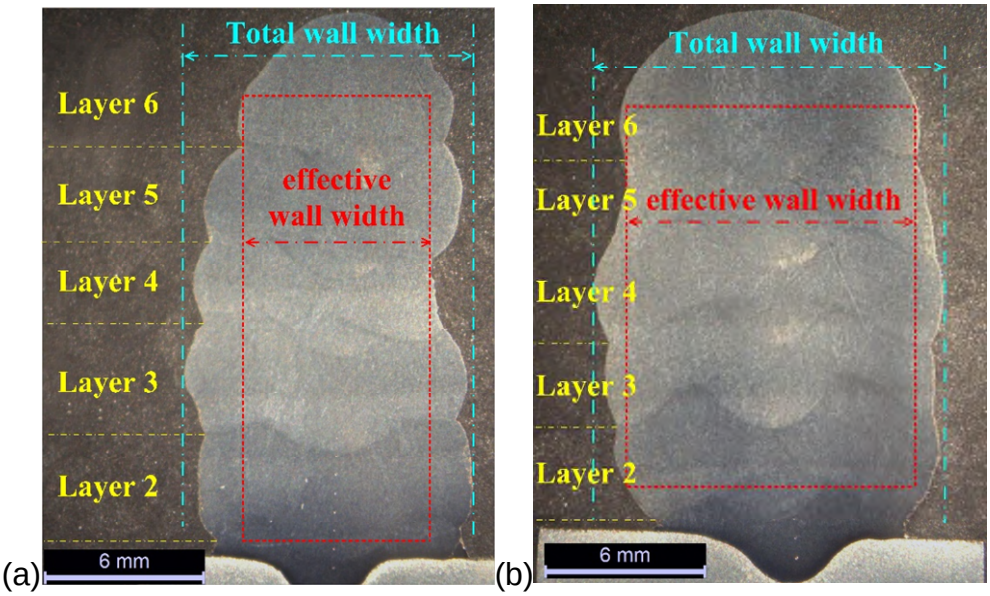

Figure 4-10 Transverse cross-section of the two CMT-WAAM walls (from Fig. 4-9) (a) torch shielding only (b) torch + tent shielding.

A detailed measurement of the wall dimensions is presented in Table 4-3. It can be seen that the surface waviness (as defined by Martina et al. [25]) of the torch-shielding wall is much greater than the counterpart (1.9mm versus 1.2mm). In consequence, extra tent shielding helps to improve the surface finish and the deposition efficiency (from 64.6% to 70.7%). When more layers are deposited, such an improvement would be even more significant.

Table 4-3 Measurements of the two walls.

		torch shielding only	torch + tent shielding
width	total wall width (TWW) / mm	10.8	13.0
	effective wall width (EWW) / mm	7.0	10.7
	surface waviness (SW) / mm *SW=(TWW-EWW)/2*	1.9	1.2
area	total wall area (TWA) / mm^2	179.0	214.3
	effective wall area (EWA) / mm^2	115.7	151.5
	deposition efficiency (DE) / % *DE=EWA/TWA*	64.6	70.7

4.3.7 Structural quality

4.3.7.1 Microstructure

Even though the surfaces of the two walls are significantly different due to different levels of oxidation, the bulk materials are more or less the same: a combination of cellular and dendritic martensitic microstructure with the dendrites growing perpendicularly to the fusion boundary, as shown in Fig. 4-11. Besides, no visible oxides in the form of inclusions are found in the cross-sections.

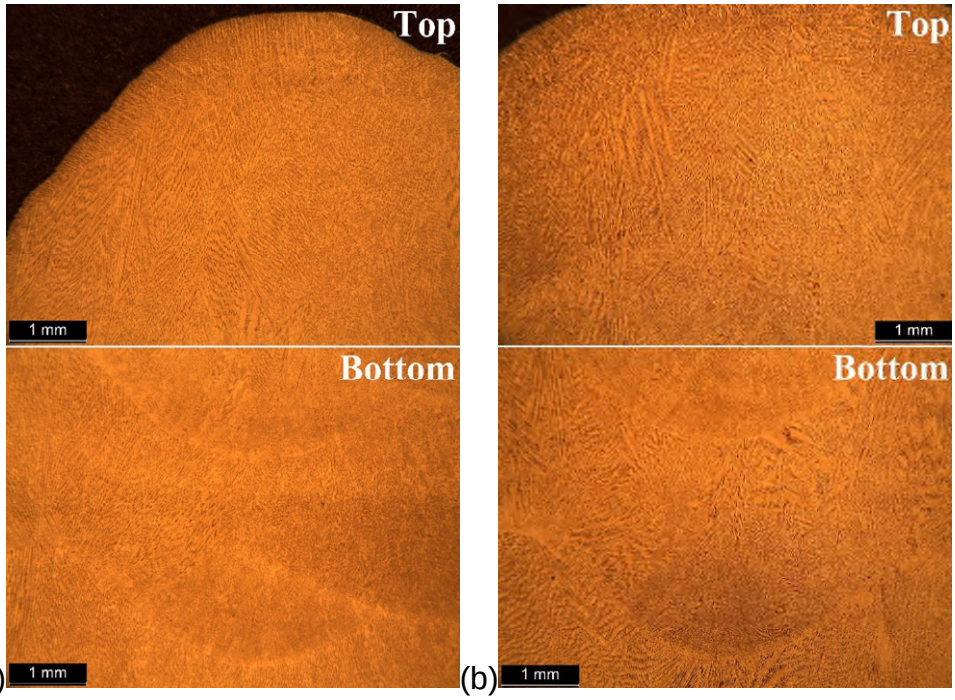

Figure 4-11 Microstructure of the two CMT-WAAM walls (a) torch shielding only (b) torch + tent shielding.

4.3.7.2 Microhardness

The microhardness measurements of the two walls in both as deposited and aged (3 hrs at 482°C) conditions along the central line from the top to the bottom are presented in Fig. 4-12. In the as deposited condition, both walls show a noticeable hardness increase from the top to the bottom (from around 33 HRC to around 43 HRC) due to the aging effect from successive depositions; after aging, the hardness variation is eliminated and the hardness of both walls is increased to around 52 HRC (52.5 HRC with extra tent shielding, 52.1 HRC without) which is comparable to the aged wrought maraging steel of the identical grade (50-55

HRC [26]). Despite the slight variation in values, the effect of oxide accumulation on the microhardness is negligible since the bulk materials of the two six-layer walls underwent identical thermal cycles and therefore resulted in very similar microstructural characteristics.

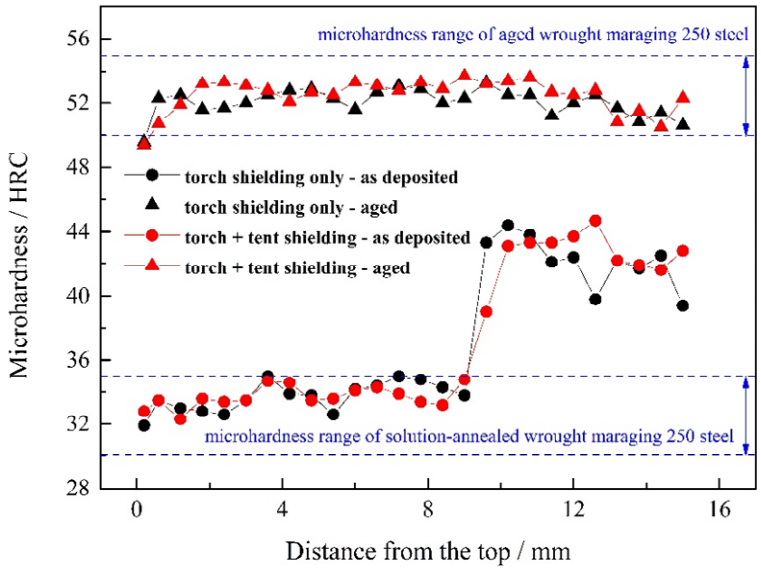

Figure 4-12 Microhardness of the two CMT-WAAM walls from the bottom to the top.

4.3.7.3 Tensile test

Fig. 4-13 presents the two additional walls built for the tensile test with the CMT-WAAM process. The wall built with torch shielding only displays great waviness on the surface (Fig. 4-13a), and during deposition, especially after a certain number of layers, the weld pool collapses from time to time as the accumulated oxides worsen the surface condition. In comparison, the wall built with torch plus tent shielding shows a much better surface finish with regular layer geometries and an almost constant layer height increment.

(a)

(b)

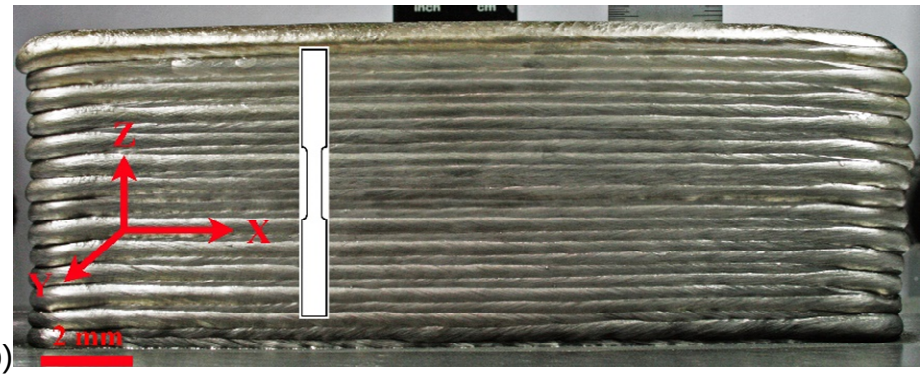

(c)

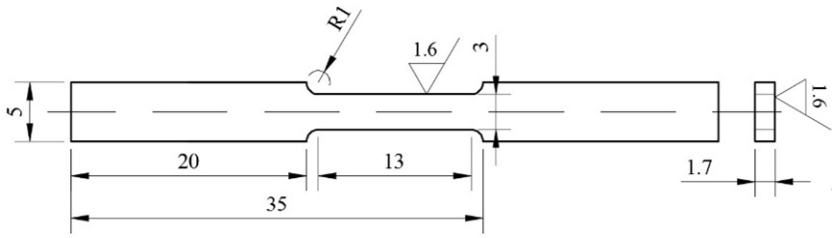

Figure 4-13 Two additional walls built for the tensile test using CMT process (a) torch shielding only (wall size: 180×68×9.8mm) (b) torch + tent shielding (wall size: 185×68×11.3mm) and (c) tensile test specimen drawing.

Tensile samples were taken along the Z direction, as shown in Fig. 4-13b. Fig. 4-14 presents the tensile test results. It can be seen that the UTS value of the material deposited with torch shielding only is 11% higher (1165 versus 1048 MPa) than the torch plus tent shielding condition, while the elongation is 19% lower (13.7% versus 17.0%) than the latter.

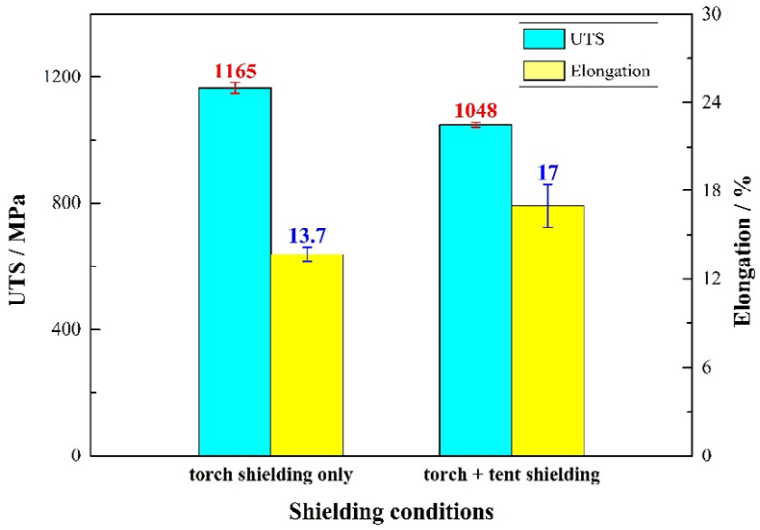

Figure 4-14 Tensile test results (error bar: standard deviation).

4.3.7.4 Fracture surface

Fig. 4-15 shows the fracture surface morphology of two typical tensile samples from the preceding two walls. A few dispersed spherical particles (a few to a few hundred nanometres in size) are found in the fracture surface of the material deposited with torch shielding only, whereas they are not observed in the torch plus tent shielding condition. Further EDS analysis proves that those particles are mainly Al, Ti and Fe oxides, as shown in Table 4-4.

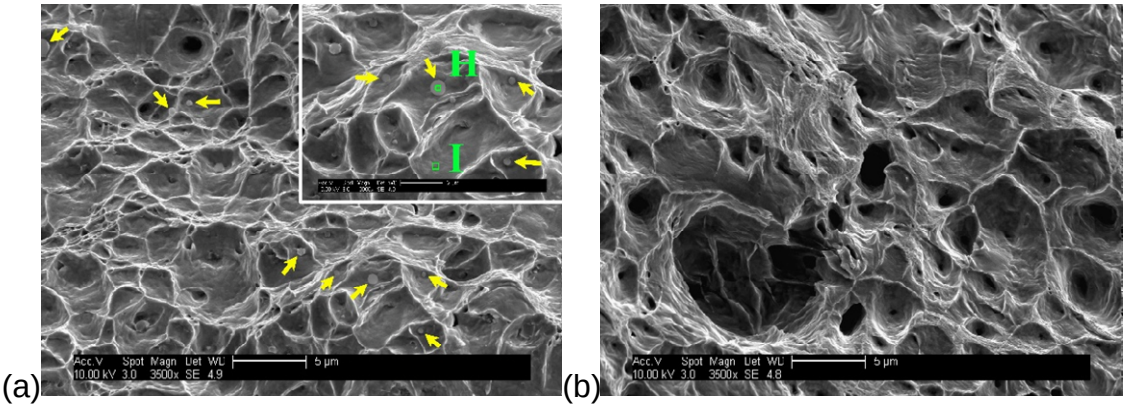

(a) (b)

Figure 4-15 Fracture surface of tensile specimens built using (a) torch shielding only (b) torch + tent shielding.

Table 4-4 EDS analysis of marked areas in Fig. 4-15a (wt. %).

Spectrum Label	O	Al	Ti	Fe	Co	Ni	Mo
H	42.5	39.42	4.76	11.19	0.15	-	1.97
I	-	0.81	-	69.03	8.68	17.85	3.63

4.3.7.5 Oxide strengthening mechanism

The strength difference between the two walls could be due to a number of factors, such as grain size, precipitate size and amount, and fraction of retained austenite. In the present study, the two walls were built with identical parameters except for the shielding condition, therefore oxides could be one of the strengthening sources. Oxides trapped in the material can have different effects which primarily depends on their size and distribution. When trapped in the form of large scales, oxides will reduce ductility and tensile strength both and will lead to a catastrophic failure very quickly. However, the dispersed oxides (up to a few hundred nanometers in diameter) may result in reinforcement of the matrix material. In a research conducted by Hassan and Gupta [27], it was found that the microhardness, UTS and ductility of the pure magnesium were increased significantly by adding 1.1 volume percentage of 50 nm sized Al_2O_3 due to the grain refinement induced by the nanosized additions. In the present research, the possible strengthening effect from the oxides (up to a few hundred nanometers in diameter) could be attributed to the load-bearing effect, i.e., the strengthening due to obstacle posed by closely spaced hard particles to the dislocation motion and matrix transferring the load to the nanosized reinforcements, as explained by S.Jayalakshmi and M.Gupta [28].

4.4 Conclusions

1. Deoxidizing elements in the wire combine with oxygen to form oxides on the surface of the layer; upon deposition, these oxides decompose, re-form, float to the weld pool surface and accumulate layer by layer with newly formed oxides.
2. Oxides in maraging steel are mainly Al, Ti, and Fe oxides and they distribute in different layers inside the oxide layer depending on their densities and diffusion rates.

3. The oxide accumulation leads to increased surface waviness and adversely affects the wetting and spreading of the subsequent deposition by providing various wetting angles and resistance against the liquid metal.
4. The surface oxides destabilize the arc and weld pool and thereby, the surface finish of the WAAM structure. Extra tent shielding substantially improved the surface waviness and deposition efficiency by 37% and 9%, respectively.
5. Dispersed oxides (up to a few hundred nanometers in diameter) are found to be trapped in the material deposited with torch shielding only and they may be one of the strengthening sources to result in an 11% increase in UTS and 19% decrease in elongation due to the load bearing effect.

4.5 References

[1] D. Herzog, V. Seyda, E. Wycisk, C. Emmelmann, Additive manufacturing of metals, Acta Mater. 117 (2016) 371–392. doi:10.1016/j.actamat.2016.07.019.

[2] E. Atzeni, A. Salmi, Economics of additive manufacturing for end-usable metal parts, Int. J. Adv. Manuf. Technol. 62 (2012) 1147–1155. doi:10.1007/s00170-011-3878-1.

[3] P. Almeida, S. Williams, Innovative process model of Ti–6Al–4V additive layer manufacturing using cold metal transfer (CMT), Solid Free. Fabr. Symp. (2010) 25–36. http://utwired.engr.utexas.edu/lff/symposium/proceedingsArchive/pubs/Manuscripts/2010/2010-03-Almeida.pdf.

[4] J. Ding, P. Colegrove, F. Martina, S. Williams, R. Wiktorowicz, M.R. Palt, Development of a laminar flow local shielding device for wire+arc additive manufacture, J. Mater. Process. Technol. 226 (2015) 99–105. doi:10.1016/j.jmatprotec.2015.07.005.

[5] S.W. Williams, F. Martina, A.C. Addison, J. Ding, G. Pardal, P. Colegrove, Wire+Arc Additive Manufacturing, Mater. Sci. Technol. 32 (2016) 641–647. doi:10.1179/1743284715Y.0000000073.

[6] B. Cong, J. Ding, S. Williams, Effect of arc mode in cold metal transfer process on porosity of additively manufactured Al-6.3%Cu alloy, Int. J. Adv. Manuf. Technol. 76 (2014) 1593–1606. doi:10.1007/s00170-014-6346-x.

[7] B. Cong, Z. Qi, B. Qi, H. Sun, G. Zhao, J. Ding, A Comparative Study of Additively Manufactured Thin Wall and Block Structure with Al-6.3%Cu Alloy Using Cold Metal Transfer Process, Appl. Sci. 7 (2017) 275. doi:10.3390/app7030275.

[8] J. Gu, J. Ding, S.W. Williams, H. Gu, P. Ma, Y. Zhai, The effect of inter-layer cold working and post-deposition heat treatment on porosity in additively manufactured aluminum alloys, J. Mater. Process. Technol. 230 (2016) 26–34. doi:10.1016/j.jmatprotec.2015.11.006.

[9] P. a. Colegrove, H.E. Coules, J. Fairman, F. Martina, T. Kashoob, H. Mamash, L.D. Cozzolino, Microstructure and residual stress improvement in wire and arc additively manufactured parts through high-pressure rolling, J. Mater. Process. Technol. 213 (2013) 1782–1791. doi:10.1016/j.jmatprotec.2013.04.012.

[10] S. Berumen, F. Bechmann, S. Lindner, J.-P. Kruth, T. Craeghs, Quality control of laser- and powder bed-based Additive Manufacturing (AM) technologies, Phys. Procedia. 5 (2010) 617–622. doi:10.1016/j.phpro.2010.08.089.

[11] T. Furumoto, M.R. Alkahari, T. Ueda, M.S.A. Aziz, A. Hosokawa, Monitoring of Laser Consolidation Process of Metal Powder with High Speed Video Camera, Phys. Procedia. 39 (2012) 760–766. doi:10.1016/j.phpro.2012.10.098.

[12] S. Ríos, P.A. Colegrove, F. Martina, S.W. Williams, Analytical process model for wire + arc additive manufacturing, Addit. Manuf. 21 (2018) 651–657. doi:10.1016/j.addma.2018.04.003.

[13] V.R. Ryabov, G.F. Deyev, Surface Phenomena in Welding and Surfacing, E.O. Paton Electric Welding Institute, Kyiv, 1998.

[14] G.F. Deyev, D.G. Deyev, Surface Phenomena in Fusion Welding Processes, 1st ed., CRC Press, Boca Raton, FL, 2006.

[15] J. Lee, T. Tanaka, M. Yamamoto, S. Hara, Effect of Oxygen on Surface Tension of Liquid Ag-Sn Alloys, Mater. Trans. 45 (2004) 625–629. doi:10.2320/matertrans.45.625.

[16] K. Morohoshi, M. Uchikoshi, M. Isshiki, H. Fukuyama, Surface Tension of Liquid Iron as Functions of Oxygen Activity and Temperature, ISIJ Int. 51 (2011) 1580–1586. doi:10.2355/isijinternational.51.1580.

[17] C.H. Cáceres, B.I. Selling, Casting defects and the tensile properties of an Al-Si-Mg alloy, Mater. Sci. Eng. A. 220 (1996) 109–116. doi:10.1016/S0921-5093(96)10433-0.

[18] K. Kempen, E. Yasa, L. Thijs, J.P. Kruth, J. Van Humbeeck, Microstructure and mechanical properties of selective laser melted 18Ni-300 steel, Phys. Procedia. 12 (2011) 255–263. doi:10.1016/j.phpro.2011.03.033.

[19] E. Yasa, K. Kempen, J. Kruth, Microstructure and mechanical properties of Maraging Steel 300 after selective laser melting, in: Proc. 21st Int. Solid Free. Fabr. Symp., 2010: pp. 383–396. http://utwired.engr.utexas.edu/lff/symposium/proceedingsArchive/pubs/Manuscripts/2010/2010-32-Yasa.pdf.

[20] L. Thijs, J. Van Humbeeck, K. Kempen, E. Yasa, J.-P. Kruth, Investigation on the inclusions in maraging steel produced by Selective Laser Melting, in: 5th Int. Conf. Adv. Res. Virtual Rapid Prototyp., 2011: pp. 297–304. doi:doi:10.1201/b11341-48\r10.1201/b11341-48.

[21] H. Guleryuz, H. Cimenoglu, Oxidation of Ti-6Al-4V alloy, J. Alloys Compd. 472 (2009) 241–246. doi:10.1016/j.jallcom.2008.04.024.

[22] D. Bonn, J. Eggers, J. Indekeu, J. Meunier, Wetting and spreading, Rev. Mod. Phys. 81 (2009) 739–805. doi:10.1103/RevModPhys.81.739.

[23] Y. Miao, X. Xu, B. Wu, X. Li, D. Han, Effects of bypass current on the stability of weld pool during double sided arc welding, J. Mater. Process. Technol. 214 (2014) 1590–1596. doi:10.1016/j.jmatprotec.2014.02.029.

[24] Y. Miao, X. Xu, B. Wu, D. Han, Y. Zeng, T. Wang, Effects of bypass current on arc characteristics and metal transfer behaviour during MIG-TIG double sided arc welding, J. Mater. Process. Technol. 224 (2015) 40–48. doi:10.1016/j.jmatprotec.2015.04.026.

[25] F. Martina, J. Mehnen, S.W. Williams, P. Colegrove, F. Wang, Investigation of the benefits of plasma deposition for the additive layer manufacture of Ti-6Al-4V, J. Mater. Process. Technol. 212 (2012) 1377–1386. doi:10.1016/j.jmatprotec.2012.02.002.

[26] A. International, ASM Handbook: Volume 4 Heat Treating, in: ASM Handb., ASM International, 1991: p. 2173. doi:10.1016/S0026-0576(03)90166-8.

[27] S.F. Hassan, M. Gupta, Enhancing physical and mechanical properties of Mg using nanosized Al2O3 particulates as reinforcement, Metall. Mater. Trans. A. 36 (2005) 2253–2258. doi:10.1007/s11661-005-0344-4.

[28] S.Jayalakshmi, M.Gupta, Metallic Amorphous Alloy Reinforcement in Light Metal Matrices, 2015. doi:10.1007/978-3-319-15016-1.

5 Microstructural evolution and mechanical properties of maraging steel produced by wire + arc additive manufacture process

This chapter is based on the following publication.

X. Xu*, S. Ganguly, J. Ding, S. Guo, S. Williams, F. Martina, Microstructural evolution and mechanical properties of maraging steel produced by wire + arc additive manufacture process, Mater. Charact. 143 (2018) 152–162. doi:10.1016/j.matchar.2017.12.002.*

Based on the study in Chapter 4, extra shielding in the form of an Ar-filled tent was provided to the maraging steel deposition process. WAAM maraging steel parts with good surface finish and structural integrity were obtained. This chapter further studied the microstructural evolution of the WAAM maraging steel in response to the inherent thermal history (as deposited condition) as well as the industry standard heat treatment. The inferiority in mechanical properties of the heat treated WAAM maraging steel to the wrought alloy was explained, and possible solutions were proposed.

Abstract: Wire + arc additive manufacture is developed for producing large-scale metallic components. In this paper, maraging steel parts were produced, and the microstructure and mechanical properties were investigated. The microhardness and tensile strength of the as deposited alloy reduced from the bottom to the top due to the transient thermal cycling, which resulted in partial aging and non-uniform formation of intermetallic compounds along the building direction. Solutionizing, followed by 3 hours aging, significantly reduced the microstructural heterogeneity and increased the mechanical properties by 24.7% through the formation of large amounts of finely distributed precipitates. The as deposited alloy possessed superior strength to the wrought alloy in solutionized condition but inferior to the later in aged condition, which was attributed to the less pronounced aging response of the low-angle columnar grains characterized microstructure and the presence of retained and reverted austenite.

Keywords: wire + arc additive manufacture; maraging steel; precipitates; mechanical properties; heat treatment.

5.1 Introduction

Wire + arc additive manufacture (WAAM) has been developed for the fabrication of large-scale (meter scale) metallic structures for advanced applications [1,2]. In this process, an electric arc is used as the heat source and the commercial welding wire is used as the feedstock material [3]. Usually, a pre-programmed robot arm is deployed to control the movement of the deposition path in a layer-by-layer manner to manufacture full-dense functional components. The feasibility of WAAM process has been verified by various materials ranging from titanium [4], aluminium [5,6], steel [7] to Inconel [8]. Compared with other existing additive manufacturing (AM) process, WAAM is characterized by low equipment cost, high deposition rate, reduced lead time and large-scale and full density parts [9].

Maraging steels are developed to combine superior high strength (yield strength commercially ranging from 1030 to 3450 MPa) with good fracture toughness [10]. The absence of carbon makes maraging steels different from conventional steels in that they are strengthened by the intermetallic compounds precipitated from the supersaturated martensite during the age hardening of the ductile low-carbon iron-nickel lath martensitic matrix [11]. In the solutionized condition, maraging steels are relatively soft with excellent machinability and weldability; a subsequent aging heat treatment can significantly improve the strength. Due to the low coefficient of expansion of maraging steel, the size change after aging is negligible (e.g. 0.0009 inch/inch for 250-grade maraging steel). The combination of these advantages makes maraging steels attractive to different sectors such as aircraft, aerospace [12], die-casting, tooling and weapon applications.

The maraging steels gain optimum mechanical properties through an aging heat treatment. However, due to the very small size (nanometer scale) and coherent distribution of these precipitates and the complex alloying system in maraging steel, there have long been a lack of effective characterization methods and a great deal of discussion on the strengthening mechanism [13]. The prevailing idea is that Mo acts as the primary hardener by forming ribbon-shaped Ni_3Mo and

Ti serves as the secondary hardener through the formation of spherical-shaped Ni_3Ti. Further aging is reported to cause the in situ transformation from the metastable Ni_3Mo to the equilibrium Fe_2Mo. Fe_7Mo_6 is another precipitate that is often reported [14]. Cobalt does not precipitate as it does not form precipitates with Fe, Ni, Mo and Ti, but it reduces the solubility of Mo in the Fe-Ni alloys, thus increasing the amount of Ni_3Mo formed during aging [15].

So far, only a few attempts have been made with selective laser melting (SLM) process to additively manufacture maraging steel parts [16-19]. The UTS of maraging steel produced by SLM are comparable to the wrought alloy in aged condition: 2094 MPa [19] and 2217 MPa [20] of SLM 300-grade maraging steel compared to 2050 MPa of the wrought alloy of the same grade. However, the SLM process is featured with low deposition rate due to the size of the powder used (normally a few to a few hundred micrometres). Besides, due to the fast scanning speed and cooling rate in SLM, unmelted powder particles were found trapped in the additively manufactured parts as inclusions [17]. Full density is not always guaranteed (relative density ranging from 90.9% to 99.9% [19]) as a result of the unmelted particles and oxides inclusions, which adversely affected the mechanical properties of the AM parts [21]. As reported [18], the SLM processed alloy showed a reduced toughness of 30-40% in the aged condition.

The aging temperature of maraging steel is relatively low (482°C) and will be frequently passed during the repeating melting-cooling deposition process, causing some extent aging effect. However, this transient aging is quite different from the conventional artificial aging where the components are deliberately kept at a certain temperature and hold for some duration. In addition, the aging response depends on the microstructure. In contrast to the wrought alloy where the whole part undergoes uniform thermal processing, different layer of the AM component goes through different numbers of thermal cycles based on the deposition sequence and the design of deposition. Therefore, when manufacturing a component by AM, different microstructure and mechanical properties can be expected from the conventional wrought route alloy.

Until now, few researches have been carried out to apply arc based AM process to manufacturing maraging steel components. The present research is aimed at understanding the application of WAAM process to produce maraging steel structures. Microstructural evolution, phase transformation and its effect on the aging response have been investigated and correlated to the mechanical properties of the WAAM products.

5.2 Materials and methods

The WAAM system in the present research mainly consisted of a six-axis FANUC robot, a plasma power source, a plasma torch, an external wire feeder and a working platform, as shown in Fig. 5-1. The entire setup was placed in an enclosure filled with pure argon gas and the oxygen level was controlled below 500 ppm through an oxygen analyser. The wire used for the study was MARVAL 18S of 1.2 mm in diameter which is designed to weld 200 and 250-grade maraging steel. The chemical composition of the wire and the wrought 250-grade maraging steel, and the nominal chemical composition of the 200-grade maraging steel are listed in Table 5-1. It can be seen that the chemical composition of the wire is in between the 200 and 250-grade maraging steel, yet closer to the 250-grade one.

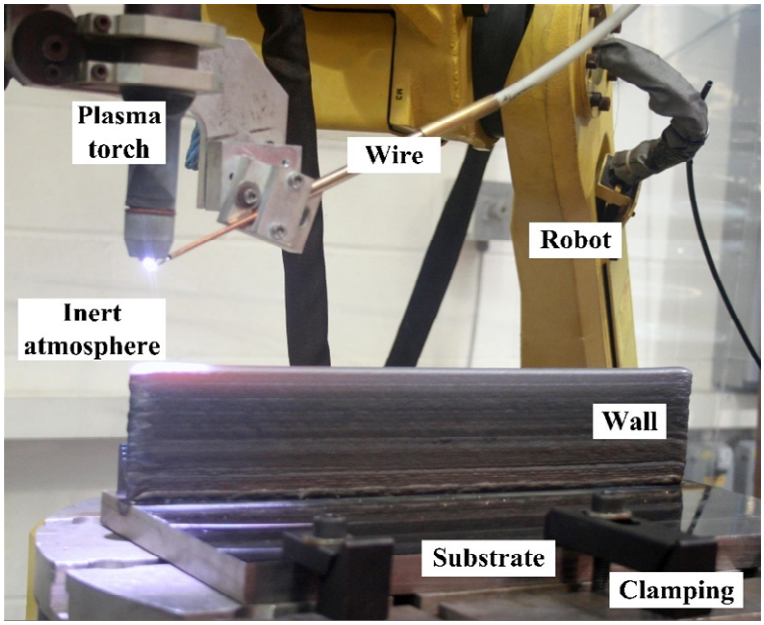

Figure 5-1 Experimental setup of the WAAM system. (Plasma arc, current=180A, WFS=1.8m/min, TS=0.2m/min)

Table 5-1 Chemical composition of the MARVAL 18S wire, maraging 200 and 250-grade steel (wt. %).

	Ni	Mo	Co	Ti	Al	C	Fe
Wire[a]	18.28	4.69	8.21	0.44	0.11	<0.01	Balance
18Ni 200 [15]	18	3.3	8.5	0.2	0.1	<0.03	Balance
18Ni 250[b]	18.3	4.8-4.9	7.7	0.5	0.07-0.08	0.004	Balance

[a]from data sheet of the wire package
[b]from date sheet provided by Smiths Metal Centres

A 21-layer maraging steel linear wall structure was deposited to study the microstructural evolution of the as deposited WAAM component and its response to a standard aging heat treatment. A piece of wrought 250-grade maraging steel was also prepared following the same heat treatment procedure to investigate the microstructural difference between the maraging steels produced in two different processing routes. Subsequently, a large linear wall (dimension: 400×123×10mm) was deposited to study the mechanical properties of the maraging steel produced by WAAM. The heat treatment applied to the as deposited wall structure consists of two steps: solutionizing at 815 °C with a holding time calculated as 1 hour for every inch of thickness, air-cooling to room

temperature, and then aging at 482°C for 3 hours followed by air-cooling to room temperature, as recommended by ASM handbook for 250-grade maraging steel [22].

Samples were transverse cross-sectioned from the as deposited wall for metallographic analysis, microhardness measurement and heat treatment evaluation by following a procedure consisting of mounting, grinding, polishing and etching (with 10% nital solution) successively. The microstructure was analysed with an OLYMPUS Confocal Scanning Laser Microscope (OLS3000) and a Scanning Electron Microscope (SEM, FEI XL30-SFEG) equipped with the energy-dispersive spectrometry detector (EDS, which was also used to measure the elemental composition of the WAAM material in the research). The microhardness was measured with the Zwick/Roell Hardness Tester along the central line from the bottom (the area near the substrate) to the top of the wall structure under a load of 1 kg (holding time: 15s). The electron backscatter diffraction (EBSD) analysis was used to quantitatively analyse precipitates distribution in both as deposited and heat treated condition. Tensile test samples were prepared according to BS EN ISO 6892-1:2009 standard in a proportional design to evaluate the mechanical properties with Instron 5500R electromechanical testing machine (load cell: 100kN, crosshead speed: 1mm/min) at room temperature. The samples are painted with the graphite and then equipped with the reflective tape to measure the elongation during the tensile test (gauge length = 28mm) through the laser extensometer. Two sets of tensile coupons were taken from the WAAM wall to represent the as deposited and heat treated conditions respectively. The volume fraction of austenite was estimated by X-ray diffraction (XRD) analysis [10] using the SIEMENS D5005 diffractometer with Cu Kα radiation (λ=1.5418 Å) at room temperature. The XRD was operated at 40 kV and 40 mA with the scan rate of 0.04°/s over the 2θ range from 20 to 90°. DIFFRAC.EVA V4.1 software was used to analyse the XRD patterns.

5.3 Results

5.3.1 Microhardness and macrostructure

Fig. 5-2 presents the overall macrostructure of the as deposited maraging steel wall and the microhardness variation from the bottom to the top part in both as deposited and heat treated conditions. Defects, such as inclusions or porosities, are not observed in the macrostructure, indicating a fully dense as deposited WAAM part. Uniformly distributed layer bands composed of the martensitic structure with a fine dispersion of reverted austenite [23] are observed in the previously deposited layers from successive thermal cycles.

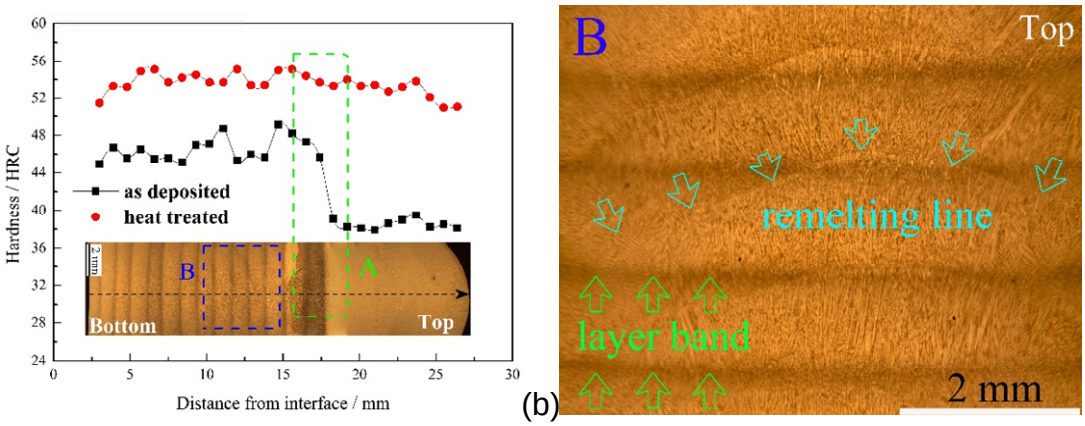

Figure 5-2 Microhardness measurements and macrostructure of the WAAM maraging steel (a) microhardness measurements (b) enlarged Zone B from Fig. 5-2a.

As shown in Fig. 5-2a, in the as deposited condition the WAAM structure is not uniform in microhardness from the bottom to the top: the material is harder (ranging from 44 to 49 HRC) in the bottom part but gets softened significantly near and above the first layer band to around 32 HRC. After heat treatment, the hardness increases to between 52 to 56 HRC and the variation from bottom to the top layers becomes less pronounced. Considering that the low-carbon iron-nickel martensite formed after solutionizing is relatively soft (around 33 HRC), it can thus be inferred that the maraging steel produced by WAAM is non-uniformly age hardened to different extents from the bottom to the top along the building direction with the bottom aged more.

5.3.2 Microstructure

The microstructure of the WAAM component in the as deposited and heat treated conditions is displayed in Fig. 5-3. A typical dendritic structure with long columnar grains is observed at the bottom part of the as deposited material which clearly displays the iron-nickel martensitic matrix decorated with austenite (shown as white pools) between the dendrites; whereas the top part is also dendritic with less columnar grains and shows less contrast after etching with little austenite observed.

As shown in Fig. 5-3b, after the heat treatment, the formation of a large amount of precipitates all over the WAAM structure adds to the contrast near the top part after etching. The microstructure throughout the cross section shows a greater proportion of discrete austenitic islands along the inter-dendritic boundaries. Besides, the low-carbon lath martensite becomes thinner and the aspect ratio of the austenitic islands becomes lower, transforming from dendritic shape to a more circular shape after heat treatment.

Fig. 5-4 shows the microstructure of the heat treated maraging steel produced by the traditional wrought process. Different from the dendritic microstructure of the WAAM product, the microstructure of the wrought maraging steel is characterized by equiaxed grains with the average grain size of around 30 µm. Such microstructural difference is due to the thermal extraction orientation and uniformity during the solidification process: for a linear wall structure produced by WAAM, the heat is extracted preferentially from the top to the bottom and the thermal conduction is constrained along the wall-thickness direction, which facilitates the columnar grains formation; while in the traditional wrought process, the thermal conduction is uniformly in all directions, which leads to the equal growth of dendrites in all directions during the crystallization process to form equiaxed grains. Generally, equiaxed microstructure provides isotropic mechanical properties. It should also be highlighted that few retained austenite is observed among the lath martensitic matrix in the wrought material.

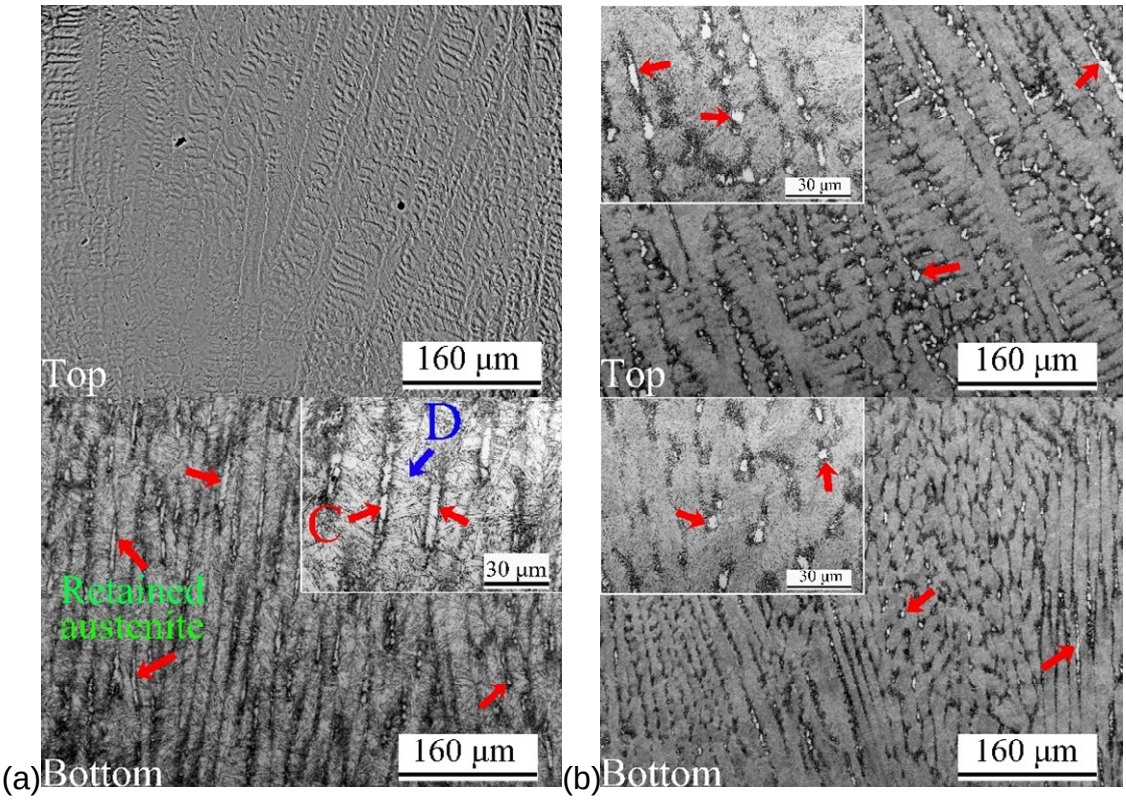

Figure 5-3 Microstructure of the maraging steel produced by WAAM process (a) as deposited (b) heat treated.

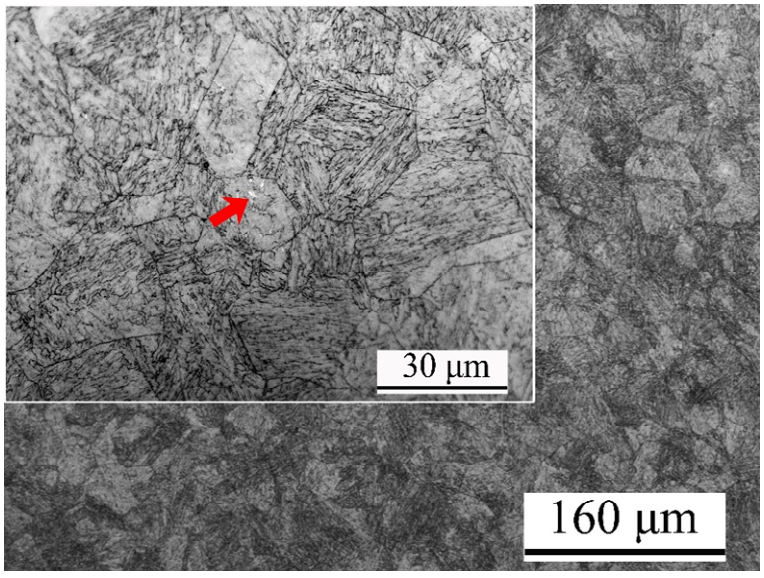

Figure 5-4 Microstructure of the heat treated maraging steel produced by wrought process.

Table 5-2 shows the EDS elemental analysis results of the austenite and martensitic matrix from Fig. 5-3a. As can be seen, the austenite is rich in Ti

(1.39% compared to 0.44% in wire) and Mo (5.16% compared to 4.69% in wire); in comparison, the martensitic matrix in the vicinity of the austenite shows less content in Ti (0.08% to 0.44% in wire) and Mo (3.09% to 4.69% in wire). Such a Ti depleted zone could occur due to the enhanced elemental segregation caused by the austenite reversion during the deposition process. Fig. 5-5 presents the EDS mapping results of the austenite and its surrounding martensitic matrix, which also proves that the austenite is rich in Mo and Ti compared to the matrix. Therefore, it can also be concluded that the formation of the austenite was promoted by the element segregation, mainly Ti and Mo [24].

Table 5-2 EDS elemental analysis of the austenite and martensitic matrix (wt. %).

	Ti	Mo	Ni	Co	Rest (Fe, Al, C)
C	1.39	5.16	19.85	8.89	Balance
D	0.08	3.09	17.41	8.38	Balance
wire	0.44	4.69	18.28	8.21	Balance

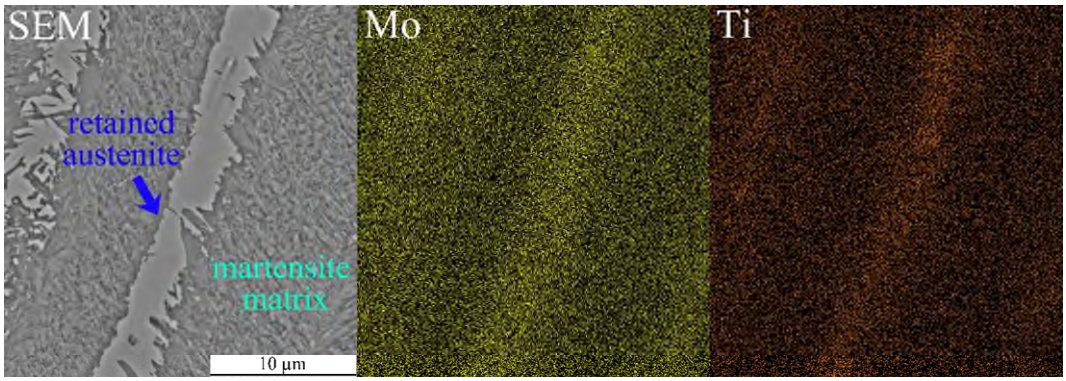

Figure 5-5 EDS mapping of the austenite and the martensitic matrix.

As has been reported, the austenite in maraging 250-grade steel forms when heated at 650°C or higher [25]; however, compared to the as deposited condition, larger amount of austenite forms when the WAAM built component is aged at only 482 °C (Fig. 5-3b), which indicates that such elemental segregation could also lower the austenite reversion temperature.

5.3.3 Precipitates formed in WAAM

In the WAAM process, the as deposited material undergoes repeated thermal cycles from subsequent depositions and partial aging effect could occur, which

has been verified by the previous hardness measurement. Fig. 5-6 presents the SEM results of the precipitates formed in the WAAM structure. Due to the lack of aging effect, few precipitates are found in the top part of the as deposited maraging steel; while some spherical precipitates are observed to be dispersed in the martensitic matrix near the bottom part, which is in agreement with the previous hardness measurement that the bottom part is harder than the top part. Such a microstructural heterogeneity is eliminated through a solution and a subsequent aging heat treatment, which allows controlled release of the solute atoms and formation of the uniformly distributed precipitates, as shown in Fig. 5-6b.

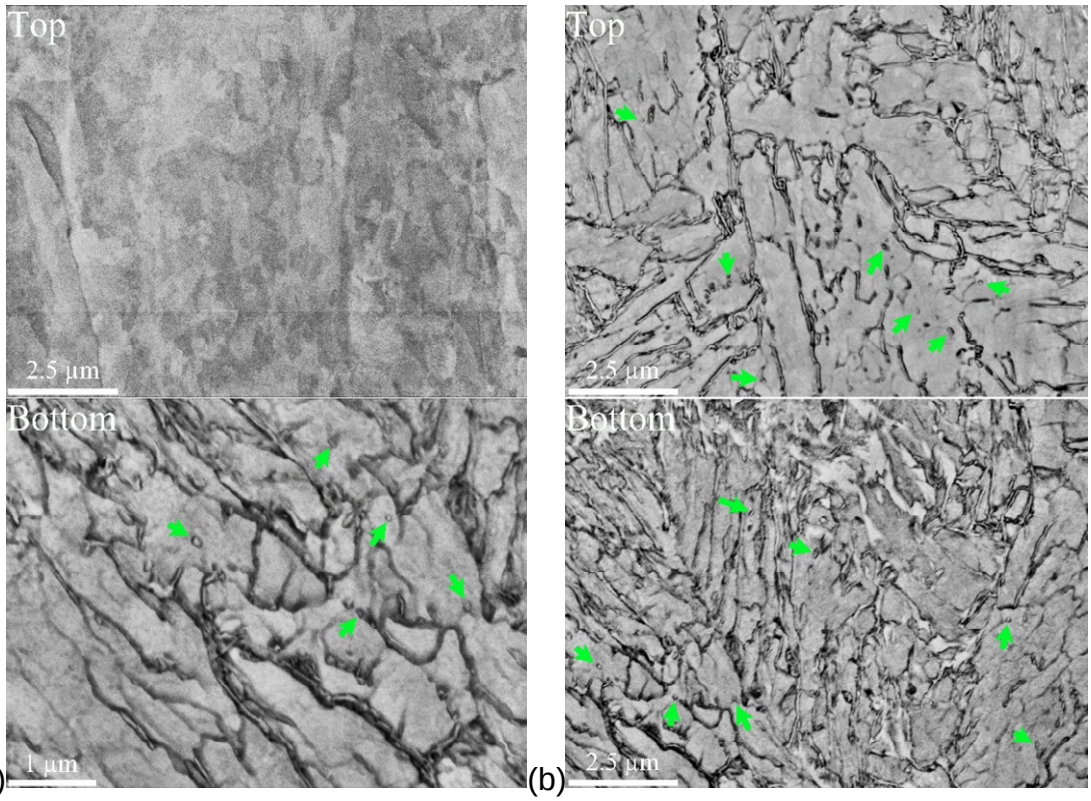

Figure 5-6 Precipitates in the maraging steel produced by WAAM (BSE mode) (a) as deposited (b) heat treated.

Fig. 5-7 illustrates the EBSD phase mapping results of the main precipitates- Ni_3Mo, Ni_3Ti, Fe_2Mo and Fe_7Mo_6 [26,27] for the bottom and top parts in both as deposited and heat treated conditions. As has been reported, the size of these precipitates is very small (nanometer scale [13,28]). In Figs. 5-7a and 5-7b,

significant amounts of the precipitates are observed in finely dispersed condition throughout the martensitic matrix, preferentially on dislocations and within the lath martensite. Fig. 5-7c shows the calculated content (percentage in area) of the precipitates for Figs. 5-7a and 5-7b. As can be seen, under the as deposited condition, the bottom part has larger, around twice, the amount of precipitates than the top part. After 3 hours of aging, the amount of precipitates near the top part increased significantly, Fe_2Mo from 0.0827% to 0.335%, Fe_7Mo_6 from 0.286% to 0.742%, Ni_3Mo from 0.0974% to 0.189% and Ni_3Ti from 0.0656% to 0.159%. The increase near the bottom after aging is less significant in Fe_2Mo (from 0.2195% to 0.2379%) but noticeable in Fe_7Mo_6 (from 0.523% to 0.792%), Ni_3Mo (0.217% to 0.456%) and Ni_3Ti (from 0.158% to 0.305%). Such an increase in the top part brings the amount of precipitates across the WAAM structure to almost the same level, making the heat treated WAAM part uniform in phase contents.

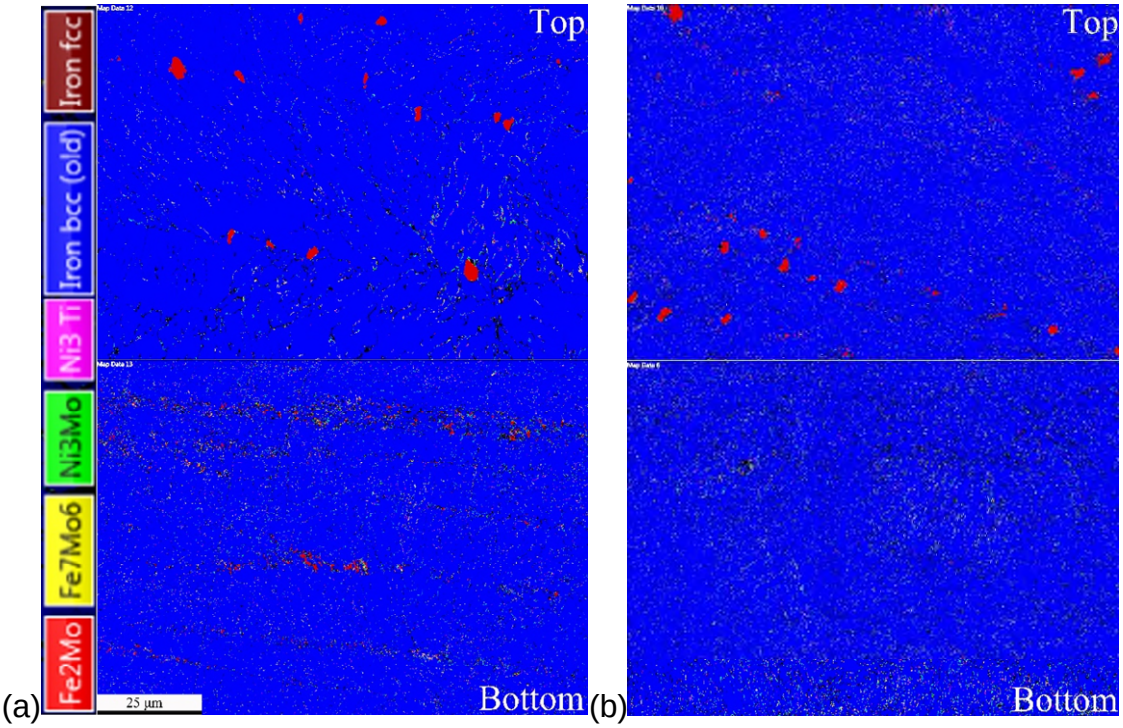

(a) (b)

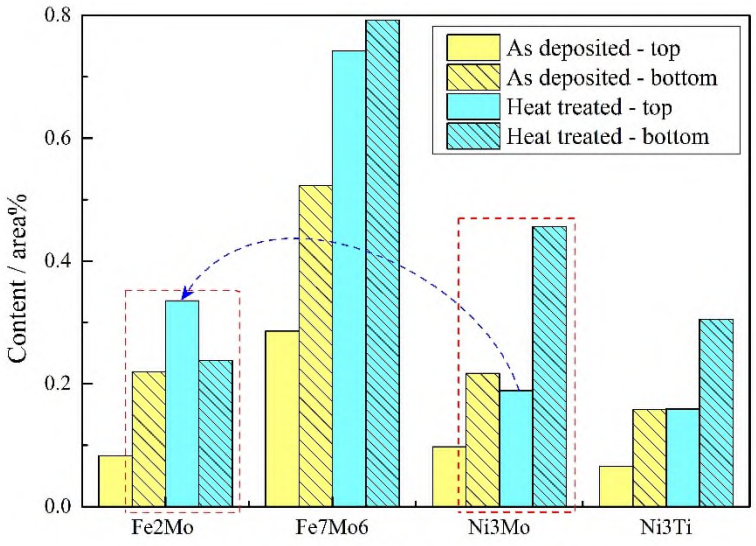

(c)

Figure 5-7 EBSD phases distribution in (a) as deposited (b) heat treated condition and (c) content of precipitates.

5.3.4 Mechanical properties

The linear wall structure for the tensile test was deposited in an alternating direction manner to make it equal heights at both ends. An effective zone is selected 15mm away from both ends and 10mm away from the substrate to eliminate the ends effects and the dilution effect from the substrate, as shown in Fig. 5-8a. Samples numbering according to their locations and the dog-bone drawing used in the experiment are shown in Figs. 5-8b and 5-8c, respectively.

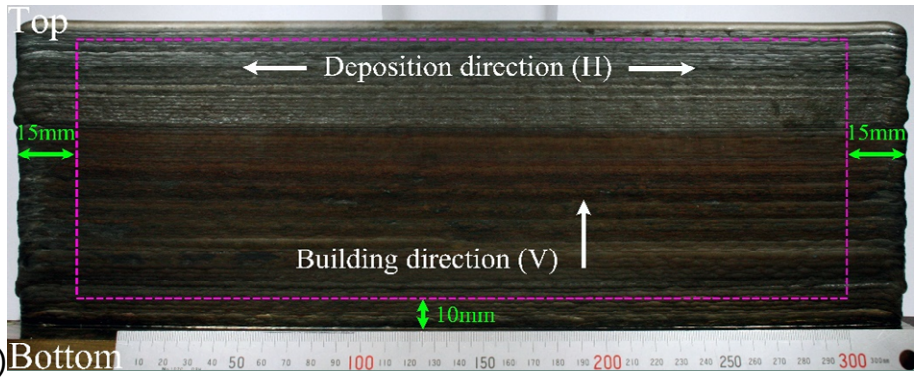

(a)

(b)

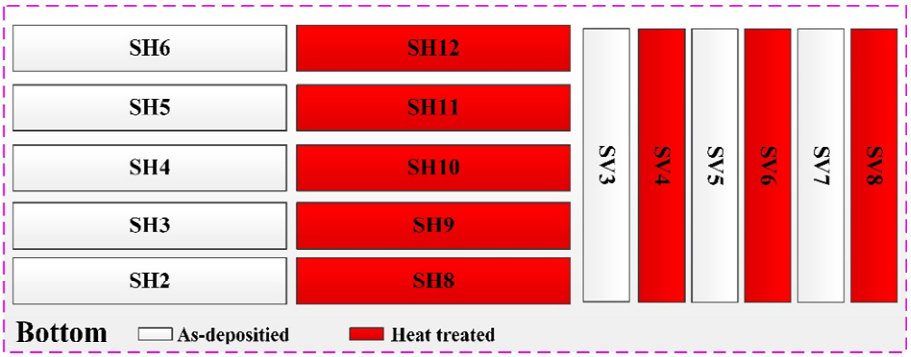

(c)

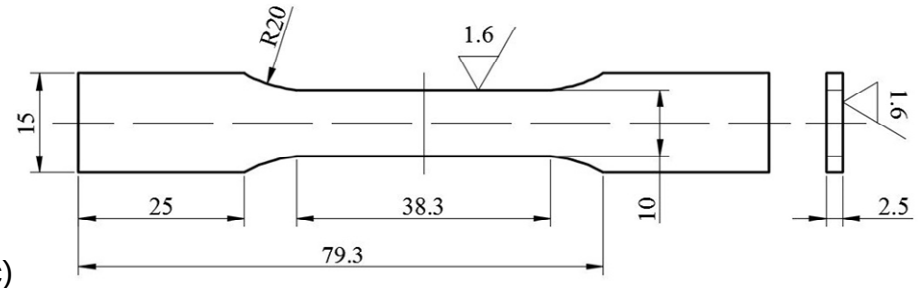

Figure 5-8 Maraging steel wall for tensile test, sample numbering and dog-bone drawing (a) as deposited maraging steel wall structure (b) samples numbering and locations (c) dog-bone drawing.

5.3.4.1 Testing results

Fig. 5-9 and Table 5-3 present the mechanical testing results of the maraging steel prepared by the WAAM process along both the deposition direction (Horizontal) and building direction (Vertical). In the as deposited condition, the UTS and 0.2%YS generally reduce from the bottom to the top: from 1282 MPa to 994 MPa and from 1048 MPa to 878 MPa, respectively, which is in line with the microhardness measurements and the phase content statistical results. However, such variation is not observed in the vertical direction. On average, the UTS and 0.2%YS in the horizontal direction are 9.0% and 8.5% higher than the vertical direction, respectively, indicating the anisotropy to some extent. This is partially due to the existence of the layer bands in the as deposited material, which reduce the tensile strength in the direction perpendicular to them. After the standard aging heat treatment, the UTS and 0.2%YS values at each corresponding location increase noticeably, with the UTS increased by 26.1% (horizontal) and 31.1% (vertical) and the 0.2%YS increased by 44.1% (horizontal)

and 47.3% (vertical). Although the anisotropy of mechanical properties is still present after heat treatment, with the UTS and 0.2%YS in the horizontal direction 4.8% and 6.2% higher than the vertical direction, the variations in UTS and 0.2%YS values from the bottom to the top are virtually eliminated. The elongation values in the as deposited condition are generally consistent in both directions with only one exception (sample SV5); after heat treatment, the scattering in elongation measurements becomes significant but in general, the elongation drops when compared to the as deposited condition. A typical comparison of the strain-stress curve of the tensile test samples in different conditions is present in Fig. 5-10.

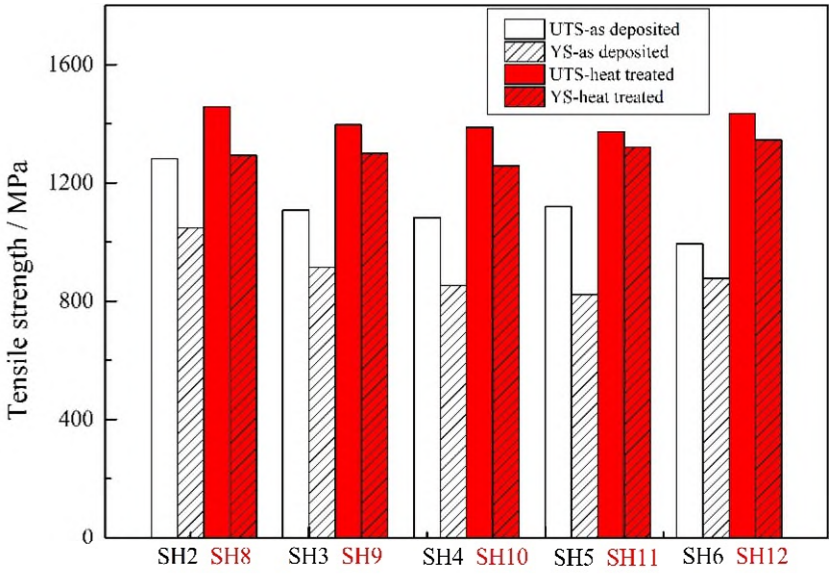

(a)

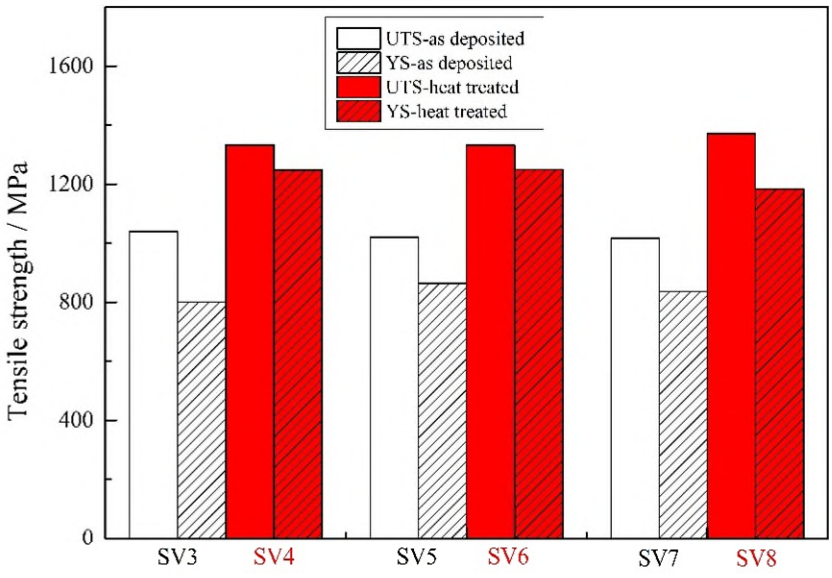

(b)

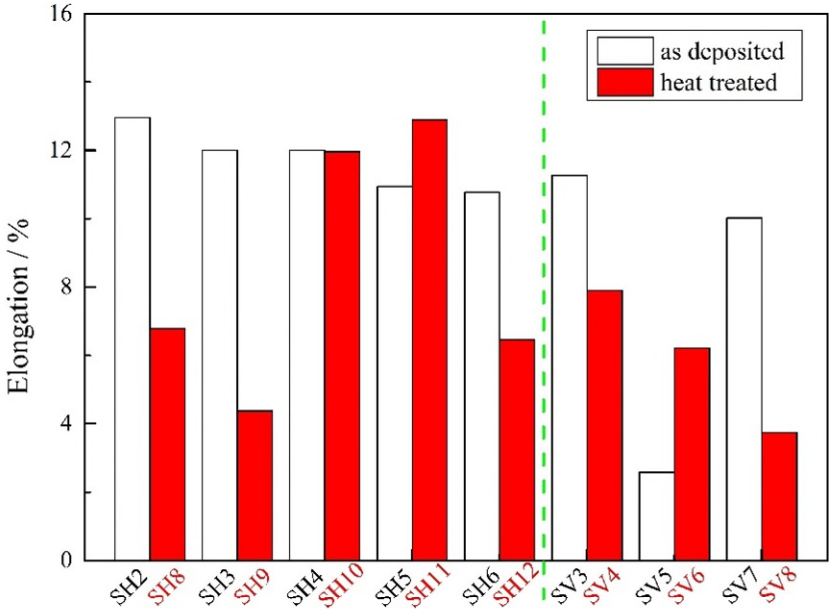

(c)

Figure 5-9 Mechanical testing results (a) tensile strength-horizontal (b) tensile strength-vertical (c) elongation.

Table 5-3 Summary of mechanical properties of maraging steel.

		UTS/MPa	0.2%YS/MPa	Elongation/%
as deposited	WAAM (horizontal)	1118±94	904±78	11.7±0.8
	WAAM (vertical)	1026±10	833±26	8.0±3.8
unaged	Wrought 200 [15]	965-1000	760-807	17-18
	Wrought 250 [15]	1000-1140	725-895	8-16
aged	WAAM (horizontal)	1410±32	1303±29	8.5±3.3
	WAAM (vertical)	1345±19	1227±31	6.0±1.7
	Wrought 200 [29]	1450	1380	12
	Wrought 250 [29]	1760	1720	10

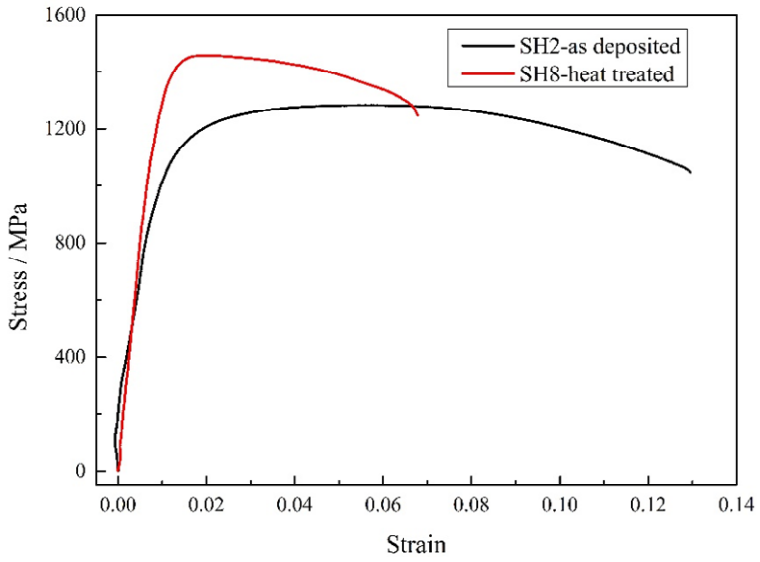

Figure 5-10 Strain-stress curve of the as deposited and heat treated WAAM maraging steel.

From the summary of Table 5-3, it should also be noticed that the mechanical properties of the maraging steel produced by WAAM in the as deposited condition are comparable, or even better than those of the unaged wrought maraging 200 and 250-grade steel regarding UTS, 0.2%YS and elongation. However, after heat treatment, the WAAM structure shows relatively lower mechanical properties than the wrought alloy, wherein the overall average UTS is 50 MPa and 360 MPa lower and the 0.2%YS is 91 MPa and 430 MPa lower than the aged 200 and 250-grade maraging steel respectively.

5.3.4.2 Fracture surface

Fig. 5-11 presents the typical fracture surfaces of the tensile test specimens. The as deposited material generally shows a ductile manner fracturing with large deformation, resulting from the microvoid coalescence. In contrast, the heat treated material shows more brittle fractures in a quasi-cleavage and ductile combined manner. Dimples are found in both conditions wherein the dimples in the as deposited material are of a larger amount and more uniform in size. Microcracks are found in the heat treated material, which initiates the fast failure during the tensile test (as indicated by the yellow arrow in Fig.5-11b and 5-11d). Nano-sized pores are observed to be dispersed in both conditions with smooth

inner morphology, which results from the nanosize precipitates being pulled out of the matrix during the tensile test (see pink arrow in Fig. 5-11c).

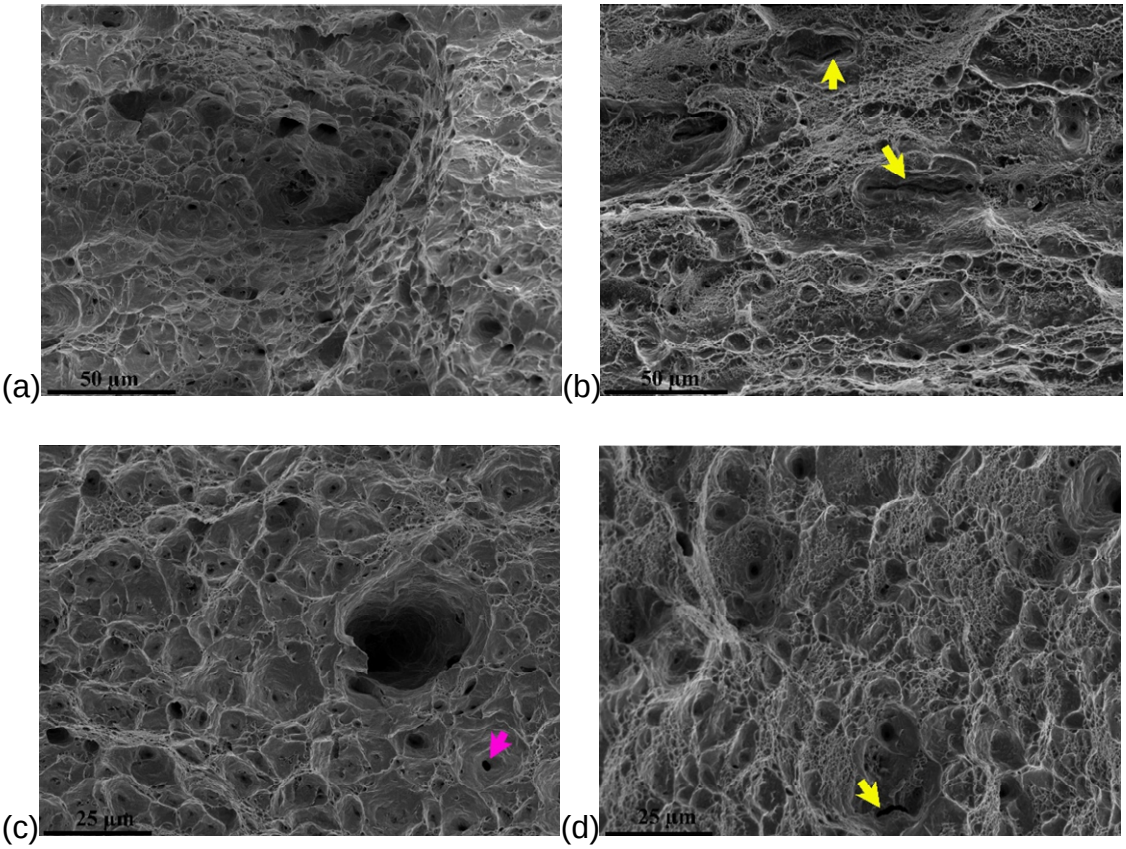

Figure 5-11 Fracture surface of the tensile test samples (a) as deposited-horizontal (b) heat treated-horizontal(c) as deposited-vertical (d) heat treated-vertical.

Fig. 5-12 shows the optical micrographs of the joint fracture surfaces from the longitudinal section. As can be seen, the ductile fracture surface shows a typical cup and cone fracture with the shear lip 45° with respect to the base of the cup and cone, indicating the micro void coalescence happened during the tensile test. In contrast, the brittle fracture surface in the heat treated material shows a characteristic flat edge; the elongated austenites are also observed to distribute among the elongated matrix material, which is not observed in the same area in the as deposited material.

(a)

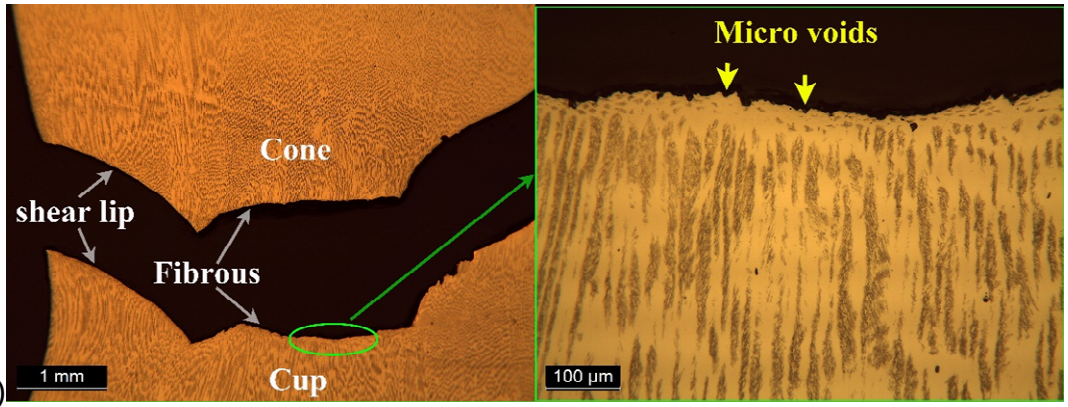

(b)

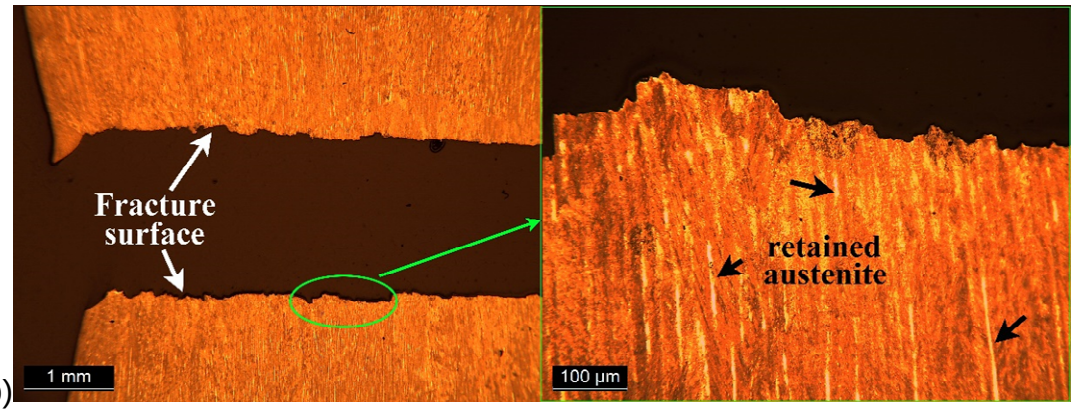

Figure 5-12 Optical microscopy of the joint fracture surface (longitudinal section) (a) as deposited (b) heat treated.

5.4 Discussion

The layer-by-layer additive manufacture is different from the traditional manufacture process in a unique manner characterized by local melting and directional thermal conduction, which results in all the differences in microstructure evolution and mechanical properties from the wrought alloy.

5.4.1 WAAM process and thermal flow

The remelting boundary lines in Fig. 5-2b indicate the layer-by-layer building manner in the WAAM process: the transferred heat and mass from the arc and molten wire re-melt a certain amount of the previous layer and the liquid metal solidifies upon it to form a new layer.

In the layer-by-layer manufacture of the linear wall, the heat mostly flows from the top layer (where the weld pool is located) to the bottom. The orientation of the

dendritic growth depends on the thermal gradient of the solidifying liquid and the solute enrichment of the liquid near the liquid-solid interface [30,31]. Thus, from Fig. 5-2b, it can be seen that the dendrites grow perpendicular to the re-melting line and towards the top part since the heat was extracted towards the bottom/substrate in the WAAM process.

5.4.2 Transient aging effect

The inherent low aging temperature (482°C) of maraging steel is the decisive factor of the variation of microhardness, mechanical properties and precipitates formation of WAAM maraging steel along the building direction in the as deposited condition. Since the temperature of the weld pool of maraging steel is well above 1413°C, materials within some range near the weld pool can always be reheated up to reach such an aging temperature for a short duration. Due to the rapid aging response of the Al-Ti-hardened alloy, the accumulation of such durations will result in a transient aging effect to result in some extent of diffusion and precipitation to strengthen the material. However, this transient aging effect is not comparable to a proper aging due to the limited dwelling time and lack of constant temperature.

During the WAAM process, the transient thermal cycling from the successive deposits heat treats the previously deposited materials, thus the deposits closer to the bottom underwent numerous thermal cycles of a different magnitude to be aged more and gets harder than the top part. The uniformity of the microhardness after a proper aging (3 hrs at 482°C) heat treatment is due to the isotropically developed precipitation, which acts as a dislocation barrier in all directions [32]. It should be noticed that the topmost layer band is also the interface between the soft and the hard zones. As shown in Fig. 5-2a, there is a significant microhardness drop around first layer band (Zone A). Above this interface, the material cools down from the weld pool temperature, passes the austenitizing temperature zone and becomes entirely lath martensitic; due to the lack of successive thermal cycles, few precipitates are formed, and thus, the material is relatively softer.

During the deposition process, the top layer is heated well above the melting point (1413°C) at which the maraging steel was fully austenitic; after cooling down to room temperature, the structure transforms to fully martensitic in a supersaturated state with all the alloying elements remain in solid solution. In case of the successive layer depositions where the transient thermal cycles facilitate the diffusion, solute atoms diffuse out from the unit cell and form precipitates. The precipitates etch faster which is evident in the bottom part of the structure in the as deposited condition (as shown in Fig. 5-3a).

From the previous explanation, it can be inferred that different parts undergoing a different number of thermal cycles will have different amounts of intermetallic compounds precipitated: the more thermal cycles, the more precipitates. In the WAAM process, the as deposited material near the bottom part underwent more thermal cycles than the top, leading to more diffusion of solute atoms and formation of intermetallic compounds near the bottom part, which, however, was nowhere near to a controlled aging treatment. After solution heat treatment, all solute atoms went into solution, so the effect of thermal cycling was minimized and the actual aging time for the heat treated WAAM part was 3 hours. Considering that the 21-layer part was built within 1.5 hours, the real dwelling time near 482 °C was much less than 1.5 hours. Thus, the amount of precipitates of the top and bottom parts of the as deposited and heat treated structures should follow the sequence (less to more): as deposited top, as deposited bottom, heat treated top and bottom, which is verified in Fig. 5-7c. However, in Fig. 5-7c there are exceptions in the content of Fe_2Mo in the heat treated condition: the bottom part has noticeably less Fe_2Mo, and in the content of Ni_3Mo: the top part after a standard aging heat treatment has less Ni_3Mo than the bottom in the as deposited condition. It can thus be inferred that during heat treatment, the metastable Ni_3Mo could transfer to the more stable Fe_2Mo phase [14]. The difference of the Ni_3Ti content between the top and the bottom parts of the heat treated structure may result from the segregation of Ti element.

5.4.3 Explanation of the inferior mechanical properties

Apparently, the aging heat treatment of the WAAM maraging steel doesn't provide the strength increase as expected. Explanations are given as below.

5.4.3.1 Aging specification

From Table 5-3, the as deposited material possesses superior mechanical properties to the wrought maraging steel in the solutionized condition. However, after aging the WAAM material shows mechanical properties much lower than the wrought material, which indicates that the aging response of the WAAM maraging steel is not as profound as that of the wrought material.

The aging response critically depends on the microstructural condition of a component. The WAAM material has very different grain boundary structures from a wrought alloy and is lacking in initial compositional homogeneity. WAAM components are characterised by dendritic structures with low angle grain boundaries and segregation and thermal straining from the previously deposited layers due to successive deposition, whereas the wrought maraging steel features equiaxed grains with high grain boundaries.

In this study, the aging heat treatment used for a wrought alloy was applied to a WAAM structure, which may not be the optimum one for a WAAM component. More underpinning studies on the aging response for WAAM built structures need to be carried out. A possible solution could also be cold straining in between layer deposition to initiate re-crystallisation and thereby creating a structure comprises of high angle grain boundaries [33].

5.4.3.2 Wire composition and quality

The WAAM process is featured by melting the commercial welding wire to form the product. Therefore, all those in the wire go into the deposits including the alloying elements and the defects such as inclusions and porosities [3].

Maraging steels are precipitation hardened with Mo as the primary and Ti as the secondary hardener, hence having certain contents of such alloying elements in the as deposited material is the prerequisite of forming enough amount of

intermetallic compounds to generate expected materials strengthening. However, three factors would affect the content of the alloying elements. Firstly, the chemical compositions of the wire and the wrought maraging steel are not identical (see Table 5-1). Secondly, the evaporation of alloying elements under the high-temperature electric arc will lead to element loss. Thirdly, when O is present, even in very low content, the higher affinity of Ti with O than with Ni leads to oxides formation and reduction of the amount of precipitates formed during age hardening.

Furthermore, the filler wire is one of the main sources of inclusions, nitrogen and oxygen; in the arc, inclusions can be vaporized and atomized to provide N and O to the weld pool and new inclusions will form through metallurgical reactions [2]. Fig. 5-13 shows the longitudinal section of the wire used in this research. A small amount of elongated inclusions is found in the wire. The EDS elemental analysis reveals that this is titanium nitride (as shown in Fig. 5-13 and Table 5-4), which is generated during the wire production process. It has been reported that the materials properties of maraging steels are greatly affected by the inclusion content, and TiN is one of the most commonly reported inclusions found in the wrought maraging steel. Severe grain boundary embrittlement will occur if Ti(C,N) is present at the grain boundary [34], resulting in a fast failure during the tensile test. Such influence is more noticeable in the aged condition when the material is more brittle [18]. Even though TiN was not detected in the WAAM maraging steel due to limited analysis in this research, it is reasonable to assume its presence in the WAAM material with the wire as the feedstock. Cleanness and purity are crucial for high strength steel to display its outstanding mechanical properties; therefore, higher quality wires are required to produce WAAM maraging steel that can compete with the wrought material.

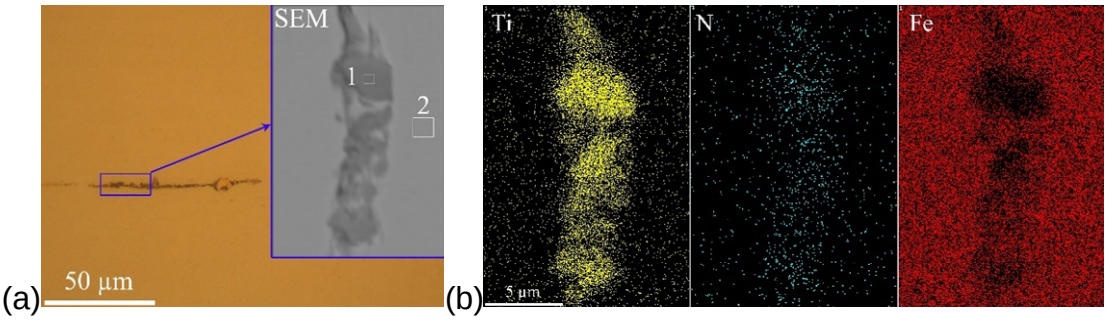

Figure 5-13 Inclusions in the wire (a) optical microscopy (b) EDS elemental mapping.

Table 5-4 EDS elemental analysis of the inclusions (at. %).

	N	Ti	Fe	Rest (Co, Al, C, Si, Mn)
1	33.42	56.7	7.28	balance
2	-	0.53	69.42	balance

5.4.3.3 Austenite content

The soft austenite existing in the maraging steel has been reported to lower the strength of maraging steels as it doesn't harden during the aging heat treatment [23] and thus should be kept to a minimum if high tensile strength is desired. The austenite in maraging steel consists of two sources: retained austenite and reverted austenite. The retained austenite forms when the material cools down from austenitizing temperature [35] while the reverted austenite forms mostly during the aging process by diffusion-controlled reaction [36]. The percentage of retained austenite in particular limits the usefulness of maraging steel as a high strength material [37].

In this paper, the austenite quantification is carried out using the direct comparison method based on the assumption that the integrated intensities of X-ray diffraction peaks for each phase are proportional to the volume fraction of that phase [38]. Fig. 5-14 shows the XRD patterns for the top part of WAAM maraging steel under different conditions (as deposited, standard heat treated and solutionized) and for the heat treated wrought maraging steel. Table 5-5 summarises the corresponding austenite content. As can be seen, the diffractogram does not show any peaks of the intermetallic compounds under

heat treated condition, which may be due to the low phase content (less than 5% [14]) and the very dispersed distribution [37]. The top part in the as deposited condition does not undergo successive thermal cycles, thus only tiny austenite peaks are observed in the diffractogram; in contrast, more austenite peaks are found at the same position after the standard heat treatment, indicating a larger amount of austenite forming (13.1% versus 8.3%). Solutionizing eliminates the elemental segregation, which helps reduce the austenite amount compared to the as deposited condition (2.1% versus 8.3%). However, the wrought maraging steel hardly contains austenite even under heat treated condition, which might be due to the different microstructure from the WAAM part. The different microstructure leads to a different response to elements segregation and austenite formation, which is one of the major issues weakening the mechanical properties of WAAM maraging steels.

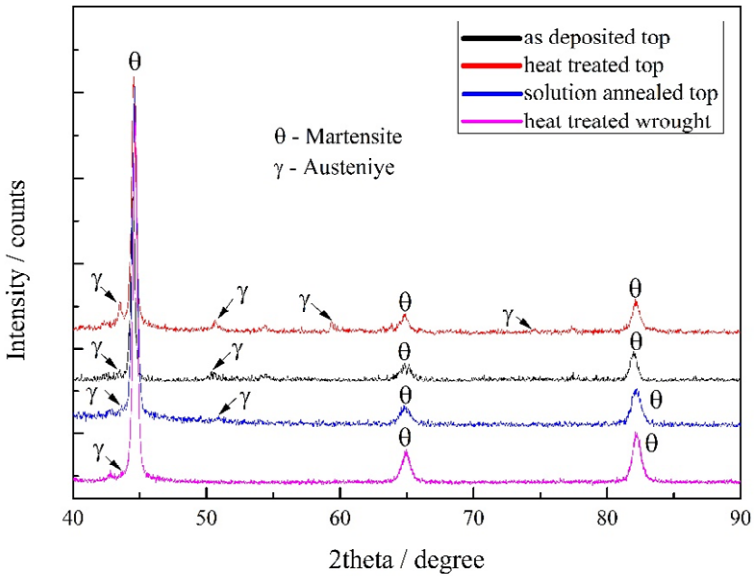

Figure 5-14 X-ray diffractogram of the maraging steel.

Table 5-5 Volumetric fraction of the austenite (%) [1].

	Austenite γ	Martensite θ
Heat treated wrought	0.94	99.06
Solutionized top	2.1	97.9
As deposited top	8.3	91.7
Heat treated top	13.1	86.9

5.5 Conclusions

The WAAM process has been applied to produce defect-free and full dense maraging steel components. In the as deposited condition, the microstructure features uniformly distributed layer bands and upwards dendritic growth perpendicular to the remelting line; the mechanical properties show slight anisotropy with the vertical direction lower than the horizontal, yet both of them are superior to that of solutionized wrought material. However, the properties are not uniform with the softer material at the top in the region where less thermal cycles have been experienced and less intermetallic compounds are precipitated, as indicated by the microhardness measurements and EBSD phase statistics results. A standard solution + aging heat treatment designed for the wrought 250-grade maraging steel has been applied to WAAM maraging steel, which eliminates the microstructural heterogeneity from the bottom to the top and gives an increase in strength of 24.7% (this is still not quite as high as the heat treated wrought alloy). More austenites are detected after heat treatment, which is promoted by the segregation of Mo and Ti. The low angle columnar grains dominated WAAM alloy shows a less pronounced aging response to the equiaxed grain dominated wrought alloy, which is the main reason for lower mechanical properties attained. Besides, the wire quality (TiN inclusions) should also be considered if higher mechanical properties are to be achieved. Future studies will be conducted to create a more tailored heat treatment cycle for the WAAM materials and investigate intermediate cold working in order to create the

[1] Please note that the texture might results in some inaccuracy in the calculated phase fractions. The calculation results here have omitted the texture effect.

microstructure with higher angle grain boundary to further increase the mechanical properties.

5.6 References

[1] B. Cong, J. Ding, S. Williams, Effect of arc mode in cold metal transfer process on porosity of additively manufactured Al-6.3%Cu alloy, Int. J. Adv. Manuf. Technol. 76 (2014) 1593–1606. doi:10.1007/s00170-014-6346-x.

[2] J. Gu, J. Ding, S.W. Williams, H. Gu, P. Ma, Y. Zhai, The effect of inter-layer cold working and post-deposition heat treatment on porosity in additively manufactured aluminum alloys, J. Mater. Process. Technol. 230 (2016) 26–34. doi:10.1016/j.jmatprotec.2015.11.006.

[3] S.W. Williams, F. Martina, A.C. Addison, J. Ding, G. Pardal, P. Colegrove, Wire + Arc Additive Manufacturing, Mater. Sci. Technol. 00 (2015) 1–7. doi:10.1179/1743284715Y.0000000073.

[4] F. Martina, J. Mehnen, S.W. Williams, P. Colegrove, F. Wang, Investigation of the benefits of plasma deposition for the additive layer manufacture of Ti-6Al-4V, J. Mater. Process. Technol. 212 (2012) 1377–1386. doi:10.1016/j.jmatprotec.2012.02.002.

[5] J. Gu, J. Ding, S.W. Williams, H. Gu, J. Bai, Y. Zhai, P. Ma, The strengthening effect of inter-layer cold working and post-deposition heat treatment on the additively manufactured Al– 6.3Cu alloy, Mater. Sci. Eng. A. 651 (2016) 18–26. doi:10.1016/j.jmatprotec.2015.11.006.

[6] B. Cong, R. Ouyang, B. Qi, J. Ding, Influence of Cold Metal Transfer Process and Its Heat Input on Weld Bead Geometry and Porosity of Aluminum-Copper Alloy Welds, Rare Met. Mater. Eng. 45 (2016) 606–611. doi:10.1016/S1875-5372(16)30080-7.

[7] T. Skiba, B. Baufeld, O. Van Der Biest, Microstructure and Mechanical Properties of Stainless Steel Component Manufactured by Shaped Metal Deposition, ISIJ Int. 49 (2009) 1588–1591. doi:10.2355/isijinternational.49.1588.

[8] B. Baufeld, Mechanical properties of INCONEL 718 parts manufactured by shaped metal deposition (SMD), J. Mater. Eng. Perform. 21 (2012) 1416–1421. doi:10.1007/s11665-011-0009-y.

[9] J. Ding, P. Colegrove, F. Martina, S. Williams, R. Wiktorowicz, M.R. Palt, Development of a laminar flow local shielding device for wire + arc additive manufacture, J. Mater. Process. Technol. 226 (2015) 99–105. doi:10.1016/j.jmatprotec.2015.07.005.

[10] J. An, F. Meng, X. Lv, H. Liu, X. Gao, Y. Wang, Y. Lu, Improvement of mechanical properties of stainless maraging steel laser weldments by post-weld ageing treatments, Mater. Des. 40 (2012) 276–284. doi:10.1016/j.matdes.2012.03.020.

[11] Y. Li, W. Yan, J.D. Cotton, G.J. Ryan, Y. Shen, W. Wang, Y. Shan, A new 1 . 9 GPa maraging stainless steel strengthened by multiple precipitating species, J. Mater. 82 (2015) 56–63. doi:10.1016/j.matdes.2015.05.042.

[12] V. Rajkumar, N. Arivazhagan, Role of pulsed current on metallurgical and mechanical properties of dissimilar metal gas tungsten arc welding of maraging steel to low alloy steel, J. Mater. 63 (2014) 69–82. doi:10.1016/j.matdes.2014.05.055.

[13] O. Moshka, M. Pinkas, E. Brosh, V. Ezersky, L. Meshi, Addressing the issue of precipitates in maraging steels - Unambiguous answer, Mater. Sci. Eng. A. 638 (2015) 232–239. doi:10.1016/j.msea.2015.04.067.

[14] J.M. Pardal, S.S.M. Tavares, M.P. Cindra Fonseca, H.F.G. Abreu, J.J.M. Silva, Study of the austenite quantification by X-ray diffraction in the 18Ni-Co-Mo-Ti maraging 300 steel, J. Mater. Sci. 41 (2006) 2301–2307. doi:10.1007/s10853-006-7170-y.

[15] ASM International, ASM Handbook: Volume 1 Properties and selection: irons steels and high performance alloys, 10th ed., ASM International, Materials Park, Ohio, 2001. doi:10.1016/S0026-0576(03)90166-8.

[16] S.L. Campanelli, A. Angelastro, C.G. Signorile, G. Casalino, Investigation on direct laser powder deposition of 18 Ni (300) marage steel using mathematical model and experimental characterisation, Int. J. Adv. Manuf. Technol. 89 (2017) 885–895. doi:10.1007/s00170-016-9135-x.

[17] L. Thijs, J. Van Humbeeck, K. Kempen, E. Yasa, J.-P. Kruth, Investigation on the inclusions in maraging steel produced by Selective Laser Melting, in: 5th Int. Conf. Adv. Res. Virtual Rapid Prototyp., 2011: pp. 297–304. doi:doi:10.1201/b11341-48\r10.1201/b11341-48.

[18] K. Kempen, E. Yasa, L. Thijs, J.P. Kruth, J. Van Humbeeck, Microstructure and mechanical properties of selective laser melted 18Ni-300 steel, Phys. Procedia. 12 (2011) 255–263. doi:10.1016/j.phpro.2011.03.033.

[19] S.L. Campanelli, N. Contuzzi, A.D. Ludovico, Manufacturing of 18 Ni Marage 300 Steel Samples by Selective Laser Melting, Adv. Mater. Res. 83–86 (2009) 850–857. doi:10.4028/www.scientific.net/AMR.83-86.850.

[20] E. Yasa, K. Kempen, J. Kruth, Microstructure and mechanical properties of Maraging Steel 300 after selective laser melting, in: Proc. 21st Int. Solid Free. Fabr. Symp., 2010: pp. 383–396. http://utwired.engr.utexas.edu/lff/symposium/proceedingsArchive/pubs/Manuscripts/2010/2010-32-Yasa.pdf.

[21] G. Casalino, S.L. Campanelli, N. Contuzzi, A.D. Ludovico, Experimental investigation and statistical optimisation of the selective laser melting process of a maraging steel, Opt. Laser Technol. 65 (2015) 151–158. doi:10.1016/j.optlastec.2014.07.021.

[22] A. International, ASM Handbook: Volume 4 Heat Treating, in: ASM Handb., ASM International, 1991: p. 2173. doi:10.1016/S0026-0576(03)90166-8.

[23] F.H. Lang, N. Kenyon, Welding of Maraging Steels, Weld. Res. Concil. (1971) 41.

[24] S.D. Meshram, G. Madhusudhan Reddy, S. Pandey, Friction stir welding of maraging steel (Grade-250), Mater. Des. 49 (2013) 58–64. doi:10.1016/j.matdes.2013.01.016.

[25] C.R. Shamantha, R. Narayanan, K.J.L. Iyer, V.M. Radhakrishnan, S.K. Seshadri, S. Sundararajan, S. Sundaresan, Microstructural changes during welding and subsequent heat treatment of 18Ni (250-grade) maraging steel, Mater. Sci. Eng. A. 287 (2000) 43–51. doi:10.1016/S0921-5093(00)00838-8.

[26] J.M. Pardal, S.S.M. Tavares, V.F. Terra, M.R. Da Silva, D.R. Dos Santos, Modeling of precipitation hardening during the aging and overaging of 18Ni-Co-Mo-Ti maraging 300 steel, J. Alloys Compd. 393 (2005) 109–113. doi:10.1016/j.jallcom.2004.09.049.

[27] S.P. Sagar, N. Parida, S. Das, R.N. Ghosh, Precipitation Hardening Study of Ageing of Maraging Steel Using Ultrasonic Technique, Mater. Sci. (2006) 7–8.

[28] J. Millán, S. Sandlöbes, A. Al-Zubi, T. Hickel, P. Choi, J. Neugebauer, D. Ponge, D. Raabe, Designing Heusler nanoprecipitates by elastic misfit stabilization in Fe-Mn maraging steels, Acta Mater. 76 (2014) 94–105. doi:10.1016/j.actamat.2014.05.016.

[29] ASTM, Standard Specification for Superstrength Alloy Steel Forgings 1, Astm. (2015) 1–7. doi:10.1520/A0579.

[30] J.D. Hunt, Steady state columnar and equiaxed growth of dendrites and eutectic, Mater. Sci. Eng. 65 (1984) 75–83. doi:10.1016/0025-5416(84)90201-5.

[31] I. Yadroitsev, P. Krakhmalev, I. Yadroitsava, P. Bertrand, I. Smurov, Energy input effect on the microstructure, morphology and stability of single track from metallic powder in selective laser melting, J. Mater. Process. Technol. 213 (2013) 606–613. doi:http://dx.doi.org/10.1016/j.jmatprotec.2012.11.014.

[32] K.J.A. Brookes, Maraging steel for additive manufacturing - Philipp Stoll's paper at DDMC 2016, Met. Powder Rep. 71 (2016) 149–152. doi:10.1016/j.mprp.2016.04.087.

[33] P. a. Colegrove, H.E. Coules, J. Fairman, F. Martina, T. Kashoob, H. Mamash, L.D. Cozzolino, Microstructure and residual stress improvement in wire and arc additively manufactured parts through high-pressure rolling, J. Mater. Process. Technol. 213 (2013) 1782–1791. doi:10.1016/j.jmatprotec.2013.04.012.

[34] P. Würzinger, R. Rabitsch, W. Meyer, Production of maraging steel grades and the influence of specified and nonspecified elements for special applications, J. Mater. Sci. 39 (2004) 7295–7302. doi:10.1023/B:JMSC.0000048744.03279.ec.

[35] B. AlMangour, J.M. Yang, Improving the surface quality and mechanical properties by shot-peening of 17-4 stainless steel fabricated by additive manufacturing, Mater. Des. 110 (2016) 914–924. doi:10.1016/j.matdes.2016.08.037.

[36] E.A. Jägle, P. Choi, J. Van Humbeeck, D. Raabe, Precipitation and austenite reversion behavior of a maraging steel produced by selective laser melting, J. Mater. Res. 29 (2014) 2072. doi:10.1557/jmr.2014.204.

[37] I. Journal, O.F. Advanced, H. Ahmed, H. Central, Evaluation of Relatively Low Strength Maraging Evaluation of Relatively Low Strength Maraging Steel, (2015).

[38] Astm, Standard Practice for X-Ray Determination of Retained Austenite in Steel with Near Random Crystallographic Orientation 1, Astm. 03 (2009) 1–7. doi:10.1520/E0975-13.necessary.

6 Improving mechanical properties of wire + arc additively manufactured maraging steel through plastic deformation enhanced aging response

This chapter is based on the following submission.

X. Xu*, S. Ganguly, J. Ding, D. Philip, F. Martina, X. Liu, S. Williams, Improving mechanical properties of wire + arc additively manufactured maraging steel through plastic deformation enhanced aging response. Mater. Sci. Eng. A. (Revise)*

From Chapter 5, the less pronounced aging response of WAAM maraging steel was attributed to the lack of high-angle grain boundaries. Hence, this chapter applied the interpass cold rolling to the conventional WAAM process, aiming to introduce plastic deformation to the deposit and induce recrystallization to create high angle grain boundaries, thereby enhancing the aging response of WAAM maraging steel.

Abstract: Maraging steel gains ultrahigh strength through aging; however, wire + arc additively manufactured maraging steel features a columnar-dendritic structure with associated segregation and shows a much less pronounced aging response. In this paper, plastic deformation was introduced through interpass cold rolling during the layer-by-layer deposition process. After aging, mechanical testing showed a substantial strength improvement from 1410MPa (unrolled) to 1750MPa (50kN rolled). Rolling induced partial recrystallization to break the dendritic structure and form high-angle grain boundaries, which promoted the atoms diffusion to enable a more uniform solutionizing process and improved the subsequent aging response by 105-110%. The main contribution of the overall strengthening of the rolled alloy was attributed to the effective aging process, accounting for more than 95% of the entire strength increase.

Keywords: wire + arc additive manufacture; plastic deformation; maraging steel; dislocation density; age hardening.

6.1 Introduction

Maraging steel is a family of low-carbon (below 0.03%) steel that combines ultrahigh strength with excellent fracture toughness [1]. Maraging steel derives the high strength by the dispersion of a large amount of nanosized precipitates from the age hardening of an extremely ductile body-centred cubic (bcc) lath martensitic structure. The unique hardening mechanism results in strengths up to 3450MPa [2], as compared to other steels with similar crystallographic structures. The high strength-to-weight ratio, ease of machining in the annealed condition, superior dimension stability during age hardening, and good weldability make maraging steel widely used in the aerospace and tooling industry.

Additive Manufacture (AM) is a novel approach for building near-net-shape components in a layer-by-layer manner [3]. In Directed Energy Deposition (DED) AM, the feedstock (powder or wire) is melted by a heat source (laser, electron beam or arc), and the deposition path is controlled by a robot or a CNC system to form the desired geometry. Compared to conventional subtractive manufacture (SM), AM is attractive for the fabrication of metallic components due to substantially reduced material wastage of expensive metals (such as Ti-6Al-4V, Inconel superalloys and maraging steels), shortened lead times and greater design freedom [4].

Despite these advantages, the implementation of AM in engineering applications requires the AM parts to possess equivalent or even superior mechanical properties to the SM counterparts. Currently, the benefits above are not realised due to the limitation in properties, and AM is mostly exploited in powder bed processes where the design capability is utilised to provide weight savings. The conventional metal billet or forging production procedure involves melting, casting and subsequent thermomechanical processing, through which the entire billet or forging undergoes a uniform processing and ends up with a relatively homogeneous microstructure and largely isotropic characteristics [5]. Due to the inherent characteristics of DED AM, the deposited material undergoes a unique processing featuring localised melting, rapid solidification and non-uniform heating-cooling cycles. These conditions often result in a spatially differential

microstructure of dendritic nature associated with segregation and largely anisotropic properties in comparison to that attained in a conventionally processed material [6]. For example, in AM of Ti-6Al-4V alloy, undesirable, coarse-columnar, primary β grain structures have been widely reported to result in a strong texture and mechanical anisotropy in an AM component in contrast to the fine equiaxed grains, nearly random grain orientation and isotropic mechanical properties in a wrought alloy [7,8].

In AM of maraging steels, most research has focussed on the laser/powder based process [1,9–14]; however, the solidification results in non-steady amorphous-nanocrystalline composite microstructures [14] due to the extremely high cooling rate (up to 108 K/s [15]). Furthermore, unmelted particles or lack of fusion defects (micrometre scale) often result in components that are not fully-dense (relative density ranging from 90.9% to 99.9% [11]), leading to a loss of toughness. In an earlier study the authors used Wire + Arc Additive Manufacture (WAAM) [4], a DED AM process using wire as the feedstock and an arc as the heat source, to deposit fully-dense maraging steel components [6,16]; the resulting microstructure was characterized by severe elemental segregations and a large proportion of columnar grains due to the inherent directional heat conduction. The UTS was comparable to the annealed wrought alloy in the as-deposited condition (1118MPa vs 1000MPa [6]); however, the aging response of the WAAM maraging steel was found to be so less pronounced that the UTS only achieved 1410MPa [6] (wrought: 1760MPa). The strength loss was attributed to the slight mismatch of elemental composition between the wire and the plate of the same grade, impurities in the wire and the high content of retained and reverted austenite [6], but the main reason was believed to be the lower aging response of the as deposited microstructure.

As a material production process, AM is similar to casting since both involve melting and solidification process only, though the former features freeforming and a higher cooling rate. AM components are built through solidification of liquid metal droplets and therefore are likely to exhibit the disadvantages associated with solidified structures, e.g. dendritic structure and segregation. Wrought alloys

have superior properties to cast alloys due to additional thermomechanical processing, which involves several passes of rolling and repeated heating of the structure to eliminate elemental segregation and induce dynamic recrystallization. For instance, by applying cold rolling to wrought maraging steels, the remaining austenite in the as-quenched samples was transformed to martensite and the plastic deformation induced high-density dislocations accelerated the hardening response during the subsequent aging process; when applying 15% thickness reduction, the yield strength was reported to improve from 1286MPa to 1700MPa [17].

The mechanical properties of AM alloys are usually benchmarked with respect to wrought alloys. In order to achieve similar microstructural features and mechanical properties, rolling has been applied to different alloys in WAAM. For Ti-6Al-4V, it was found that with in-process rolling the normally coarse centimetre-scale columnar β structure was refined to below 100μm and both α and β phase textures were weakened to close to random since the deformation caused the new β orientations to develop through local heterogeneities in the deformed structure [7]. For aluminium alloy, rolling proved to eliminate pores larger than 5μm in diameter [18] and enhanced the microhardness and tensile strength due to the high-density dislocations and fine sub-grains with relatively low misorientations [19]. For low alloy steel, rolling with profiled and slotted roller was reported to reduce distortion and surface waviness, and the residual stress measured in the rolled parts were lower than those in the unrolled parts; grain refinement was also observed when the rolled alloy was reheated during subsequent depositions [20].

With the aim to improve the mechanical properties of WAAM maraging steel to the level comparable to the wrought alloy, the present research studied the application of interpass cold rolling to induce plastic deformation during the layer-by-layer deposition process. Although cold rolling with different thickness reduction ratios has been shown to enhance the aging response of wrought maraging steel, interpass rolling in WAAM process, where rolling and deposition are applied alternatively, is a totally different scenario. Rolling-induced plastic

strain would be partially released by the following depositions, and the non-equilibrium intrinsic aging effect [14] also makes the rolled microstructure, phase distribution and mechanical properties unpredictable. Therefore, the efficacy of using interpass cold rolling, the final microstructure, and the aging response of the rolled WAAM maraging steel are yet to be investigated, and so is the underlying strengthening mechanism, which are the subject of the present paper.

6.2 Experimental

6.2.1 Interpass rolling assisted WAAM process

The interpass rolling assisted WAAM system consisted of two subsystems: the WAAM deposition system and the rolling system, as shown in Fig. 6-1. The former consisted of a plasma power source (Fronius, TransTig 5000) and a wire feeder. A trailing shield device [21] was attached around the torch to provide additional shielding (99.99% Ar, 200 l/min) and prevent the deposits from being excessively oxidised after deposition. A three-axis CNC gantry system was deployed to control the deposition paths, and the same rolling assembly (as reported in [7,8,19,20]) was attached to the CNC gantry. A rigid flat roller (width: 20mm, diameter: 100mm) was placed above and aligned with the deposition paths; after each deposition, the roller was lowered down to contact the deposit and apply compressive pressure through a hydraulic cylinder. As the rolling rig travelled along (speed: 2m/min), the deposit was flattened through the plastic flow of the material, thereby introducing strain and stored energy[2] to the deposit. In this study, the interpass rolling strategy was applied, i.e., rolling and deposition were applied in an alternating manner.

[2] During the rolling process, the hydraulic cylinder works on the deposit through the roller and transfers the mechanical energy to the internal energy stored in the deformed deposit.

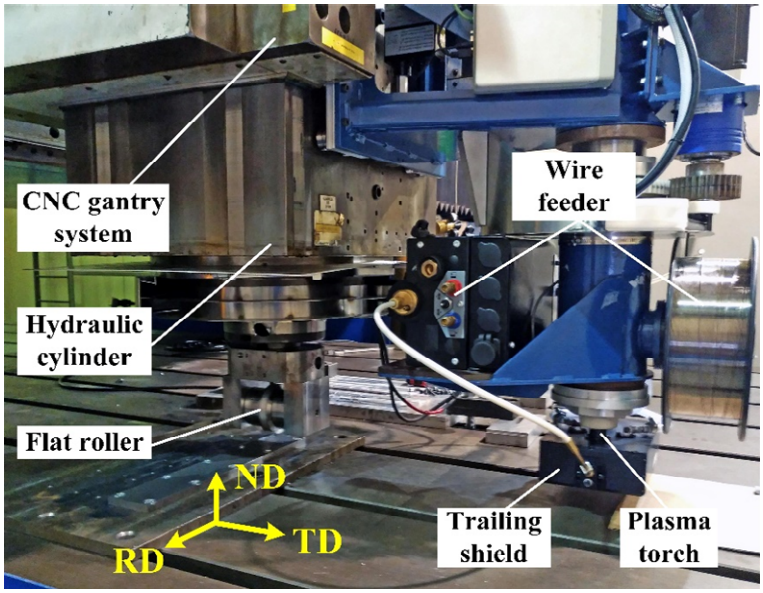

Figure 6-1 Experimental setup of the interpass rolling assisted plasma-WAAM system. (RD: rolling direction; ND: normal direction; TD: transverse direction.)

Two interpass rolled linear wall structures of the same length (400mm) and height (123mm) were produced with the load of 50kN and 75kN respectively for mechanical testing and microstructural analysis. Rolling was applied when the topmost deposit cooled down below 121°C, as suggested by [22], to minimise the austenite formation. To ensure consistency with the previous research [6] and therefore a meaningful comparison of the mechanical test results, the same wire (see Table 6-1 for the composition), deposition parameters (current=180A, WFS=1.8m/min, TS=0.2m/min) and heat treating procedure (solutionizing at 815°C, air cooling to room temperature; then aging at 482°C for 3h and air cooling to room temperature) were applied to the interpass rolled walls.

Table 6-1 The chemical composition of the maraging steel wire (wt. %).

Ni	Mo	Co	Ti	Al	C	Fe
18.28	4.69	8.21	0.44	0.11	<0.01	Balance

6.2.2 Analytical methods

The sample preparation process and equipment make and model of the metallographic study, optical microscopy (OM), microhardness test, tensile test, X-ray diffraction (XRD) analysis and electron backscatter diffraction (EBSD)

analysis had been reported in details in [6]. The polished samples were etched with 10% Nital solution for 10s for microstructure study, and for 60s to reveal the prior-austenite grain boundary above and near the first layer band [6] in the as-deposited condition. The EBSD data were analysed with the software HKL-Channel 5. Tensile test specimens were extracted in both horizontal (along wall length) and vertical direction (along wall height) according to BS EN ISO 6892-1: 2009 standard [6]. At least three specimens were tested for each direction and heat treating condition, and t-test [23] is applied to check the statistical difference of the testing results (statistical significance threshold=0.05). The grain size is determined using the line intercept method [24]. Austenite quantification by XRD was carried out using the direct comparison method [6]. Transmission electron microscopy (TEM) (JEM-2100F, JEOL) operating at 200kV was used to characterise the dislocation distribution in the rolled WAAM material. Thin-foil TEM samples were prepared by focused ion beam (FIB).

6.3 Results

6.3.1 Microhardness

Fig. 6-2 presents the microhardness variation of the unrolled and interpass rolled WAAM maraging steel wall structures measured from the top surface towards the substrate. In the as-deposited condition (Fig. 6-2a), the microhardness of all the samples shows a low level of 30-35HRC near the top and then a sudden rise to 40-45HRC at which level the microhardness generally remains towards the substrate despite some fluctuations; the only difference is where the microhardness rise begins and it turns out that the rolled samples possess a larger softer zone than the unrolled alloy. As has been explained in the previous work [6], the material near the top is relatively soft due to the lack of subsequent thermal cycles so that no appreciable intrinsic aging [14] occurs to harden the matrix. The critical point where pronounced aging firstly takes place is also where the microhardness rises sharply; in terms of metallographic morphology, it is where the topmost layer band [6] locates (see dash lines in Fig. 6-2). After aging (Fig. 6-2b), the microhardness all of the samples is significantly improved to the same high level of 50-53HRC which is comparable to the wrought alloy, and the

microhardness variation from the top to the bottom is eliminated. The microhardness measurement doesn't show any enhanced aging response resulting from the interpass rolling.

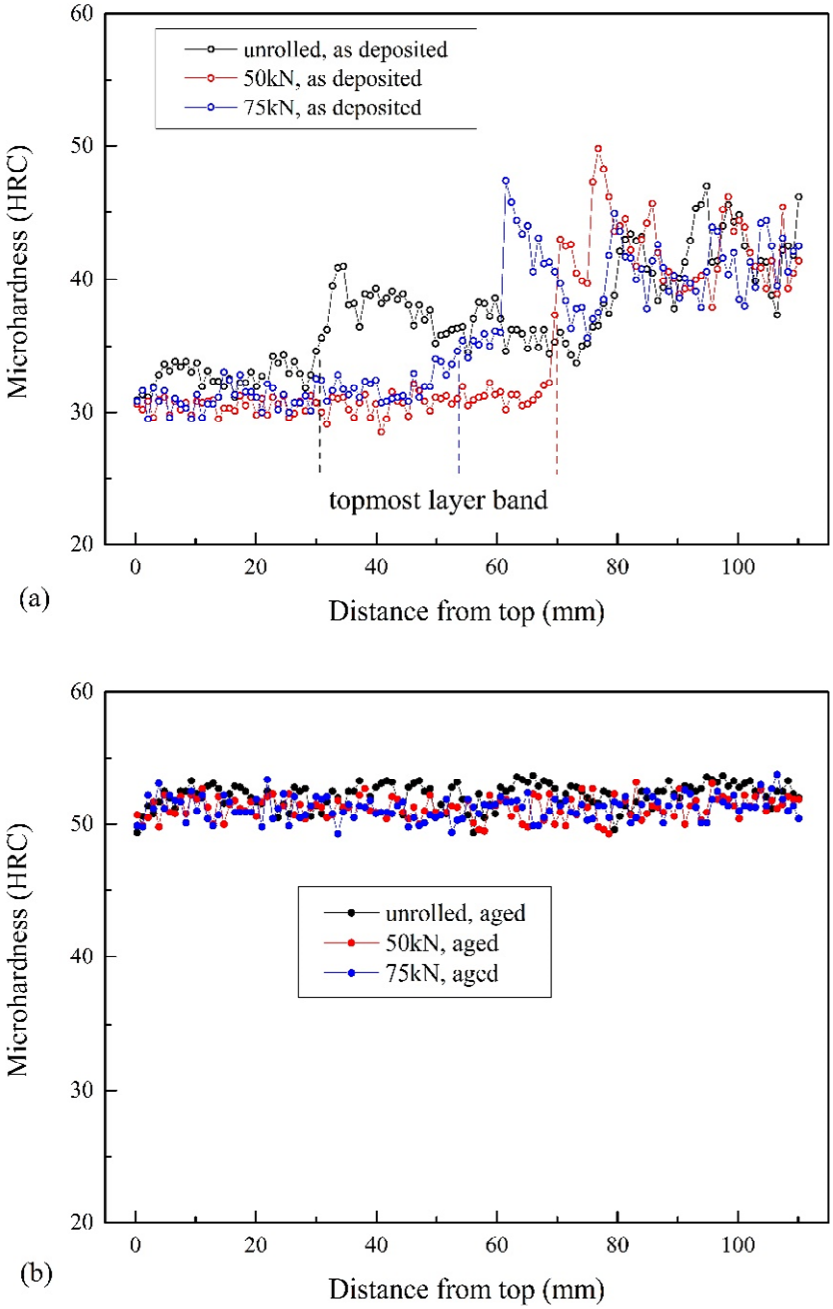

Figure 6-2 Microhardness variation of WAAM maraging steel wall from the top to the substrate (a) as deposited condition (b) aged condition.

6.3.2 Dendrites reorientation

Fig. 6-3 presents the optical micrographs of the 75kN rolled WAAM maraging steel in the aged condition. In the topmost layer (Fig. 6-3a) where rolling and subsequent thermal cycles are absent, the microstructure shows a typical cellular/dendritic solidification morphology: bundles of long and linear columnar dendrites are observed to develop across the layers and perpendicular to the interlayer boundaries. Austenite shown as white pools is found dispersed in the martensitic matrix preferentially at the interdendritic area (Fig. 6-3a). At 20mm away from the top (Fig. 6-3b), the layer shows as being squeezed: the linear columnar dendrites are replaced by many short and highly-distorted sub-columnar dendrites with random orientation; the size of the columnar dendrites is thereby greatly reduced, and the long dendrites tend to evolve to a more cellular structure through dynamic recrystallization. At some point, the dendritic structure can fully evolve into a cellular one (Fig. 6-3c), and the deformed cells are more preferentially oriented along TD. In addition, austenites are found to disperse among the intercellular regions with the aspect ratio greatly reduced.

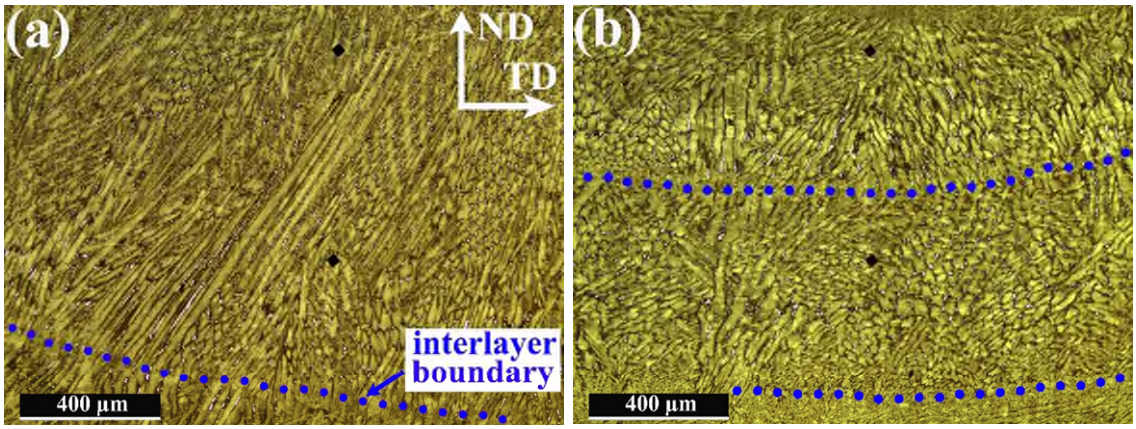

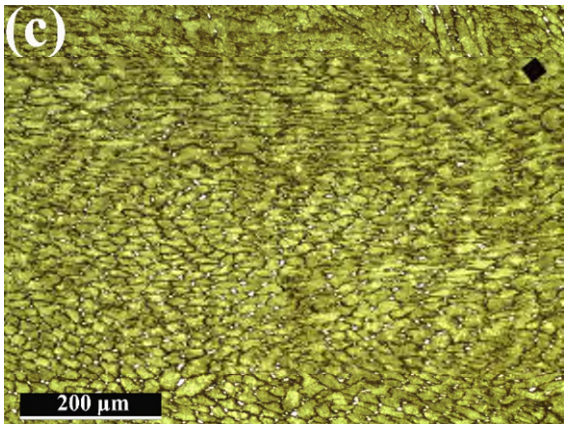

Figure 6-3 Optical micrographs of the 75kN rolled WAAM maraging steel at (a) topmost layer (b) 20mm and (c) 40mm down away from the top. Please note the black marks are hardness test indentations, not porosities.

6.3.3 Grain recrystallization

Fig. 6-4 shows the grain micrographs of the unrolled and rolled WAAM alloy in the as-deposited condition. Images are all taken at 25mm away from the top surface (right above the topmost layer band of the unrolled alloy), the reason being that below the topmost layer band the elemental segregation (blue arrows in Fig. 6-4) is so excessive that the prior-austenite grain boundaries are hidden. Due to the high content of alloying elements in maraging steel, the dendrite arms are fully developed across different grains and show better etching response than the prior-austenite grain boundaries; as such, some exemplary prior-austenite grain boundaries are marked with black lines for better visibility. Long and columnar grains are observed to grow along ND in the unrolled alloy; after rolling, those low-angles grains evolve to a large number of high-angle grains through recrystallization induced by the rolling and subsequent heat-cooling process. Segregation sites are not observed at the same position in the rolled micrographs, indicating a more homogeneous structure after rolling.

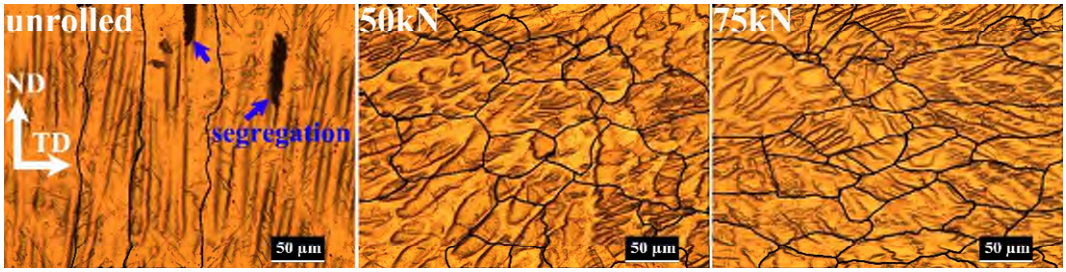

Figure 6-4 Optical micrographs showing the prior-austenite grain boundaries of the unrolled, 50kN and 75kN rolled WAAM maraging steel.

6.3.4 Mechanical testing results

Fig. 6-5 presents the mechanical testing results of the WAAM maraging steel attained after interpass rolling (see Table 6-2 for the detailed data). The UTS and 0.2%YS tested in the horizontal direction show a more pronounced standard deviation due to the intrinsic aging effect causing different levels of hardening along the wall height. In the as deposited condition, 50kN rolling results in a slight UTS change of 20MPa (t-test, p-value=0.83) and -13MPa (t-test, p-value=0.33) in the horizontal and vertical direction respectively, whilst 75kN results in a 34MPa (t-test, p-value=0.66) and 4MPa change respectively; therefore rolling does not have any statistically significant effect on the strength. After aging, the UTS obtained with 50kN rolling is significantly improved from 1138MPa to 1750MPa, and from 1013MPa to 1735MPa in the horizontal and vertical directions respectively, which is very close to the wrought alloy (1760MPa). Rolling with a higher load of 75kN does not show further strength improvement in the horizontal direction after aging. The elongation generally reduces after aging, and the WAAM alloy shows inferior elongation to the wrought alloy in the aged condition; therefore, rolling does not improve the ductility. Even though the 0.2%YS and elongation of the rolled material are slightly inferior to the wrought alloy, the overall WAAM maraging steel is hardened to a considerable level to marginally reach the wrought level through the applied interpass rolling.

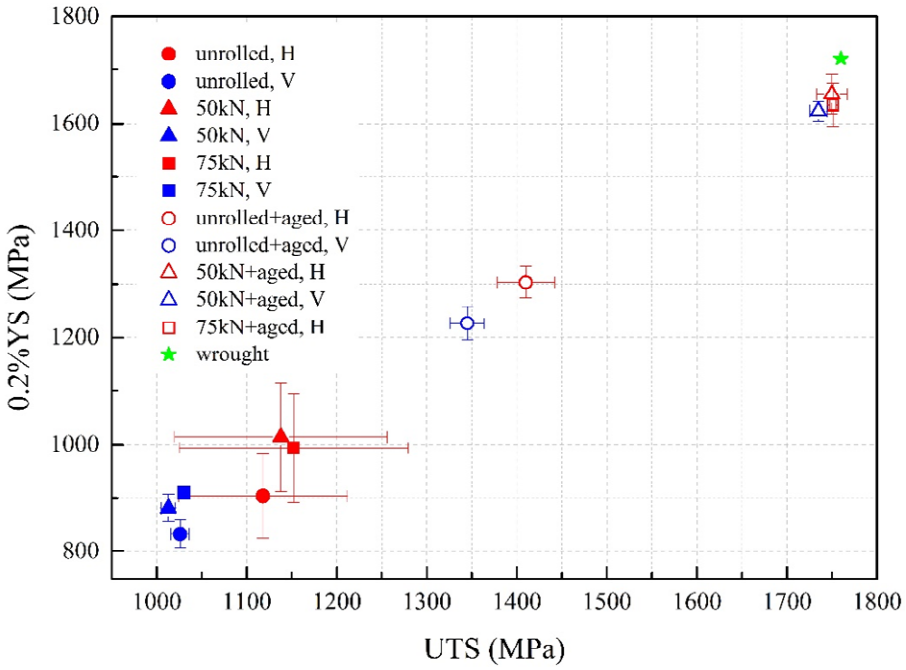

(a)

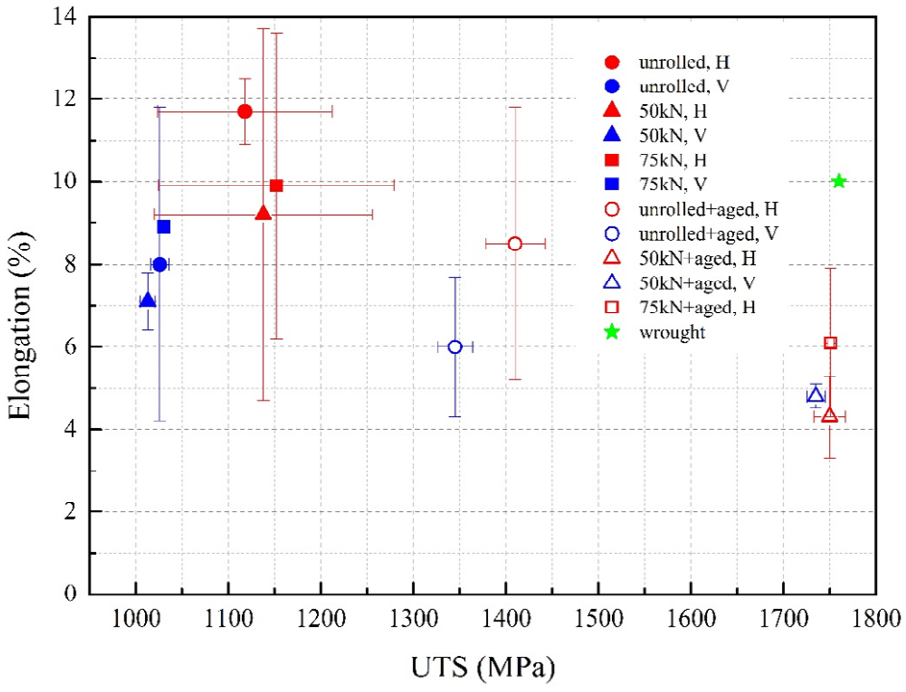

(b)

Figure 6-5 Mechanical properties of the WAAM maraging steel (H-horizontal, V-vertical; error bar represents the standard deviation) (a) UTS-0.2%YS (b) UTS-Elongation.

Table 6-2 Mechanical properties of the WAAM maraging steel.

					UTS/MPa	0.2%YS/MPa	Elongation/%
WAAM	as deposited	unrolled		H	1118±94	904±78	11.7±0.8
				V	1026±10	833±26	8.0±3.8
		rolled	50kN	H	1138±118	1014±102	9.2±4.5
				V	1013±8	882±25	7.1±0.7
			75kN	H	1152±127	993±101	9.9±3.7
				V	1030	910	8.9
	aged	unrolled		H	1410±32	1303±29	8.5±3.3
				V	1345±19	1227±31	6.0±1.7
		rolled	50kN	H	1750±17	1654±37	4.3±1.0
				V	1735±10	1623±18	4.8±0.3
			75kN	H	1751±3.4	1634±41	6.1±1.8
				V	-	-	-
wrought	solution [2]				1000-1140	725-895	8-16
	aged [34]				1760	1720	10

6.4 Discussion

6.4.1 Strengthening contribution

Table 6-3 presents the strength increase in the horizontal direction through different processings benchmarked by the unrolled WAAM maraging steel in the as deposited condition. As can be seen, aging the unrolled alloy results in a strength increase of 292MPa, whilst interpass rolling the WAAM alloy with 50kN leads to a strength increase of 20MPa and the strengthening seems independent from the rolling load [25] such that with 75kN rolling the increment is 34MPa. Furthermore, if the WAAM alloy is rolled + aged, a considerable strength increase of 632MPa and 633MPa are observed with the rolling load of 50kN and 75kN respectively.

The strength increase of the rolled alloy comes from a synergic effect of rolling and heat treatment: rolling is likely to result in work hardening, recrystallization and austenite content reduction in the as deposited condition, heat treatment will result in the formation of large amount of precipitates, and rolling induced grain structure change will also affect the aging response. Considering that the aging temperature (482°C) is relatively low, the grain structure of the rolled alloy after

aging can be assumed to be the same as that in the as deposited condition; actually, the possible grain coarsening and austenite reversion during aging will only result in strength loss. Though the strength improvement from rolling only is not statistically significant, for the overall 632MPa (50kN) strengthening with rolling and aging, rolling only, which is the resultant effect of work hardening, recrystallization and austenite content reduction, contributes maximum 20MPa (3.2%) and aging contributes at least 612MPa (96.8%). The pure aging response is enhanced from 292MPa to 612MPa (increased by 110%) when rolling is applied. The same goes for rolling with 75kN and rolling contributes 34MPa (5.4%) and aging contributes to 599MPa (94.6%); the aging response is increased by 105%.

Table 6-3 Strength increase in the horizontal direction through different methods (MPa).

aging	rolling		rolling + aging	
	50kN	75kN	50kN	75kN
292	20	34	632	633

Maraging steel is strengthened through age hardening, whilst the aging response of an alloy is highly dependent on its microstructure. The enhanced aging response of the rolled maraging steel indicates a significant change in the microstructure as compared with the unrolled alloy. The direct effects of rolling on the deposit and how they affect each strengthening mechanism is discussed as follows.

6.4.2 Effects of rolling on the deposit

6.4.2.1 Dislocation multiplication

Irreversible plastic deformation of the top deposit results in not only the motion of existing dislocations but also the increase of dislocation density within the crystal structure. This happens through two mechanisms: elongation of existing dislocations to increase the line length per unit volume, and generation of massive new dislocations through the Frank-Read mechanism [26]. Once the rolling induced shear stress exceeds the critical shear stress which is required for

generating new dislocations, the existing dislocation will pass the semi-circular equilibrium state and spontaneously generates new dislocations.

Fig. 6-6 compares the dislocation quantity of the unrolled and 75kN rolled WAAM maraging steel in the as deposited condition. In the unrolled alloy (Fig. 6-6a), dislocations formed during the solidification process are found to tangle with each other within the martensitic laths; the different contrast between adjacent laths indicates the difference in Burger's vector of the dislocations. After 75kN rolling (Fig. 6-6b), the overall dislocation density is significantly increased with the newly generated dislocations added up; higher-density dislocation clusters are observed in the laths and generally do not uniformly arrange themselves in the rolled alloy.

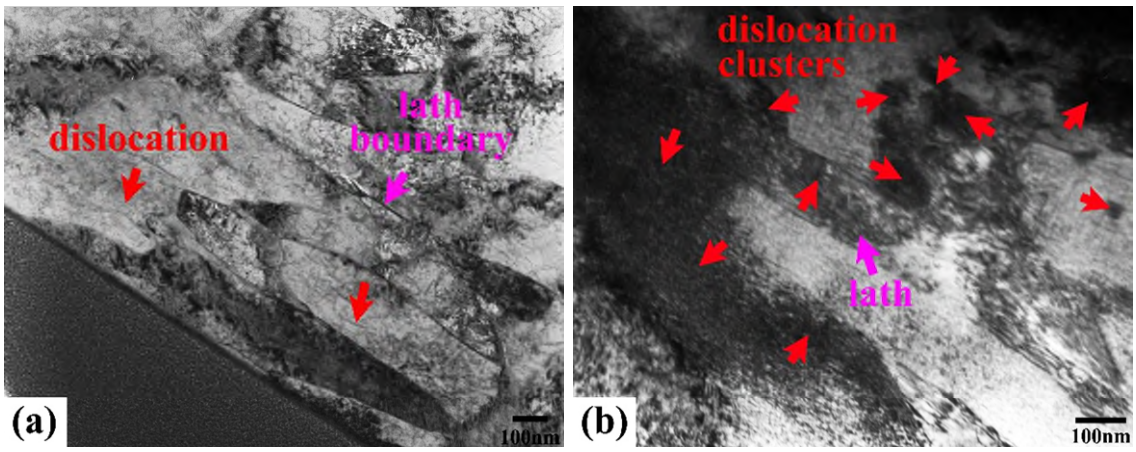

Figure 6-6 TEM bright field images showing dislocations in the (a) unrolled and (b) 75kN rolled WAAM maraging steel in the as deposited condition.

6.4.2.2 Energy stored in the deposit

Upon rolling, the deposit is flattened by squeezing the material so that the deposit gets shorter in the ND and wider in the TD. Consequently, the rolling system works on the deposit by transferring the mechanical energy to the internal energy. The internal energy is stored in the deposit in the form of shear strain and crystal defects such as stacking faults, point defects, dislocations, and twins [5]. Such energy would provide the driving force for a series of metallurgical reactions to take place during the complex rolling assisted WAAM process, as will be described later on.

6.4.2.3 Texture weakening

Fig. 6-7 presents the pole figures of the martensitic matrix of the unrolled and rolled WAAM maraging steel measured at the same area as Fig. 6-4. A strong texture in {100} family planes is observed in the unrolled condition, with the main axis having an intensity of 15 times random; after rolling, the intensity is reduced to 2.57 and 3.55 times random with 50kN and 75kN rolling respectively. Due to the directional thermal conduction (from top to bottom) in the WAAM solidification process, some facets of a crystal grow faster ({100} in cubic structures) than others and the crystals at which one of these planes faces in the direction of growth will usually out-compete crystals in other orientations. Furthermore, the cyclic heating from subsequent layers and the inherent low thermal conductivity of maraging steel (19.7 W/mK, about 1/3 of 0.5% C steel) allow enough activation energy and time for atoms to find places in existing crystals, rather than starting new crystals with a random orientation. Consequently, directional growth of columnar grains is observed in the unrolled WAAM maraging steel. Interpass rolling causes a significant amount of flattening of the deposits, which destroys the crystalline order and reorients the crystallites in these directions by grain flow. In case of a subsequent thermal process, the new crystallites that arise will have a more random texture to weaken the overall texture that formed in the unrolled condition.

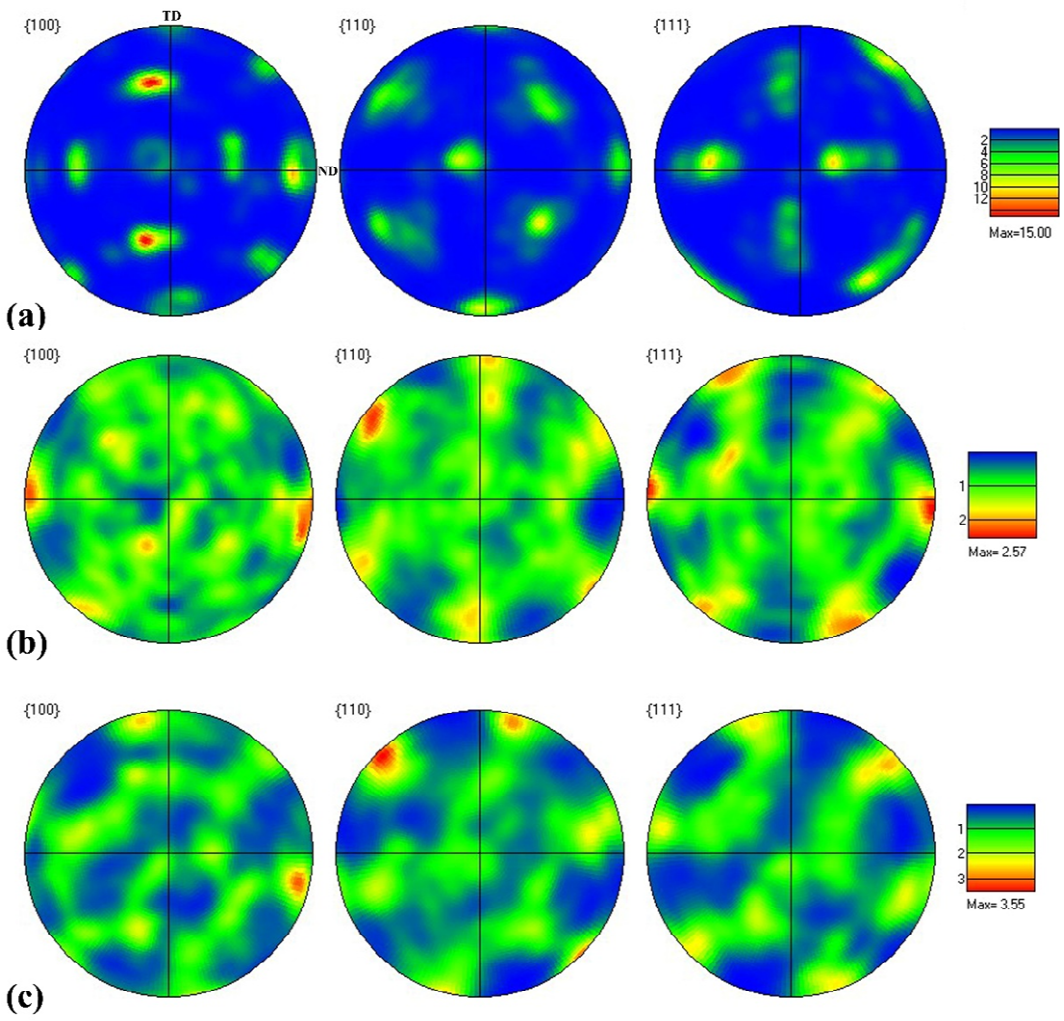

Figure 6-7 Pole figures showing (a) strong {100} texture in the unrolled condition and greatly weakened texture after rolling with (b) 50kN and (c) 75kN (half width: 10°, cluster size: 5°).

6.4.3 Strengthening mechanisms

The overall principle of strengthening an alloy is to hinder the dislocation movements. The dislocation itself can act as an obstacle to other dislocation's motion; besides, grain boundaries and precipitates can play the same role. Underlying strengthening mechanisms responsible for the interpass rolling of WAAM maraging steel are discussed as follows.

6.4.3.1 Grain boundary strengthening

6.4.3.1.1 Recrystallization

The grain morphology evolution from Fig. 6-4 indicates the recrystallization during the rolling-WAAM process. On the one hand, thermal cycling between M_f (temperature when austenite-to-martensite transformation finishes) and a temperature considerably above the solution temperature has been reported to refine the grains of maraging steels [2]; on the other hand, rolling induced energy stored in the deposits provides the driving force for recrystallization during multiple thermal cycles when the material is heated above recrystallization temperature.

It is worth noting that the recrystallization occurred during the rolling-WAAM process is different from a conventional one in three aspects. Firstly, the plastic deformation of the deposits is not in a one-shot thickness reduction manner but a non-uniform accumulative manner; secondly, the thermal history is in a fast-heating-fast-cooling manner featured by numerous cyclic temperature pulses rather than a controlled heating-cooling process; thirdly, the recrystallization process is accompanied by the recovery process which releases the stored energy and reduces the activity of subsequent recrystallization process.

6.4.3.1.2 Grain size

Fig. 6-8 shows the EBSD results measured in the same area as Fig. 6-4 to characterise the grain size. In the unrolled alloy, the prior-austenite shows as columnar grains containing numerous subgrains and primarily orients along the building direction; the lengths are comparable to the entire map, and the thicknesses are generally less than 50μm (Fig. 6-8a). With 50kN rolling, the prior-austenite shows as equiaxed grains also containing a significant number of subgrains; the average grain size is 40μm which is comparable to the wrought alloy (30μm [6]).

Grain boundaries are discontinuities in polycrystalline alloys and act as barriers to dislocation motion, by hindering their transmission and creating the dislocation pile-ups at the grain boundaries [27]. According to the Hall-Petch relation, the smaller the grain size, the higher the strength. Though rolling induced recrystallization have changed the grain morphology, the grain sizes are almost

the same; hence the strengthening from grain size reduction will not be expected to be considerable.

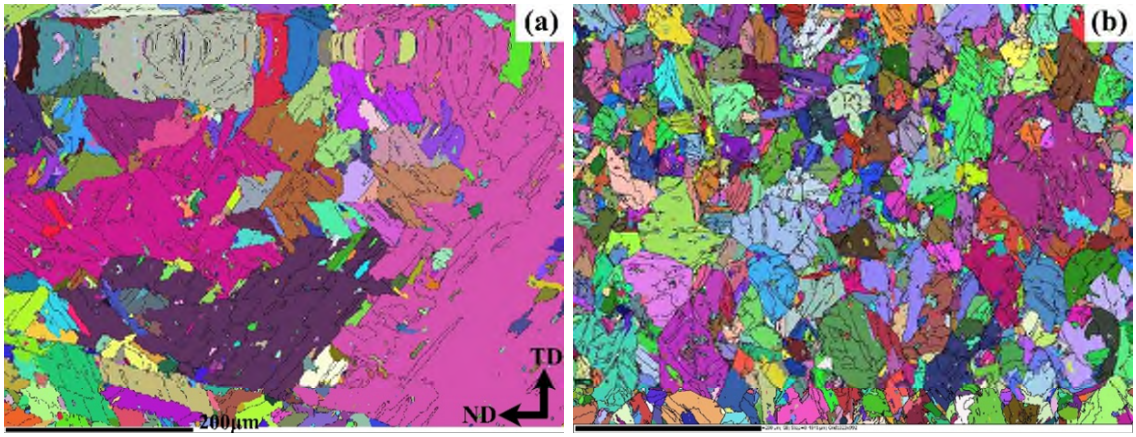

Figure 6-8 Randomly coloured grains after grain reconstruction for (a) unrolled (b) 50kN rolled WAAM maraging steel (black lines are grain boundaries with misorientation greater than 15°).

6.4.3.2 Precipitation hardening

6.4.3.2.1 Enhanced solutionizing process

From the microhardness measurements (Fig. 6-2), it is worth noting that after rolling the location of the topmost layer band is moved further away from the top, indicating an enlarged supersaturated martensitic area (softer zone). The unrolled alloy shows an earlier and more pronounced response to the non-equilibrium intrinsic aging effect than the rolled one: the same amount of temperature pulses cannot provide enough driving force to trigger appreciable precipitation and hardening in the rolled alloy at the same location. It can thus be postulated that rolling promotes the alloying atoms diffusion and dissolution into the matrix to create a more supersaturated matrix, and the solute atoms tend to be more thermodynamically stable in the highly strained matrix. Besides, the high-angle grain boundaries formed as a result of recrystallization allows more atoms mobility and diffusion paths into solution. It is also postulated that the strong {100} texture in the unrolled alloy does not favour the atoms dissolution from some crystal planes, as compared to the randomly oriented crystals.

Nucleation of precipitates occurs at the solutionizing stage since the kinetic barrier of the surface energy is easier to be overcome at a high temperature. For maraging steels, precipitates nucleate preferentially at dislocations or lath boundaries within the lath martensite [2]. Thanks to the dislocation multiplication induced by rolling, the more supersaturated matrix resulting also from rolling will then result in a more significant nucleation during solutionizing; in the subsequent aging stage, those nuclei will grow to form larger amount of precipitates to strengthen the matrix.

6.4.3.2.2 Precipitates quantity

When a moving dislocation meets the precipitates, the interaction ends up with the dislocation bypassing the precipitates in the form of Orowan looping or bypass slip if the precipitates are hard, or the precipitates being sheared if they are soft, thereby strengthening the material. Fig. 6-9 shows the precipitates and dislocations interacting within a lath of the aged WAAM maraging steel. Dispersed nanoscale precipitates embedded in the martensitic matrix are found as pinning points impeding the movement of the linear dislocations.

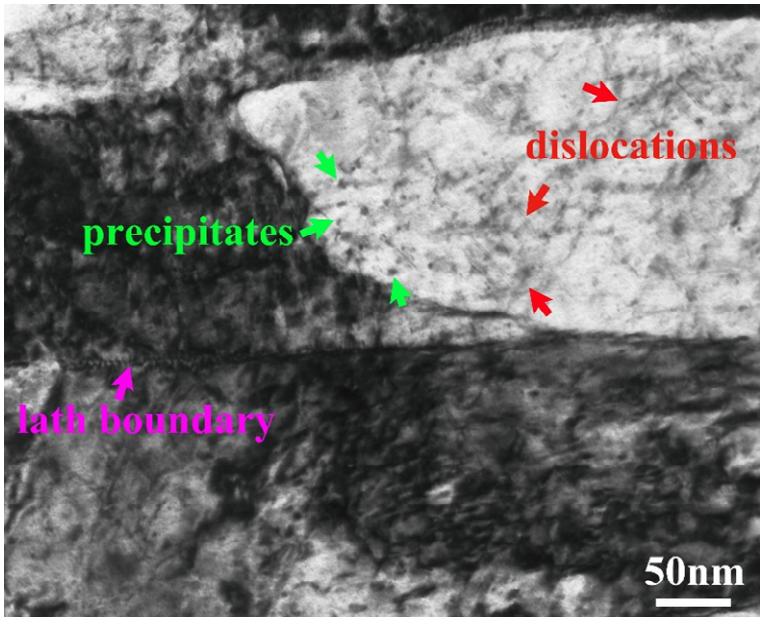

Figure 6-9 TEM bright field image showing the precipitates impeding dislocation motion in the aged WAAM maraging steel.

The strengthening obtained from aging Δσa is dependent on the metallic system, volume fraction and size of the precipitates [28]. Since the unrolled and rolled WAAM maraging steel possess the same alloying system and undergo identical heat treatment, the major difference between them is the volume fraction of precipitates after aging. By applying the Taylor factor to the Ashby-Orowan relationship [28], the $\Delta\sigma_a$ can be given by Equation (6-1)

$$\Delta\sigma_a = \left(0.538Gbf^{1/2}/X\right)\ln(X/2b) \quad \textbf{(6-1)}$$

Where *G* is the shear modulus, *b* is the Burgers vector of the dislocation, *f* is the volume fraction of the precipitates and *X* is the spatial diameter of the precipitate.

Table 6-4 compares the volumetric fraction of the precipitates formed in the aged WAAM alloy. The precipitates of interest are the most widely reported Ni_3Mo, Ni_3Ti, Fe_2Mo and Fe_7Mo_6 [6]. As can be seen, the quantity of precipitates formed are almost doubled after rolling, and there is no significant difference between 50kN and 75kN rolling. Therefore, the improved aging response of the rolled alloy can be attributed to two reasons: firstly, the high-density dislocations within the laths provide massively more preferred nucleation sites for the precipitates; secondly, the dislocations also increase the diffusion rate of solute atoms by providing preferred diffusion paths [29]. A larger amount of precipitates distort the lattice around them and together with the increased grain boundaries, act as barriers to the dislocation motion to provide extra strength to the WAAM maraging steel.

Table 6-4 The volume fraction of the precipitates measured through EBSD phase mapping (%).

unrolled	50kN rolled	75kN rolled
1.4 [6]	2.2	2.4

6.4.3.3 Austenite content reduction

From Fig. 6-10, the retained austenite is reduced greatly from 8.3% to 0.5% in the as deposited condition with 75kN rolling due to the strain induced shear transformation of austenite to martensite [30]. After aging, the formation of

reverted austenite increases the overall austenite content to 3.6% in the rolled alloy, which is still much lower than the unrolled counterparts (13.1%). The higher austenite content in the rolled alloy than the wrought one may account for the slightly lower 0.2%YS and elongation.

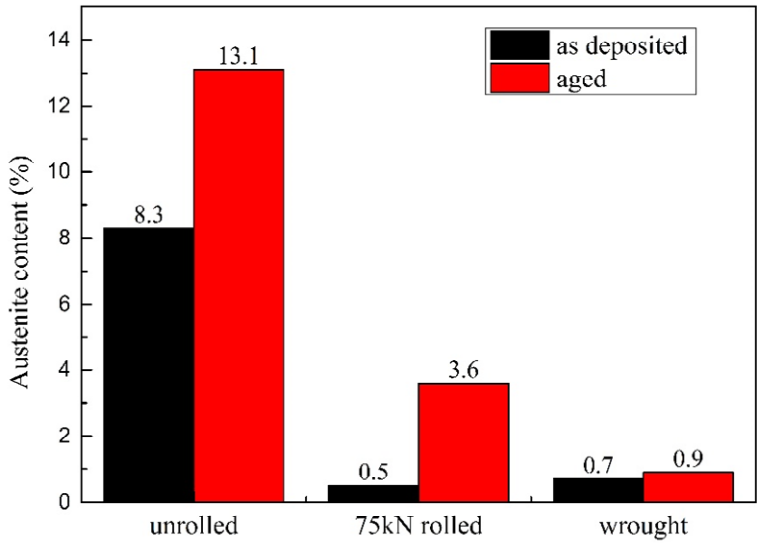

Figure 6-10 Volumetric fraction of the austenite measured above the first layer band (data of unrolled and wrought alloy from [6]).

6.4.3.4 Work hardening

Cold working usually leads to a strength increase known as work hardening due to the increased dislocation density. However, in the interpass rolling assisted WAAM process the heat input from successive depositions acts as a non-equilibrium annealing of the strained material and restores the lattice to be of lower dislocation density through recovery and recrystallization [31]; besides, maraging steels possess very low work-hardening rate and can be cold worked with little gains in hardness [2]. Therefore, work hardening in the present study is not expected to contribute greatly to the overall strengthening.

6.5 Conclusions

1. By applying 50kN interpass cold rolling, the UTS of WAAM maraging steel is improved from 1410MPa to 1750MPa which meets the wrought standard (1760MPa). Rolling with higher loads does not show further strength increase.

2. With rolling applied, the aging response is improved by 110% (50kN) and 105% (75kN). Among all the active strengthening mechanisms, aging contributes to more than 95% of the overall strength increase.
3. Rolling results in dendrites reorientation to destroy the previous crystalline order and form new crystallites to weaken the {100} texture from 15 times random to 2.57, which, together with precipitates formation, reduces the anisotropy level from 65MPa to 15MPa with 50kN rolling.
4. Rolling induced energy store triggers recrystallization to form a large number of high-angle grain boundaries, which allows greater atomic mobility and diffusion paths into solution, thus creating a more supersaturated matrix in the solutionizing stage.
5. Rolling induces dislocation multiplication to provide more preferred nucleation sites and diffusion paths for the precipitates clustering, thereby enhancing the aging response.
6. With 75kN rolling, austenite was reduced from 8.3% to 0.5% in the as deposited condition; after aging the austenite was higher than wrought alloy (3.6% vs 0.9%) but lower than the unrolled alloy (13.1%).

6.6 References

[1] S.L. Campanelli, A. Angelastro, C.G. Signorile, G. Casalino, Investigation on direct laser powder deposition of 18 Ni (300) marage steel using mathematical model and experimental characterisation, Int. J. Adv. Manuf. Technol. 89 (2017) 885–895. doi:10.1007/s00170-016-9135-x.

[2] ASM International, ASM Handbook: Volume 1 Properties and selection: irons steels and high performance alloys, 10th ed., ASM International, Materials Park, Ohio, 2001. doi:10.1016/S0026-0576(03)90166-8.

[3] B. Cong, J. Ding, S. Williams, Effect of arc mode in cold metal transfer process on porosity of additively manufactured Al-6.3%Cu alloy, Int. J. Adv. Manuf. Technol. 76 (2014) 1593–1606. doi:10.1007/s00170-014-6346-x.

[4] S.W. Williams, F. Martina, A.C. Addison, J. Ding, G. Pardal, P. Colegrove, Wire + Arc Additive Manufacturing, Mater. Sci. Technol. 00 (2015) 1–7. doi:10.1179/1743284715Y.0000000073.

[5] K. Huang, R.E. Logé, A review of dynamic recrystallization phenomena in metallic materials, Mater. Des. 111 (2016) 548–574. doi:10.1016/j.matdes.2016.09.012.

[6] X. Xu, S. Ganguly, J. Ding, S. Guo, S. Williams, F. Martina, Microstructural evolution and mechanical properties of maraging steel produced by wire + arc additive manufacture process, Mater. Charact. (2018). doi:10.1016/j.matchar.2017.12.002.

[7] J. Donoghue, A.A. Antonysamy, F. Martina, P.A. Colegrove, S.W. Williams, P.B. Prangnell, The effectiveness of combining rolling deformation with Wire-Arc Additive Manufacture on β-grain refinement and texture modification in Ti-6Al-4V, Mater. Charact. 114 (2016) 103–114. doi:10.1016/j.matchar.2016.02.001.

[8] F. Martina, P.A. Colegrove, S.W. Williams, J. Meyer, Microstructure of Interpass Rolled Wire + Arc Additive Manufacturing Ti-6Al-4V Components, Metall. Mater. Trans. A Phys. Metall. Mater. Sci. 46 (2015) 6103–6118. doi:10.1007/s11661-015-3172-1.

[9] E.A. Jägle, P.-P. Choi, J. Van Humbeeck, D. Raabe, Precipitation and austenite reversion behavior of a maraging steel produced by selective laser melting, J. Mater. Res. 29 (2014) 2072–2079. doi:10.1557/jmr.2014.204.

[10] K. Kempen, E. Yasa, L. Thijs, J.P. Kruth, J. Van Humbeeck, Microstructure and mechanical properties of selective laser melted 18Ni-300 steel, Phys. Procedia. 12 (2011) 255–263. doi:10.1016/j.phpro.2011.03.033.

[11] S.L. Campanelli, N. Contuzzi, A.D. Ludovico, Manufacturing of 18 Ni Marage 300 Steel Samples by Selective Laser Melting, Adv. Mater. Res. 83–86 (2009) 850–857. doi:10.4028/www.scientific.net/AMR.83-86.850.

[12] E. Yasa, K. Kempen, J. Kruth, Microstructure and mechanical properties of Maraging Steel 300 after selective laser melting, in: Proc. 21st Int. Solid Free.

Fabr. Symp., 2010: pp. 383–396. http://utwired.engr.utexas.edu/lff/symposium/proceedingsArchive/pubs/Manuscripts/2010/2010-32-Yasa.pdf.

[13] G. Casalino, S.L. Campanelli, N. Contuzzi, A.D. Ludovico, Experimental investigation and statistical optimisation of the selective laser melting process of a maraging steel, Opt. Laser Technol. 65 (2015) 151–158. doi:10.1016/j.optlastec.2014.07.021.

[14] C. Tan, K. Zhou, W. Ma, P. Zhang, M. Liu, T. Kuang, Microstructural evolution, nanoprecipitation behavior and mechanical properties of selective laser melted high-performance grade 300 maraging steel, Mater. Des. 134 (2017) 23–34. doi:10.1016/j.matdes.2017.08.026.

[15] E.A. Jägle, P. Choi, J. Van Humbeeck, D. Raabe, Precipitation and austenite reversion behavior of a maraging steel produced by selective laser melting, J. Mater. Res. 29 (2014) 2072. doi:10.1557/jmr.2014.204.

[16] X. Xu, J. Ding, S. Ganguly, C. Diao, S. Williams, Oxide accumulation effects on wire + arc layer-by-layer additive manufacture process, J. Mater. Process. Tech. 252 (2018) 739–750. doi:10.1016/j.jmatprotec.2017.10.030.

[17] Y. Lian, J. Huan, J. Zhang, C. Zhao, W. Gao, Z. Zhang, M. Ma, Effects of cold rolling on the microstructure and properties of Fe-Cr-Ni-Mo- Ti maraging steel, Mater. Sci. Eng. A. 712 (2018) 663–670. doi:10.1016/j.msea.2017.12.041.

[18] J. Gu, J. Ding, S.W. Williams, H. Gu, P. Ma, Y. Zhai, The effect of inter-layer cold working and post-deposition heat treatment on porosity in additively manufactured aluminum alloys, J. Mater. Process. Technol. 230 (2016) 26–34. doi:10.1016/j.jmatprotec.2015.11.006.

[19] J. Gu, J. Ding, S.W. Williams, H. Gu, J. Bai, Y. Zhai, P. Ma, The strengthening effect of inter-layer cold working and post-deposition heat treatment on the additively manufactured Al– 6.3Cu alloy, Mater. Sci. Eng. A. 651 (2016) 18–26. doi:10.1016/j.jmatprotec.2015.11.006.

[20] P. a. Colegrove, H.E. Coules, J. Fairman, F. Martina, T. Kashoob, H. Mamash, L.D. Cozzolino, Microstructure and residual stress improvement in wire and arc additively manufactured parts through high-pressure rolling, J. Mater. Process. Technol. 213 (2013) 1782–1791. doi:10.1016/j.jmatprotec.2013.04.012.

[21] J. Ding, P. Colegrove, F. Martina, S. Williams, R. Wiktorowicz, M.R. Palt, Development of a laminar flow local shielding device for wire + arc additive manufacture, J. Mater. Process. Technol. 226 (2015) 99–105. doi:10.1016/j.jmatprotec.2015.07.005.

[22] F.H. Lang, N. Kenyon, Welding of Maraging Steels, Weld. Res. Concil. (1971) 41.

[23] P. Baldi, A.D. Long, A Bayesian framework for the analysis of microarray expression data: regularized t -test and statistical inferences of gene changes, Bioinformatics. 17 (2001) 509–519. doi:10.1093/bioinformatics/17.6.509.

[24] ASTM, ASTM E112-13: Standard test methods for determining average grain size, ASTM Int. (2013) 1–28. doi:10.1520/E0112-13.1.4.

[25] Z. Yang, J. Su, J. Chen, Effect of Prior Cold Rolling Deformation on Strengthening of Maraging Steel, Iron Steel. 43 (2008) 66–69.

[26] Y. Estrin, H.S. Kim, F.R.N. Nabarro, A comment on the role of Frank-Read sources in plasticity of nanomaterials, Acta Mater. 55 (2007) 6401–6407. doi:10.1016/j.actamat.2007.07.052.

[27] Helena Van Swygenhoven, Grain Boundaries and Dislocations, Science (80-.). 296 (2002) 66–67. doi:10.1126/science.1071040.

[28] T. Gladman, Precipitation hardening in metals, Mater. Sci. Technol. 15 (1999) 30–36. doi:10.1179/026708399773002782.

[29] A. International, ASM Handbook: Volume 4 Heat Treating, in: ASM Handb., ASM International, 1991: p. 2173. doi:10.1016/S0026-0576(03)90166-8.

[30] P. Haušild, V. Davydov, J. Drahokoupil, M. Landa, P. Pilvin, Characterization of strain-induced martensitic transformation in a metastable austenitic stainless steel, Mater. Des. 31 (2010) 1821–1827. doi:10.1016/j.matdes.2009.11.008.

[31] J.W. Morris, Dislocation Plasticity : Overview, Introd. to Mater. Sci. i (2007) 1–36. http://www.mse.berkeley.edu/groups/morris/MSE205/Extras/dislocation plasticity.pdf.

[32] ASTM, Standard Specification for Superstrength Alloy Steel Forgings 1, Astm. (2015) 1–7. doi:10.1520/A0579.

7 Investigation of process factors affecting mechanical properties of INCONEL 718 superalloy in wire + arc additive manufacture process

This chapter is based on the following submission.

X. Xu*, J. Ding, S. Ganguly, S. Williams, Investigation of process factors affecting mechanical properties of INCONEL 718 superalloy in wire + arc additive manufacture process, J. Mater. Process. Tech. (under review)*

This chapter concerns the WAAM research on INCONEL 718 and focuses on the key factors that could affect the mechanical properties of WAAM INCONEL 718, including the wire source and industry standard heat treatment. Effect of oxides on the mechanical properties was also studied. A comparison was made with the INCONEL 718 produced by laser/powder based process.

Abstract: This paper systematically evaluated the effect of oxides, wire source and heat treatment on the mechanical properties of wire + arc additively manufactured (WAAM) INCONEL 718. Comparison of the as deposited grain structure was made with laser-powder based AM and wrought INCONEL 718. Results showed that oxides formed during deposition had no effect on the mechanical properties since a 0.5μm thick passivation layer consisting of Cr_2O_3 and Al_2O_3 formed upon deposition and prevented further oxides from forming inside the bulk. Wires from different suppliers resulted in around 50 MPa difference in UTS possibly due to the slight compositional variation and uncertainties in TiN inclusion. Standard heat treatment improved the strength from 824 MPa to 1110 MPa in the horizontal direction, but the average strength was 105 MPa lower than the wrought alloy. The as deposited WAAM INCONEL718 featured large columnar grains and massive Laves phase, as compared to the fine grains of laser powder bed fusion and wrought INCONEL 718. This starting microstructure led to less favourable and less numerous precipitates forming during heat treatment, which is the main reason for the strength mismatch. A different heat treatment would not help due to the starting microstructure.

Keywords: INCONEL 718; wire + arc additive manufacture; mechanical properties; heat treatment; oxides.

7.1 Introduction

INCONEL 718 superalloy (IN718) is an age-hardenable Ni-Cr austenitic material with a wide service temperature range from -257°C to 704°C [1]. Since IN718 was developed in the 1960s, the combination of high tensile, fatigue and creep-rupture strength, excellent oxidation resistance and outstanding resistance to postweld cracking has made IN718 the most widely used Ni-based superalloy in aircraft engine history [2].

Since IN718 is an important but expensive material widely used in various sectors, cost-effective manufacturing methods are required to ease machining, reduce material wastage, enhance design freedom, and shorten lead-times. Metal additive manufacturing (AM) offers these benefits through the manufacturing principle of depositing materials in a layer-by-layer manner according to a CAD model to achieve a near net-shaped component. So far, various AM techniques have been applied to IN718, particularly in laser-powder based AM process including laser powder bed fusion (PBF) and laser direct metal deposition (DMD) process. The tensile properties of the PBF IN718 were found to be equivalent or superior to the wrought alloy after heat treatment [3]. However, the laser-powder AM parts were frequently associated with porosity (relative density 98.4% % [4]) and unmelted powder particles issues [5], depending highly on powder source and process parameters. Although hot isostatic pressing (HIP) proved to be able to solve these issues, it would also coarsen the grain size substantially [6]. Besides, production quantity and component dimension are the limiting factors of the PBF process [7]. Wire + Arc Additive Manufacture (WAAM) is an AM process that has high deposition rate and suitable for large-scale components as an electric arc is used as the heat source and wire as the feedstock [8,9]. Initial WAAM studies using MIG [10] and TIG [11,12] proved the feasibility of depositing simple IN718 features; however, the effect of heat treatment was not investigated and the relationship between the deposition process and the material properties is yet to be studied.

Mechanical properties are a major concern for WAAM IN718 before its implementation in industry. Therefore, more fundamental research is required to gain an understanding of how the critical factors in AM processes can affect the mechanical properties of the final product. Mechanical properties of an alloy are determined by the defects (porosities and inclusions), alloying chemistry, microstructure, and heat treatment, depending on the strengthening mechanism of the particular alloy. Porosity is usually not an issue for most of the WAAM alloys, excluding aluminium alloys [13], since the feedstock is fully melted during deposition to form a fully-dense component.

As has been reported, control of oxides, one of the major inclusion types, was crucial for producing high-quality IN718 bulk, and oxygen level should be less than 3ppm to minimise the oxides precipitation at temperatures above the liquidus [14]. However, WAAM is an open building process, and the environment contains sufficient oxygen; even when using additional global shielding [15], the oxygen level can still be above a few hundred ppm. WAAM features a big melt pool, slow cooling rate (as compared to PBF process, and limited heat conduction route; besides, the low thermal conductivity of IN718 (11.4 W/mK [16]) leads to more prolonged exposure time of the high-temperature deposit to the surrounding environment, all of which makes oxidation during WAAM IN718 inevitable. In WAAM maraging steel, oxides were found to be dispersed inside the bulk and resulted in the decrease in elongation [17]. IN718, in particular, is known to be sensitive to an oxidation assisted crack growth mechanism [18], and the oxide film in IN718 has poor wetting with the parent metal and could contribute to a lack of bonding or a crack [19]. So far, it is not clear if the oxides would enter the bulk during WAAM process of IN718 and effect of oxides on the mechanical properties of WAAM IN718 is yet to be investigated.

The feedstock can be another source of inclusions. In laser-powder based AM process, the powder source was reported to influence the product quality: Zhao et al. [20] deposited IN718 using gas atomized (GA) and plasma rotation electrode preparation (PREP) powders respectively and found that the former gave lower ductility due to the hollow particles resulting in porosities in the as-

deposited material. In the case of WAAM, the feedstock wire currently used is an off-the-shelf product which is commercially designed for welding purposes [8]. Wires provided by various suppliers may have slightly different chemical compositions and contain different level of defects. As an age hardenable alloy, the content of the hardening constituents in IN718 determines the upper limit of the quantity of the precipitates that can form in the metallurgical system, which further determines the age hardening effect and the overall mechanical properties. Hence, the effect of wires from different suppliers on the mechanical properties of the WAAM IN718 was investigated.

Heat treatment is a key requirement for IN718 in order to achieve optimum properties. IN718 gains high strength through the precipitation of various secondary phases into the austenitic matrix (γ phase) at a temperature range of 593-816°C. The most common phases include γ′ ($Ni_3(Al,Ti)$), γ" (Ni_3Nb) and metal carbides (MC, $M_{23}C_6$, M_6C, M_7C_3). The WAAM alloy usually has a different microstructure from the wrought alloy owing to its inherently different thermal history. Therefore, it is necessary to understand how various phases precipitate and distribute during the WAAM process and the resultant effect on the mechanical behaviour of WAAM IN718. Also, the response of WAAM microstructure to the standard heat treatment needs to be investigated.

Hence, this paper reports on the effect of key factors in WAAM process, including oxides formation, wire variations and heat treatment, on the mechanical properties of WAAM IN718. A comparison will be made between the IN718 produced by WAAM, laser-powder based AM and wrought process.

7.2 Experimental

7.2.1 Setup and deposition procedures

Fig. 7-1 shows the WAAM setup for IN718 deposition. The system consisted mainly of a CMT power source (Fronius, VR 7000), a CMT torch, a wire feeder and a 6-axis ABB robot for controlling the deposition path.

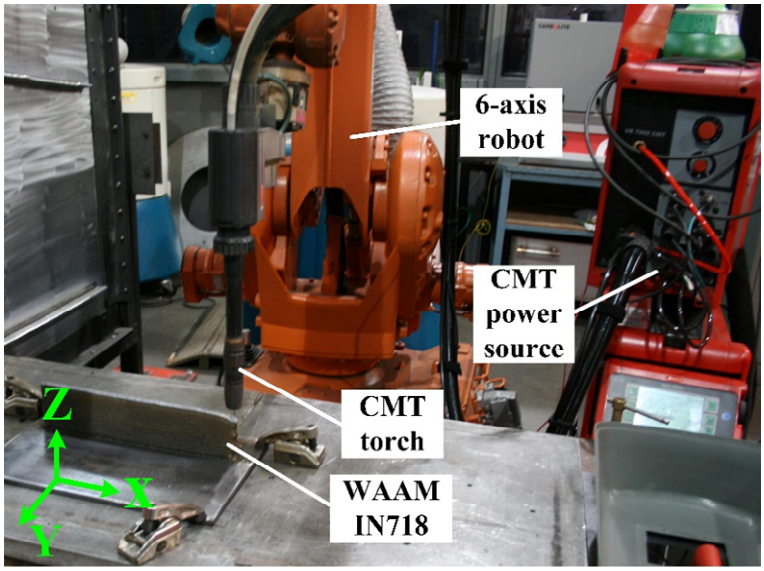

Figure 7-1 Experimental setup of the CMT-WAAM system (X-along wall length, Z-along wall height).

For oxides study, two comparative linear wall structures (54 layers) were deposited: one built in a normal layer-by-layer manner regardless of oxides formation; the other was applied mechanical grinding using an angle grinder to completely remove the oxide layer formed on the top deposit before the next deposition. The wire used for this study is labelled Wire A (1.2mm, conforming to AMS5832E). Deposition parameters are as follows: CTWD=14mm, WFS=7m/min, TS=6mm/s, shielding gas flow rate=15l/min, and interpass cooling time=3mins.

For wire source study, Wire B (1.2mm, conforming to AMS 5832) from a different supplier was used to deposit the third wall with identical process parameters. No interpass grinding was applied. The elemental composition of the wires was measured using energy dispersive spectrometry (EDS); to minimise the measurement error, the entire transverse cross-section of the wire was divided into ten segments, and a full EDS analysis was carried out for each segment to compute the average elemental composition, as shown in Table 7-1.

Table 7-1 Elemental composition of the wires (wt. %).

	Ni	Cr	Nb+Ta	Mo	Ti	Al	Co	Mn	Fe
Wire A	52.3	18.81	5.33	3.2	0.96	0.53	0.35	0.15	Balance
Wire B	53.15	19.42	5.22	2.95	0.96	0.47	0.41	0.11	Balance

7.2.2 Heat treatment

The industrial standard heat treatment conforming to Aerospace Material Specifications (AMS) was applied to WAAM IN718, as described in Table 7-2. Before solution treatment, all samples underwent a 10mins ultrasonic bath in acetone for degreasing; then samples were thoroughly rinsed using clean water and dried before putting into the furnace. A piece of wrought IN718 alloy conforming to AMS 5596 specification was applied the identical heat treatment for comparison. The thermal history of the samples during heat treatment was monitored by attaching a thermal couple to a sample, and an oscilloscope (Yokogawa DL750 ScopeCorder) was used to record the temperature data (sample rate 5S/s).

Table 7-2 Heat treating procedure applied in this study (AMS-5662M for forged IN718).

Step 1-Solution	hold at 970-980°C for 1h
Step 2-Aging	hold at 718°C for 8h; furnace cool to 620°C, hold for 8h

7.2.3 Analytical methods

Samples were cross-sectioned, mounted, ground, and polished before further analysis. The microstructure was revealed by electrolytic etching in 10% oxalic acid solution using 6V for 10s. Morphology of oxides, grain boundaries and secondary phases was observed using an optical microscope (OM) and scanning electron microscopy (SEM, FEI XL30-SFEG). EDS (Oxford Instrument) was used for elemental analysis, and electron back-scatter diffraction (EBSD) analysis was applied to characterise the grain structure. Microhardness test was performed using Zwick/Roell hardness tester under a load of 1 kg and holding time of 15s.

Tensile test coupons were extracted along both horizontal (X) and vertical direction (Z) using the material leaving out 20mm from both ends and 10mm from the top and the substrate. Machining was carried out after heat treatment. The dog-bones are prepared according to BS EN 2002-1:2005 standard in a non-proportional manner with a gauge length of 24mm, as shown in Fig. 7-2. The room temperature tensile test was conducted on an Instron 5500R electromechanical testing machine with a load cell of 100kN and a crosshead speed of 1mm/min. For each condition, at least three samples were tested.

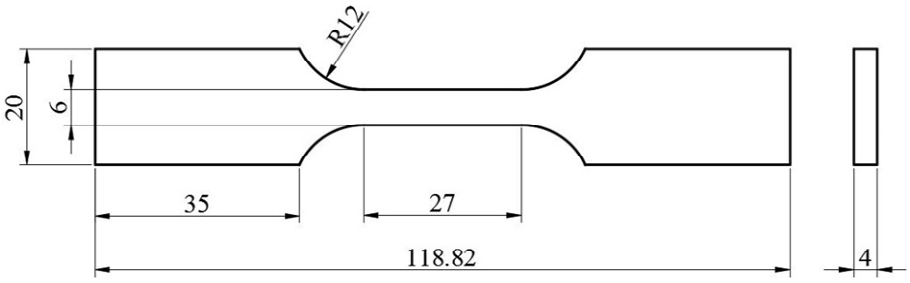

Figure 7-2 Tensile coupon dimensions.

7.3 Results

7.3.1 Effect of oxides

7.3.1.1 Oxides formation and accumulation

Fig. 7-3a shows the comparison of the top deposit before and after mechanical grinding; after grinding the oxide layer is entirely removed and the shining fresh alloy is exposed for the next deposition. Fig. 7-3b shows numerous discrete oxide islands formed immediately after one more deposition on the oxide-free surface. As can be seen, the oxides formation is so active that one deposition is enough to produce oxides that almost entirely cover the top deposit. The left side in Fig. 7-3a shows the final oxide layer formed on the top deposit in the normally built wall (without intermediate grinding): the discrete oxide islands observed in Fig. 7-3b are replaced by an entire thin oxide layer which is very smooth and coherent to the pure alloy.

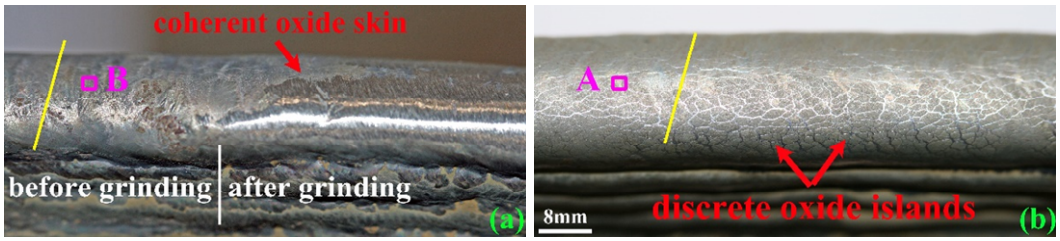

Figure 7-3 (a) Final oxide layer formed on the topmost deposit in the normally built WAAM IN718 wall (b) oxide islands formed after one deposition on the oxide-free surface.

Fig. 7-4 shows the SEM images of Zone A and B in Fig. 7-3, representing the morphology of the oxide layer when it forms after one deposition and after 54 times deposition respectively. In the oxide layer formed after one layer deposition (Fig. 7-4a), numerous individual oxides particles of complex compositions (Area C in Table 7-3) are observed and do not fully cover the surface of the pure metal (Area D in Fig. 7-4a). By contrast, after 54 layers deposition, the oxides join together to form a dense and smooth skin showing a networked morphology (Zone E in Table 7-3), which fully covers the pure alloy.

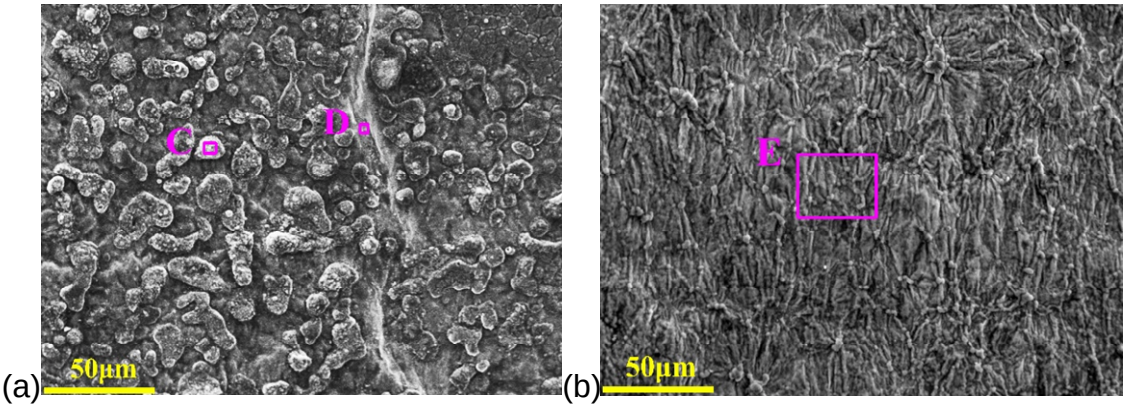

Figure 7-4 SEM images of Zone A and B in Fig. 7-3 showing the oxides morphology (a) Zone A (b) Zone B.

Fig. 7-5 compares the thickness of the oxide layer near the top of the wall shown in Fig. 7-3. In the oxide layer formed after one deposition (Fig. 7-5b), discrete oxide islands are observed with a random thickness, and some could reach up to 2μm. After 54 layers of deposition, the uniform oxide layer possesses a thickness

of around 0.5μm, indicating that there is no oxide accumulation happening during the layer-by-layer deposition process.

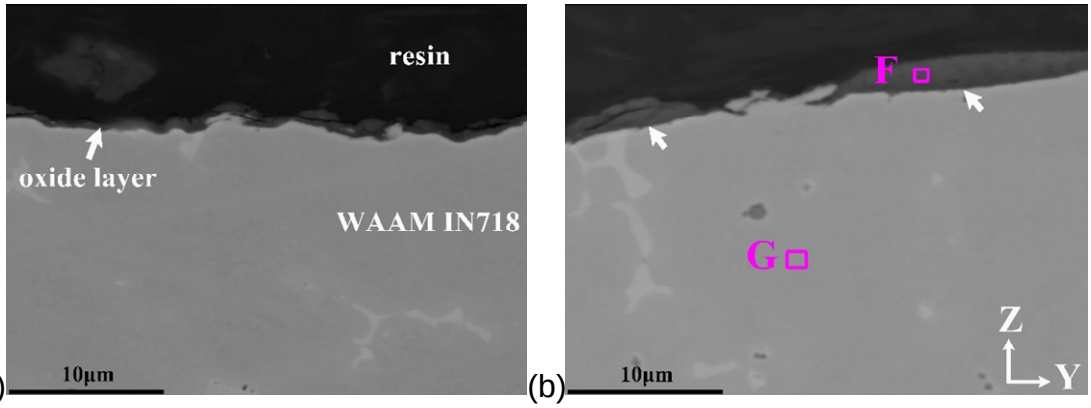

Figure 7-5 SEM images of the oxide layer at the top of the walls shown in Fig. 7-3 (yellow line in Fig. 7-3 indicates the sectioning position) (a) wall in Fig. 7-3a (b) wall in Fig. 7-3b.

Table 7-3 EDS results of the selected areas (wt. %).

	O	Al	Si	Ti	Cr	Fe	Ni	Nb	Mo
C	35.79	17.69	0.24	15.83	8.75	5.66	13.9	2.13	-
D	15.06	12.55	-	3.84	13.71	13.25	35.83	3.73	2.02
E	28.37	21.39	-	4.11	8.39	7.4	21.68	8.65	-
F	39.6	41.44	0.49	5.83	3.07	1.89	5.02	3.19	-
G	-	0.63	0.18	0.89	19.64	18.66	53.15	4.08	2.77

Fig. 7-6 shows the microhardness variation of the two comparative walls measured from the top towards the substrate. Despite the small fluctuation, the microhardness of the two walls is generally identical along the height direction with a negligible average value difference of 1HV, which indicates that oxides are very unlikely to be embedded in the matrix and harden the matrix.

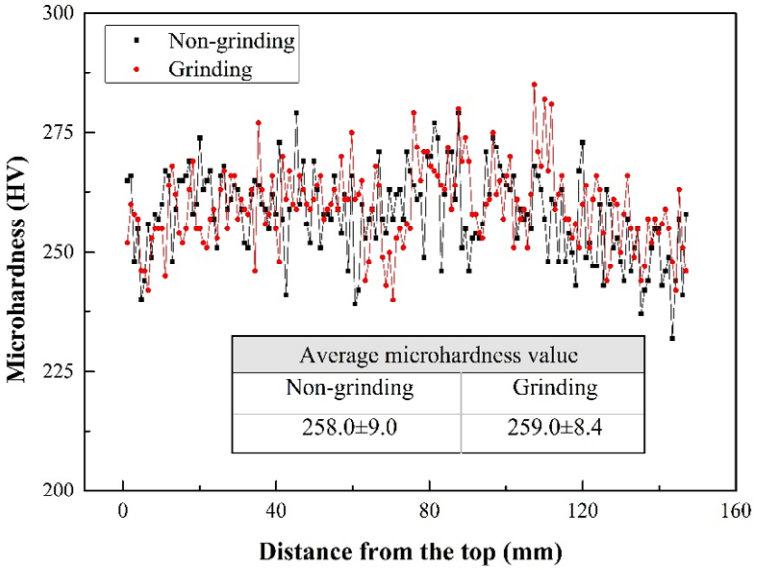

Figure 7-6 Microhardness of the two comparative walls built with and without grinding.

7.3.1.2 Mechanical properties

Fig. 7-7 shows the as deposited WAAM IN718 wall structure and the location where the tensile samples were extracted. The sample position numbering was applied to both walls. A detailed comparison of the tensile test results is presented in Fig. 7-8 and Table 7-4. From Fig. 7-8, it is found that at each corresponding position, the UTS, 0.2%YS and elongation value for the two walls are almost the same. From Table 7-4, after grinding each layer, the change in the average UTS, 0.2%YS and elongation is also negligible.

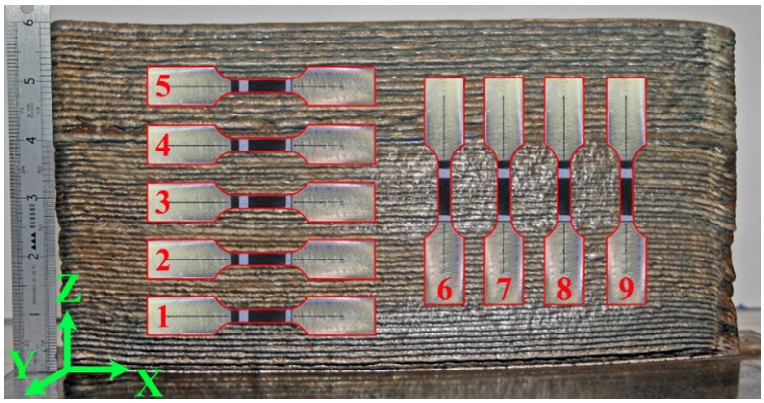

Figure 7-7 WAAM IN718 wall structure and the sample extraction positions.

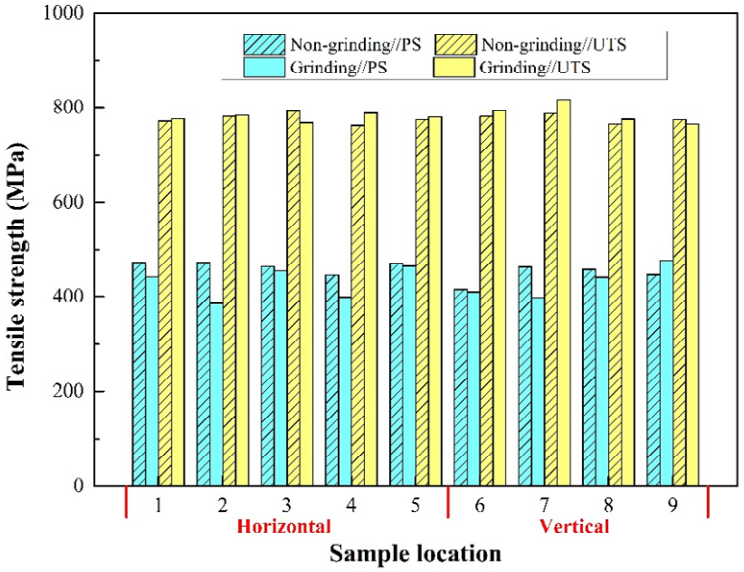

(a)

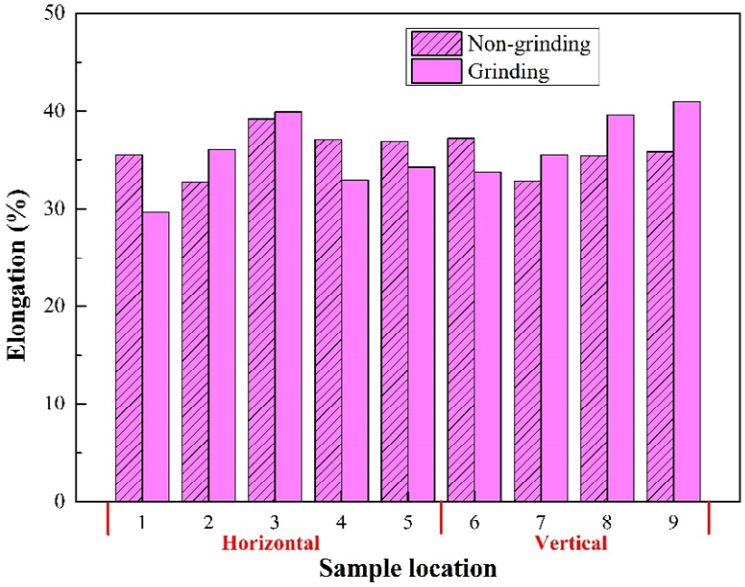

(b)

Figure 7-8 Mechanical testing results of the walls deposited with and without interpass grinding (a) UTS and 0.2%YS (b) elongation.

Table 7-4 Tensile test results of the WAAM IN718 on average.

			UTS / MPa		0.2%YS / MPa		Elongation / %	
			H	V	H	V	H	V
WAAM-AD	Wire A	Non-grinding	776±10	777±8	466±10	446±19	36.3±2.1	35.3±1.6
		Grinding	779±7	787±19	429±31	431±31	34.6±3.4	37.5±2.9
	Wire B	Non-grinding	824±15	832	514±17	416	34.0±0	30.9
WAAM-SA	Wire B	Non-grinding	1110±3	1233±16	807±1	889±5	15.5±0.3	19.4±2.8

AD-as deposited; SA-solution plus aging; H-horizontal; V-vertical.

7.3.2 Effect of wire

Table 7-4 also presents the tensile properties of WAAM IN718 deposited using two different wires. As can be seen, the average UTS obtained using Wire B is 48MPa and 55MPa higher than using Wire A in the horizontal and vertical direction respectively, but the elongation achieved is 2.3% and 4.4% lower respectively. Both UTS values are inferior to the casting standard (862MPa, see Table 7-5), but the ductility is considerably superior to the castings.

7.3.3 Effect of heat treatment

Fig. 7-9 shows the thermal history recorded during heat treatment. The real temperature for solution and double aging is 966.1°C, 713.3°C and 616.6°C respectively, which generally complies with the standard shown in Table 7-2.

From Table 7-4, the heat treatment results in a 286MPa (increased by 34.7%) and 401MPa (increased by 48.2%) increase in UTS along the horizontal and vertical direction respectively; while the elongation is observed an 18.5% and 11.5% decrease respectively. The highest individual UTS obtained is in the vertical direction, being 1248MPa which is very close to the wrought alloy (1276 MPa); however, the average strength of the heat treated WAAM IN718 is 105MPa lower than the wrought alloy.

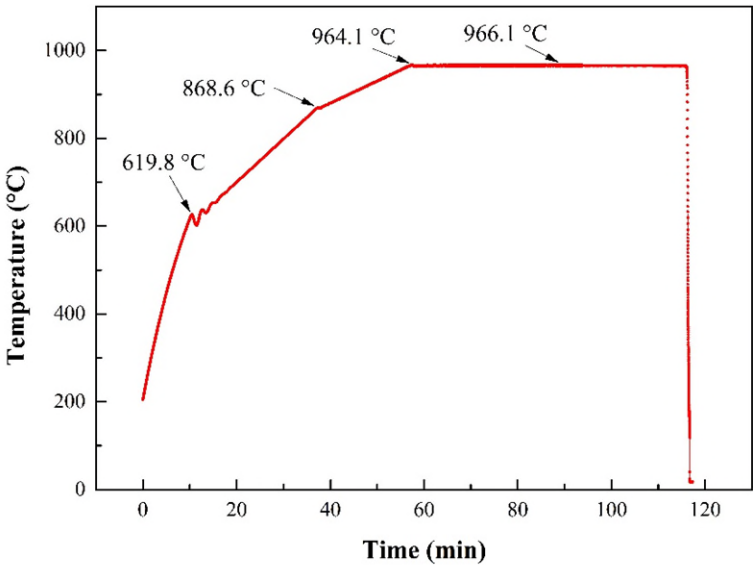

(a)

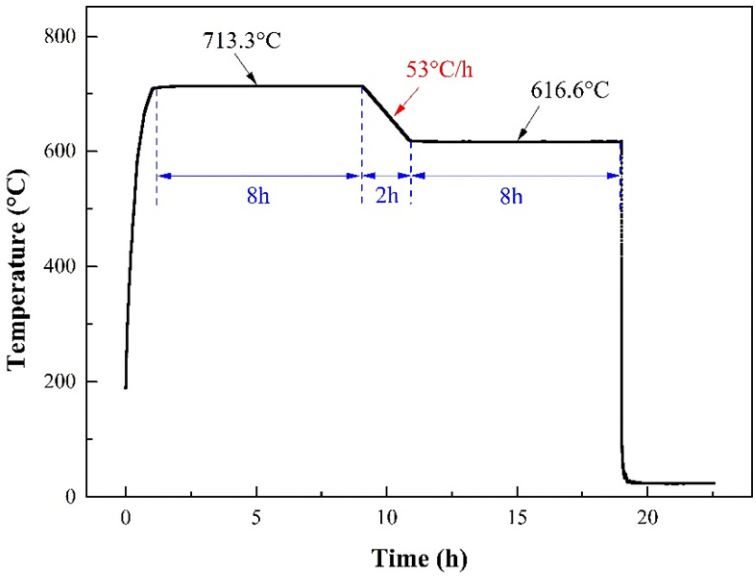

(b)

Figure 7-9 Real thermal history during heat treatment (a) solution (b) aging.

7.4 Discussion

7.4.1 Oxides characteristics

From Fig. 7-5b and Table 7-3 (Area F), the oxides formed in WAAM IN718 are mostly a mixture of Al (41.44 wt.%) and Cr (3.07 wt.%) oxides (Al_2O_3 and Cr_2O_3 according to [21]), and Mo is absent in oxides. IN718 essentially gains oxidation resistance through a passivation process, i.e., the formation of a protective Chromia (Cr_2O_3) scale. Though at the temperature higher than 1000°C the formation of volatile Cr_2O_3 results in a loss of the protective scale [22], the Al_2O_3 provides adequate oxidation resistance since Al_2O_3 resists spalling at temperatures up to 1300-1350°C [21]. Since oxides are of a lower density than the pure metal, they flow onto the top of the melt pool upon formation and solidify as a protective shell to prevent successive oxides from formation. When there is only one deposition, the oxides form as discrete islands and the quantity is not enough to fully cover the top deposit; the gaps between these islands expose the pure alloy to oxygen upon successive depositions to allow more oxides formation until they join together and firstly fully cover the top deposit to prevent further oxides formation. Due to the lack of ongoing oxides formation, no oxide accumulation is observed during the WAAM of IN718. Besides, the characteristic

of oxides in IN718 being dense prohibits oxygen diffusion through the oxide layer to the parent metal; thereby oxides are not found inside the bulk.

7.4.2 Uncertainties from the wire

From Table 7-1, the elemental composition varies slightly between suppliers, with Wire B having a slightly lower content of Nb and Al. The content of alloying elements, especially the hardening constituents, is critical for age-hardenable alloys when strength is of interest. For some alloying systems, even slight difference in element composition could make a difference to the strengthening effect. In IN718, for example, Radhakrishna and Prasad Rao [23] reported that reducing Nb content in the wire helped control the Laves phase formation and ease the homogenization process.

There could also be uncertainties in non-metallic inclusions in the wire. The thermochemistry of IN718 results in two types of inclusions, TiN and Al_2O_3, which not only influence the mechanical properties but also the solidification structure [24]; the prior-existing TiN particles act as the principal nucleation sites for NbC (which is usually an undesired carbide [25]) during solidification since they are isomorphous [26]. Fig. 7-10 shows a TiN inclusion (the dark phase) observed in Wire B. The same type of inclusion is also observed in Wire A. Fig. 7-11 presents the inclusion found in the fracture surface of the WAAM IN718 built using Wire B, which is identified as TiN through EDS analysis and proves that the inclusions also go into the WAAM alloy.

The different mechanical properties using different wires are most likely due to the compositional difference (possibly Nb) since a strength increase and ductility decrease are both observed when using Wire B; defects, such as inclusions, usually results in a reduction in both properties. However, the extreme complexity in the IN718 metallurgy makes it difficult to directly correlate the slight variations in wire composition and TiN inclusion content with the mechanical behaviour; also, accurately quantifying the variations between the wires is difficult given that there could be significant variations along the length of the wire. The present results indicate that the wire source could be a key factor that affects the mechanical properties of the WAAM alloy, which is possibly because wires from

different manufacturers do not have an identical chemical composition and inclusion level.

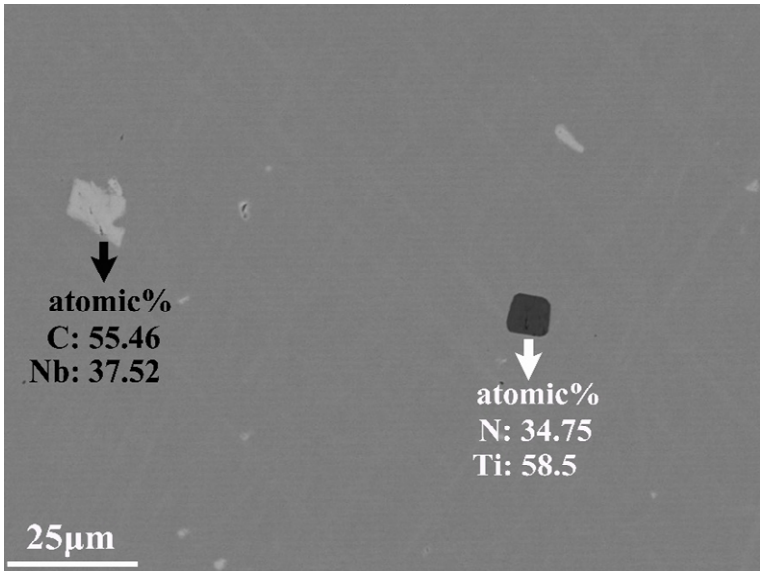

Figure 7-10 Inclusions observed in Wire B.

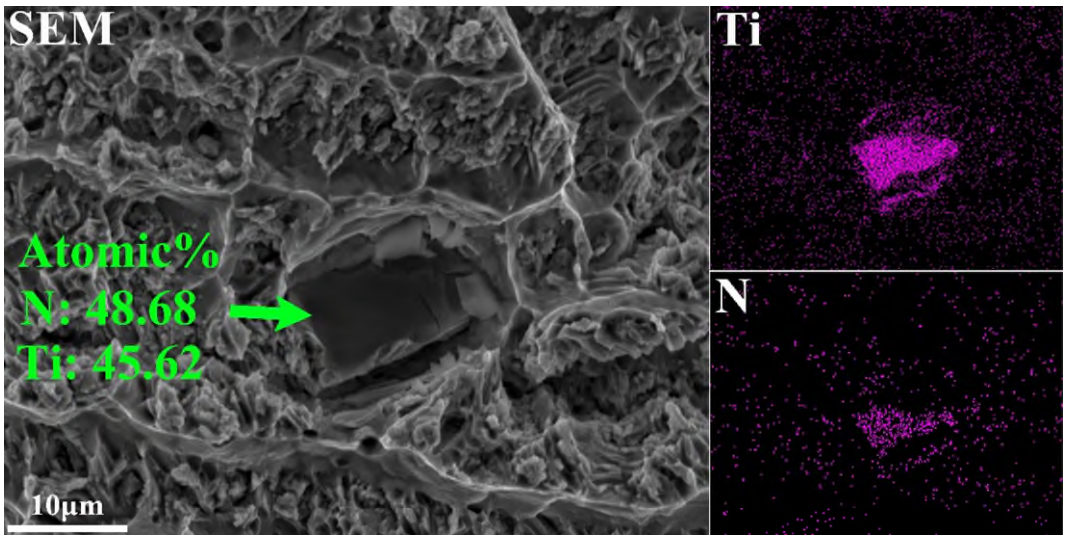

Figure 7-11 TiN inclusion found in the fracture surface of the WAAM IN718 built using Wire B.

7.4.3 Mechanical properties

7.4.3.1 Comparison with other AM products

Table 7-5 summarises the mechanical properties of IN718 obtained using various AM processes. The WAAM IN718 possesses essentially the same strength as

shaped metal deposition (SMD, using gas tungsten arc process) product, but the elongation is much higher (32.9% against 28%), which is possibly due to the different heat input, wire variations and tensile coupon design (bar with the dimension of 25×8×3mm, gauge length 25mm [11]). In the as deposited condition, the strength of WAAM IN718 is slightly lower than the casting (827MPa against 862MPa), but the ductility is considerably higher (32.9% against 5%). The strength of laser-powder AM IN718 varies among literature but is generally higher than the WAAM alloy in the as deposited condition: the DMD process produces slightly higher strength (847MPa [6] and 904MPa [2] against 827MPa), and the PBF process gives significantly better strength (1126MPa [3] against 827MPa). In comparison with all the literature, WAAM IN718 generally possesses the highest ductility, which is due to the slower cooling rate as compared to laser-powder based process [11].

After solution plus aging, the UTS of WAAM IN718 is 105MPa lower than the wrought alloy. However, when the same heat treatment was applied to laser-powder AM IN718, the resultant strength is superior to WAAM alloy, being 1221MPa [2], 1371MPa [3] and 1430MPa [7] against 1171MPa. Note that the wrought standard is 1276MPa, so the heat treatment generally works well for PBF IN718, but less effective for DMD product [2].

Table 7-5 Comparison of the strength of IN718 produced by various AM process (on average).

	UTS / MPa	0.2%YS / MPa	Elongation / %
WAAM*-AD	827±13	482±48	32.9±1.5
WAAM*-SA	1171±62	848±41	17.4±2.8
SMD-AD [11]	828±8	473±6	28±2
DMD-AD [6]	847	525	29
DMD-AD [2]	904	552	16.2
DMD-SA [2]	1221	1007	16
PBF-AD [3]	1126	849	22.8
PBF-SA [3]	1371	1084	10.1
PBF-SA [7]	1430	1185	18.6
Casting AMS5383	862	758	5
Wrought AMS5662	1276	1034	12

* *using Wire B*

7.4.3.2 Explanation of the inferior mechanical properties

The mechanical properties of IN718 are determined by the austenite grain size and the content, morphology and size of the precipitates [27]. These aspects are discussed as follows.

7.4.3.2.1 Grain morphology

Since the precipitation behaviour during heat treatment is determined by the starting grain structure, it is relevant to compare the grain structure of the as deposited WAAM IN718 with the wrought alloy, as shown in Fig. 7-12. The WAAM alloy shows columnar grain boundaries typical of the WAAM process, as indicated by the green arrows in Fig. 7-12a (grain boundary depicted for better visibility); the thickness of the columnar grain can be as big as 200 µm at the half height position of the wall structure. The same large columnar grain structure is also observed in WAAM Ti6Al4V as a result of the epitaxial growth due to the directional heat flow [28]. In contrast, the wrought alloy shows a finely equiaxed grain structure with the average grain size of 7.5 (ASTM E112, 26.7 µm). Fig. 7-13 presents the EBSD grain map of the as deposited WAAM IN718 wall structure

right above the substrate; numerous columnar grains show a directional growth along the building direction (Z) which is also the heat flow direction. Thanks to the higher cooling rate due to the presence of the substrate, the columnar grains are smaller as compared to those observed at the half height (Fig. 7-12a), with the thickness varying between 50-150μm and the length being comparable to the whole map.

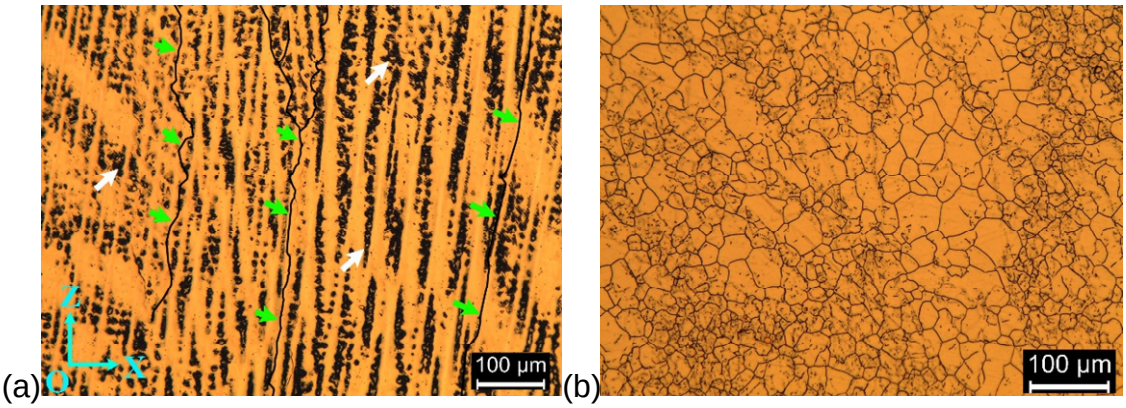

Figure 7-12 Grain boundaries of IN718 produced by WAAM and wrought process (a) WAAM (as deposited, half height of the wall) (b) wrought (solutionized).

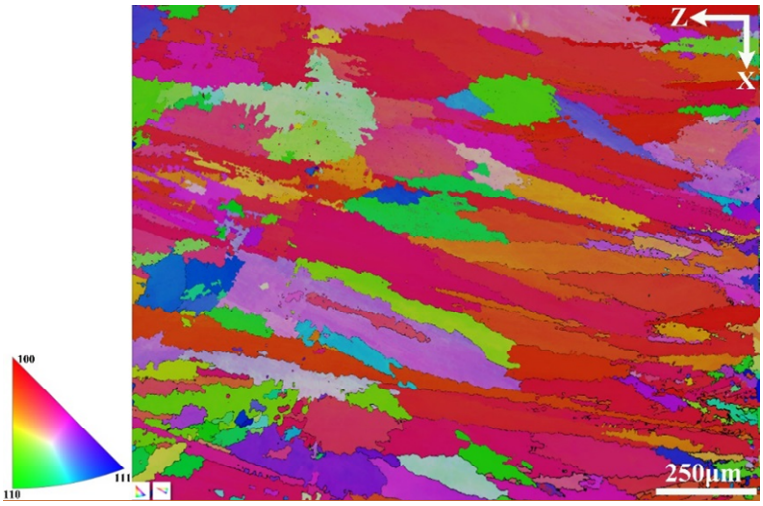

Figure 7-13 EBSD orientation map showing the columnar grains near the bottom of the WAAM IN718 wall structure in the as deposited condition.

After solution treatment, the WAAM grain structure ready for subsequent aging is much coarser as compared to the as deposited alloy in Fig. 7-12a. So the grains have greater thickness and less grain boundary area compared to the wrought alloy. The superiority of the PBF IN718 in the heat treated condition compared to

the wrought material was due to the fine grains and small dendrite arm spacing resulting from the high cooling rate [2]; according to [7], the grain size (around 4μm) was 10 times and 100 times finer than the forged (around 50μm) and cast (around 800μm) microstructure respectively. Note that precipitation of the secondary phases at the grain boundaries is more effective in strengthening; the lack of grain boundaries in WAAM IN718 due to the large columnar grains makes such precipitation less likely to happen, as compared with the finely equiaxed grains in the wrought alloy.

7.4.3.2.2 Precipitates

As has been reported [29], the chemical composition, distribution, location and possible coagulation during the thermal and mechanical treatments are decisive in the microstructural and mechanical properties development in IN718.

Fig. 7-14 presents the SEM micrographs of the precipitates formed in response to the heat treatment. In wrought IN718 (Fig. 7-14b), the nanosized precipitates are found to embed and disperse uniformly throughout the matrix. Particularly at the grain boundaries, the hardening phases are observed to precipitate in either spherical shape or needle shape (indicated by pink arrows in Fig. 7-14b) with the length filling and orienting along the grain boundary, which serves as the impediment of grain boundary migration to strengthen the material.

In contrast, the precipitates in WAAM 718 are found to be of different morphology and distribute much less uniformly. After heat treatment, most of the Laves phase has been transformed to the acicular δ phase which tends to cluster where the previous Laves phase is located and shows an overall directional distribution. Numerous secondary phase islands (indicated by yellow arrows in Fig. 7-14a) as big as 10μm are observed which are complex mixtures of the newly formed precipitates (δ phase and metal carbides) and the untransformed Laves phase [2]. Besides, no obvious grain boundaries are observed even at a low magnification (Fig. 7-14a).

The formation of the Laves phase, δ, and γ′+γ" requires 10-12%, 6-8%, 4% or below of Nb respectively [2]. Therefore, the residual Laves phase and formation

of δ phase depleted the Nb needed for precipitating the desired γ′ and γ" phases. The incoherent δ phase does not contribute to the strengthening [2] and the presence of Laves phase is reported to aid in the crack initiation and propagation due to their brittle nature [23].

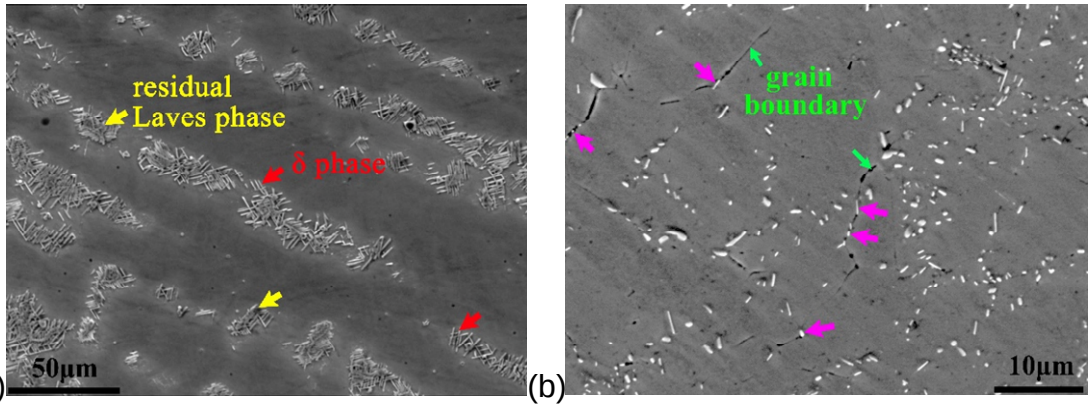

(a) (b)

Figure 7-14 SEM images showing the precipitates morphology and distribution in WAAM IN718 and wrought IN718 after aging (a) WAAM (b) wrought.

7.4.3.2.3 Heat treating standard

IN718 derives excellent mechanical properties from precipitation hardening, and the hardening effect of the precipitates depends on their type, quantity, morphology, size, and location, which is a result of the heat treatment (time, temperature and cooling method) and the starting grain structure. For proper aging to take place, the aging constituents (Al, Ti, and Nb) must be in solution first; if they are precipitated as some other phase, the full strength will not be attained. As has been reported [1], the heat treating procedure applied in the present study produces the highest room-temperature tensile strength of wrought IN718. Many variants of this procedure have been developed to suit different starting grain structure. For example, homogenisation (see Table 7-6) is applied before SA in cast IN718 to minimise the elemental segregation and dissolve undesired phases, and HIPing is adopted before SA in DMD process to eliminate the unmelted powder particles and porosity [5]. Even though various heat treatment gives different mechanical behaviour, simply applying a different heat treatment would not make a difference in this study for the following two reasons.

Firstly, the starting grain structure cannot be improved simply by heating when mechanical working is absent. A finely equiaxed grain structure is desired for good mechanical behaviour; however, the WAAM alloy features larger columnar grains which, when heated to high temperature and held for some period will only to coarsen. The resultant grain structure is still not favourable for subsequent heat treatment.

Secondly, eliminating the Laves phase and avoiding grain coarsening is contradictory. On the one hand, Nb and Mo segregation are inevitable during the solidification process due to the inherent thermal conduction and non-equilibrium thermal cycles experienced in WAAM, which leads to the formation of detrimental Laves phase at the interdendritic area [30]. On the other hand, the normal solution temperature is not high enough to promote sufficient Nb diffusion and dissolve the Laves phase, as has been shown in Fig. 7-14a; the aging temperatures are only designed to precipitate γ′ and γ" strengthening phases in the γ matrix. In laser-powder based AM research, both homogenisation and HIPing using a higher temperature than solution treatment for a long duration (few hours) are reported to dissolve the Laves phase completely but results in considerable grain coarsening. From Table 7-6, HIPing restores the ductility but also results in a strength loss due to the grain growth [5], which is the same case when homogenisation is applied [2]. Hence, it is impossible to dissolve the undesired Laves phase without causing grain coarsening.

Segregation is less severe in laser-powder based AM process due to the fast cooling rate [5]. By contrast, Nb segregation would be more severe in the WAAM process due to the much lower cooling rate [31]. Besides, the grain size of the PBF IN718 is much smaller than the WAAM alloy; note that the DMD process has a higher heat input and lower cooling rate than the PBF, so the grains produced are also larger and the heat treatment works less effectively than the latter. These two factors make the starting grain structure different; thereby the same heat treatment procedure works better for the PBF IN718.

Table 7-6 Summary of mechanical properties of laser AM IN718 after various heat treatment.

	UTS / MPa	0.2%YS / MPa	Elongation / %
DMD-HSA [2]	1194	949	19.9
DMD-SA [5]	1436	1257	13 (reduction in area)
DMD-HIP+SA [5]	1380	1155	20.4 (reduction in area)

A-aging (without prior solution); HSA-homogenization+solution+aging (AMS-5383D for cast IN718);
Homogenization-hold at 1093°C for 1-2hrs; HIP[1]-100MPa, 1160°C for 3hrs.

7.4.4 Future work

The current study indicates that it is difficult to make the WAAM alloy microstructurally and metallurgically identical to a wrought alloy through solidification conditions and composition alone. The large columnar grains in WAAM IN718 lead to less favourable and numerous precipitates forming, which is the main reason for the strength mismatch. In future studies, process improvement based on thermomechanical processing may be considered to reduce the elemental segregation by promoting Nb diffusion and induce recrystallization to produce a larger area of high-angle grain boundaries, thereby improving the mechanical behaviour.

7.5 Conclusions

High-quality deposits free from process defects were obtained by WAAM deposition of IN718. It was found that,

1. Coherent oxides consisting of Cr_2O_3 and Al_2O_3 form so actively that with one deposition they almost fully cover the deposit; oxides don't accumulate during the layer by layer building process, ending up with only 0.5μm thick after 54 layers deposition.
2. Oxides show no effect on the mechanical properties since the protective oxide layer prevents further oxygen from entering the bulk and forming oxides in the bulk.

3. Wires from two suppliers produce a UTS difference of around 50MPa, which is most likely due to the slight difference in elemental composition.
4. The as deposited WAAM IN718 has large columnar grains with the thickness of 50-150μm near the substrate, orienting along the building direction, as opposed to the finely equiaxed grains in the wrought alloy with an average grain size of 26.7 μm.
5. The strength of the heat treated WAAM IN718 is 105MPa lower than the wrought alloy. This is mainly because the large columnar grains is not a favourable starting microstructure for heat treatment such that precipitates formed are of different types, fewer in number and less uniformly distributed compared to those found in the wrought alloy.
6. A different heat treatment by varying the time and temperature will not enhance the mechanical behaviour unless thermo-mechanical working is introduced to produce a more favourable starting microstructure.

7.6 References

[1] Special Metals, INCONEL alloy 718, in: 2007: pp. 1–28. doi:SMC-066.

[2] H. Qi, M. Azer, a. Ritter, Studies of Standard Heat Treatment Effects on Microstructure and Mechanical Properties of Laser Net Shape Manufactured INCONEL 718, Metall. Mater. Trans. A. 40 (2009) 2410–2422. doi:10.1007/s11661-009-9949-3.

[3] D. Zhang, W. Niu, X. Cao, Z. Liu, Effect of standard heat treatment on the microstructure and mechanical properties of selective laser melting manufactured Inconel 718 superalloy, Mater. Sci. Eng. A. 644 (2015) 32–40. doi:10.1016/j.msea.2015.06.021.

[4] Q. Jia, D. Gu, Selective laser melting additive manufacturing of Inconel 718 superalloy parts: Densification, microstructure and properties, J. Alloys Compd. 585 (2014) 713–721. doi:10.1016/j.jallcom.2013.09.171.

[5] P.L. Blackwell, The mechanical and microstructural characteristics of laser-deposited IN718, J. Mater. Process. Technol. 170 (2005) 240–246. doi:10.1016/j.jmatprotec.2005.05.005.

[6] C. Zhong, A. Gasser, J. Kittel, K. Wissenbach, R. Poprawe, Improvement of material performance of Inconel 718 formed by high deposition-rate laser metal deposition, Mater. Des. 98 (2016) 128–134. doi:10.1016/j.matdes.2016.03.006.

[7] T. Trosch, J. Strößner, R. Völkl, U. Glatzel, Microstructure and mechanical properties of selective laser melted Inconel 718 compared to forging and casting, Mater. Lett. 164 (2015) 428–431. doi:10.1016/j.matlet.2015.10.136.

[8] S.W. Williams, F. Martina, A.C. Addison, J. Ding, G. Pardal, P. Colegrove, Wire + Arc Additive Manufacturing, Mater. Sci. Technol. 00 (2015) 1–7. doi:10.1179/1743284715Y.0000000073.

[9] B. Cong, J. Ding, S. Williams, Effect of arc mode in cold metal transfer process on porosity of additively manufactured Al-6.3%Cu alloy, Int. J. Adv. Manuf. Technol. 76 (2014) 1593–1606. doi:10.1007/s00170-014-6346-x.

[10] D. Clark, M.R. Bache, M.T. Whittaker, Shaped metal deposition of a nickel alloy for aero engine applications, J. Mater. Process. Technol. 203 (2008) 439–448. doi:10.1016/j.jmatprotec.2007.10.051.

[11] B. Baufeld, Mechanical properties of INCONEL 718 parts manufactured by shaped metal deposition (SMD), J. Mater. Eng. Perform. 21 (2012) 1416–1421. doi:10.1007/s11665-011-0009-y.

[12] G. Asala, A.K. Khan, J. Andersson, O.A. Ojo, Microstructural Analyses of ATI 718Plus® Produced by Wire-ARC Additive Manufacturing Process, Metall. Mater. Trans. A Phys. Metall. Mater. Sci. 48 (2017) 4211–4228. doi:10.1007/s11661-017-4162-2.

[13] J. Gu, J. Ding, S.W. Williams, H. Gu, P. Ma, Y. Zhai, The effect of inter-layer cold working and post-deposition heat treatment on porosity in additively manufactured aluminum alloys, J. Mater. Process. Technol. 230 (2016) 26–34. doi:10.1016/j.jmatprotec.2015.11.006.

[14] a. Mitchell, Melting Processes and Solidification in Alloys 718-625, Superalloys 718, 625 Var. Deriv. (1991) 15–27. doi:10.7449/1991/Superalloys_1991_15_27.

[15] X. Xu, S. Ganguly, J. Ding, S. Guo, S. Williams, F. Martina, Microstructural evolution and mechanical properties of maraging steel produced by wire + arc additive manufacture process, Mater. Charact. (2017). doi:10.1016/j.matchar.2017.12.002.

[16] MatWeb Web Page, IN718 from Matweb, (n.d.). http://www.matweb.com/search/DataSheet.aspx?MatGUID=94950a2d209040a09b89952d45086134&ckck=1.

[17] X. Xu, J. Ding, S. Ganguly, C. Diao, S. Williams, Oxide accumulation effects on wire + arc layer-by-layer additive manufacture process, J. Mater. Process. Tech. 252 (2018) 739–750. doi:10.1016/j.jmatprotec.2017.10.030.

[18] R. Molins, G. Hochstetter, J.C. Chassaigne, E. Andrieu, Oxidation effects on the fatigue crack growth behaviour of alloy 718 at high temperature, Acta Mater. 45 (1997) 663–674. doi:10.1016/S1359-6454(96)00192-9.

[19] Y.N. Zhang, X. Cao, P. Wanjara, M. Medraj, Oxide films in laser additive manufactured Inconel 718, Acta Mater. 61 (2013) 6562–6576. doi:10.1016/j.actamat.2013.07.039.

[20] X. Zhao, J. Chen, X. Lin, W. Huang, Study on microstructure and mechanical properties of laser rapid forming Inconel 718, Mater. Sci. Eng. A. 478 (2008) 119–124. doi:10.1016/j.msea.2007.05.079.

[21] C.J. Wang, S.M. Chen, Microstructure and cyclic oxidation behavior of hot dip aluminized coating on Ni-base superalloy Inconel 718, Surf. Coatings Technol. 201 (2006) 3862–3866. doi:10.1016/j.surfcoat.2006.07.242.

[22] G. a. Greene, C.C. Finfrock, Oxidation of Inconel 718 in Air at High Temperatures, Oxid. Met. 55 (2001) 505–521. doi:10.1023/A:1010359815550.

[23] C.H. Radhakrishna, K. Prasad Rao, The formation and control of Laves phase in superalloy 718 welds, J. Mater. Sci. 32 (1997) 1977–1984. doi:10.1023/A:1018541915113.

[24] a. Mitchell, The Present Status of Melting Technology for Alloy 718, Superalloys 718 Metall. Appl. (1989) 1–15. doi:10.7449/1989/Superalloys_1989_1_15.

[25] ASM International, ASM Handbook: Volume 2 Properties and selection: Nonferrous alloys and special-purpose materials, 1990.

[26] A. Mitchell, Primary carbides in Alloy 718, 7th Int. Symp. Superalloy 718 Deriv. (2010) 161–167. doi:10.1002/9781118495223.ch11.

[27] C. Zonglin, W. Shaogang, L.I. Weihong, Quantitative Phase Analysis of Inconel 718 by X-ray Diffraction, J. Mater. Sci. Lett. 16 (1997) 769–771. doi:10.1023/A:1018553703030.

[28] F. Martina, P.A. Colegrove, S.W. Williams, J. Meyer, Microstructure of Interpass Rolled Wire + Arc Additive Manufacturing Ti-6Al-4V Components, Metall. Mater. Trans. A Phys. Metall. Mater. Sci. 46 (2015) 6103–6118. doi:10.1007/s11661-015-3172-1.

[29] A.J. Brand, K. Karhausen, R. Kopp, Microstructural simulation of nickel base alloy Incone* 718 in production of turbine discs, Mater. Sci. Technol. 12 (1996) 963–969. doi:https://doi.org/10.1179/mst.1996.12.11.963.

[30] H. Xiao, S. Li, X. Han, J. Mazumder, L. Song, Laves phase control of Inconel 718 alloy using quasi-continuous-wave laser additive manufacturing, Mater. Des. 122 (2017) 330–339. doi:10.1016/j.matdes.2017.03.004.

[31] G.D.J. Ram, A.V. Reddy, K.P. Rao, G.M. Reddy, Microstructure and mechanical properties of Inconel 718 electron beam welds, Mater. Sci. Technol. 21 (2005) 1132–1138. doi:10.1179/174328405X62260.

8 Enhancing mechanical properties of wire + arc additively manufactured INCONEL 718 superalloy through interpass rolling

This chapter is based on the following submission.

X. Xu*, *S. Ganguly, J. Ding, C. Seow, S. Williams, Enhancing mechanical properties of wire + arc additively manufactured INCONEL 718 superalloy through in-process thermomechanical processing, Mater. Des. (Revise)*

From Chapter 7, the inferior mechanical properties of the heat treated WAAM IN718 to the wrought alloy is attributed to the grain structure. The key to improving the mechanical properties is to change the grain structure. This chapter presented the subsequent work of introducing interpass rolling to enhance the mechanical properties of WAAM IN718.

Abstract: Plasma arc and wire based additive manufacture was applied to produce INCONEL 718 superalloy (IN718) components in a layer by layer manner; further, interpass cold rolling was introduced to the deposition process. Mechanical testing showed that with rolling applied, the strength of the solution plus aging treated WAAM IN718 was improved from 1056MPa (unrolled) to 1351MPa (rolled) which met the wrought standard (1276MPa), and the material anisotropy was eliminated. The unrolled IN718 featured large columnar grains developing along the building direction, with the length and width as great as 11mm and 0.8mm respectively; rolling induced plastic deformation triggered a non-uniform recrystallization upon successive depositions, which produced a recrystallized core with small columnar grains and massive finely equiaxed grains with the grain size of 12.7μm. The overall strengthening produced by interpass rolling was attributed mostly (76%) to the rolling induced recrystallization which produced grain size reduction strengthening and created larger grain boundary area to allow more precipitation at the grain boundaries, and partially (24%) due to the improved aging response of the recrystallized grain structure.

Keywords: INCONEL 718; wire + arc additive manufacture; thermomechanical processing; mechanical properties; recrystallization.

8.1 Introduction

INCONEL 718 superalloy (IN718) is a precipitation hardenable Ni-based alloy outstanding for its capability of retaining mechanical properties at elevated temperatures [1]. The combination of excellent tensile and creep strength, corrosion resistance, and weldability makes IN718 the most widely used superalloy in today's turbine engine applications, accounting for 55-70% of the Ni-base superalloys in modern jet engines [2] and more than 30% of the total weight [3].

IN718 gains high strength through the precipitation of a wide variety of secondary phases into the austenitic matrix (γ phase). The most common secondary phases include γ" (Ni_3Nb, ordered bct D022 structure), γ′ ($Ni_3(Al,Ti)$, L12 structure) and metal carbides. In terms of volume (16% [3]) and influence, the primary strengthening phase is γ", a lens-like disc-shaped/needle-shaped precipitate with the size of 30-50nm; besides, a small volume fraction (4%vol. [3]) of γ′, a cubic or spherically shaped precipitate with the size of 50-100nm [4], is also reported to affect the microstructure stability [5]. If the hardening constituents are precipitated as other phases or are combined in other forms, the full strength of IN718 will not be attained [6]; therefore, other phases such as Laves phase and δ phase (Ni_3Nb, orthorhombic), which form due to the variations in composition, processing or high-temperature exposure [7], are undesirable.

IN718 is an expensive alloy and its machining remains a challenge. The inherent characteristics, such as high work hardening rate, low thermal conductivity, adherence to the cutting edge and presence of abrasive carbides, make the machining difficult since high temperature and stress are generated at the tool-workpiece interface to result in short tool life and metallurgical damage to the workpiece [8]. Therefore, cost-effective manufacturing methods are required to reduce material wastage and ease the machining process. Metal additive manufacture (AM) [9] provides the above benefits by building near-net-shape components in a layer by layer manner. So far, AM research on IN718 is mainly focused on various laser-powder processes: the powder bed fusion process could produce IN718 with equivalent or superior mechanical properties than

wrought alloy due to the fast cooling rate induced fine grains [1,10]; while the blown powder process produced IN718 with comparable or slightly inferior strength [3,11] due to the relatively high heat input.

Wire + arc additive manufacture (WAAM) [12], which adopts the electric arc as the heat source and the commercial welding wire as the feedstock [13–15], is outstanding for its low equipment cost, high building rate and large-scale (meters scale) product. In contrast to the laser-powder based AM process, there is very few research on WAAM of IN718. So far, limited trials have been carried out using tungsten inert gas (TIG) [2,16] or metal inert gas (MIG) [17] which prove the feasibility to deposit simple features using WAAM; however, plasma arc has not been applied to deposit IN718 and the heat treatment response of the WAAM IN718 is yet to be studied.

In this paper, the plasma arc based WAAM process was applied to produce IN718 components and a complete microstructure and mechanical properties study was carried out to understand the relationship between the WAAM microstructure and the macro properties. Furthermore, in process interpass rolling was applied to the layer by layer deposition process, aiming to improve the microstructure of the WAAM IN718 and thereby the mechanical properties to the level comparable to the wrought alloy.

8.2 Experimental

8.2.1 Rolling-WAAM system and deposition procedure

The in-process thermomechanical processing assisted WAAM process is realized by integrating two subsystems: WAAM deposition system and cold rolling system, as shown in Fig. 8-1a. The former deploys a plasma arc (power source: Fronius TransTig 5000) as the heat source, and a 3-axis CNC gantry system is used to control the deposition path. The chemical composition of the 1.2mm IN718 wire is listed in Table 8-1. A laminar flow local shielding device developed at Cranfield University [18] is attached around the torch to provide additional shielding to the deposits (purified Ar, flow rate 200 l/min). The latter consists of a rigid flat roller (diameter 100mm, width 20mm) and a hydraulic cylinder through

which the force could be loaded to induce plastic deformation in the top deposit; the motion of the rolling system is controlled by the same CNC system and is aligned with the deposition path.

To study the effect of an individual rolling pass on the deposit, a 5-layer single pass wall structure was deposited, then only the top deposit was applied one pass of cold rolling with 50kN and 75kN respectively, as shown in Fig. 8-1b. To evaluate the overall effectiveness of rolling on improving the mechanical properties of WAAM IN718, two comparative linear wall structures (Length: 400mm, Height: 134mm) were deposited: the first was deposited in a normal layer-by-layer manner; whilst the second was applied 75kN interpass cold rolling (hereinafter, rolling or rolled), i.e., rolling and deposition took place in turns so that the deposition was always on a plastically deformed deposit. Each rolling was applied 2 mins after the deposition finished. All depositions were along X axis (see Fig. 8-1a). The process parameters were kept consistent: CTWD=8mm, Current=180A, WFS=4m/min, torch TS=7.5m/min, roller TS=2m/min, plasma Ar flow rate=0.8 l/min, shielding Ar flow rate=10 l/min, and interpass cooling time=3mins.

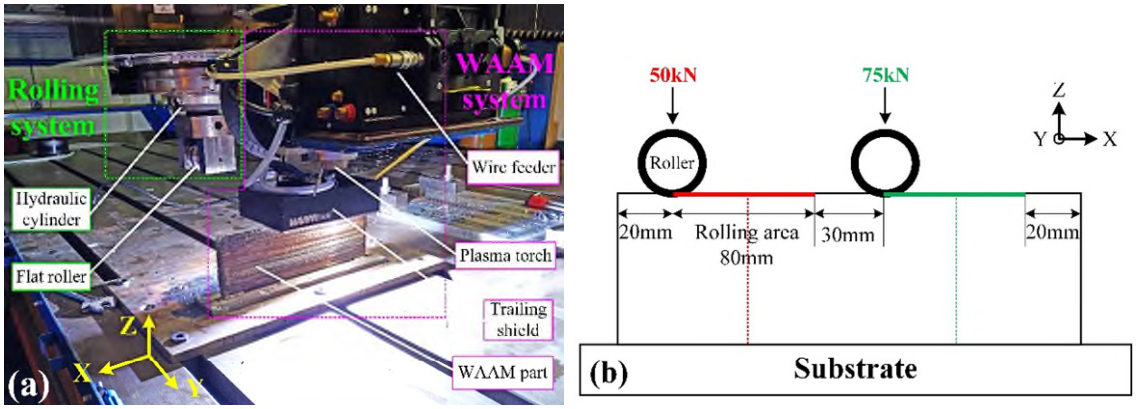

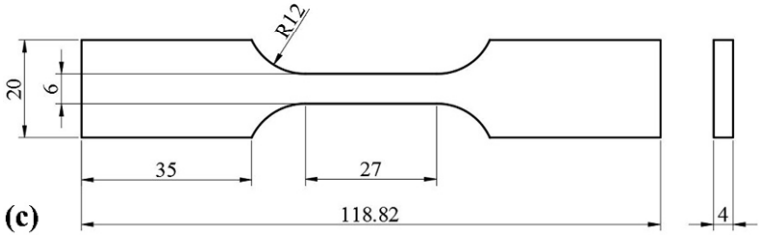

Figure 8-1 (a) Experimental setup of the in-process rolling assisted plasma-WAAM system and (b) principle of one pass rolling study (c) dimensions of the tensile coupons (gauge length 24mm).

Table 8-1 Chemical composition of the IN718 wire (wt. %).

Ni	Cr	Nb+Ta	Mo	Ti	Al	Co	Mn	Fe
53.15	19.42	5.22	2.95	0.96	0.47	0.41	0.11	Balance

8.2.2 Mechanical testing and microstructural analysis

Heat treatment conforming to Aerospace Material Specifications (AMS-5662M, for forged IN718) was applied to the WAAM IN718: solution treatment at 970°C for 1h, water quenching; aging at 718°C, hold for 8h; furnace cool to 620°C, hold for 8h, air cool (hereinafter, solution plus aging treatment). Tensile coupons were extracted along both horizontal (X) and vertical (Z) directions, and the tensile coupon design conforming to BS EN 2002-1: 2005 standard is shown in Fig. 8-1c. Room temperature mechanical testing was carried out on the Instron 5500R Electro-mechanical machine with a load cell of 100kN and a crosshead speed of 1mm/min, and three samples were tested for each condition.

Samples for microstructural analysis underwent a metallographic preparation consisting of mounting, grinding and polishing. The microstructure was revealed by electrolytic etching in 10% oxalic acid solution using 6V for 10s. The grain size was determined using the line intercept method [19]. Microhardness was measured using Zwick/Roell hardness tester under a load of 1 kg and holding time of 15s. Optical microscope and scanning electron microscopy (SEM, FEI XL30-SFEG) were used to observe the precipitates. Phase identification was carried out using X-ray diffraction (SIEMENS D5005) with Cu Kα radiation (λ = 1.5418 Å). Grain structure was characterized by Electron backscatter diffraction (EBSD) analysis. In parallel, a piece of wrought IN718 (HAYNES® 718 alloy)

conforming to AMS 5596 specification was prepared and underwent the same heat treatment and analysis for a comparative study.

8.3 Results

8.3.1 Microhardness

Fig. 8-2 shows the microhardness variation of the one-pass and interpass rolled wall structure measured along the central axis of YZ plane. The sample sectioning positions are indicated by the dash lines in Fig. 8-1b. From Fig. 8-2a, with one pass rolling a noticeable hardness increase is observed near the top and the hardening depth could reach 5mm. Hardening occurs instantly from the top surface, gets more pronounced to reach the peak value at 1.6-2.2mm depth, then reduces all the way till the unhardened level. Generally, the higher the load, the higher microhardness value at the same depth; the peak microhardness obtained after 50kN and 75kN rolling is 324HV and 355HV respectively, as compared to the 230HV of the unhardened level.

Fig. 8-2b presents the microhardness variations of the two comparative walls built with and without rolling. In the as deposited condition, the microhardness generally remains a constant level from the top to the substrate despite the slight fluctuation, indicating a very sluggish response of IN718 to the intrinsic aging effect [20,21] from the layer-by-layer deposition process. With rolling applied, the WAAM IN718 shows a considerable hardness increase of 71HV in the as deposited condition. After solution plus aging treatment, the microhardness value of both unrolled and rolled alloy shows a significant increase of 158HV and 113HV respectively, and the rolled alloy still shows a slightly higher (26HV) microhardness than the unrolled one.

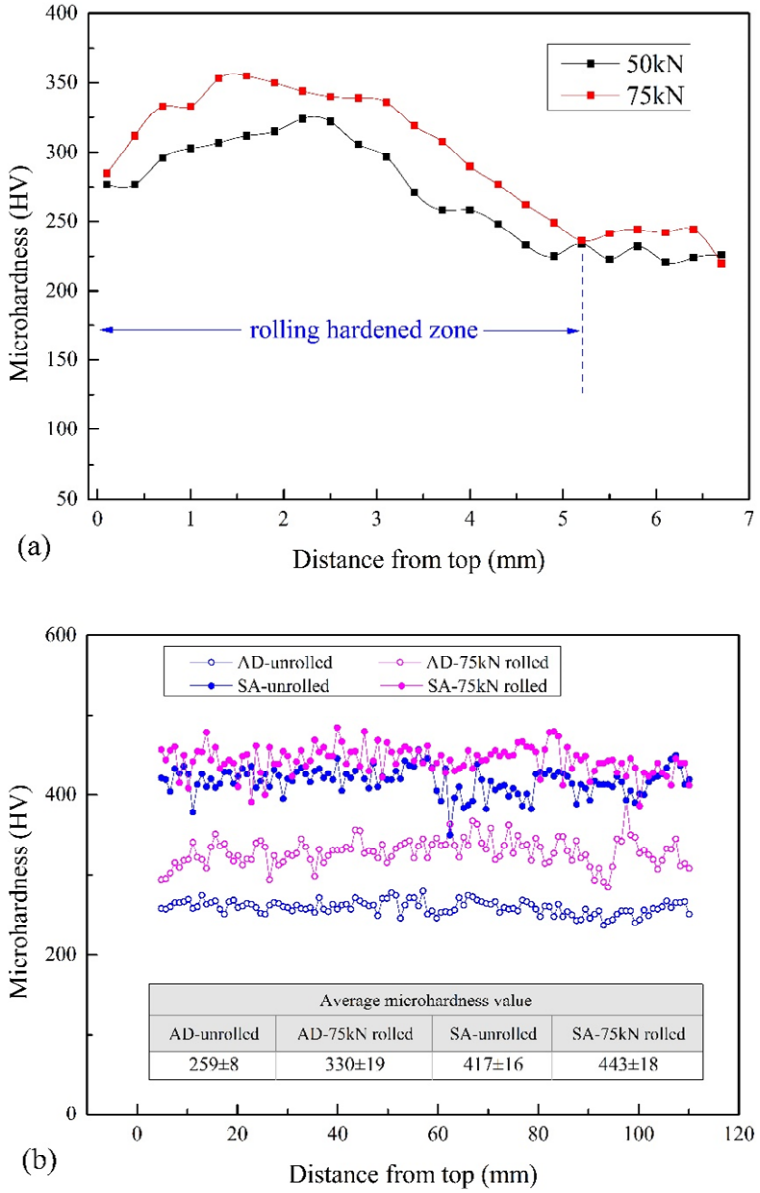

Figure 8-2 Microhardness of the wall built with (a) one pass rolling on top and (b) interpass rolling (AD: as deposited; SA: solution plus aging treated).

8.3.2 Macrostructure

Fig. 8-3 shows the macrostructure of the unrolled and rolled WAAM IN718 along the YZ plane. Sequentially appeared remelting lines (yellow dotted lines in Fig. 8-3) indicate the layer by layer building principle in which the subsequent depositions partially remelt the previous one and solidifies on top to form a new layer. The unrolled alloy exhibits a typical solidified dendritic structure: large columnar grains are observed to grow along the wall height and could cross

several layers with the lengths comparable to the wall height. By contrast, the rolled alloy exhibits a duplex grain structure with a recrystallized core in the central area covering half the wall thickness and smaller columnar grains located near the wall sides. Note that the tensile coupons are extracted along the XZ plane and in the central area of the thickness, i.e., in the fully recrystallized area. Although the columnar grains show different orientations such that they grow divergently upwards in the unrolled alloy but convergently upwards in the rolled one, they both show an epitaxial growth in a direction perpendicular to the remelting line. Such a difference is due to the different remelting line shape: in the unrolled alloy, the deposit shows a cap shape, and the next deposition does not re-melt the previous deposit to an extent great enough to change the convex shape; in case of the rolled alloy, the deposition is on a flattened surface so the remelting easily creates a concave shaped remelting line.

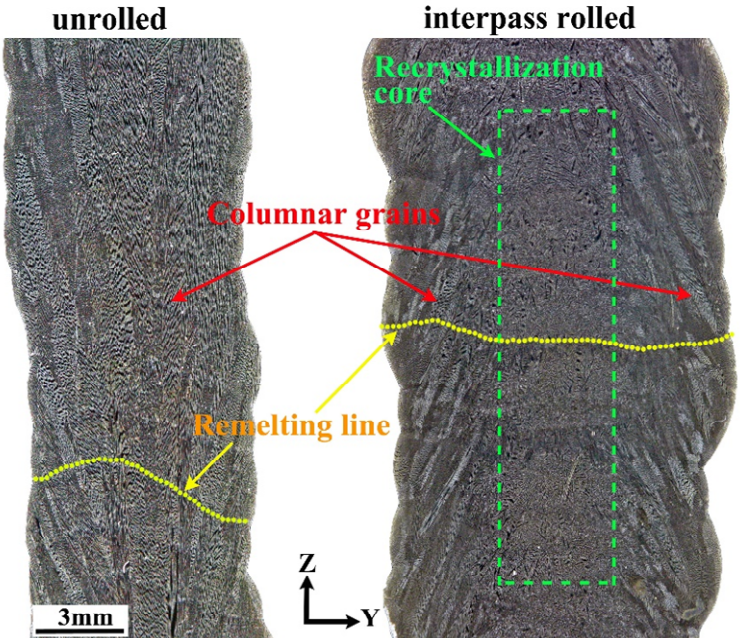

Figure 8-3 Macrostructure of the unrolled and rolled WAAM IN718. (Images taken near the top of the wall, covering 1/4 of the wall height.)

8.3.3 Microstructure

Fig. 8-4 and Fig. 8-5 show the microstructure of the unrolled and rolled WAAM IN718 respectively. Micrographs were taken at the half height of the wall. In the as deposited condition, the unrolled WAAM IN718 (Fig. 8-4a) exhibits a dendritic

structure with the dendrites developing along the building direction (Z); massive Laves phases (white arrows in Fig. 8-4a) are observed to distribute in the interdendritic regions. After solution plus aging treatment, the dendritic microstructure generally remains unchanged, but a higher magnification shows that some Laves phases are dissolved through the thermodynamic diffusion process and the amount of Laves phase is reduced (Fig. 8-4b). When rolling is applied (Fig. 8-5a), the microstructure is less dendritic and the orientation of the dendrites within a layer is highly disordered; particularly, the long dendrites do not necessarily grow perpendicularly to the interlayer boundary. With solution plus aging treatment applied, the similar diffusion and reduction of Laves phase are observed (Fig. 8-5b) and the secondary phases distribution is more dispersed as compared to the unrolled alloy (Fig. 8-4b).

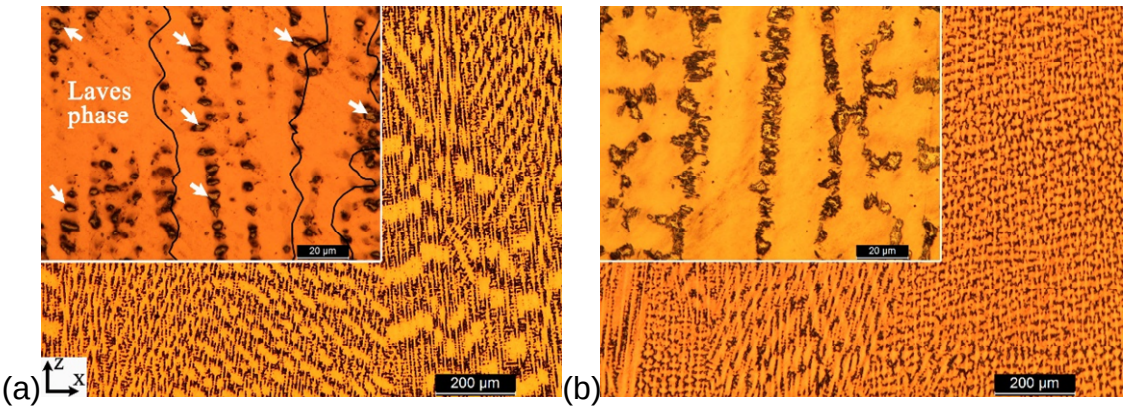

Figure 8-4 Microstructure of the unrolled WAAM IN718 (a) as deposited (grain boundary depicted for better visibility) (b) solution plus aging treated.

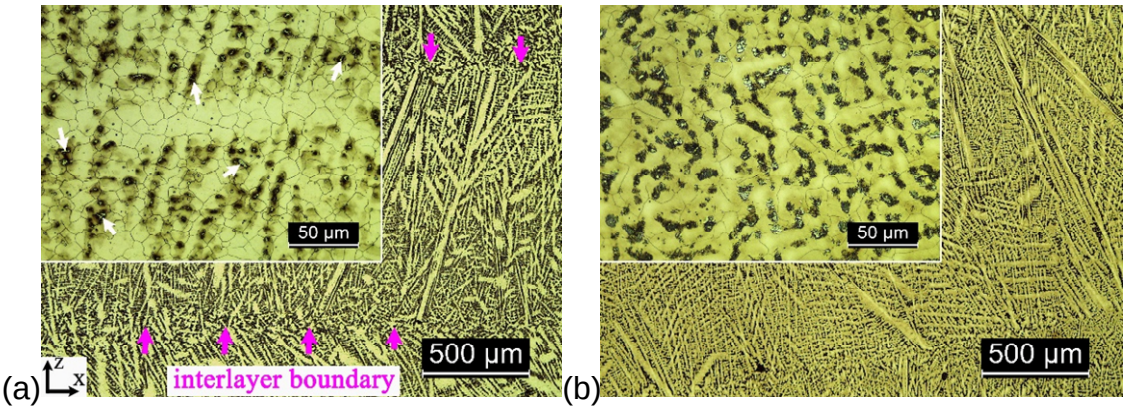

Figure 8-5 Microstructure of the rolled WAAM IN718 (a) as deposited (b) solution plus aging treated.

8.3.4 Mechanical testing results

Table 8-2 presents the tensile test results of the unrolled and rolled WAAM IN718 under different heat treatment conditions. Without rolling, the average UTS of the as deposited WAAM IN718 is 793MPa, and with rolling only applied the UTS is increased to 1078MPa (increased by 35.9%) which is accompanied by a 7.1% elongation reduction in the horizontal direction. A full heat treatment, solution plus aging, of the unrolled WAAM IN718 improved the UTS to 1056MPa (increased by 33.2%), which is essentially the same efficacy as rolling only does, except that the elongation is only around half of that resulted from rolling only; however, the UTS is still 220MPa lower than the wrought standard (1276MPa). Solution treatment results in a UTS reduction of 58MPa and 118MPa for the unrolled and rolled alloys respectively, which indicates that the rolled alloy responses to the intrinsic aging effect [22,23] more effectively; however, the UTS of the rolled alloy is still 225MPa higher than the unrolled alloy. After solution plus aging treatment, the UTS of the rolled alloy is improved from 1078MPa to 1351MPa (increased by 25.3%) which meets the wrought standard; besides, both the 0.2%YS and elongation meet the wrought standard.

From Table 8-2, the elongation generally increases after solution treatment except for the unrolled alloy in the horizontal direction but reduces after aging yet still exceeding the wrought level (12%). Compared with the unrolled alloy, the rolled alloy shows a higher ductility in both solution and solution plus aging treated condition but slightly lower ductility in the as deposited condition.

Table 8-2 Mechanical testing results of WAAM IN718.

			UTS / MPa			0.2%YS / MPa		Elongation / %	
			H	V	Average	H	V	H	V
WAAM	AD	unrolled	818±13	756±7	793±32	525±7	506±2	33.3±2.5	27.9±1.3
		75kN rolled	1082±13	1072±6	1078±12	763±8	687±1	26.2±2.2	26.6±1.3
	S	unrolled	763±32	693±0	735±42	384±8	384±11	24.4±3.7	32.5±3.0
		75kN rolled	967±8	949±11	960±13	540±13	530±6	37.0±2.1	32.8±1.0
	SA	unrolled	1102±78	988±6	1056±82	790±9	791±14	14.7±1.3	12.8±1.2
		75kN rolled	1348±10	1356±10	1351±11	1057±19	1035±20	15.1±3.3	17.4±1.1
wrought AMS5662 [3]			1276			1034		12	

AD: as deposited; S: solution treated; SA: solution plus aging treated; H: horizontal; V: vertical

8.4 Discussion

8.4.1 Recrystallization

8.4.1.1 Duplex grain structure

The duplex grain structure in Fig. 8-3 indicates that the recrystallization during the rolling assisted WAAM process is not spatially complete, which is related to the non-uniform hardening distribution from an individual rolling pass when using the flat roller, as shown in Fig. 8-6. As can be seen, one pass of rolling can generate a noticeable hardening zone which is near the central axis of the wall thickness, covering around half of the thickness and a depth of nearly 5mm from the rolling surface; the material does not get hardened significantly outside this zone. Actually, the material outside this zone will never get hardened even during the entire interpass rolling assisted WAAM process because the rolling load applied in this study is unidirectionally along Z, rather than in all directions. The peak hardening zone (red colour in Fig. 8-6) is not right at the top but at an area 0.5-2.5mm below the top and 0.5-2.5mm away from the central axis. The peak hardening point possesses a value that is almost double of the non-deformed material. Since the stored energy induced by rolling provides the thermodynamic driving force to trigger recrystallization [24,25], the hardened zone in the central

area shows a more pronounced recrystallization as compared to the area outside it, thus resulting in the duplex grain structure.

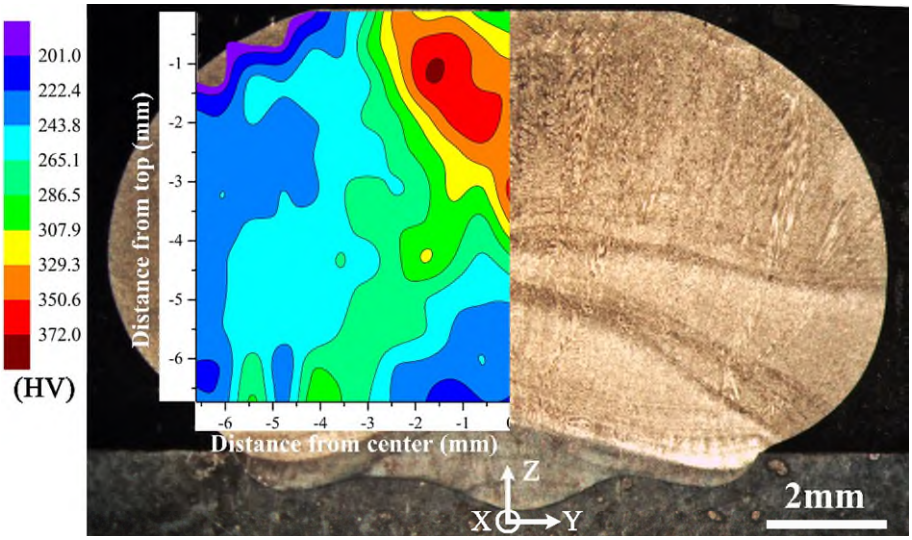

Figure 8-6 Microhardness mapping of the 75kN one-pass top rolled 5-layer wall structure.

8.4.1.2 Effective rolling for recrystallization

Another key element to trigger recrystallization is that the strained material must be heated up to the recrystallization temperature range, but not the melting range. Hence the relationship between the rolling hardened depth and the remelting depth upon next deposition is crucial: the former must be greater than the latter to allow some strained material to be heated up to the temperature just below liquidus; if the other way around, all the strained material will be fully melted and the deposit will only be a normal solidified dendritic structure, without any recrystallization.

Owing to the fcc crystal structure and the high work hardening coefficient [8] of IN718, each individual rolling pass can be so effective that the appreciable hardening depth can be as great as 5mm, while the remelting depth is below 1.2mm (layer height in this study). As a result, around 80% of the hardened material remains below solidus and is subject to high temperature upon next deposition, which provides the two key elements for recrystallization to happen. Such recrystallization is not a uniform one for the following reasons. Firstly, the level of recrystallization is strongly dependent on the stored energy; while the

strain hardening at a certain position could be partially released by the heat input from the following depositions and recrystallization process and could also be enhanced upon the following rolling passes. Secondly, the recrystallization temperature is not kept at a constant value but in the form of thermal pulses; also, the fast cooling rate does not leave enough time to allow the recrystallization to proceed thoroughly, and any successive depositions that can heat the strained material to recrystallization temperature would promote the recrystallization process. Thirdly, the growth of the recrystallized grains is subject to non-uniform thermal pulses and discrete duration periods; thereby being unpredicted. The entire rolling assisted WAAM process is essentially an ongoing “deposition-non-uniform recrystallization” pattern.

8.4.2 Grain morphology, grain size, and texture

The insets in Fig. 8-4a and Fig. 8-5a also show the grain boundary morphology of the unrolled and rolled WAAM IN718 in the as deposited condition. The unrolled alloy features low-angle grain boundaries showing the columnar grains (Fig. 8-4a), while the rolled alloy shows a finely recrystallized equiaxed grains with an average grain size of 12.7μm. Fig. 8-7 shows the grain morphology of the rolled WAAM IN718 and the wrought IN718 in the solution treated condition which are also the respective starting microstructure of the following aging treatment. The elemental segregation is more severe in the WAAM alloy as compared to the wrought alloy. The average grain size of the rolled WAAM IN718 is measured to be 15.7μm, which is slightly larger than the as deposition condition due to the slight grain growth during solution treatment. However, the size of the fully recrystallized grains is still finer than the wrought alloy (26.7μm, data from the specification sheet) possibly because the fast cooling rate in WAAM deposition, which is essentially a micro casting process, does not allow enough time for the grain growth, whereas the grains in the wrought alloy develop from conventional castings which possess much bigger starting grains.

(a) 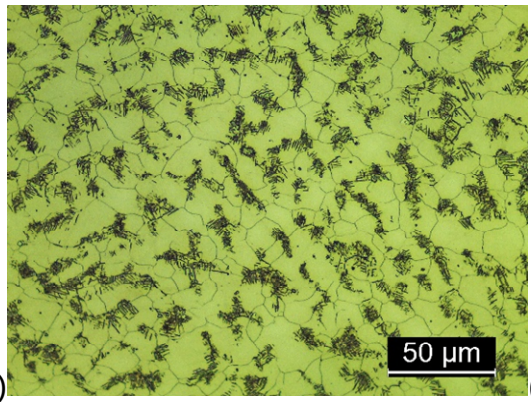

(b) 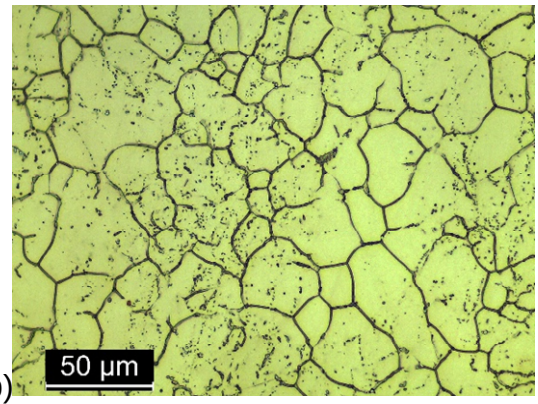

Figure 8-7 Grain morphology of the rolled WAAM and wrought IN718 after solution treatment (a) rolled WAAM (b) wrought.

Fig. 8-8 presents long EBSD orientation maps for both unrolled and rolled WAAM IN718 showing the respective grain morphology in the solution plus aging treated condition. In the unrolled alloy, very large columnar grains are observed to extend along the wall height direction (Z): the length of the columnar grains can be more than 11mm and the width could be more than 0.8mm (Fig. 8-8a). Besides, the majority of the crystals in the unrolled alloy show a preferred {101} orientation in IPF X. By contrast, the rolled WAAM IN718 shows an overall non-uniformly recrystallized grain structure (Fig. 8-8b): the area that undergoes more thermal cycles shows a fully recrystallized grain structure with finely equiaxed grains and evidence of grain growth, while the area undergoes less thermal cycles remains largely columnar grains but the size is much smaller (length less than 1mm, width less than 0.1mm) as compared to the unrolled alloy. From Fig. 8-9a, the columnar grains dominated area is separated by the finely equiaxed grain bands which correspond to the interlayer boundaries as shown in Fig. 8-5a. Though the recrystallized area accounts for more than 50% in Fig. 8-8b, the grains structure of the rolled WAAM IN718 is not improved to a level identical to the wrought alloy. Additionally, the crystals in the rolled WAAM IN718 shows a much more random orientation from IPF X, as compared to the unrolled alloy.

(a) 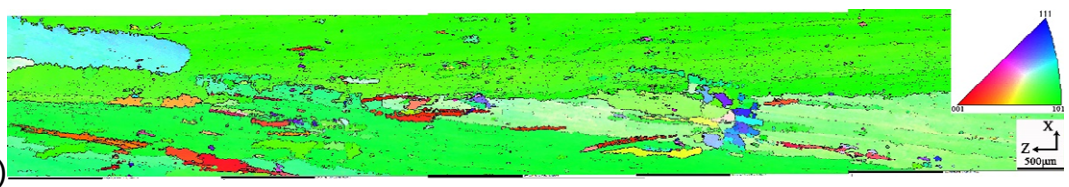

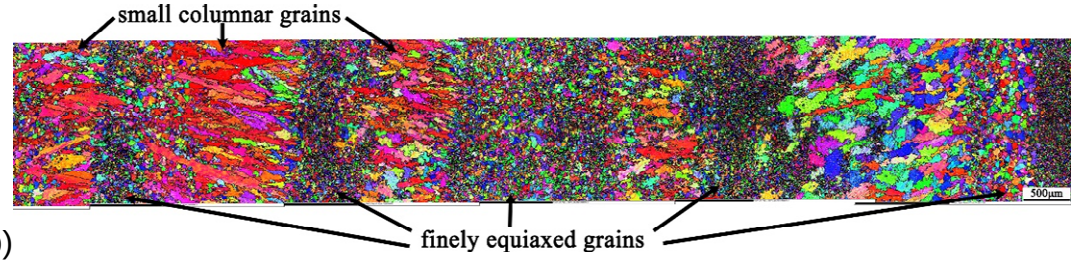

(b)

Figure 8-8 Long EBSD orientation map of the WAAM IN718 after solution plus aging treatment (IPF X; black lines are grain boundaries with misorientation greater than 15°) (a) unrolled (b) rolled.

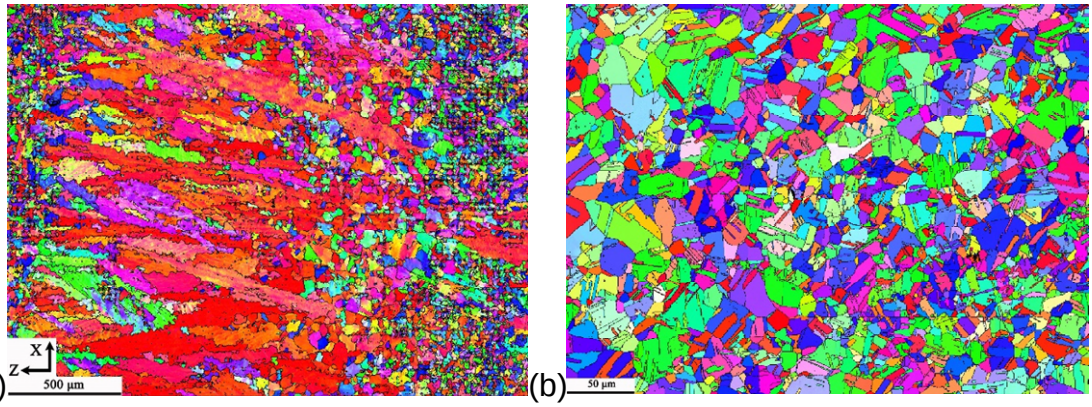

(a) (b)

Figure 8-9 EBSD orientation map of IN718 produced by different process after solution plus aging (IPF X; black lines are grain boundaries with misorientation greater than 15°) (a) rolled (b) wrought.

Another benefit from recrystallization is the mitigation of texture. From Table 8-2, the unrolled WAAM IN718 shows a noticeable anisotropy with the UTS difference between the horizontal and vertical direction being 114MPa in the solution plus aging treated condition, which is due to the strong {100} texture showing an intensity of 45.05 times more random (Fig. 8-10a). By contrast, the rolled WAAM IN718 shows an intensity of only 5.51 (Fig. 8-10b), which is close to the wrought alloy of 2.7 (Fig. 8-10c). The significant texture weakening is responsible for the essential isotropic mechanical properties of the rolled WAAM IN718 in which the UTS difference is only 8MPa in the solution plus aging treated condition.

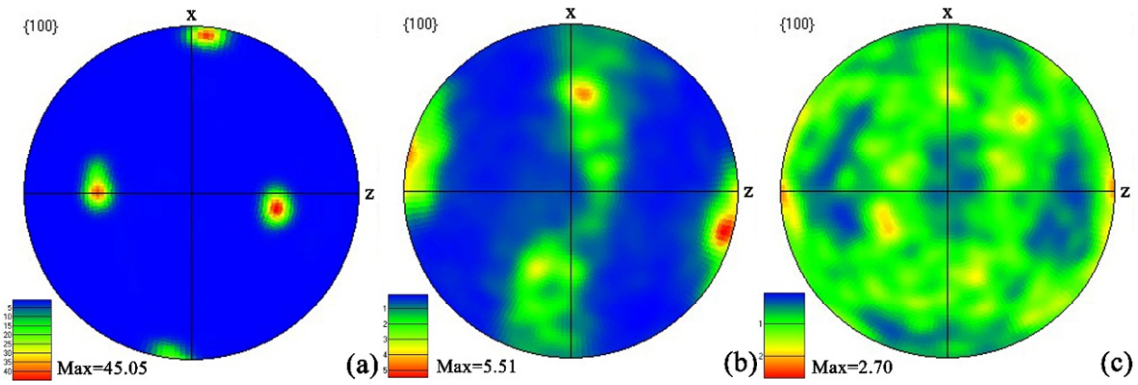

Figure 8-10 Pole figures showing the texture of the IN718 in solution plus aging treated condition (a) unrolled (b) rolled (c) wrought.

8.4.3 Precipitates

Fig. 8-11 shows the X-ray diffraction patterns and the phase index results of the IN718 produced by WAAM and wrought process. As can be seen, the peak of the δ phase appears after heat treating the rolled WAAM IN718, but not in the wrought alloy. The typical (111) and (200) peaks for the γ matrix is very insignificant in the as deposited unrolled WAAM IN718 and they even disappear after solution plus aging treatment, which is likely due to the considerable texture of the unrolled WAAM alloy as shown in Fig. 8-10a. Peaks of γ′ and γ" are not detected due to the very fine nature of these precipitates [26].

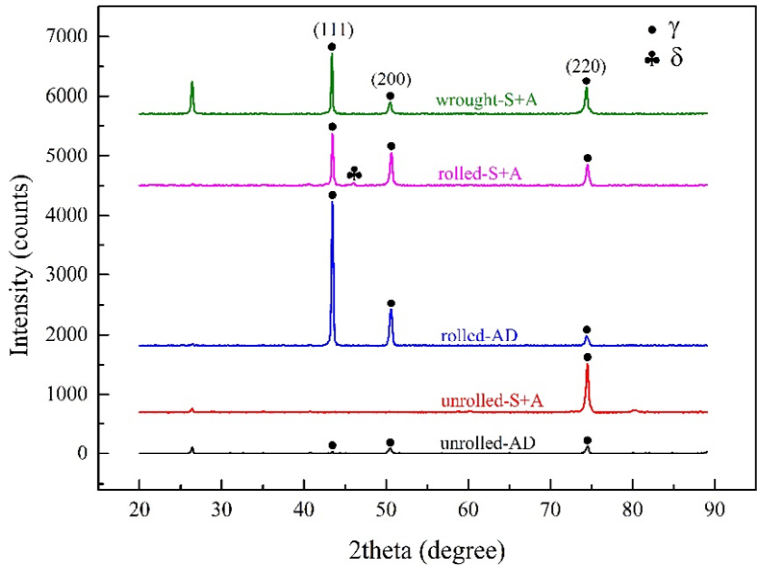

Figure 8-11 X-ray diffraction patterns of IN718 produced by different processes.

Fig. 8-12a shows the morphology and distribution of the precipitates formed in the unrolled WAAM IN718 after solution plus aging treatment. Discrete islands of residual Laves phase are still present since the solution treatment does not dissolve all the Laves phase [3]; besides, a large number of acicular δ phase is observed and generally clusters near the residual Laves phase. Rolling does not eliminate the Laves phase, and both residual Laves phase and δ phase are observed in the rolled alloy after solution plus aging, as shown in Fig. 8-12b; however, despite the complexity of the precipitates, some nanoscale secondary phases are observed to precipitate at the grain boundaries. Neither Laves phase nor large acicular δ phase is found in the wrought alloy, and the precipitates formed in the wrought alloy are all in nanoscale which disperse very uniformly throughout the austenitic matrix and preferentially precipitate along the grain boundaries.

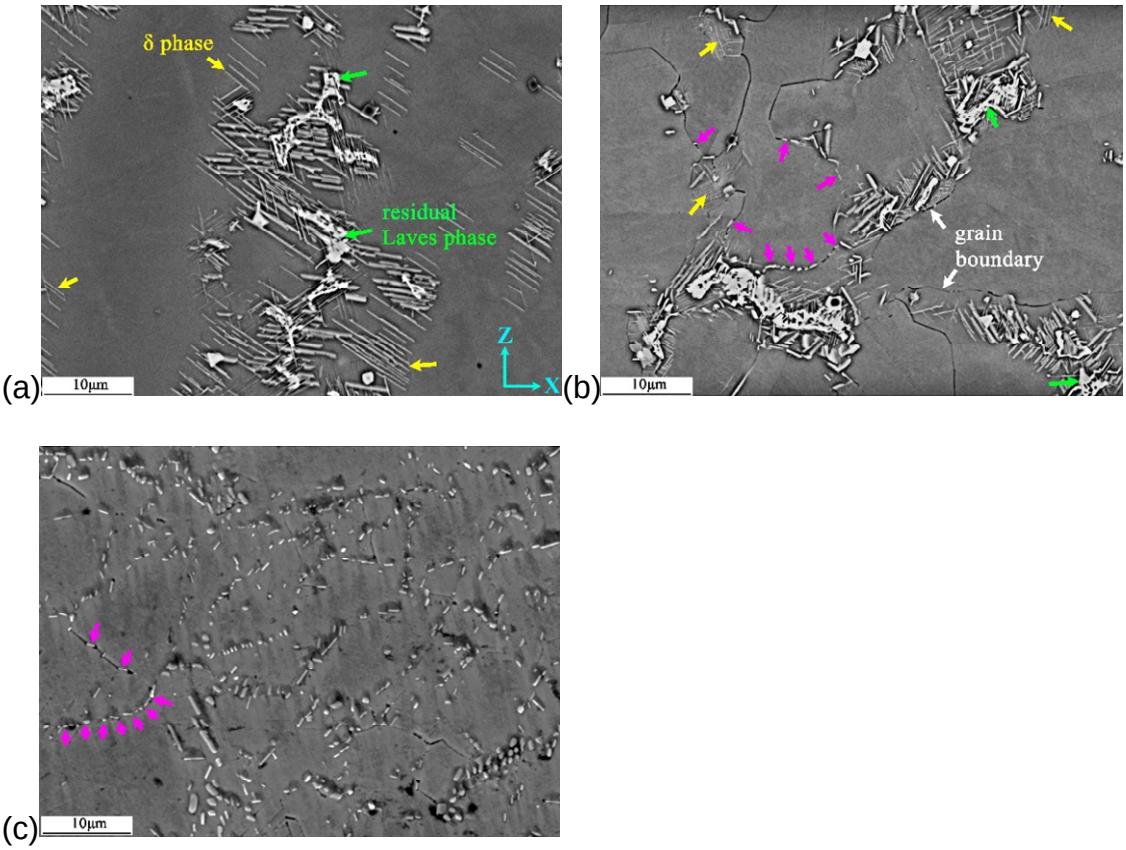

Figure 8-12 Precipitates in WAAM and wrought IN718 after solution plus aging (a) unrolled (b) rolled (c) wrought.

8.4.4 Strengthening mechanism

WAAM is a manufacturing process which accumulates material by solidifying the melted droplet, therefore the WAAM alloy is essentially a solidified freeform structure featuring dendritic microstructure. The inherent dendrites growth and non-equilibrium thermal history in WAAM process inevitably result in the Nb segregation and formation of Nb-rich brittle Laves phase at the interdendritic area, which is known to be detrimental to mechanical properties of IN718 [27]. Besides, the directional thermal conduction route in WAAM process also promotes epitaxial growth of the dendrites, which facilitates the development of very big columnar grains, as shown in Fig. 8-8a. Big columnar grains, on the one hand, provide less effective grain boundary strengthening according to the Hall-Petch relationship [28]; on the other hand, possess less grain boundary area to allow precipitation at the grain boundary. Solution treatment does not dissolve all the Laves phase since the solution temperature of 980°C is not high enough to promote a complete Nb diffusion, therefore some residual Laves phase still presents in the heat treated WAAM IN718 (Fig. 8-12a). Homogenization (1093°C, 1-2hrs) using a higher temperature is reported to completely dissolve the Laves phase but results in grain coarsening at the same time [3]. Hence, the unrolled WAAM IN718 possesses inferior mechanical properties mostly due to the large columnar grains featured microstructure, which cannot be improved simply by a different heat treatment without introducing plastic deformation.

During the manufacturing process, the wrought IN718 undergoes several rounds of rolling and heating-cooling cycles. Undesired Laves phase can be completely dissolved by heating up to the homogenization temperature, and the resultant grain coarsening can be restored through several rounds of recrystallization which end up with finely equiaxed grains. Besides, the large grain boundary area allows massive nanoscale secondary phases to precipitate at the grain boundary, as shown in Fig. 8-12c, which is effective in hindering the grain boundary motion.

Similarly, the rolling applied in this study plays the same role. However, due to the same solution temperature, the Laves phase formed after deposition are not completely dissolved to saturate the matrix with Nb and the residual Laves

phases are also observed in the rolled alloy (see green arrows in Fig. 8-12b); instead, the Laves phases are in situ transformed to acicular δ phase, which depletes the Nb required for γ" formation [3]. This is the reason why the aging response of the unrolled and rolled alloy are not very different (321MPa vs. 391MPa). Thus, the main strengthening mechanism, when comparing the unrolled and rolled WAAM IN718 in the solution plus aging treated condition, is recrystallization. On the one hand, the average grain size in the recrystallized core is 17.6μm after solution plus aging treatment (Fig. 8-5b), which is significantly smaller than the centimetre scale columnar grains in the unrolled alloy (Fig. 8-5a) and thereby having a much greater grain boundary strengthening effect. On the other hand, the grain size is even smaller than the wrought alloy, thereby providing a larger grain boundary area for the precipitation at the grain boundaries, as shown in Fig. 8-12b.

To conclude, the strength inferiority of the unrolled alloy to the wrought alloy is mostly due to the undesired large columnar grains providing less grain boundary strengthening. The applied rolling is effective because it restores the grain size to somewhere close to the wrought alloy by inducing recrystallization.

8.4.5 Strengthening contribution

From Table 8-2, the precipitation hardened rolled alloy shows a strength 295MPa higher than the unrolled alloy. Such a strengthening after interpass rolling is applied could be a synergic effect of recrystallization and precipitation hardening. Though it is difficult to precisely specify the respective contribution of rolling and heat treatment, a semi quantitative discussion can be given here.

The UTS difference in the as deposited condition is 285MPa, which is a consequence of recrystallization and the intrinsic aging effect. Note that the precipitates formed in response to the intrinsic aging effect will be dissolved and slight grain coarsening might take place during solution treatment. From Fig. 8-5a and Fig. 8-7a, the average grain size increases from 12.7μm to 15.7μm after solution treatment, which is not a significant coarsening. Therefore, by comparing the UTS in the solution treated condition it can be inferred that for the entire 285MPa increase, the grain structure change contributes to slightly more than

225MPa, and the better intrinsic aging response of the rolled grain structure contributes to around 60MPa.

Further, when aging is applied, the strength increase is 321MPa and 391MPa for the unrolled and rolled WAAM IN718 respectively. Again, a slight grain coarsening, from 15.7μm to 17.6μm, is observed after the double aging treatment. Hence, for the overall 295MPa strength increase in the solution plus aging treated condition, grain structure change contributes slightly less than 225MPa (76%), and the better aging response from the recrystallized grain structure contributes to the remaining, around 70MPa (24%).

8.4.6 Future work

From this paper, although interpass rolling improves the mechanical properties of the WAAM IN718 to a level superior to the wrought alloy, it does not manage to make the WAAM alloy microstructurally and metallurgically identical to a wrought alloy. Firstly, the rolling induced recrystallization is not spatially uniform and some area still remains columnar grains with smaller size, as compared to complete finely equiaxed grains in the wrought alloy. On the other hand, Laves phase form as a result of the characteristic thermal process in WAAM and still exist in the rolled alloy after solution plus aging treatment, which is not observed in the wrought alloy. Though the present study shows that the non-uniformly recrystallized grains structure and the residual Laves phases have no effect on the room temperature tensile properties, it is not sure if they could affect other properties, such as creep and rupture strength at high temperatures. In the future, the authors will evaluate the effect of the residual columnar grains and Laves phase on the high-temperature mechanical behaviours; besides, the rolling strategy will be optimized to induce a more complete and uniform recrystallization.

8.5 Conclusions

1. After precipitation hardening, the strength of the unrolled WAMM IN718 is 1056MPa, 220MPa inferior to the wrought alloy, while the strength of the interpass rolled alloy is 1351MPa, 75MPa higher than the wrought alloy;

besides, both 0.2%YS and elongation of the rolled alloy meet the wrought standard.

2. The inferior strength and anisotropy of the unrolled WAAM IN718 are due to the very large columnar grains. Interpass rolling results in a non-uniform recrystallization, which produces finely equiaxed grains and small columnar grains and eliminates anisotropy.
3. An effective rolling must generate a hardening depth greater than the remelting depth to allow recrystallization to take place upon the next deposition.
4. The higher UTS of the rolled alloy than the unrolled alloy (295MPa) results mainly (76%) from the rolling induced recrystallization.
5. The interpass rolled WAAM IN718 is not microstructurally and metallurgically identical to the wrought alloy; residual Laves phase and massive δ phase are found in the solution plus aging treated condition but their effect on the mechanical properties are not clear yet.

8.6 References

[1] D. Zhang, W. Niu, X. Cao, Z. Liu, Effect of standard heat treatment on the microstructure and mechanical properties of selective laser melting manufactured Inconel 718 superalloy, Mater. Sci. Eng. A. 644 (2015) 32–40. doi:10.1016/j.msea.2015.06.021.

[2] B. Baufeld, Mechanical properties of INCONEL 718 parts manufactured by shaped metal deposition (SMD), J. Mater. Eng. Perform. 21 (2012) 1416–1421. doi:10.1007/s11665-011-0009-y.

[3] H. Qi, M. Azer, a. Ritter, Studies of Standard Heat Treatment Effects on Microstructure and Mechanical Properties of Laser Net Shape Manufactured INCONEL 718, Metall. Mater. Trans. A. 40 (2009) 2410–2422. doi:10.1007/s11661-009-9949-3.

[4] Y.N. Zhang, X. Cao, P. Wanjara, M. Medraj, Oxide films in laser additive manufactured Inconel 718, Acta Mater. 61 (2013) 6562–6576. doi:10.1016/j.actamat.2013.07.039.

[5] M. Sundararaman, R. Kishore, P. Mukhopadhyay, Strain hardening in underaged INCONEL 718, Metall. Mater. Trans. A. 25 (1994) 653–656. doi:10.1007/BF02651609.

[6] Special Metals, INCONEL alloy 718, in: 2007: pp. 1–28. doi:SMC-066.

[7] ASM International, ASM Handbook: Volume 2 Properties and selection: Nonferrous alloys and special-purpose materials, 1990.

[8] D.G. Thakur, B. Ramamoorthy, L. Vijayaraghavan, Effect of cutting parameters on the degree of work hardening and tool life during high-speed machining of Inconel 718, Int. J. Adv. Manuf. Technol. 59 (2012) 483–489. doi:10.1007/s00170-011-3529-6.

[9] S. Gorsse, C. Hutchinson, M. Gouné, R. Banerjee, Additive manufacturing of metals: a brief review of the characteristic microstructures and properties of steels, Ti-6Al-4V and high-entropy alloys, Sci. Technol. Adv. Mater. 18 (2017) 584–610. doi:10.1080/14686996.2017.1361305.

[10] T. Trosch, J. Strößner, R. Völkl, U. Glatzel, Microstructure and mechanical properties of selective laser melted Inconel 718 compared to forging and casting, Mater. Lett. 164 (2015) 428–431. doi:10.1016/j.matlet.2015.10.136.

[11] C. Zhong, A. Gasser, J. Kittel, K. Wissenbach, R. Poprawe, Improvement of material performance of Inconel 718 formed by high deposition-rate laser metal deposition, Mater. Des. 98 (2016) 128–134. doi:10.1016/j.matdes.2016.03.006.

[12] S.W. Williams, F. Martina, A.C. Addison, J. Ding, G. Pardal, P. Colegrove, Wire + Arc Additive Manufacturing, Mater. Sci. Technol. 00 (2015) 1–7. doi:10.1179/1743284715Y.0000000073.

[13] B. Cong, J. Ding, S. Williams, Effect of arc mode in cold metal transfer process on porosity of additively manufactured Al-6.3%Cu alloy, Int. J. Adv. Manuf. Technol. 76 (2014) 1593–1606. doi:10.1007/s00170-014-6346-x.

[14] B. Cong, R. Ouyang, B. Qi, J. Ding, Influence of Cold Metal Transfer Process and Its Heat Input on Weld Bead Geometry and Porosity of Aluminum-Copper

Alloy Welds, Rare Met. Mater. Eng. 45 (2016) 606–611. doi:10.1016/S1875-5372(16)30080-7.

[15] B. Wu, Z. Pan, D. Ding, D. Cuiuri, H. Li, Z. Fei, The effects of forced interpass cooling on the material properties of wire arc additively manufactured Ti6Al4V alloy, J. Mater. Process. Technol. 258 (2018) 97–105. doi:10.1016/j.jmatprotec.2018.03.024.

[16] G. Asala, A.K. Khan, J. Andersson, O.A. Ojo, Microstructural Analyses of ATI 718Plus® Produced by Wire-ARC Additive Manufacturing Process, Metall. Mater. Trans. A Phys. Metall. Mater. Sci. 48 (2017) 4211–4228. doi:10.1007/s11661-017-4162-2.

[17] D. Clark, M.R. Bache, M.T. Whittaker, Shaped metal deposition of a nickel alloy for aero engine applications, J. Mater. Process. Technol. 203 (2008) 439–448. doi:10.1016/j.jmatprotec.2007.10.051.

[18] J. Ding, P. Colegrove, F. Martina, S. Williams, R. Wiktorowicz, M.R. Palt, Development of a laminar flow local shielding device for wire + arc additive manufacture, J. Mater. Process. Technol. 226 (2015) 99–105. doi:10.1016/j.jmatprotec.2015.07.005.

[19] ASTM, ASTM E112-13: Standard test methods for determining average grain size, ASTM Int. (2013) 1–28. doi:10.1520/E0112-13.1.4.

[20] X. Xu, S. Ganguly, J. Ding, S. Guo, S. Williams, F. Martina, Microstructural evolution and mechanical properties of maraging steel produced by wire + arc additive manufacture process, Mater. Charact. (2018). doi:10.1016/j.matchar.2017.12.002.

[21] P. Kürnsteiner, M.B. Wilms, A. Weisheit, P. Barriobero-Vila, E.A. Jägle, D. Raabe, Massive nanoprecipitation in an Fe-19Ni-xAl maraging steel triggered by the intrinsic heat treatment during laser metal deposition, Acta Mater. 129 (2017) 52–60. doi:10.1016/j.actamat.2017.02.069.

[22] C. Tan, K. Zhou, W. Ma, P. Zhang, M. Liu, T. Kuang, Microstructural evolution, nanoprecipitation behavior and mechanical properties of selective

laser melted high-performance grade 300 maraging steel, Mater. Des. 134 (2017) 23–34. doi:10.1016/j.matdes.2017.08.026.

[23] E.A. Jägle, P.-P. Choi, J. Van Humbeeck, D. Raabe, Precipitation and austenite reversion behavior of a maraging steel produced by selective laser melting, J. Mater. Res. 29 (2014) 2072–2079. doi:10.1557/jmr.2014.204.

[24] J. Donoghue, A.A. Antonysamy, F. Martina, P.A. Colegrove, S.W. Williams, P.B. Prangnell, The effectiveness of combining rolling deformation with Wire-Arc Additive Manufacture on β-grain refinement and texture modification in Ti-6Al-4V, Mater. Charact. 114 (2016) 103–114. doi:10.1016/j.matchar.2016.02.001.

[25] F. Martina, P.A. Colegrove, S.W. Williams, J. Meyer, Microstructure of Interpass Rolled Wire + Arc Additive Manufacturing Ti-6Al-4V Components, Metall. Mater. Trans. A Phys. Metall. Mater. Sci. 46 (2015) 6103–6118. doi:10.1007/s11661-015-3172-1.

[26] G.P. Dinda, A.K. Dasgupta, J. Mazumder, Laser aided direct metal deposition of Inconel 625 superalloy: Microstructural evolution and thermal stability, Mater. Sci. Eng. A. 509 (2009) 98–104. doi:10.1016/j.msea.2009.01.009.

[27] H. Xiao, S. Li, X. Han, J. Mazumder, L. Song, Laves phase control of Inconel 718 alloy using quasi-continuous-wave laser additive manufacturing, Mater. Des. 122 (2017) 330–339. doi:10.1016/j.matdes.2017.03.004.

[28] N. Hansen, Hall-petch relation and boundary strengthening, Scr. Mater. 51 (2004) 801–806. doi:10.1016/j.scriptamat.2004.06.002.

9 Investigation of dilution control during wire + arc additive manufacture of Inconel 625/low alloy steel multi-material structure

This chapter is an extended version of the following conference publication.

X. Xu*, *J. Ding, S. Ganguly, S. Williams, Wire + arc additive manufacture of inconel 625/low alloy steel multi-material functional structure for Oil & Gas applications. Proceedings of MSSM2018, 07-10 Aug 2018, UWS, Paisley, UK, P49-54.*

While the previous chapters presented the work on WAAM of a single material, this chapter presented the investigation on WAAM of IN625/low alloy steel multi-material structure. While the requirement of a single material is strength, the requirement for the multi-material structure is the control of dilution. This chapter studied the process parameters affecting the bead dimensions as well as the building strategies controlling the dilution level.

Abstract: Inconel 625 is widely used in Oil & Gas industry for steel pipe cladding due to its excellent corrosion resistance. In this study wire +arc additive manufacture was applied to produce Inconel 625/low alloy steel multi-material structure utilizing the design freedom to integrate the steel pipe production and cladding process; critical factors including deposition parameters, sequence and strategies were studied to understand how the dilution responds to thermal energy. Results showed that layer height could be controlled by adjusting wire feed speed, and the alloy with a lower melting point should be deposited after the one with a higher melting point to minimize the dilution. The key to dilution control is to have liquid Inconel 625 cover the steel right below the arc to prevent it from being excessively exposed to the arc. Using the proposed quasi bottom-dilution strategy with two layers cladding, defect-free multi-material structures can be built with good structural integrity, and the Fe content in the clad layer is controlled to below 5%, yet more work is needed to reduce the thickness of the clad layer.

Keywords: wire + arc additive manufacture; multi-material structure; Inconel 625; dilution.

9.1 Introduction

Corrosion-resistant pipes which can withstand dynamic stress and corrosive fluids at high temperatures and pressures [1] are highly demanded in the oil and gas extracting process. So far, cladding using Inconel superalloys is the most widely used and economic process to substantially improve the durability and corrosion resistance of the low-cost carbon steel pipes, given that a solid nickel alloy pipe cost about five times more than the carbon steel with internal cladding [2]. In this way, the outstanding strength and toughness of the carbon-manganese steels are combined with corrosion resistance from the clad material while keeping a low cost.

Inconel, referring to a family of Ni-Cr based superalloys, is known for oxidation and corrosion resistance in extreme environments subject to high pressure and heat, because a stable passivating oxide layer can form to protect the alloy from further attack. Inconel 625 (IN625), in particular, is typically used as a one of the most important cladding material in Oil & Gas sector due to its good creep resistance, high rupture strength, outstanding weldability and excellent corrosion and oxidation resistance within a wide service temperature range from cryogenic to 982°C [3]; the addition of 9% Mo and 3% Nb offers both high-temperature and wet corrosion resistance [4]. Besides, IN625 and low alloy steel have similar coefficients of thermal expansion (12.8 [5] against 10.1-14.9 μm/m°C [6]).

Manufacturing of functional pipes with internal IN625 cladding is a complicated multi-step process involving forging, bending, welding, and cladding, which leads to high cost, long lead-time, and becoming particularly challenging for small bore components. So far, the popular cladding processes such as mechanical lining and roll bonding suffer from major concerns involving integrity and supply [1]. Additive Manufacturing (AM) is a technology that promises to reduce cost by minimizing material wastage and lead-time to market [7-10]. The layer-by-layer building principle of AM enables the control of the composition and phase fraction within a layer; therefore, AM provides the possibility to build multi-material structures with a controlled composition within each layer. Owing to the intrinsic characteristics, various AM process is naturally suitable for specific applications.

For instance, selective laser melting delivers net-shaped components with high resolution; however, the deposition rate is relatively low, and the part size is limited by the enclosed working envelope [11-13]. Consequently, this class of process is best suited to small structures with high complexity.

Among various AM processes, Wire + Arc Additive Manufacture (WAAM) [14-16] is outstanding for its high deposition rate, low equipment invest and infinite parts building size, since WAAM adopts commercial welding wire as the feedstock material and an arc (generated by a conventional welding power source) as the heat source and no vacuum environment is required. WAAM provides the possibility to manufacture complex-shaped components made of multiple materials using one process by merely changing the feedstock type, thereby providing an alternative method to produce multifunctional structures. So far, WAAM has been demonstrated to be a cost-effective process for the production of large-scale metallic components using a single alloy, such as Ti6Al4V [17], aluminium [18], maraging steel [19], and Inconel [20]; however, the feasibility of manufacturing multi-material structure is yet to be verified.

Two major challenges are confronted before applying WAAM to manufacture a complex-shaped multi-material structure. Building the steel pipe structure can be easily accomplished using WAAM in a layer by layer manner; however, when it comes to certain geometries, say elbow structure, effective strategies need to be developed to vary the layer height while keeping the layer width constant within one layer, which is the first challenge. Another challenge is how to control the Fe diffusion during the arc melting process, in other words, control of dilution. The principal requirement for cladding is to control the Fe content in the clad layer to be less than 5% for corrosion resistance; besides, the clad layer should not exceed 2.5mm [21-23]. The Fe content in the IN625 filler wire is usually less than 5% [3]; however, it is likely to increase in the clad layer because of the remelting of the steel substrate and its dissolution in the clad layers [21]. Besides, arc, as a heat source, is divergent as compared to the focused energy beam such as laser and electron beam, therefore, leading to more difficulties in precisely and accurately control the energy input and the resulting dilution.

In this study, WAAM is applied to integrate the steel pipe fabrication with the internal IN625 cladding process, aiming to provide a one-stop manufacturing solution for the metallurgically clad pipes with high production rates, regardless of the size, thickness, and shape of the pipe section. A systematic study to implement WAAM process to produce an IN625/low alloy steel multi-material structure has been presented, including layer height control, deposition sequence and deposition strategy studies, aiming at producing a defect-free multi-material structure with good structural integrity and controlling the Fe content in the clad layer to be below 5%. This study will enhance the scientific understanding of the relationship between the WAAM process and the dilution for multi-material structure building.

9.2 Experimental

9.2.1 Experimental setup and materials

The non-consumable arc, plasma and TOPTIG [24] arc, were selected as the heat source in this study due to the process stability and the possibility to feed wire independently from the arc power. For the initial process study, a plasma arc (power source: MIGATRONIC 240-320AC/DC) based dual-wire feeding system was established in a glovebox to allow multi-material deposition in the same setup, as shown in Fig. 9-1a. The two wires were positioned symmetrically with respect to the plasma torch, and the wire feed speeds could be adjusted independently. The torch motion was controlled by a three-axis CNC system. For the deposition strategy study, a TOPTIG robotic system (Air Liquide) was deployed utilizing its greater torch accessibility provided by the compact torch design and torch manoeuvrability provided by the robotic system, as shown in Fig. 9-1b. A welding camera (Redman MC500) was attached to the torch throughout the study to monitor the deposition process. The IN625 wire and low alloy steel wire used in this study are ERNiCrMo-3 and ER90S-B3 (mod.) respectively. Both wires are 1.2mm in diameter, and the chemical compositions are presented in Table 9-1 and Table 9-2 respectively; note that the Fe content in the IN625 wire is below 1%.

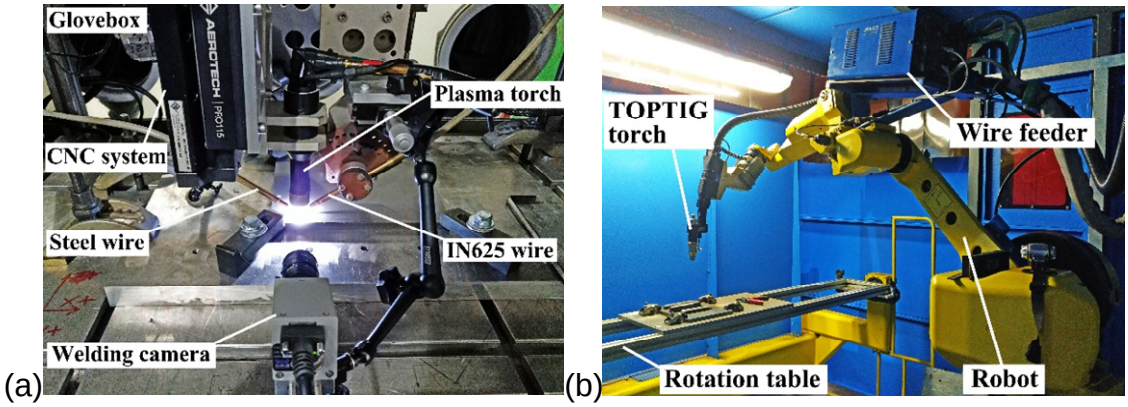

Figure 9-1 WAAM systems for the multi-material deposition study (a) plasma-based dual-wire system (b) TOPTIG system.

Table 9-1 Chemical composition of the IN625 wire (wt. %).

Ni + Co	Cr	Mo	Nb + Ta	Fe	Ti	Al	Cu	Mn	Si
>58	20-23	8-10	3.15-4.15	<1	<0.4	<0.4	<0.5	<0.5	<0.5

Table 9-2 Chemical composition of the low alloy steel wire (wt. %).

Ni	Cr	Mo	Mn	Cu	C	Si	S	P	Fe
<0.1	2.4	1	0.5	0.1	0.1	0.5	0.01	0.015	Balance

9.2.2 Deposition strategies

9.2.2.1 Path definition

Fig. 9-2 illustrates the typical deposition paths applied in this study. For the parallel path, each layer consists of several individual single passes: the arc extinguishes at the end of one pass and reignites at the start of the next deposition; thereby parallel is a discontinuous building path. In contrast, oscillation is a continuous path since each layer consists of only one pass which proceeds in an oscillating manner, and the arc only extinguishes at the end of the pass.

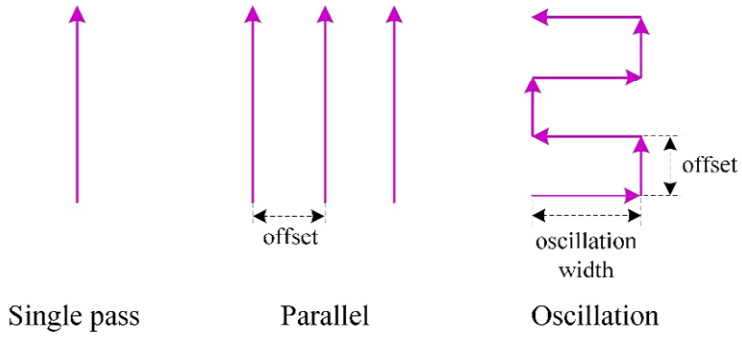

Figure 9-2 Illustration of the deposition path (lines indicate the torch motion path).

9.2.2.2 Layer height study

This study investigated the process parameters that determine the bead dimensions, aiming at keeping the bead width constant while varying the bead height by simply adjusting some parameters. Different combinations of WFS and TS were tested in the glovebox using the plasma process in the form of single pass bead-on-plate experiments.

9.2.2.3 Deposition sequence study

The melting point of ER90S-B3 and ERNiCrMo-3 wire is around 1427°C and 1290-1350°C respectively. Given the approximately 100°C difference, a comparative study of deposition sequence effect on Fe diffusion was carried out using the plasma process. Two single pass beads of different alloys were deposited side by side with an overlap of 33% of the bead width of a single pass [25]. In the first experiment, steel was deposited first, whereas in the second, IN625 was deposited first. Parameters: current=200A, WFS_{steel}=1.2m/min, $WFS_{Inconel}$=1.6m/min, TS=2mm/s.

9.2.2.4 Deposition strategies study

Two deposition strategies referred to as side-dilution and quasi bottom-dilution were developed for the multi-material structure building using the TOPTIG process. Since the steel part is much thicker than the IN625 clad layer in the final product, two variants within each strategy are proposed using parallel and oscillation path respectively to deposit the thick steel part. Fig. 9-3a illustrates the parallel variant of the side-dilution strategy within one layer: the middle steel pass is deposited first, the side steel the second, and the IN625 the last; successive

layers following the same pattern are deposited on top of the previous layer. In the side-dilution strategy, the substrate keeps horizontal and the torch remains vertical so that the dissimilar alloys are deposited side by side and the dilution between the final steel part and the IN625 layer is also in a side by side mode. For the oscillation variant, the steel part was deposited using one oscillation pass continuously within one layer, as shown in Fig. 9-3b. The parameters used are the same as those used in the deposition sequence study.

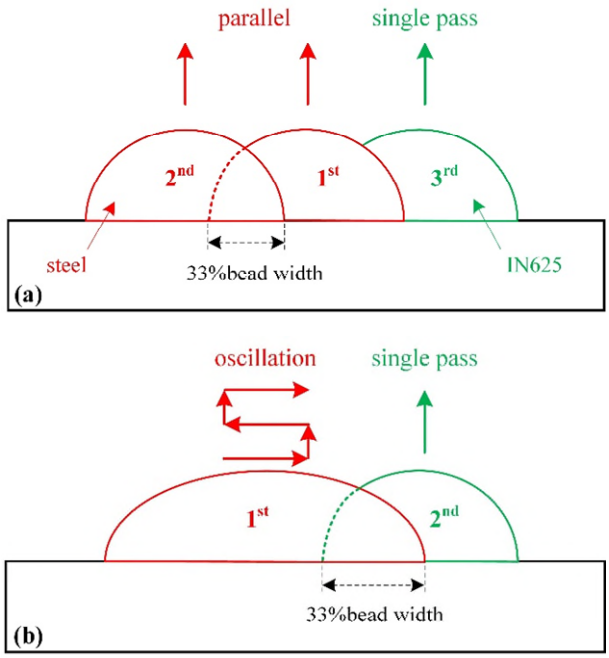

Figure 9-3 Illustration of the different side-dilution strategy variants within one layer (a) parallel (b) oscillation.

Fig. 9-4 illustrates the quasi bottom-dilution strategy. In this strategy, the thick steel wall part is built by WAAM first, using either parallel or oscillation path. Then either the substrate (Fig. 9-4a) or the torch (Fig. 9-4b) is inclined by 45° to allow IN625 cladding deposition on the side of the steel wall. This deposition strategy is quite similar to the normal cladding procedure where the torch is vertical to the steel plate and the dilution happens at the bottom of the melt pool and the steel plate, except that in the present strategy the angle between the torch and the substrate is 45° due to the practical consideration of WAAM process, such as the torch accessibility and system programming.

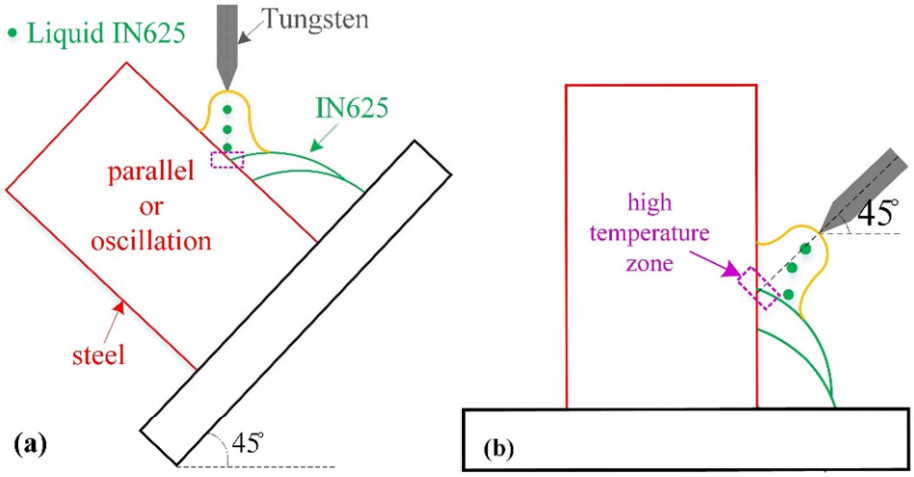

Figure 9-4 Illustration of the quasi bottom-dilution strategy (a) inclining the substrate (b) inclining the torch.

9.2.3 Analytical methods

Samples were transversely cross-sectioned from the multi-material structure near the interface before going through the metallographic preparation consisting of mounting, grinding and polishing. The polished samples were etched by 10% Nital for 10s. A camera was used to take the overview image of the WAAM structure, an optical microscope was applied to observe the interface morphology and the scanning electron microscope (SEM, FEI XL30-SFEG) equipped with the energy- dispersive spectroscopy detector (EDS, Oxford Instrument) was utilised to measure the Fe content from the interface to the clad layer.

9.3 Results

9.3.1 Layer height control

A set of experiment is designed wherein the TS (2 mm/s) and CTWD (8 mm) is kept constant while the WFS is increased stepwise with a slight accompanying current compensation, as shown in Table 9-3. The resulting bead dimensions are plotted in Fig. 9-5. As the WFS increases from 1.2 m/min to 2.6 m/min, the bead width is almost constant (around 9.5 mm) while the layer height increases from 1.2mm to 2.8mm.

Table 9-3 Design of experiments for layer height control study.

Current / A	200	205	210	215	220	225
WFS m/min	1.2	1.6	2	2.2	2.4	2.6

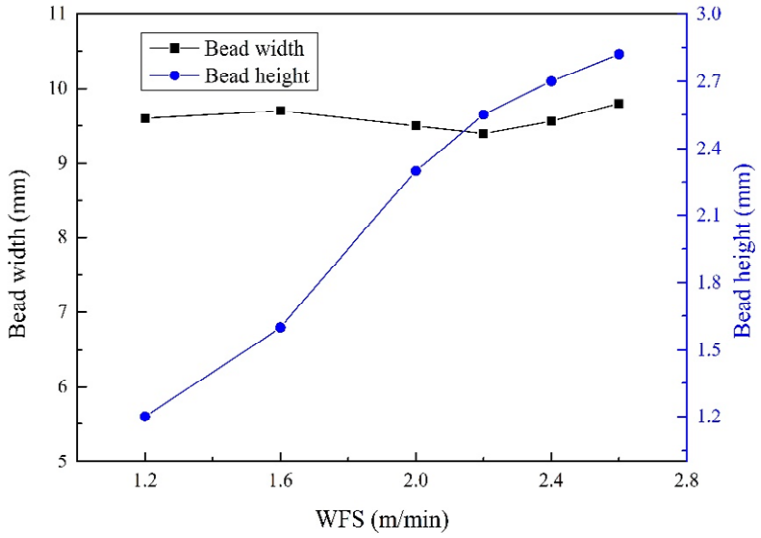

Figure 9-5 Bead dimension variation using different process parameters

9.3.2 Deposition sequence

Fig. 9-6 presents the bead shape and optical micrographs of the interface after etching in the deposition sequence study. Naturally, the IN625 is corrosion resistant, but the low alloy steel is not, therefore under the same etching condition, the two alloys will show a different level of corrosion response. When IN625 is deposited after steel, a sharp and clear interface (indicated by the white arrow in Fig. 9-6a) between the two alloys is observed with the steel part being etched but the IN625 part being not, which indicates a limited mutual mixing of the two alloys. In contrast, when steel is deposited after IN625 (see Fig. 9-6b), no obvious interface can be observed and both alloy parts show corrosion resistance, indicating a strong mixing of the two alloys. It can be inferred that upon depositing the alloy of a higher melting point, the previous bead will be largely remelted and a newly mixed bead will be formed through a metallurgical reaction. Therefore, the alloy with a lower melting point should be deposited after the alloy with a higher melting point during the multi-material deposition when dilution is to be controlled.

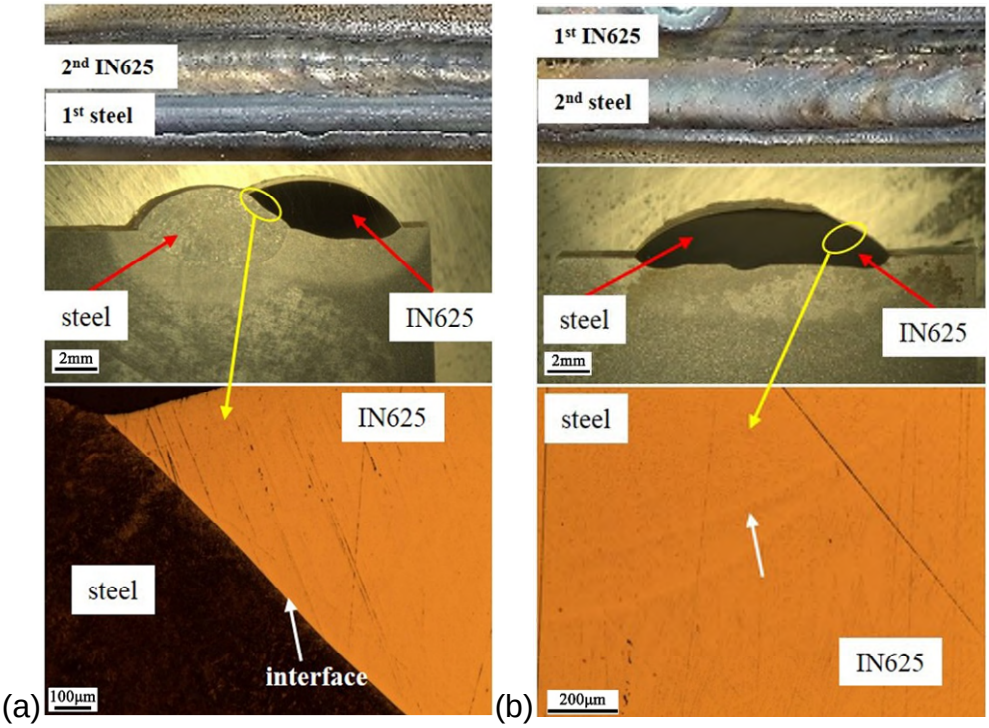

Figure 9-6 Effect of deposition sequence on the dilution level at the interface using plasma process (a) 1st steel, 2nd IN625 (b) 1st IN625, 2nd steel.

Fig. 9-7 shows the EDS elemental mapping results and EDS elemental analysis of the overlapped beads in Fig. 9-6. The numbers in the images represent the Fe content. As can be seen in Fig. 9-7a, when IN625 is deposited after steel, the typical elements Ni and Cr remain at the IN625 part, and Fe also remains mostly at the steel part. By contrast, when steel is deposited after IN625, as shown in Fig. 9-7b, the resulting mutual mixture causes a pronounced atomic diffusion: Ni and Cr are found to distribute all over the steel part. The Fe content measures in the IN625 layer is around 25% when IN625 is deposited after steel but increased to around 29.49-33.68% when IN625 is deposited before steel, both of which do not meet the 5% requirement.

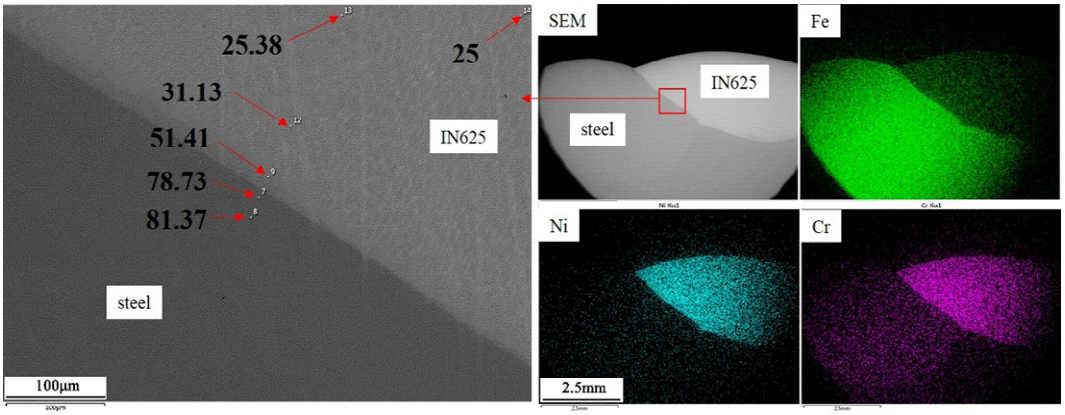

(a) EDS-Fe content (wt.%) Elemental mapping

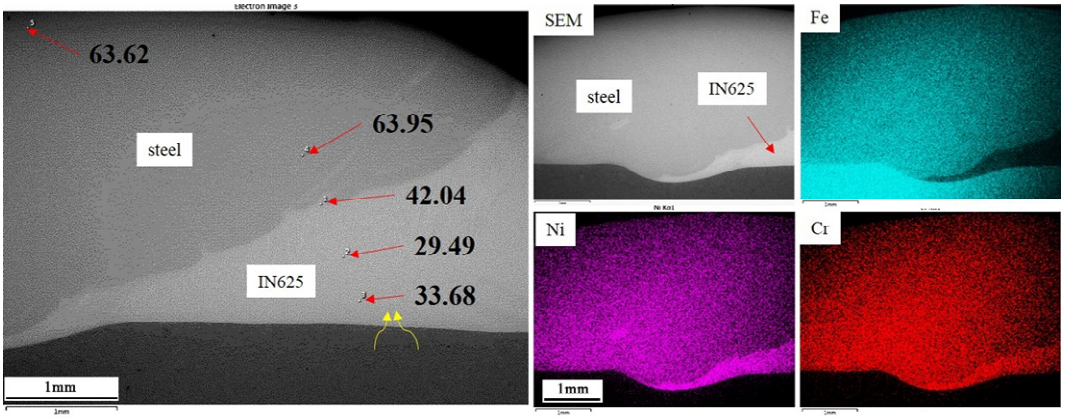

(b) Elemental mapping EDS-Fe content (wt.%)

Figure 9-7 SEM-EDS elemental mapping and EDS elemental analysis of the overlapped bead (a) 1st steel, 2nd IN625 (b) 1st IN625, 2nd steel.

9.3.3 Deposition strategy

9.3.3.1 Side-dilution

Fig. 9-8a shows the process monitoring in the parallel variant of the side-dilution strategy described in Fig. 9-3a, and the as deposited multi-material structure is shown in Fig. 9-8b. From Fig. 9-8a, the deposition process is steady, and the resulting bead shape is uniform with the plasma arc as the heat source; the final product also shows a good surface finish (Fig. 9-8b) and no defect, such as lack of fusion, can be observed from the cross-section, as shown in Fig. 9-8c (the sectioning position is indicated by the white line in Fig. 9-8b). From Fig. 9-8c, the thickness of one IN625 clad layer is around 3-4mm when using the side-dilution strategy; the macrostructure of the multi-material structure shows a staggered

morphology, indicating the mutual remelting during the side-by-side and layer-by-layer deposition process. The 1st steel passes show a moderate corrosion resistance, as compared with the 2nd steel passes and the 3rd IN625 passes. EDS analysis indicates that the Fe content in the IN625 layer far away from the interface is 22.98% and 18.42% near the bottom and the top respectively, which are far exceeding the requirement of 5%. The multi-material structure built using the oscillation variant of the side-dilution strategy (see Fig. 9-3b) is presented in Fig. 9-9. Good surface finish and defect-free structure are obtained, and similar staggered interface morphology is observed, indicating the same mutual mixing process upon the next deposition. The Fe content in the clad layer, being 18.82% and 13.59% at the bottom and the top respectively, is still much higher than the standard.

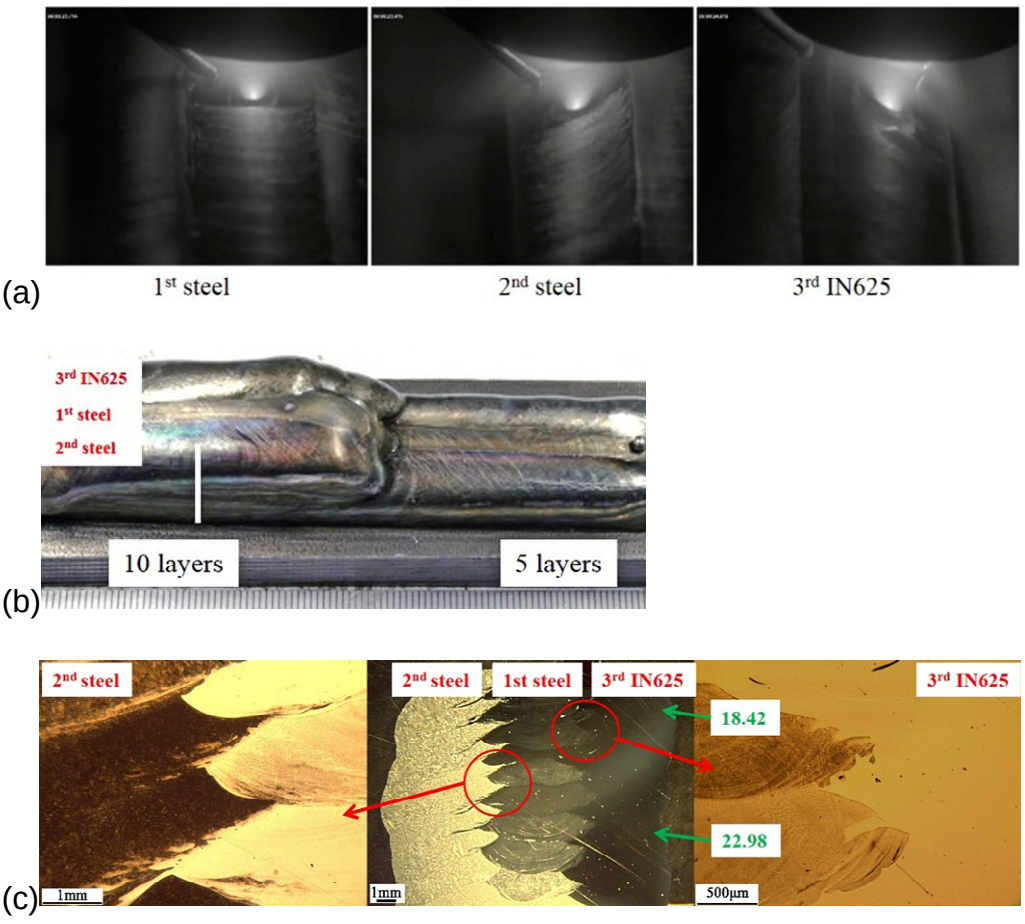

Figure 9-8 (a) Process monitoring for the parallel variant of the side-dilution strategy (b) the resulting multi-material structure and (c) macrographs of the multi-material structure and EDS results. (Using plasma process.)

(a) 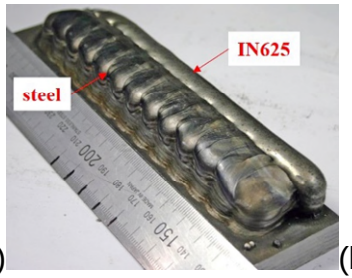

(b) 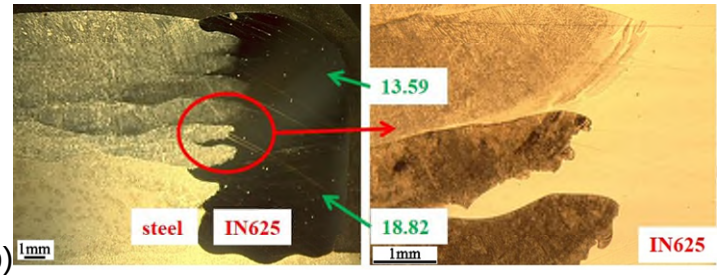

Figure 9-9 (a) Overview of the multi-material structure (b) cross-section of the multi-material structure built using the oscillation variant of the side-dilution strategy. (Using plasma process.)

9.3.3.2 Quasi bottom-dilution

Fig. 9-10 shows the multi-material deposition process using the quasi bottom-dilution strategy, wherein the thick steel wall is deposited first utilizing the oscillation path. Then two strategy variants, inclining the substrate or the torch by 45° as illustrated in Fig. 9-4, are implemented on either side of the steel wall for IN625 cladding. The final product is also shown in Fig. 9-10: the oscillated steel wall shows a certain level of surface waviness, but both the multi-material structure and the clad layer shows a good surface finish.

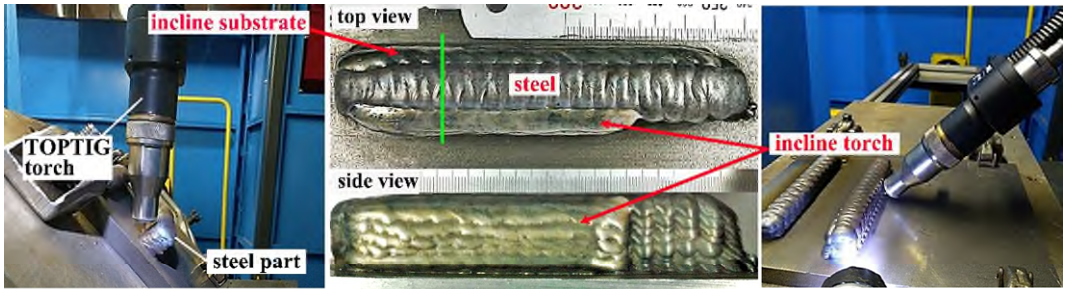

Figure 9-10 Quasi bottom-dilution strategy with the steel wall deposited using oscillation path (current=200A, WFS=1.6m/min, TS=2mm/s).

Fig. 9-11 shows the cross-section image and the Fe content measurements of the multi-material structure from Fig. 9-10. It can be seen that good structural integrity can be achieved by inclining either the torch or the substrate. A sound bonding between the steel wall and the clad layer is achieved, and no lack of fusion is observed despite the surface waviness of the oscillated steel wall. A clear interface is observed, indicating a limited dilution between the two alloys. The staggered morphology of the cross-section is not observed due to the quasi

bottom-dilution principle preventing the multi-material structure from mutual remelting. Inclining the torch results in the Fe content in the clad layer to be higher than 10%, while inclining the substrate leads to a Fe content as low as 8.54% which is very close to the requirement of 5%. The Fe content is lower than that measured in the structure built using side-dilution strategy.

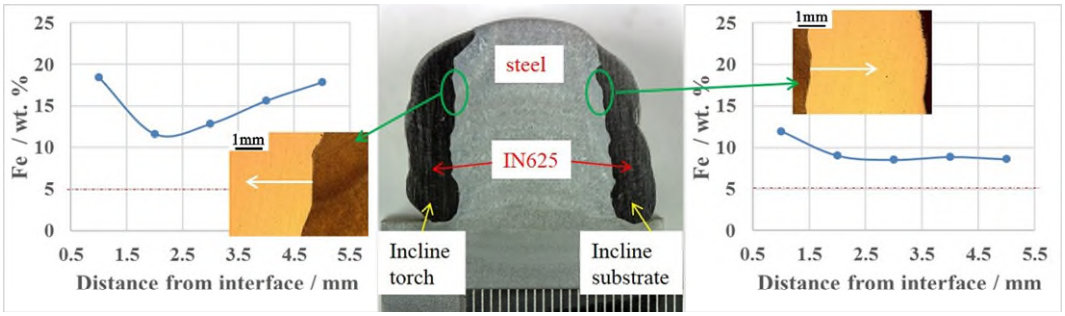

Figure 9-11 Cross-section and Fe distribution near the interface of the multi-material structure in Fig. 9-10 (sample sectioning position indicated by green line in Fig. 9-10; white arrow lines show the location and direction of the Fe measurements).

Furthermore, a steel wall structure is deposited using the parallel path, aiming at minimizing the surface waviness to reduce the likelihood of generating lack of fusions between the clad layer and the steel part. Inclining the substrate is applied in this deposition to reduce the Fe content in the clad layer, and one and two layers IN625 are cladded respectively, as shown in Fig. 9-12. Good bonding, similar to that observed in cladding the oscillated steel wall (see Fig. 9-11), is achieved. The Fe content in the clad layer is above 12%, which is slightly higher than that measured in the oscillated wall (Fig. 9-11) possibly due to the different surface waviness: the greater waviness in the oscillated steel wall provides larger reaction area for the dilution to happen; under the same arc energy, the smooth surface of the parallel wall provides less reaction area, thereby the dilution is more severe. When one more layer of IN625 is cladded, the Fe content is reduced to below 5% starting from 4mm away from the interface; and the entire thickness of the clad layer is around 7mm.

(a)

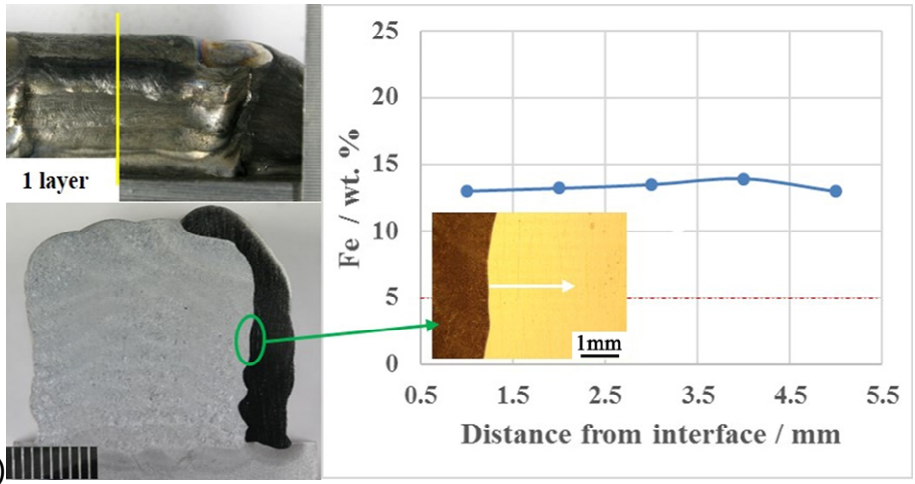

(b)

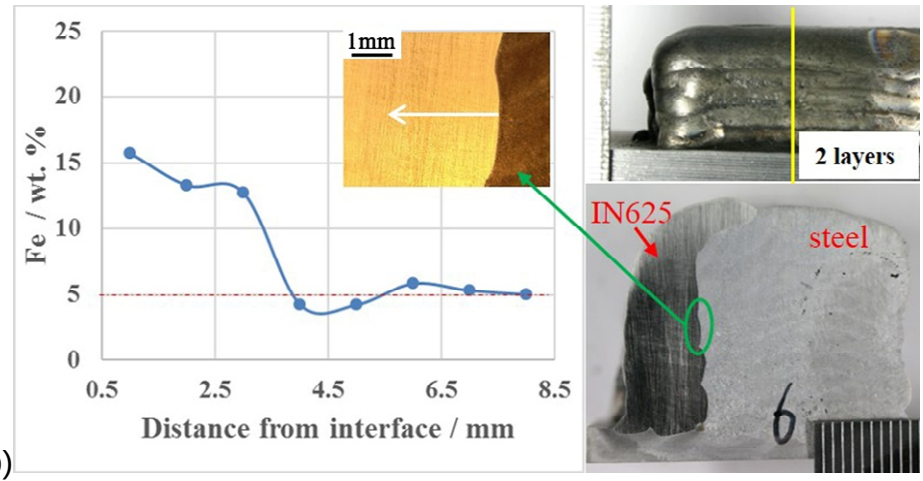

Figure 9-12 Cross section observation and Fe content measurement of the multi-material structure built using the parallel variant of the quasi bottom-dilution strategy (a) 1 layer cladding (b) 2 layers of cladding.

9.4 Discussion

9.4.1 Arc energy consumption

From Section 3.1, when keeping the current and TS constant, increasing the WFS proves to be an effective way of increasing the bead height while keeping the bead width constant. In arc deposition process, the arc serves as the heat source. The total energy provided by the arc is determined by the arc current and voltage, of which only a certain amount is delivered to the substrate and the rest is lost to the environment, known as arc efficiency (0.47 for plasma arc welding [26]). Among this net energy delivered to the substrate, only a small portion is used for

melting, and the rest is lost to the adjacent base metal through thermal conduction, known as melting efficiency (0.05-0.25 for plasma arc welding [26]).

Particularly in WAAM process in this study, the melting includes both the wire and the substrate. Considering that the wire is only 1.2mm in diameter, most of the melting energy is consumed for heating up the substrate and generating the melt pool, and only a very small amount (5-10%[3]) is used to melt the wire. Consequently, adding more wire (increasing the WFS) within some range does not affect the energy used for heating up the substrate. Note that the current and TS determines largely the melt pool shape, thereby the bead width; when the current and TS are constant, adding more wire mostly leads to the increase of bead height.

9.4.2 Mutual remelting during side-dilution strategy

The side-dilution strategy is more natural to implement since the side-by-side and layer-by-layer building principle makes it easier for WAAM to be applied if the geometry is the only concern. As has been shown by the deposition sequence study, IN625 should be deposited after steel to avoid excessive remelting. However, this only works within one layer. When depositing the next layer on top, the steel deposition will remelt the IN625 pass in the previous layer; besides, the previous IN625 pass is also partially exposed to the arc and therefore gets remelted by the arc directly, as shown in Fig. 9-13. These two mechanisms result in the mutual remelting between adjacent passes and successive layers, which is evidenced by the staggered morphology observed in the cross-section shown in Fig. 9-8c and Fig. 9-9b. The mutual remelting can be so excessive that distinguishing atoms of each alloy (Ni and Cr for IN625; Fe for steel) can be mixed thoroughly and found in the final structure far away from its initial deposit (as shown in Fig. 9-7b), which is not desired when dilution needs to be controlled.

[3] Calculated using the following process parameters: current=200-225A, voltage=22-23V, arc efficiency= 0.47; WFS=1.2-2.6m/min, wire diameter=1.2mm, density of IN625=8440kg/m3; special heat capacity of IN625=410J/kg°C; melting point of IN625=1290-1350°C, room temperature=25°C.

The excessive remelting mainly occurs when depositing steel by the side of the IN625 layer at the same level. Therefore, a possible solution is to keep a distance between the steel deposition and the IN625 deposition, thus preventing the clad layer from being remelted by the arc and steel deposition. This is the general idea of the quasi bottom-dilution strategy, as will be discussed next.

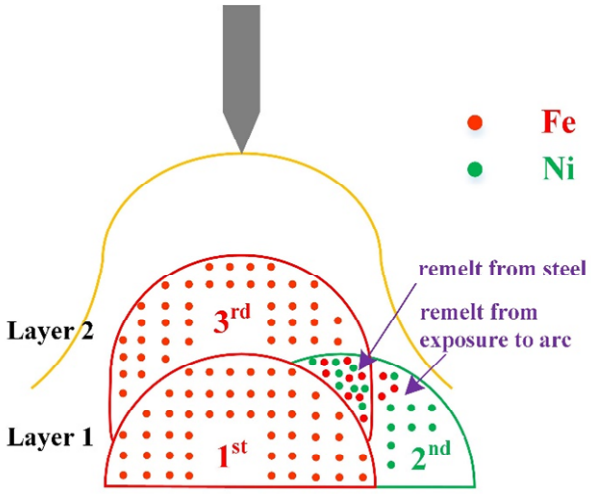

Figure 9-13 Illustration of the remelting process in side-dilution strategy during WAAM.

9.4.3 Control of dilution

In the conventional cladding process, the dilution is well controlled because the dilution is through a “bottom” manner: the diffusion mainly takes place at the bottom of melt pool boundary. Though the area right below the arc has the highest energy input from the arc, it is covered by the liquid IN625, and the diffusion happens at the liquid IN625-solid steel interface, thereby being a very limited level. Given this, the WAAM strategy should be as close as possible to the bottom-dilution manner.

The control of Fe diffusion in the present study is essentially the control of dilution in IN625 and low alloy steel dissimilar metal joining. When an IN625 layer is deposited on the steel part, as shown in Fig. 9-14, the Equation (9-1) holds [27,28] due to the energy conservation. The left side of the equation represents the melting power delivered by the arc, and the right side represents the power required for melting the filler metal and heating up the base metal.

$$\eta_a \eta_m P = V_{fm} E_{fm} + V_{bm} E_{bm} \quad \textbf{(9-1)}$$

Where η_a is the arc efficiency, η_m is the melting efficiency, P is the arc power, V_{fm} is the volumetric melting rate of filler metal, V_{bm} is the volumetric melting rate of base metal, E_{fm} is the melting enthalpy of filler metal, E_{bm} is the melting enthalpy of base metal, D is the dilution.

Given the dilution definition,

$$D = V_{bm}/(V_{fm} + V_{bm}) \quad \textbf{(9-2)}$$

The dilution can also be given as

$$D = \frac{1}{1 + \frac{E_{bm}}{\frac{\eta_a \eta_m P}{V_{fm}} - E_{fm}}} \quad \textbf{(9-3)}$$

From Equation (9-3), it can be seen that for a given alloy and welding process, dilution only depends on the ratio of volumetric filler metal feed rate to the melting power[4]. Particularly in WAAM process, it is the ratio of WFS to arc power: the higher the WFS and the lower arc power, the lower the dilution. Therefore, in order to control the Fe dilution in the multi-material structure during the WAAM process, more cladding material and less energy should be applied to the steel part that is to be cladded.

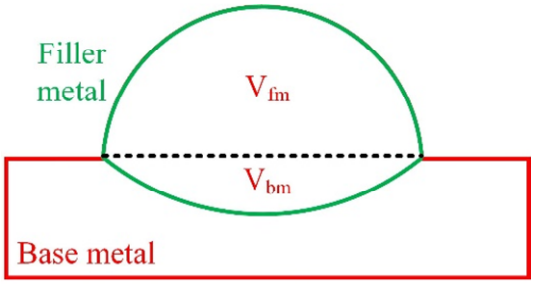

Figure 9-14 Illustration of the dilution for one-layer cladding.

[4] Bear in mind that there are still limitations to this equation as the enthalpies, arc efficiencies and melting efficiencies of the alloys are not constants.

Based on the above understanding, the reason why the side-dilution strategy fails to control the Fe content can be attributed to the remelting, which is essentially due to the excessive arc energy input. Besides, from Fig. 9-11, inclining the substrate results in a lower Fe content in the clad layer than inclining the torch. This can be explained using the illustration in Fig. 9-4. When inclining the substrate, the torch still keeps vertical, the wire is fed to the arc centre of the highest temperature, and the molten metal falls down to cover the steel part right below the arc. Note that the area right below the arc, as indicated by the purple dash rectangular in Fig. 9-4, has the highest temperature as compared to the area far away from the arc centre. Therefore, the steel part right below the arc is covered by the melt IN625 which has a lower melting point and prevents the steel from being excessively exposed to the arc. By contrast, when the torch is inclined, the arc keeps its shape along the tungsten electrode axis due to the arc stiffness [29]; however, the molten metal falls down vertically due to gravity or travels a bit horizontally due to the limited force applied by the plasma jet. Consequently, the steel part right below the arc is excessively exposed to the high-temperature arc and is subject to a higher energy input, as shown in Fig. 9-4b. It can be concluded that preventing the as deposited material from being excessively exposed to the arc, especially where the arc provides the highest temperature, is essential in avoiding excessive Fe diffusion.

Another effective method for Fe diffusion control, apart from the dilution control theory, is to have more than one clad layers. The more layers help to further dilute the undesired atoms and thereby control the atoms content to meet a certain requirement, which has been proved in Section 3.3.2.

9.4.4 Future work

The present work preliminarily shows that the proposed quasi bottom-dilution strategy could build the multi-material structure with the Fe content controlled below 5% in the clad layer; however, this is realized at 4mm away from the interface and the thickness of the clad layer is around 7mm which is much greater than the desired 2.5mm. In the future, process parameters will be optimized based on the dilution control theory to control the bead dimensions and reduce

the heat input and clad layer thickness, which may sacrifice the build rate at the same time. Besides, the inclination angle will be increased to near 90° to make the IN625 deposition more similar to the conventional cladding process, which involves the application of coordinate motion in the robotic programming. Using another IN625 wire containing less Fe (for example 0.5% [21]) is also an option. Based on these modifications, a demonstrator pipe will be produced, and the dilution level will be checked.

9.5 Conclusions

In the present study, the feasibility of applying the WAAM process to build IN625/low alloy steel multi-material structure with good structural integrity and desired dilution control was investigated. The following conclusions can be drawn.

1. In plasma process, a proposed method to control the bead height while keeping the bead width constant is by altering the WFS while keeping the TS constant, since the bead width is controlled by current and only a very small portion of the arc energy is used to melt the wire.
2. Given the around 100°C melting point difference, it is advised to deposit the alloy with lower melting point (IN625) after the alloy with higher melting point (steel) to avoid massive remelting and mixing upon depositing the latter alloy.
3. Both parallel and oscillation variants prove to be capable of building defect-free multi-material structures with the good surface finish and structural integrity.
4. Side-dilution strategy results in a staggered morphology at the cross-section of the multi-material structure, indicating a mutual remelting between deposition passes and layers which is responsible for the high Fe content in the clad layer.
5. The area right below the arc has the highest energy input. Therefore the steel part in this area should avoid being exposed to the arc directly; having the molten metal covering this area also helps to reduce the Fe diffusion.

6. Inclining the substrate results in less Fe diffusion than inclining the torch, since the former makes use of the melt IN625 to prevent the steel part right below the arc from being exposed to the arc.
7. The quasi bottom-dilution strategy with two layers cladding results in the Fe content in the clad layer to be below 5% starting from 4mm away from the interface, and the entire thickness of the clad layer is around 7mm.

9.6 References

[1] A. Sherman, Fusion cladding: Prevents pipeline wear and corrosion, Adv. Mater. Process. 171 (2013) 17–21.

[2] A. Samant, E. Vogli, A. Sherman, A. Ghildyal, Corrosion resistant alloy cladding for the oil & gas industry using a high-density infrared fusion cladding process, (2013) 1–19. http://www.abakaninc.com/media/Cladding-Using-High-Density-Infrared-Fusion-Cladding-Process.pdf.

[3] Special Metals, INCONEL alloy 625, in: 2013: pp. 1–18. doi:SMC-066.

[4] ASM International, ASM Handbook: Volume 2 Properties and selection: Nonferrous alloys and special-purpose materials, 1990.

[5] MatWeb Web Page, Special Metals INCONEL® Alloy 625, (n.d.). http://www.matweb.com/search/DataSheet.aspx?MatGUID=4a194f59f35a427dbc5009f043349cb5&ckck=1.

[6] MatWeb, Overview of materials for Low Carbon Steel, 2013 (2013). http://www.matweb.com/search/DataSheet.aspx?MatGUID=d1bdbccde4da4da4a9dbb8918d783b29.

[7] J.J. Lewandowski, M. Seifi, Metal Additive Manufacturing: A Review of Mechanical Properties, Annu. Rev. Mater. Res. 46 (2016) 151–186. doi:10.1146/annurev-matsci-070115-032024.

[8] S.H. Huang, P. Liu, A. Mokasdar, L. Hou, Additive manufacturing and its societal impact: A literature review, Int. J. Adv. Manuf. Technol. 67 (2013) 1191–1203. doi:10.1007/s00170-012-4558-5.

[9] D. Herzog, V. Seyda, E. Wycisk, C. Emmelmann, Additive manufacturing of metals, Acta Mater. 117 (2016) 371–392. doi:10.1016/j.actamat.2016.07.019.

[10] S. Singh, S. Ramakrishna, R. Singh, Material issues in additive manufacturing: A review, J. Manuf. Process. 25 (2017) 185–200. doi:10.1016/j.jmapro.2016.11.006.

[11] M.H. Farshidianfar, A. Khajepour, A.P. Gerlich, Effect of real-time cooling rate on microstructure in Laser Additive Manufacturing, J. Mater. Process. Technol. 231 (2016) 468–478. doi:10.1016/j.jmatprotec.2016.01.017.

[12] S.M. Thompson, L. Bian, N. Shamsaei, A. Yadollahi, An overview of Direct Laser Deposition for additive manufacturing; Part I: Transport phenomena, modeling and diagnostics, Addit. Manuf. 8 (2015) 36–62. doi:10.1016/j.addma.2015.07.001.

[13] N. Shamsaei, A. Yadollahi, L. Bian, S.M. Thompson, An overview of Direct Laser Deposition for additive manufacturing; Part II: Mechanical behavior, process parameter optimization and control, Addit. Manuf. 8 (2015) 12–35. doi:10.1016/j.addma.2015.07.002.

[14] S.W. Williams, F. Martina, A.C. Addison, J. Ding, G. Pardal, P. Colegrove, Wire+Arc Additive Manufacturing, Mater. Sci. Technol. 32 (2016) 641–647. doi:10.1179/1743284715Y.0000000073.

[15] X. Xu, J. Ding, S. Ganguly, C. Diao, S. Williams, Oxide accumulation effects on wire+arc layer-by-layer additive manufacture process, J. Mater. Process. Tech. 252 (2018) 739–750. doi:10.1016/j.jmatprotec.2017.10.030.

[16] B. Cong, R. Ouyang, B. Qi, J. Ding, Influence of Cold Metal Transfer Process and Its Heat Input on Weld Bead Geometry and Porosity of Aluminum-Copper Alloy Welds, Rare Met. Mater. Eng. 45 (2016) 606–611. doi:10.1016/S1875-5372(16)30080-7.

[17] F. Martina, P.A. Colegrove, S.W. Williams, J. Meyer, Microstructure of Interpass Rolled Wire + Arc Additive Manufacturing Ti-6Al-4V Components,

Metall. Mater. Trans. A Phys. Metall. Mater. Sci. 46 (2015) 6103–6118. doi:10.1007/s11661-015-3172-1.

[18] J. Gu, J. Ding, S.W. Williams, H. Gu, J. Bai, Y. Zhai, P. Ma, The strengthening effect of inter-layer cold working and post-deposition heat treatment on the additively manufactured Al– 6.3Cu alloy, Mater. Sci. Eng. A. 651 (2016) 18–26. doi:10.1016/j.jmatprotec.2015.11.006.

[19] X. Xu, S. Ganguly, J. Ding, S. Guo, S. Williams, F. Martina, Microstructural evolution and mechanical properties of maraging steel produced by wire + arc additive manufacture process, Mater. Charact. 143 (2018) 152–162. doi:10.1016/j.matchar.2017.12.002.

[20] D. Clark, M.R. Bache, M.T. Whittaker, Shaped metal deposition of a nickel alloy for aero engine applications, J. Mater. Process. Technol. 203 (2008) 439–448. doi:10.1016/j.jmatprotec.2007.10.051.

[21] M. Rozmus-Górnikowska, Ł. Cieniek, M. Blicharski, J. Kusiński, Microstructure and Microsegregation of an Inconel 625 Weld Overlay Produced on Steel Pipes by the Cold Metal Transfer Technique, Arch. Metall. Mater. 59 (2014) 16–19. doi:10.2478/amm-2014-0185.

[22] J.K. M. Rozmus-Górnikowska*, M. Blicharski, Influence of weld overlaying methods on microstructure and chemical composition of Inconel 625 boiler pipe coatings, Kov. Mater. 52 (2014) 1–7.

[23] M. Solecka, P. Petrzak, A. Radziszewska, The Microstructure of Weld Overlay Ni-Base Alloy Deposited on Carbon Steel by CMT Method, Solid State Phenom. 231 (2015) 119–124. doi:10.4028/www.scientific.net/SSP.231.119.

[24] T. Opderbecke, S. Guiheux, TOPTIG: Robotic TIG welding with integrated wire feeder, Weld. Int. 23 (2009) 523–529. doi:10.1080/09507110802543146.

[25] Y.K. Bandari, T.O.H. Charrett, F. Michel, J. Ding, S.W. Williams, R.P. Tatam, Compensation Strategies for Robotic Motion Errors for Additive Manufacturing (AM), Proc. 27th Annu. Int. Solid Free. Fabr. Symp. (2016) 8–10.

[26] J.N. Dupont, A.R. Marder, Thermal Efficiency of Arc Welding Processes, Weld. Res. Suppl. (1995) 406s–416s. doi:10.1016/j.jmatprotec.2014.12.002.

[27] J.N. Dupont, Dilution in Fusion Welding, ASM Handbook, Weld. Fundam. Process. 6A (2011) 115–121.

[28] J.N. DuPont, A.R. Marder, Dilution in single pass arc welds, Metall. Mater. Trans. B Process Metall. Mater. Process. Sci. 27 (1996) 481–489. doi:10.1007/BF02914913.

[29] J. Shi, Y. Zhou, L. Liu, Application of Pulsed Laser-TIG Hybrid Heat Source in Root Welding of Thick Plate Titanium Alloys, Appl. Sci. 7 (2017) 527. doi:10.3390/app7050527.

10 Summary

10.1 Overall discussion

10.1.1 Effect of oxides formation

A remarkable benefit from WAAM is the relatively low environmental requirement when compared with laser powder bed fusion and electron beam based AM process which involves essentially always an inert gas-filled chamber and a vacuum environment respectively. WAAM is more of an open process and high standard shielding is not always necessary. For example, WAAM of titanium alloys is always carried out using extra shielding (global shielding or local shielding), while WAAM of aluminium alloys and low carbon steels are usually carried out using torch shielding only. Using a perfect shielding providing the lowest possible oxygen level seems always to be beneficial, which, however, results in extra equipment (tent or chamber) and consumables (inert gas) investment, additional pumping and vacuuming time (from hours to days), and greater restriction to robot motion and occasional in-process maintenance. Besides, it is impossible to eliminate the oxygen in the WAAM environment even when every step is taken care of, and the wire could also contain a certain level of oxygen. The high affinity of some alloying elements to oxygen makes oxides formation inevitable during the layer by layer deposition process, though it may not be a significant amount. Hence, it is necessary to understand the oxides formation mechanism in various materials and whether or not they would affect the deposition process and the final products.

In WAAM of maraging steel, a mixture of Fe, Al and Ti oxides formed, floated to the weld pool surface and accumulated layer by layer, resulting in incremental deterioration of the surface condition making it more rough and porous with the progress of deposition. This adversely affects the stability of arc and the wetting and spreading behaviour of the weld pool in successive layers. The accumulation of oxides also added to the uncertainty of the layer dimension, worsen the surface finish and adversely impact upon the structural integrity. When depositing with torch shielding only, despite majority of the oxides floated to the weld pool surface, some oxide islands could be entrapped in between layers to cause lack

of fusion issues, and oxides of a few hundred nanometres were found to be dispersed in the additively manufactured structure and resulted in an 11.2% increase in UTS and a 19.4% decrease in elongation due to the due to the load bearing effect when compared to the structure built using torch plus tent shielding.

However, in WAAM of Inconel 718, a coherent oxide layer consisting of Cr_2O_3 and Al_2O_3 form so actively that with one deposition they almost fully cover the deposit. However, oxides don't accumulate during the layer by layer building process, ending up with only 0.5μm thick after 54 layers deposition; besides, oxides show no effect on the mechanical properties since the protective oxide layer prevents further oxygen from entering the bulk and forming oxides in the bulk.

The fact that oxides could affect both the surface waviness and mechanical properties of WAAM maraging steel but not Inconel 718 is determined by the types and characteristics of the oxides formed in the two alloys. The oxides formed in WAAM maraging steel is mostly a mixture of Al, Ti and Fe oxides and the Fe content could be as high as 62.41 wt.%. These oxides have a rough and porous nature, which provides varying wetting angles for the molten pool to cause irregular solidification front boundary and allows more passages for oxides to form inside the bulk. In contrast, the oxides formed in Inconel 718 are mainly a mixture of Cr_2O_3 and Al_2O_3 which are dense and coherent to the matrix in nature; therefore, these oxides do not deteriorate the surface condition for the next deposition. Besides, these oxides are known to be protective, thus preventing the thick oxide scale from formation.

10.1.2 Wire composition and wire quality

WAAM utilizes the commercial welding wire as the feedstock. The wire is fully melted and then solidifies to form a deposit therefore all that in the wire will go to the deposit, including alloying elements and defects. Since the wire is designed for welding purposes, it may not be perfect for WAAM for three reasons. Firstly, the wire may not contain identical alloying contents to the wrought alloy, while for some age hardening alloys the variation in the content of hardening constituents may affect the mechanical properties; in case of the multiple materials study,

using a wire with lower Fe content would also help to reduce the final Fe content in the clad layer. Secondly, the inclusions in the wire can also go to the WAAM part. For example, the TiN is found in both the wire and the fracture surface of Inconel 718, which might result in uncertainties in the mechanical behaviours during service. Thirdly, some alloying element such as Si is added in the wire for deoxidizing purpose in welding, which might not be necessary for WAAM in an inert atmosphere.

Chapter 6 shows that there is an around 50MPa strength difference of the WAAM Inconel 718 when using wires from two different suppliers; the literature also shows that using an Inconel 718 wire containing a low content of Nb could help control the formation of Laves phases in the welds. Hence, the wire source and quality should be taken into consideration when quality WAAM parts are of interest, and more efforts can be made to design wires with the composition customized to suit particular WAAM applications.

10.1.3 Process parameters and deposition strategies

Process parameters and building strategies could determine the bead shape, heat input and the resulting microstructure. In case of building complex-shaped components, a varying bead shape within one layer can be realized also by adjusting the parameters especially when using a process where the heat input and the wire feeding are independent of each other; for example, in the plasma arc based WAAM process, by adjusting the wire feed speed while keeping the travel speed constant, one can get a bead shape with varying bead height but constant bead, width which is beneficial for elbow structure building.

The selection of process parameters also needs to consider the metallurgical requirement. For example, when depositing maraging steel, the previous layer should be cooled down to below 121°C to minimize the austenite formation. The deposition strategies can make a difference to the WAAM microstructure. From the multiple materials study, different strategies can change the energy input into the as deposited material, which further determines the dilution level. Hence, a proper selection of process parameters and building strategies is crucial to obtain

the desired geometry, microstructure and mechanical properties of the WAAM parts.

10.1.4 Inherent thermal history

Different from the conventional casting and wrought process in which the entire part undergoes the same uniform thermal process, the thermal history in the WAAM process is in the form of numerous thermal pulses. Owing to this inherent non-uniform thermal history in WAAM, the material deposited at different locations of the component undergoes different numbers of thermal cycles, causing a consequence known as intrinsic aging effect, i.e., an inhomogeneous and non-uniform aging effect, for age-hardenable alloys. In WAAM maraging steel, the UTS difference between the bottom and the top could reach 287MPa; however, in case of WAAM Inconel 718 such difference is only 3MPa even though the material near the bottom has undergone 54 more thermal cycles. This indicates that Inconel 718, as an age-hardenable alloy, responds so slowly to the intrinsic aging effect from WAAM deposition that there is no noticeable aging taking place even after 54 layers deposition. Such a different aging response is determined by the alloying systems of the respective material. The aging response of the Nb-Al-Ti alloy system hardened IN718 is very sluggish as compared to the Al-Ti hardened alloys (such as maraging steel). No sign of hardening can be observed during the first 2-3 mins at the aging stage; during WAAM, this time is usually long enough to allow one fresh deposition to air cool through the aging temperature range yet retains softness and ductility.

Besides, due to the fast cooling rate of the WAAM deposition process, elemental segregation is inevitable in the as deposited WAAM structure, especially for high alloy materials such as maraging steel and Inconel 718. In maraging steel, Mo and Ti segregate mostly, promoting the formation of retained austenite which is undesirable when strength is of interest. In Inconel 718, Nb segregates severely, causing the formation of massive brittle Laves phases which are detrimental to the mechanical properties. In addition, the directional thermal conduction route in WAAM process favours the development of large columnar grains since the dendrites tend to grow opposite to the direction of the highest thermal gradient.

The large columnar grains featured WAAM microstructure, as compared to the finely equiaxed grains featured wrought microstructure, is the key to understand the difference in mechanical properties between the WAAM material and its wrought counterparts.

10.1.5 Standard heat treatment

Heat treatment provides the means to create a desired microstructure and phase distribution and morphology. Both maraging steel and Inconel 718 gain strength through age hardening. However, when the industrial standard heat treatment is applied, the WAAM alloys usually shows an inferior mechanical behaviour to the wrought counterparts, which proves the dependence of heat treatment response on the grain structure. When aging the wrought material, the starting grain structure features finely equiaxed grains with high angle grain boundaries and free from segregation, and the matrix is in a supersaturated state; the aging process allows controlled release of the precipitates to strengthening the matrix during the solution treatment. However, in the case of WAAM maraging steel, the starting microstructure features large columnar grains. The low angle grain boundaries provide less diffusion routes for the hardening constituents to dissolve into the matrix; thereby, the following aging response is much less pronounced to result in a UTS that is 350MPa lower than the wrought standard. The key to solving this issue is to create numerous high angle grain boundaries which would provide more diffusion paths of the solute atoms. As for Inconel 718, the starting microstructure also features large columnar grains as well as massive Laves phases. However, the standard solution treatment temperature is not high enough to completely dissolve the Laves phase. Though a higher homogenization temperature could eliminate the undesired Laves phase in the WAAM Inconel 718, it also results in noticeable grain coarsening. Thereby, after applying the standard heat treatment (solution plus double aging) to the WAAM Inconel 718, Laves phases are still present; this, together with the large columnar grain size, results in the around 220MPa lower UTS as compared to the wrought alloy.

10.1.6 Cold rolling

WAAM structures are manufactured through the solidification of molten wire; therefore, WAAM is essentially a micro casting process except that WAAM features freeforming and non-uniform thermal cycles. The as deposited WAAM material tends to exhibit the disadvantages associated with solidified structures, e.g. dendritic structure and segregation. Wrought alloys have superior properties to cast alloys due to additional thermomechanical processing, which involves several passes of rolling and repeated heating of the structure to eliminate elemental segregation and induce dynamic recrystallization. The lack of plastic deformation during the WAAM process is the reason why the epitaxial growth could keep developing and results in the large columnar grains. In the interpass cold rolling assisted WAAM process, rolling causes a significant amount of flattening of the deposits, which destroys the crystalline order and reorients the crystallites in these directions by grain flow. The energy is stored in the strained alloy; when the strained alloy is heated up to the recrystallization temperature, recrystallization will take place with the stored energy as the driving force. With interpass cold rolling applied, the mechanical properties of both WAAM maraging steel and Inconel 718 are improved to the wrought level.

In maraging steel, rolling induced recrystallization results in the formations of high-angle grain boundaries, which promotes the atomic diffusion to enable a more uniform solutionizing process and improves the subsequent aging response by 105-110%. The main contribution of overall strengthening was attributed to the enhanced aging process, accounting for more than 95% of the entire strength increase.

As for Inconel 718, rolling induced recrystallization results in a non-uniformly recrystallized core consisting of small columnar grains and massive finely equiaxed grains. The formation of the finely equiaxed grains proves the capability of rolling in inducing recrystallization in WAAM process, whereas the presence of small columnar grains indicates that such recrystallization is far from effective to induce uniform recrystallization throughout the WAAM structure. This is determined by the non-uniform thermal history and the non-uniform strain

distribution after rolling, the latter resulting from the roller shape, rolling load and rolling strategies. When applying interpass rolling to WAAM of Inconel 718, the main strengthening resulted from the recrystallization which on the one hand, produces grain size reduction strengthening, and on the other hand, creates larger grain boundary area to allow more precipitation at the grain boundaries.

10.1.7 Recommendations

1. Shielding. A proper shielding to help avoid oxidation during deposition is beneficial, especially for alloys which is not known for oxidation resistance. In WAAM the torch shielding only is not enough and it is recommended to use an additional local shielding or global shielding. For maraging steel, the oxygen content is recommended to be less than 300-500ppm.
2. Wire. A high quality and clean wire with less defects and inclusions is recommended to be selected as the feedstock in WAAM. More work should be devoted to design the WAAM-oriented wire with adjusted chemical composition.
3. Undesired phase control. For WAAM of maraging steel, retained austenite should be carefully controlled by avoiding maraging steel being exposed to a high temperature for a prolonged period. For WAAM of Inconel 718, Laves phases should be avoided; using a wire with less Nb and a post homogenization process could be helpful but bear in mind that the latter would cause grain coarsening.
4. Heat treatment. The industrial standard heat treatment designed for wrought alloy does not work for WAAM maraging steel and Inconel 718. It is recommended to apply interpass rolling to change the grain structure so that the heat treatment would work, or more efforts should be made to customize heat treatment for WAAM grain structure.
5. Dilution control. It is recommended to use a less heat input and a higher wire feed speed when depositing multiple materials so as to minimize the dilution.

10.2 Contribution to knowledge

The research gaps stated in Chapter 1 have been filled. For the first time, WAAM has been applied to produce maraging steel and Inconel 625/low alloy steel

multiple materials, and research has been conducted to improve the material properties of WAAM maraging steel and Inconel 718 through heat treatment and interpass cold rolling. By finishing the PhD programme, the following intellectual contribution has been made,

1. Oxides formed in WAAM of maraging deteriorate the surface finish and are also found to embed in the bulk to reduce the elongation; however, oxide formation shows no effect on WAAM of Inconel 718.
2. The alloying system of maraging steel shows a very quick aging response to the inherent WAAM thermal history, while the alloying system of Inconel 718 shows a very sluggish one.
3. Large columnar grains are both developed in WAAM maraging steel and Inconel 718, which results in the inferior strength to the wrought alloys.
4. Interpass cold rolling is effective in improving the strength of WAAM maraging steel and Inconel 718 by creating more high-angle grain boundaries to enhance the solutionizing and the subsequent aging process and reducing the grain size respectively.
5. Dilution can be controlled when depositing multiple materials by controlling the heating input with a proper deposition strategy established.

10.3 Conclusions

1. Oxides formation should be avoided as much as possible in WAAM.
2. WAAM can be applied to deposit maraging steel and Inconel 718.
3. WAAM can be used to build multiple materials.
4. Industrial standard heat treatments for wrought alloys does not work for WAAM maraging steel and Inconel 718.
5. Interpass cold rolling can improve the tensile strength of WAAM maraging steel and Inconel 718.

10.4 Future work

The present PhD work can be further extended into the following research directions.

10.4.1 Power source comparison

This PhD work tries to correlate the WAAM process with the WAAM material properties. The arc, serving as a heat source, has not been deeply studied. The two major arc power sources, CMT and plasma, are both applied in this search; though some difference in mechanical properties can be observed between CMT-WAAM Inconel 718 and plasma-WAAM Inconel 718 (Chapter 6 and Chapter 7), it is not clear if this is due to the different heat source characteristics, such as arc pressure and temperature distributions, since the heat input of the two processes are not controlled at the same level. In the future, a comparative study could be carried out using CMT and plasma arc respectively to produce the same WAAM alloy with identical heat input. The following microstructure study and mechanical testing will give a conclusion; if they do produce different mechanical properties even under the same heat input, then more work should be carried out to understand the effect of arc characteristics on the microstructure and mechanical properties of the WAAM alloy.

10.4.2 Structural integrity study

The entire PhD work focuses on the room temperature tensile strength of the WAAM alloy. However, before the WAAM alloy can be adopted by the industry, extensive studies regarding the structural integrity should be carried out. For example, maraging steel is known for the superior strength and toughness, but the toughness is not studied in this PhD work. Inconel 718 is mostly used at elevated temperature (up to 650°C), hence the high-temperature properties such as creep strength and rupture strength need to be studied. Besides, although the residual Laves phases do not weaken the room temperature tensile strength in the interpass rolled WAAM Inconel 718, the uncertainties they may bring about at high-temperature service need to be understood. Other properties such as fatigue strength are also of great concern to many clients.

10.4.3 WAAM microstructure modification

From the present PhD work, the inferiority of the WAAM alloy to the wrought alloy results mainly from its inherent microstructure featured by severe elemental

segregation and solidified dendritic microstructure. Since the dendrite growth is related to the thermal gradient, in the future efforts could be made to apply techniques such as active or compulsory cooling to change the thermal gradient locally and thereby the dendrites growth. Besides, although the interpass cold rolling applied in this study proves to be effective in strengthening the WAAM alloy, the ultimate recrystallization is still not complete and uniform. Therefore, in the future, more efforts should be made to develop more effective rolling-like techniques such as cold peening, hot rolling and laser shock peening, aiming to make the WAAM alloy microstructurally or metallurgically as close as possible to the wrought alloy.